Electric field-induced strain control of magnetism in in-plane and out-of-plane magnetized thin films

Dissertation
zur Erlangung des Grades
Doktor der Naturwissenschaften (Dr. rer. nat.)
am Fachbereich Physik
der Johannes Gutenberg-Universität Mainz

von:
Mariia Filianina
geboren in Nizhniy Tagil (Russland)
Mainz, 2020

Mariia Filianina

Electric Field-Induced Strain Control of Magnetism in In-Plane and Out-Of-Plane Magnetized Thin Films

Datum der mündlichen Prüfung: 6. Januar, 2021

Gutachter:	Aus Datenschutzgründen entfernt / Removed due to data privacy
Kommission:	Aus Datenschutzgründen entfernt / Removed due to data privacy

Johannes Gutenberg Universität Mainz
AG Kläui
Institut für Physik
Staudingerweg 7
55128, Mainz

Мне ни к чему одические рати
И прелесть элегических затей.
По мне, в стихах все быть должно некстати,
Не так, как у людей.

Когда б вы знали, из какого сора
Растут стихи, не ведая стыда,
Как желтый одуванчик у забора,
Как лопухи и лебеда.

Сердитый окрик, дегтя запах свежий,
Таинственная плесень на стене...
И стих уже звучит, задорен, нежен,
На радость вам и мне.

А. Ахматова

EIDESSTATTLICHE ERKLÄRUNG

Hiermit erkläre ich an Eides statt, dass ich meine Dissertation selbständig und ohne fremde Hilfe verfasst und keine anderen als die von mir angegebenen Quellen und Hilfsmittel zur Erstellung meiner Dissertation verwendet habe. Die Arbeit ist in vorliegender oder ähnlicher Form bei keiner anderen Prüfungsbehörde zur Erlangung eines Doktorgrades eingereicht worden.

Mainz, den

Mariia Filianina

ABSTRACT

Magnetism has been playing a very important role in information technology, as one bit of information in a hard disc drive is nowadays stored as the magnetization direction of a ferromagnetic domain. Conventionally, to write information, i.e. to manipulate the magnetization, large electric currents have been used producing either a magnetic field in a coil or a spin-torque in a multilayer stack required to switch the magnetization direction. These current-induced switching strategies suffer, however, from significant energy dissipation due to Joule heating. Inevitably, this results in growing energy consumption, in particular, given the rapid spread of technology.

For this reason, the research for alternative, low-power mechanisms that can be used to control the magnetization and other potentially relevant phenomena in magnetism is of interest from both a fundamental and a technological point of view. The results presented in this thesis demonstrate the electric field-induced strain control of static and dynamic properties of in-plane and out-of-plane magnetized systems, which is beneficial for applications as this approach avoids using power-hungry charge currents.

First, by investigating magnetic vortex structures in magnetostrictive Ni discs by means of time-resolved x-ray photoemission electron microscopy combined with magnetic circular dichroism as the contrast mechanism, we show that the electrically controlled strain changes the static magnetic configuration of the vortex state and leads to a strong deformation of the vortex core gyration orbit. This deformation is accompanied by a modification of the gyration eigenfrequency, which enables local tuning of the gyration resonance. This is particularly useful as it may allow for a selective switching of vortices for which the gyration eigenfrequency is tuned accordingly by electric field-induced strain. This demonstrates the feasibility of fully electrical control of magnetic vortex dynamics, which paves a way towards use in future device applications.

Secondly, we investigate energy-efficient control and engineering of the spin-orbit torques (SOTs) and the Dzyaloshinskii-Moriya interaction (DMI) in W/$Co_{20}Fe_{60}B_{20}$/MgO multilayers with perpendicular magnetic anisotropy by means of electric field-induced strain. In this thesis, by magnetotransport measurements, we show experimentally that the magnitude of the SOTs in a perpendicularly magnetized system can be tuned and even increased by piezoelectric strain. Specifically, we find that tensile strain enhances the amplitude of the damping-like torque in W/$Co_{20}Fe_{60}B_{20}$/MgO multilayers, while compressive strain leads to a decrease. We explain our experimental findings by theoretical electronic structure calculations, which reveal that uniaxial strain modifies the symmetry and orbital polarization of the states, which is then reflected in behavior of the SOTs reproducing our experimental findings.

Furthermore, we show that piezoelectric strain is a low-power means to control the magnitude of the DMI in a given system on demand and the estimated efficiency of the DMI change is found to be orders of magnitude larger than that, reported for the DMI control by gate voltage in complex HM/FM/Oxide systems. We interpret our experimental results with the help of first-principles calculations of the DMI in systems with variable strain.

Finally, we demonstrate the piezoelectric strain control of the microscopic domain structure of W/$Co_{20}Fe_{60}B_{20}$/MgO films close to the spin-reorientation transition (SRT), where the effective magnetic anisotropy is reduced and the impact of the strain-induced magnetic anisotropy is maximized. Furthermore, we find a destructive effect of x-rays on the magnetic properties of certain thin-film systems, which suggests that one needs to take care when analyzing magnetic anisotropies in such systems. Thus, this part of our results constitutes relevant insights for the field of spintronics where x-ray based techniques are widely used for investigations of magnetic systems.

KURZFASSUNG

Magnetische Eingeschaften von Materialen sind seit langem von großer technischer Bedeutung. Zum Beispiel wird digitale Information auf Festplatten als Magnetisierungszustand eines ferromagnetischen Elements (Domäne) nicht-flüchtig gespeichert. Üblicherweise werden diese Magnetisierungszustände durch große elektrische Ströme manipuliert, die Magnetfelder in Spulen oder Spin-Drehmomente in mehrschichtigen Systemen erzeugen. Die strominduzierten Methoden sind jedoch wegen der Dissipationsverluste der Stromerzeugung sehr ernergieintensiv. Das führt zwangsläufig zu dem steigenden Energieverbrauch durch die rasante technologische Entwicklung und deren Verbreitung. Aus diesem Grund hat die Erforschung alternativer Mechanismen, die mit geringem Energieverbrauch Magnetisierungszustände und andere potenziell relevante Phänomene im Magnetismus steuern können, enormes technologisches und physikalisches Interesse erzeugt.

Diese Dissertation beschäftigt sich mit der energieeffizienten Kontrolle von statischen und dynamischen magnetischen Eingeschaften von nanostrukturierten, ferromagnetischen Materialien durch die piezoelektrische Spannung, welche für Anwendungen von grundlegender Bedeutung ist, weil bei dieser Strategie die Verwendung von Ladungsströme mit hohem Energieverbrauch vermieden wird.

Zuerst untersuchen wir mittels Röntgenmikroskopie die statische Spinstruktur und Magnetisierungsdynamik von Nickel-Nanostrukturen die durch piezoelektrische Spannung modifiziert wurden. Wir beobachten neben den durch mechanische Spannung induzierten Modifikationen der statischen Domänenkonfiguration der magnetischen Wirbel (Vortizes), dass die elektrisch gesteuerte mechanische Spannung zu einer starken Verformung der Gyrationstajektorie des Vortexkerns führt. Die Verformung geht mit einer Modifikation der Gyrationseigenfrequenz einher, was eine lokale Kontrolle der Gyrationsresonanz ermöglicht. Dieser Befund ist besonders nützlich, da er ein selektives Schalten von Vortizes ermöglichen kann, für die die Gyrationseigenfrequenz durch energieeffizientes anlegen einer elektrischen Spannung entsprechend abgestimmt ist. Dies verspricht eine vollständig elektrische Steuerung der magnetischen Vortexdynamik, die wichtig für den zukünftige Mikrowellen-Anwendungen ist.

Im nächsten Teil der Dissertation untersuchen wir die energieeffiziente Kontrolle der Spin-Bahn-Drehmomente (spin-orbit torques, SOTs) und der Dzyaloshinskii-Moriya-Wechselwirkung (Dzyaloshinskii-Moriya interaction, DMI) in dünnen W/$Co_{20}Fe_{60}B_{20}$/MgO mehrschichtigen Filmen mit senkrechter magnetischer Anisotropie durch E-feldinduzierte Spannung. Mittels Transportmessungen zeigen wir erstmals experimentell, dass die Größe der SOTs in einem senkrecht magnetisierten System durch piezoelektrische Spannung eingestellt und sogar erhöht werden kann. Durch den Vergleich mit fortschrittlichen *ab initio* Berechnungen der elektronischen Struktur, identifizieren wir den mikroskopischen Ursprung der beobachteten Reaktion der SOTs auf eine angelegte Spannung. Die theoretische Ergebnisse zeigen, dass die Spannung die Symmetrie und die Orbitalpolarisation der Zustände verändert, was die Eigenschaften der SOTs eindeutig beeinflusst und unsere experimentellen Ergebnisse reproduziert.

Weiterhin analysieren wir der Einfluss der piezoelektrische Spannung auf die DMI, deren Größe sich sowohl aufgrund der Zug- als auch der Druckspannung erheblich ändert. Wir stellen fest, dass die DMI-Änderung viel größer ist als jene, die durch Gatespannung in komplexen oxidbasierten Systemen beobachtet wurde. Durch *ab initio* Berechnungen der DMI entwickeln wir ein mikroskopisches Verständnis des experimentellen Befunde. Die genannten Ergebnisse zeigen, dass das elektrische feldinduzierte Spannung zur elektrischen Kontrolle von magnetischen Eingeschaften genutzt werden kann.

Zum Schluss, demonstrieren wir die piezoelektrische Spannungskontrolle der mikroskopischen Domänenstruktur von W/$Co_{20}Fe_{60}B_{20}$/MgO-Filmen in der Nähe des Spin-Neuorientierungsübergangs, wobei die effektive magnetische Anisotropie verringert und der Einfluss der spannungsinduzierten magnetischen Anisotropie maximiert wird.

Darüber hinaus finden wir eine modifizierende Wirkung von Röntgenstrahlen auf die magnetischen Eigenschaften einiger Dünnschichtsysteme, was darauf hindeutet, dass bei der Analyse magnetischer Anisotropien in solchen Systemen diese Effekte in Betracht gezogen müssen. Daher stellt dieser Teil unserer Ergebnisse relevante Erkenntnisse für das Gebiet der Spintronik dar, wo röntgenbasierte Techniken häufig für Untersuchungen verwendet werden.

CONTENTS

LIST OF ACRONYMS

ACE	acetone
AFM	atomic force microscopy
AHE	anomalous Hall effect
AMR	anisotropic magnetoresistance
BTO	$BaTiO_2$
CPW	coplanar wave guide
DFT	density functional theory
DL	damping-like
DMI	Dzyaloshinskii-Moriya interaction
DOS	density of states
DW	domain wall
EBL	electron beam lithography
EB	exchange bias
FE	ferroelectric
FM	ferromagnetic material
FL	field-like
FOV	field of view
GMR	giant magnetoresistance
HM	heavy metal
HV	high voltage
HWHM	half-width at half-maximum
iSGE	inverse spin-galvanic effect
IT	information technology
IBE	ion beam etching
IPA	isopropanol
IP	in-plane
LLG	Landau-Lifshitz-Gilbert
MO	magneto-optic
MMA	methyl-methacrylate
MPB	morphotropic phase boundary
MIBK	methylisobutyl-ketone
ME	magnetoelastic
MLWFs	maximally localized Wannier functions
MOKE	magneto-optical Kerr effect
OHE	ordinary Hall effect
OOP	out-of-plane

PHE	planar Hall effect
PMA	perpendicular magnetic anisotropy
PZT	$Pb(Zr,Ti)O_3$
PMN-PT	$[Pb(Mg_{0.33}Nb_{0.66}O_3)]_{0.68}$-$[PbTiO_3]_{0.32}$
PEEM	photoemission electron microscopy
PEM	photo-elastic modulator
PCB	printed circuit board
PMMA	poly-methyl-methacrylate
ROI	region of interest
RKKY	Ruderman-Kittel-Kasuya-Yosida
SEM	scanning electron microscopy
SHA	spin Hall angle
STV	start voltage
SOC	spin-orbit coupling
SRT	spin-reorientation transition
SOT	spin-orbit torque
SQUID	superconducting quantum interference device
STT	spin-transfer torque
ST-FMR	spin-torque ferromagnetic resonance
SHE	spin Hall effect
TMR	tunneling magnetoresistance
VC	vortex core
VCMA	voltage-induced magnetic anisotropy
UHV	ultra-high vacuum
UV	ultra-violet
WF	writing field
XAS	x-ray absorption spectrum
XMCD	x-ray magnetic circular dichroism

INTRODUCTION

> We are a very data-hungry society, we're using more and more and more data and all of that is using more and more energy.
>
> Nicola Jones [1]

The increasingly rapid development of information technology (IT), which started with the invention of a transistor, gave rise to many novel fields such as Artificial Intelligence, Big Data, etc. On the downside, this suggests a further increase of the consumed energy required to store and manipulate the information. The amount of energy consumed for the purposes of the IT industry is expected to increase up to 10 PW h by 2030 (approximately 51 % of global electricity), taking into account the current device characteristics and the pace of advancement [2, 3]. Furthermore, energy dissipation during the switching process of the information bits is seen as a primary obstacle to continued miniaturization of the digital device's features. Indeed, defined by Moore's law [4], the tendency that the number of transistors in a circuit doubles every two years, turns out to no longer be accurate. For example, the feature size of integrated circuits was reduced from 10 nm to only 7 nm between 2016 and 2018 [5], while according to Moore's law, already 5 nm was predicted for the year 2014 [6].

The need to fit the demands of future IT has stimulated a growing research aimed to explore the novel low-power approaches to manipulate information. For decades magnetism offers an attractive alternative to transistor-based technology, as a bit of information can be stored as the magnetization direction of ferromagnetic elements, which now have the size as small as 25 nm [7]. Just like a transistor can encode two logic states (binary bits) by the presence or absence of electrons in its channel, the magnetization direction can be switched between two stable orientations, thus, encoding binary bits and allowing for memory or computing operation.

Among the advantages of the magnetic memory over the charge-based memory is its non-volatility, i.e., the ability to keep the digital data stored for years passively with no standby power dissipation. This is enabled by the magnetic anisotropy within the bits, which means that the nanomagnets have an energy barrier that separates the two bistable states and thus prevents it from flipping spontaneously [8]. From the operation point of view, it has been shown that the minimum energy dissipated to switch a charge-based transistor at a temperature T is $\propto Nk_\mathrm{B}T\ln(1/p)$, where k_B is the Boltzmann constant, N is the number of information carriers (electrons or holes) in the device and p is the bit error probability [9]. On the other hand, the minimum energy dissipated to switch the magnetization of single-domain nanomagnet, comprising many electron spins, can be only $\propto k_\mathrm{B}T\ln(1/p)$ [9, 10]. This is because the exchange interaction between the spins makes them rotate together, which gives the spin-based elements an advantage over a charge-based one.

The revolutionary role of the exchange interaction in magnetic memory was realized with the discovery of the giant magnetoresistance (GMR) effect by P. Grünberg and A. Fert in 1988, which, in turn, lead to the emergence of the field of spintronics [11, 12]. Spintronics utilizes the electron's spin as an additional degree of freedom along with its charge to process data. Combining these two properties of an electron, the GMR effect allows one to convert the spin information to electrical signals as it manifests itself in a drastic change of the electrical resistance with the relative orientation of the magnetization in adjacent ferromagnetic layers. A remarkable technological consequence is that the GMR and the related tunneling magnetoresistance (TMR) effects allowed for downscaling of spintronic devices without losing performance, e.g., the read-out sensitivity.

However, the advantage of the magnetic memory is often lost when taking into account the method employed to switch the magnetization. Most prominent switching strategies between two states are using the electric current-generated magnetic field [13], current-driven domain wall motion [14], current-induced spin torque [15, 16, 17], voltage control of magnetic anisotropy [18, 19] or electric field-induced strain [20] realized in, e.g., multiferroic systems [21, 22, 23]. Unfortunately, using current-induced switching strategies can be energetically inefficient due to Ohmic loss and the associated Joule heating and, in this case, the energy dissipated in the switching circuit far exceeds the energy dissipated in the magnet. On the other hand, receiving considerable attention in recent years, the electric field-induced strain mediated switching has shown the energy dissipation in the order of $10-100$ aJ,[1] which is very small compared to the state-of-the art spin torque-induced switching mechanism that dissipates 100 fJ for switching a nanomagnet in 1 ns [24].

Hence, being in the focus of the cutting edge research in the field of spintronics, the electric field-induced strain control of magnetism at the nanoscale is at the core of this thesis. The

---

[1] Assuming that all energy dissipated is to charge the capacitive piezoelectric layer employed to generate the required strain.

results presented in this thesis give an insight on the potentially attractive phenomena for spintronics, which occur in artificial multiferroic systems, consisting of a piezoelectric substrate coupled with a magnetostrictive ferromagnetic layer, where this low-power approach can be successfully employed.

The thesis is organized as follows. **Chapter 1** gives a theoretical background on magnetism in condensed matter necessary for understanding the results reported in this thesis. In particular, it introduces such fundamental concepts mentioned above as the exchange interaction, the magnetic anisotropy, and describes the origin of the novel phenomena of spintronics, such as the Dzyaloshinskii-Moriya interaction and the spin-orbit torques. Furthermore, a brief account of the mechanism underlying the electric field-induced control in multiferroics is given.

In **Chapter 2** we discuss the main experimental techniques employed for the fabrication and characterization of the studied systems. We draw particular attention to the properties of the piezoelectric substrates, which are used for the electrical generation of strain.

In **Chapter 3**, we focus on the effects of piezoelectric strain on magnetic vortex states hosted in in-plane magnetized nanostructures and on the microwave-induced vortex core gyration dynamics. Magnetic vortices are nano-objects that are potentially interesting for applications in spintronics [25, 26]owing to their four-fold degenerate ground state and the magnetic configuration, which prevents cross-talk among adjacent vortices, hence, enabling high magnetic stability of this structures. We show that electrically induced strain promises a means of low-power manipulation of these structures.

Then, we shift the focus to the heterostructures with a perpendicularly magnetized thin heavy metal (HM)/ferromagnetic material (FM) multilayer. Such perpendicular anisotropy systems are the systems of choice for applications as they exhibit better scaling behavior for higher packing density and thermal stability compared to conventionally used in-plane systems. Furthermore, the interface of the FM with the HM is known to give rise to the spin-orbit torque (SOT) [27, 28, 29], which is the most efficient mechanism among the current-induced magnetization switching schemes and, hence, a low-power tool to dynamically control the SOTs is desired to realize complex and more efficient switching concepts.

Another spin-orbit phenomenon that is naturally present in these HM/FM structures with broken inversion symmetry is the DMI. The DMI is responsible for stabilizing novel topological spin textures, e.g., homochiral domain walls [30] and magnetic skyrmions [31, 32], which are believed to hold bright prospects for innovative information processing. In order to use the DMI to tailor the magnetic properties (e.g. the chirality of the magnetic domain walls) or to “write” or “delete” skyrmions, it is necessary to tune the magnitude of this interaction to which the electric field-induced strain is expected to be an attractive tool. The results on the strain response of the

SOTs and the DMI in perpendicularly magnetized systems are discussed in **Chapters 4** and **5**, respectively.

Chapter 6 deals with a set of results, which are, to a large extent, puzzling and the interpretation of which is still debated. More specifically, we discuss the magnetic anisotropy changes observed during the x-ray irradiation and the strain-induced control of the magnetic domain structure in the vicinity of the spin reorientation transition.

The conclusions and outlooks to each topic discussed in the thesis are given at the end of each Chapter, **Chapter 7** concludes the whole thesis. Finally, the **Appendices** are comprised of sections that include mostly technical details and also contain sections about peculiarities of working with the piezoelectric substrates.

CHAPTER 1

THEORETICAL BACKGROUND

In this Chapter, we will start from the level of quantum mechanics and work our way up to the phenomenological description of magnetism in condensed matter. We will consider the different phenomenological thermodynamic contributions to the magnetic free energy, which determine the magnetic state of the system's equilibrium. Furthermore, the dynamical behavior of the magnetization and its theoretical description by the classical Landau-Lifshitz-Gilbert (LLG) equation will be introduced. In this Chapter, we will also discuss the origins of such phenomena as DMI and SOT, which are at the focus of this thesis. Finally, we will introduce the electric field-induced strain as a promising approach to control magnetism.

1.1 MICROSCOPIC ORIGINS OF MAGNETISM

Magnetic properties of solids come from the magnetism of their electrons. In fact, the electron itself is an intrinsically magnetic object. Therefore, to understand the origin of magnetism, a quantum mechanical description is necessary. For this, we will follow the description from Refs. [33, 34].

1.1.1 ATOMIC MAGNETISM

The angular momentum of an electron has two different contributions, first of which is the *intrinsic* angular momentum, called *spin*. The second contribution is its *orbital* momentum, as the electron can constitute a current running around a nucleus. In a real atom, the orbital angular momentum depends on the electronic state occupied by the electron. The proportionality

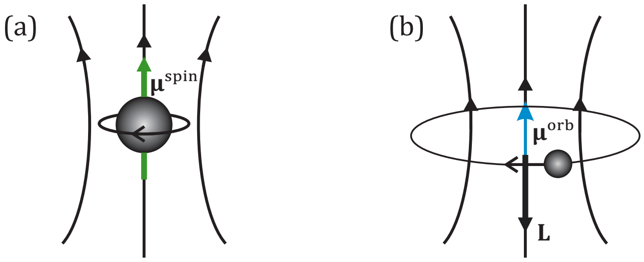

Figure 1.1: Magnetic moments associated with (a) spin angular momentum, $\boldsymbol{\mu}^{\rm spin}$, of an electron and (b) the electron's orbital motion, $\boldsymbol{\mu}^{\rm orb}$.

between the orbital angular momentum **L** and the corresponding magnetic moment $\boldsymbol{\mu}$ is given by the equation

$$\boldsymbol{\mu} = \gamma \mathbf{L}, \tag{1.1}$$

where $\gamma = -\frac{e}{2m_e}$, is the *gyromagnetic ratio*. Using the quantum numbers l= 0, 1, 2... and m_l= $0, \pm1, \pm2, ... \pm l$, we can express the component of orbital angular momentum along a fixed axis $L_z = m_l \hbar$, and its magnitude $L = \sqrt{l(l+1)}\hbar$, Thus, the component of the magnetic moment along the z direction is

$$\mu_z^{\rm orb} = -m_l \mu_{\rm B}, \tag{1.2}$$

and the magnitude of the total magnetic moment is $\sqrt{l(l+1)}\mu_{\rm B}$, where $\mu_{\rm B} = \frac{e\hbar}{2m_e}$ is the Bohr magneton.

To consider the intrinsic angular momentum of an electron, a spin quantum number $s = \pm\frac{1}{2}$ is used. Therefore, the component $S_z = m_s \hbar$ of the electron's spin angular momentum along z can have two possible values, namely $\hbar/2$ and $-\hbar/2$. In the following, these alternatives will be referred to as *"spin-up"* and *"spin-down"*, respectively. The magnitude S of the spin angular momentum of an electron is $\sqrt{s(s+1)}\hbar = \frac{\sqrt{3}}{2}\hbar$.

Likewise, the spin angular momentum gives rise to an intrinsic magnetic moment, whose component along the z axis equals to

$$\mu_z^{\rm spin} = -g m_{\rm s} \mu_{\rm B}, \tag{1.3}$$

and the magnitude equals to $\sqrt{s(s+1)}g\mu_{\rm B}$. The constant g here is known as the Landé g-factor and $g \approx 2$, so that the component of the intrinsic magnetic moment of the electron along the z axis is $\pm\mu_{\rm B}$. Strictly speaking, the g-factor is taken into account in the expression for the orbital moment as well. However, since for orbital moment it equals 1, it is usually left out. Thus, the spin angular momentum is twice as effective as the orbital one in creating a magnetic moment from the angular momentum.

As mentioned above, an electron usually has both orbital and intrinsic spin angular momentum, so that the expression for the total magnetic moment is given by the sum of the orbital and the spin contributions:

$$\boldsymbol{\mu}^{\text{total}} = \boldsymbol{\mu}^{\text{spin}} + \boldsymbol{\mu}^{\text{orb}} = -\frac{\mu_{\text{B}}}{\hbar}(\mathbf{L} + 2\mathbf{S})\,, \tag{1.4}$$

The spin and orbital angular momenta interact via so-called *spin-orbit coupling (SOC)*. This phenomenon plays an important role in magnetism being responsible for a range of interesting and important effects, such as the magnetocrystalline anisotropy, the magnetoelastic (ME) effect etc., as we will see later. For now, we will concentrate on the basic quantum mechanical description of the SOC.

The SOC can be thought of classically as if the spin magnetic moment of an electron interacts with the magnetic field in the rest frame of this electron, arising from the orbital motion of the electron itself in the electric field of the positively charged atomic nucleus. The energy associated with the SOC can, therefore, be calculated as the energy of an electron with a magnetic moment $\boldsymbol{\mu}$ in a magnetic field $\mathbf{B}$, given by $E = -\boldsymbol{\mu} \cdot \mathbf{B}$. The SOC energy, thus, takes the form

$$E_{\text{SO}} = -\boldsymbol{\mu}^{\text{spin}} \cdot \mathbf{B}_{\text{SO}} = -\lambda_{\text{SO}} \mathbf{S} \cdot \mathbf{L}, \tag{1.5}$$

where λ_{SO} is the SOC constant, that reflects the strength of the SOC.

In the presence of the SOC the Hamiltonian comprises not only the Coulomb interaction but also the SOC term. In this case, however, $\mathbf{S}$ and $\mathbf{L}$ are not separately conserved but the total angular momentum $\mathbf{J} = \mathbf{S} + \mathbf{L}$ is conserved. Likewise, there is a total angular momentum quantum number j associated with it, which takes integer values in the range between $|l - s|$ and $l + s$. The magnitude of the total angular moment then takes the from $\sqrt{j(j+1)}\hbar$ with its z component $J_z = m_j\hbar$, where $m_j = -j, -j+1, ... j-1, j$.

In an atom with many electrons, those occupying unfilled shells can combine to give rise to a non-zero net angular momentum, while the electrons in filled shells do not contribute at all. The configurations, obtained by differently combining together the spin and orbital angular momenta from the electrons in the unfilled shells,[1] define the energy of an atom. Beside the

---

[1] If the contribution of SOC is small, as is the case for light atoms, the interaction of individual spin and orbital momenta of one electron with those of the other electrons in the atom, prevails. They all combine to form a total spin angular momentum $\mathbf{S} = \sum_{i=1}^{Z} \boldsymbol{s}_i$ and a total orbital angular momentum $\mathbf{L} = \sum_{i=1}^{Z} \boldsymbol{l}_i$, where $\boldsymbol{s}_i$ and $\boldsymbol{l}_i$ are individual electrons' spin and orbital momenta. Then $\mathbf{S}$ and $\mathbf{L}$ couple together and form a total angular momentum $\mathbf{J} = \mathbf{S} + \mathbf{L}$, which is know as *LS-coupling*. For heavier atoms, where the SOC is strong, the spin and angular momenta of a single electron interact first, i.e. $\boldsymbol{j}_i = \boldsymbol{s}_i + \boldsymbol{l}_i$, and then the total momenta of all electrons in the atom interact

Pauli exclusion principle, a set of rules - *Hund's rules* - is known to describe how the electrons in an atom fill the corresponding shells, resulting in the atomic minimum energy state. As a consequence, there are elements, such as Fe, Co and Ni (known as *itinerant ferromagnets*), with not completely filled $3d$-sub-shells. This results in a non-zero atomic magnetic moment, which is one of the requirements for obtaining conventional ferromagnetism in condensed matter.

1.1.2 MAGNETISM IN CONDENSED MATTER

The presence of magnetic ordering in condensed matter implies the existence of a long-range interaction that allows individual magnetic moments to communicate with each other and align themselves in a certain way. The first interaction to think of would be the *magnetic dipolar interaction.* For two magnetic moments $\boldsymbol{\mu}_1$ and $\boldsymbol{\mu}_2$, separated by the distance $\mathbf{r}$, the energy is calculated as

$$E = \frac{\mu_0}{4\pi r^3}\left(\boldsymbol{\mu}_1 \cdot \boldsymbol{\mu}_2 - \frac{3}{r^2}(\boldsymbol{\mu}_1 \cdot \mathbf{r})(\boldsymbol{\mu}_2 \cdot \mathbf{r})\right). \tag{1.6}$$

Equation 1.6 reflects the dependence of the energy on the mutual alignment of the two magnetic moments as well as on their spatial separation. However, a quick estimate gives an energy of about 10^{-23} J for two moments of 1 μ_B each separated by 1 Å. This is equivalent to about 1 K in temperature, which is much lower than the ordering temperature of most materials (typically, hundreds of K). Thus, the magnetic dipolar interaction is too weak to account for the ordering of most magnetic materials. Therefore, there should be another mechanism of the coupling of individual magnetic moments in a solid. Such an interaction originates from the natural property of electrons being *Fermi-particles*, which we consider below.

HEISENBERG EXCHANGE INTERACTION

For simplicity, we will start with a simple system of two electrons. For each of them we introduce a wave function $\psi_i(\mathbf{r}_i)$, where the $i = 1,2$ identifies the first and the second electrons. The total system then can be described by the wave function $\psi(\mathbf{r}_1, \mathbf{r}_2)$ as an overlap of the two single-electron wave functions. Obeying quantum mechanical rules stating that the elections are indistinguishable fermions, the wave function $\psi(\mathbf{r}_1, \mathbf{r}_2)$ can be represented in either of these forms:

$$\psi(\mathbf{r}_1, \mathbf{r}_2) = \frac{1}{\sqrt{2}}[\psi_1(\mathbf{r}_1)\psi_2(\mathbf{r}_2) + \psi_1(\mathbf{r}_2)\psi_2(\mathbf{r}_1)]\chi_s, \tag{1.7}$$

$$\psi(\mathbf{r}_1, \mathbf{r}_2) = \frac{1}{\sqrt{2}}[\psi_1(\mathbf{r}_1)\psi_2(\mathbf{r}_2) - \psi_1(\mathbf{r}_2)\psi_2(\mathbf{r}_1)]\chi_t, \tag{1.8}$$

---

with each other. This situation is know as *jj-coupling* and the total angular momentum is then expressed as $\mathbf{J} = \sum_{i=1}^{Z} \boldsymbol{j}_i$.

where the χ_{s}, being antisymmetric relative to the exchange of the electrons for a *singlet* state, and χ_{t}, symmetric for a *triplet* state, are the spin parts of the wave function.

Knowing the energies of the singlet and triplet states we can re-write the Hamiltonian in the form of an effective Hamiltonian as

$$\hat{H} = \frac{1}{4}(E_{\mathrm{s}} + 3E_{\mathrm{t}}) - (E_{\mathrm{s}} - E_{\mathrm{t}})\mathbf{S}_1 \cdot \mathbf{S}_2 \,. \tag{1.9}$$

The first term in Eq. 1.9 does not depend on the spin of the system and can, therefore, be included into other constant energy terms, while the second term includes spins. The energy difference $(E_{\mathrm{s}} - E_{\mathrm{t}})$ is defined as $2J$, where J is the *exchange integral* or *exchange constant*. Hence, the spin-dependent term in the effective Hamiltonian in Eq. 1.9 takes the form

$$\hat{H}^{\mathrm{spin}} = -2J\mathbf{S}_1 \cdot \mathbf{S}_2 \,. \tag{1.10}$$

Such a representation of the effective Hamiltonian is convenient because one can directly see that the energy of the states with $\mathbf{S} = 0$ and $\mathbf{S} = 1$ depends on the sign of the exchange constant J. If $J > 0$, i.e. $E_{\mathrm{s}} > E_{\mathrm{t}}$, the triplet state is more energetically favorable, so that the spins couple *ferromagnetically*, like in Ni, Co and Fe. In the case, when $J < 0$, i.e. $E_{\mathrm{s}} < E_{\mathrm{t}}$, the singlet state is more favorable, and the spins are aligned *antiferromagnetically*.

The derivation of Eq. 1.10 described above is quite simple but only for a system with two electrons. It becomes increasingly complicated once we generalize it to many-body systems. However, if the exchange interaction is restricted to occur only between nearest neighbors, we can write down the Hamiltonian of the *Heisenberg model*:

$$\hat{H} = -\sum_{ij} J_{ij}\mathbf{S}_i \cdot \mathbf{S}_j \,, \tag{1.11}$$

where J_{ij} is the exchange constant between the i-th and the j-th spins.

The strength of the exchange interaction defines the temperature $T_{\mathrm{C}} \propto \frac{J}{k_{\mathrm{B}}}$, above which a material is no longer ferromagnetic, but is in a paramagnetic phase. When $T > T_{\mathrm{C}}$, the spontaneous magnetization of the system is lost due to large thermal excitations. For $T < T_{\mathrm{C}}$, the exchange interaction dominates and the spontaneous ferromagnetic ordering is restored. For example, the Curie temperatures of three FM, Fe, Co and Ni, used in this thesis, are 1044 K, 1388 K and 628 K, respectively [35].

If the exchange interaction is realized by the interaction of electrons from neighboring magnetic atoms, it is known as *direct exchange*. In this case, there is direct coupling between the electrons of the magnetic atoms. Quite often the direct exchange interaction is not strong enough to determine the magnetic properties of a material as the direct overlap between neighboring magnetic orbitals might be too weak. For example, in rare-earth elements, a direct exchange of the neighboring $4f$ orbitals is not possible because they are strongly localized. Even

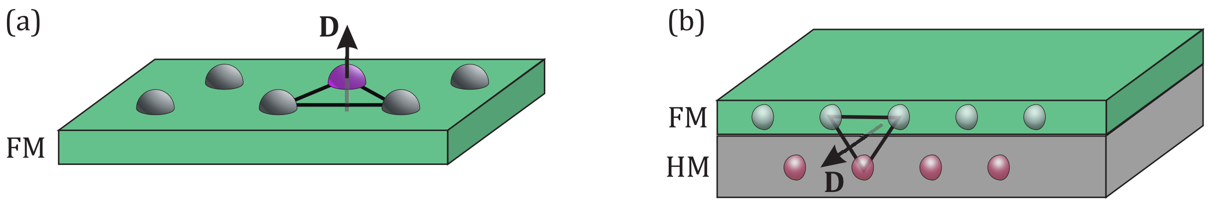

Figure 1.2: Sketch of the DMI vector (black arrow) in (a) a crystal with impurities and (b) at the interface of a FM layer and a HM layer with strong SOC. In (b) the DMI vector is perpendicular to the plane, defined by the two FM atoms (gray) and the different atom species (red) with strong SOC, i.e. pointing along the interface. For a bulk material like MnSi, the breaking of the inversion symmetry occurs within the unit cell. Adapted from [32].

in transition metals, such as Ni, Fe and Co, where the $3d$ orbitals are spread further away from the nucleus, it is not obvious why the direct exchange should lead to the observed magnetic properties. Furthermore, these materials are metals where the conduction electrons play an important role and therefore the contribution of both localized and itinerant electrons should be taken into account. Moreover, there is a number of oxides that show ferro- and antiferromagnetic alignment, which means that, in this case, the magnetic exchange interaction should be realized via oxygen orbitals. In the systems mentioned above, so-called *indirect exchange interaction* comes into play. Prominent examples of the indirect exchange interaction are superexchange, double exchange and Ruderman-Kittel-Kasuya-Yosida (RKKY) interaction, which are described elsewhere [35, 36].

Dzyaloshinskii - Moriya interaction (DMI)

Among indirect exchange interactions, of interest for this thesis is the so-called DMI, also known as the *antisymmetric exchange interaction* [37, 38]. The DMI arises in systems with large SOC and requires local environments with sufficiently low symmetry, e.g., broken inversion symmetry. Based on the origin of the symmetry break the DMI is generally classified as bulk DMI arising in non-centrosymmetric crystal structures, Fig. 1.2 (a), and interfacial DMI due to structural inversion asymmetry, typically present at FM/HM interfaces, Fig. 1.2 (b). In both cases, the interaction is mediated by a HM atom. Here, we will limit the discussion to the interfacial DMI, because it is the one that occurs in FM/HM systems considered in this thesis.

Generally, in a system without inversion symmetry, there can exist an electric field, **E**, along the symmetry violation direction (along the surface normal in the case of structure inversion asymmetry at the interface). In the static coordinate frame of a moving electron with the velocity $\mathbf{v}$, this electric field is transformed into an effective spin-orbit field, $\mathbf{B}_{\mathrm{SO}} \propto \mathbf{v} \times \mathbf{E}$, which, upon interaction with the electron's spin $\boldsymbol{\sigma}$, gives rise to an additional term in the Hamiltonian $H_{\mathrm{SO}} = \alpha_{\mathrm{R}} \boldsymbol{\sigma}(\mathbf{k} \times \mathbf{z})$, known as the Rashba term [39]. As a consequence, for the electrons moving in xy plane with momentum $\mathbf{k}$ in the presence of an electric field E_z, the two-fold degeneracy of the energy zones at $\mathbf{k} \neq 0$ is lifted [39]. The Rashba parameter α_{R}describes the strength of the SOC and the size of the resulting spin-splitting. Thus, due to the Rashba field, the conduction electrons mediating the DMI experience an additional weak spin-dependent potential in the vicinity of the HM species, which is also sensitive to the propagation direction of the electrons (see Fig. 1.3).

Phenomenologically, the DMI interaction leads to the following term in the Hamiltonian, which can be derived by second order perturbation calculation [37, 38]:

$$\hat{H}_{\mathrm{DMI}} = \sum_{i \neq j} \mathbf{D}_{ij} \cdot \left(\mathbf{S}_i \times \mathbf{S}_j \right) , \tag{1.12}$$

where $\mathbf{D}_{ij}$ is the DMI vector with respect to the moments $\mathbf{S}_i$ and $\mathbf{S}_j$, with its magnitude proportional to the SOC in the system, and it reflects the strength of the DMI.[2] The vector $\mathbf{D}$ vanishes in the configuration of the crystal field with an inversion symmetry with respect to the center between the two magnetic ions. However, in general, $\mathbf{D}$ may not vanish and then, depending on the symmetry, it lies parallel or perpendicular to the line connecting the two spins [40].

While the microscopic origin of the DMI in magnetic bilayers is still a subject of debate [41], large SOC, $d-d$ orbital hybridization, and the position of the electronic states of the HM relative to the Fermi level are thought to determine the strength of the DMI.

A systematic series of first principle calculations summarized in Fig. 1.4 (a) provides a deeper insight into the physics of the interfacial DMI in 3d-FM/HM bilayers. Specifically, there is a correlation (*i*) between the DMI and the magnetic moment of the FM layer and (*ii*) between the DMI and the relative energetic position of the 3d/5d states near the Fermi level. Both these criteria are crucial because the anisotropic exchange mechanism requires spin-flip transitions between occupied and unoccupied states which involve the spin-orbit split states [43, 44].

This idea is illustrated in Fig. 1.4 (b), where on the right the 5d W states are positioned with respect to the Fermi level and the 3d states of several FM materials. The filling of the 3d electrons on the left is according to Hund's rules. It is evident that if both spin channels are almost occupied or unoccupied, as for the case of V and Ni, the transitions between these states will not contribute to the DMI. However, in the case of Mn, where the spin channels are fully occupied

---

[2] The summation here covers all different pairs of moments but is usually restricted to the nearest magnetic neighbors due to their dominant role.

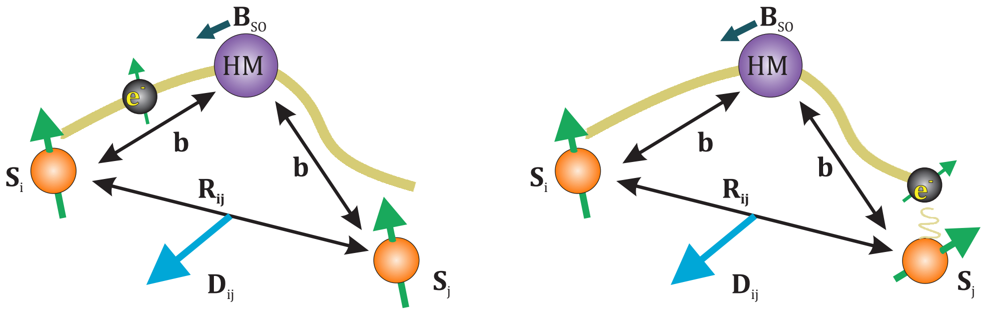

Figure 1.3: A schematic picture showing the origin of magnetic interaction between neighboring spins $\mathbf{S}_i$ and $\mathbf{S}_j$ which due to the electrons which hopping from site i to site j and then back [42]. For a ferromagnetic film the electrons move in the presence of the exchange field, in exchange split bands for which the time-reversal symmetry is lost. Additionally, the Rashba term also results in an additional interaction acting on the spin of the electron via the spin-orbit field, $\mathbf{B}_{\mathrm{SO}}$.

(unoccupied), all transitions via spin-orbit active 5d states contribute to the DMI, thus producing a higher DMI.[3] Therefore, the filling of the FM electronic states, as well as the presence of the spin-orbit 5d states at the Fermi level energetically close to the unoccupied minority states, can facilitate the spin-flip process necessary for the DMI.

To illustrate the mechanism of the involved $3d-5d-3d$ hopping, we consider a wavefunction hopping across the HM/FM interface, following the arguments in Ref. [41].[4] Whenever the electron hops onto the HM atom, the presence of the SOC causes the magnetic moment of the electron to rotate creating a swirling spin texture. As this electron hops back to the FM, its rotated magnetic moment perturbs the wave functions of the FM via the exchange interaction. This perturbation, in turn, modifies the free energy and generates the DMI [45]. Hence, the stronger the HM-FM hybridization, the stronger the perturbation of energy due to the hopping electron and the resulting DMI is, thus, larger. Therefore, according to this interpretation [41], the sign of the DMI is decided by the interplay between the spin mixing terms due to the SOC and the strength of the DMI is decided by the HM-FM hybridization.

In magnetic systems, where the Heisenberg exchange interaction and a finite DMI are both present, the total Hamiltonian of the system contains both energy terms. Thus, the competition of the symmetric (Heisenberg) and antisymmetric (DMI) exchange interactions leads to cant-

---

[3] Note that for half-filled Fe and Cr the situation is similar because the exchange gap is rather small and there are still Fe spin-down (Cr spin-up) states unoccupied (occupied).

[4] Ref. [44] assumes a different model where the DMI is attributed to the transitions between different d orbitals than the ones of the model in Ref. [41].

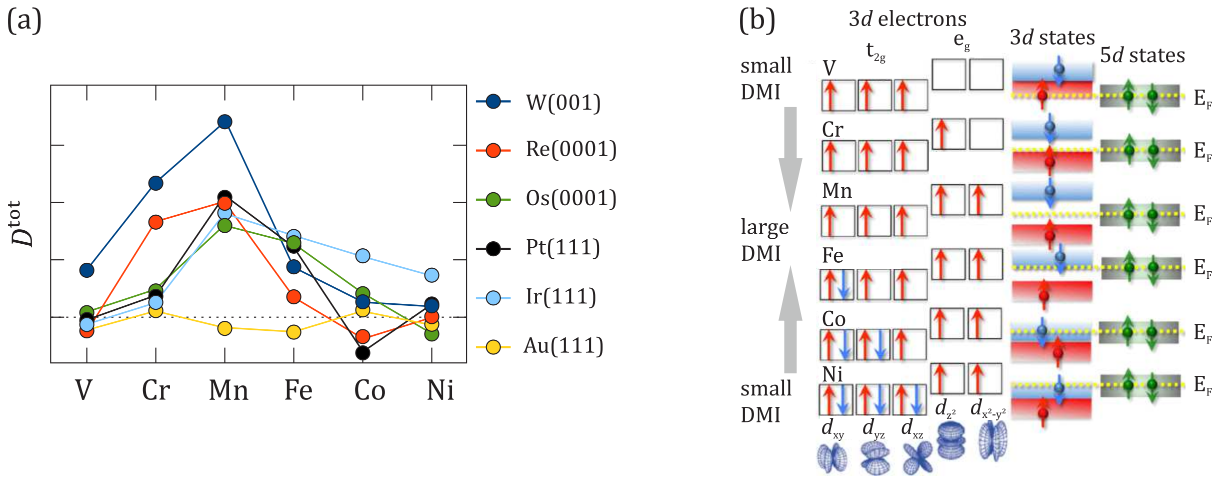

Figure 1.4: (a) Qualitative magnitudes and signs of the DMI for different metal combinations estimated from theoretical calculations in the case of a FM monolayers for perfect interfaces in Ref. [43]. (b) Left: filling of electronic states with spin-up (red) and spin-down (blue) $3d$ electrons in a $3d$ element according to Hund's first rule. Right: spin-split band positions of $3d$ states relative to the Fermi level and $5d$ W states. Note that the $5d$ states are shown degenerate at the Fermi level, since the $5d$ bandwidth is much larger than the crystal-field splitting. Adapted from [43].

ing of the neighboring magnetic moments.[5] The DMI is know to give rise to certain magnetic phases [38, 37, 46] and, as we will discuss later in Section 1.2.6, it stabilizes chiral spin structures [47, 48, 49, 50], in particular, chiral magnetic skyrmions [51, 52, 53, 54]. The impact of the DMI on the spin structure of perpendicularly magnetized films will be further considered in Sec. 1.2.6.

MAGNETISM OF ITINERANT ELECTRONS

As mentioned above, in metallic systems the exchange interaction is realized via itinerant electrons, so that the description using the Heisenberg Hamiltonian is not well-suited for these systems. Indeed, the experimentally measured magnetic moment per atom in iron of about 2.2 μ_{B} can not be understood on the basis of localized moments on ions. Thus, in metals, we need to apply a different set of arguments.

Electrons in the broad parabolic s-bands, which carry most of the current, interact with the more localized electrons of the d-orbitals, mediating the exchange interaction, and through

---

[5] If only the DMI and exchange interaction were present in the system, the interplay between both would lead to minimization of the total energy for a spiraling magnetization with a periodicity of $l_{\text{spir}} = 4\pi\frac{A}{D}$.

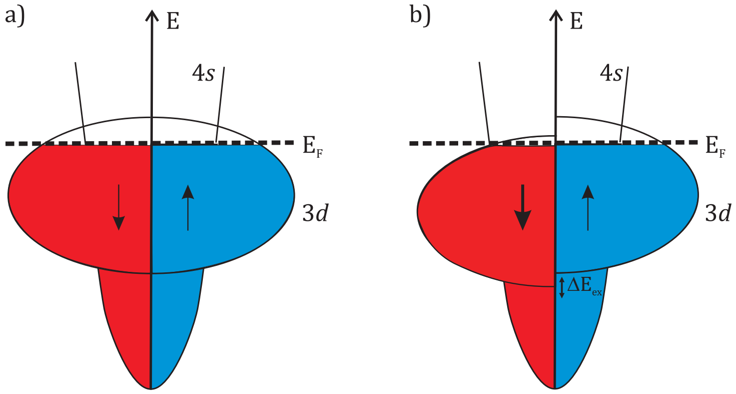

Figure 1.5: (a) Band structure of a non-magnetic metal with equally filled spin sub-bands. (b) Band structure a ferromagnetic metal, exhibiting energy split spin sub-bands, leading to a different electronic population of the two spin-sub bands and to a net magnetic moment. For convenience the *spin-up* (↑) and *spin-down* (↓) sub-bands are plotted on separate panels.

hybridization with the spin-split by the exchange field d-states, these "itinerant" electrons also acquire a polarization. Thus, we see that in a non-magnetic material, the spin sub-bands are equally populated [Fig. 1.5 (a)], but whenever there is an imbalance of spin-up and spin-down electrons in the bands, a spin polarization arises.

A simple model was proposed by Stoner to describe ferromagnetism in metals, also known as *itinerant magnetism.* According to Stoner's model the spontaneous splitting of the two spin-polarized bands occurs when the *Stoner criterion* is fulfilled [33]:

$$I \cdot N_{\uparrow,\downarrow}(E_F) > 1\,, \tag{1.13}$$

where I is the Stoner exchange parameter and $N_{\uparrow,\downarrow}(E_F)$ is the density of states (DOS) per atom for spin-up and spin-down states, defined as $N_{\uparrow,\downarrow}(E_F) = \frac{D(E_F)}{2n}$. Here $D(E_F)$ is the total DOS at the Fermi level and n is the number of atoms per unit volume. In other words, if the difference between the potential and kinetic energies of the electrons at the Fermi energy is positive, a ferromagnetic ground state is achieved in an itinerant system. Materials such as Fe, Ni and Co fulfill the Stoner criterion and, thus, exhibit a ferromagnetic ground state. For the materials that fulfill the Stoner criterion, the number of spin-up $N_\uparrow$ and spin-down $N_\downarrow$ electrons in two d sub-bands determines the magnetic moment $m = \mu_\mathrm{B}(N_\downarrow - N_\uparrow)$ at a temperature below T_C.

1.2 THERMODYNAMICAL DESCRIPTION OF MAGNETISM

In order to describe macroscopic magnetic systems it is convenient to substitute the atomistic description based on the Heisenberg Hamiltonian by a thermodynamical description based on the micromagnetic approximation. Micromagnetics allows one to simulate the macroscopic properties of a material including the best approximations to the fundamental atomic behavior of the material. Specifically, it replaces individual magnetic moments with a continuous magnetization vector field $\mathbf{M}(\mathbf{r})$, with $\mathbf{r}$ being the position vector, so that $\mathbf{M}(\mathbf{r}) = M_\mathrm{S}\,\mathbf{m}(\mathbf{r})$. M_S here is the saturation magnetization and $\mathbf{m}\cdot\mathbf{m} = 1$.

Thus, the basic micromagnetic approach is to formulate the energy in terms of continuous magnetization and to minimize this energy in order to determine static magnetization structures. For this, we follow the description from Ref. [35]. The appropriate thermodynamical potential for the given problem is the Landau free energy, F, which in the limit of T→0 can be expressed as

$$F = \int_V f(\mathbf{r})\mathrm{d}V = \int_V \left[f_\mathrm{ex}(\mathbf{r}) + f_\mathrm{str}(\mathbf{r}) + f_\mathrm{ani}(\mathbf{r}) + f_\mathrm{Z}(\mathbf{r}) + \ldots\right] \mathrm{d}V\,, \tag{1.14}$$

where $f(\mathbf{r})$ is the local magnetic free energy density, $f_\mathrm{ex}(\mathbf{r})$ is the contribution to the magnetic free energy density due to the exchange interaction, $f_\mathrm{str}(\mathbf{r})$ is due to the stray field generated by single magnetic moments, $f_\mathrm{ani}(\mathbf{r})$ includes magnetic anisotropies and $f_\mathrm{Z}(\mathbf{r})$ is the contribution due to external magnetic fields.

1.2.1 EXCHANGE ENERGY

The exchange energy, due to the short-range exchange interaction, involves a summation over the nearest neighbors. Assuming a slowly spatially varying magnetization, the exchange energy can be written

$$F_\mathrm{ex} = \frac{A}{M_\mathrm{S}^2} \int_V \left[\nabla M_x(\mathbf{r})|^2 + |\nabla M_y(\mathbf{r})|^2 + |\nabla M_z(\mathbf{r})^2\right] \mathrm{d}V\,, \tag{1.15}$$

where $\mathbf{M} = (M_x, M_y, M_z)$ and A, known as *exchange stiffness*, is a material constant, proportional to the exchange integral J. Thus, the atomic properties are included via the exchange integral which in micromagnetic terms is a phenomenological constant and can be determined experimentally.

By looking at Eq. 1.15 it is straightforward to see why the exchange interaction leads to ferromagnetism. The magnetic moments all aligned with each other are seen as a constant $\mathbf{M}$, i.e. $\nabla\mathbf{M} = 0$, which ensures that the exchange energy F_ex is minimal. The situation when the magnetic moments point in different directions is, therefore, energetically unfavorable (Fig. 1.6).

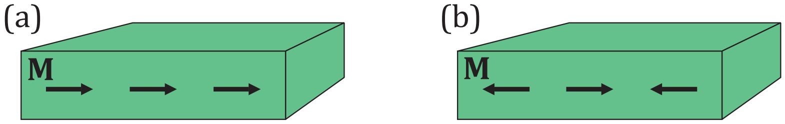

Figure 1.6: (a) Energetically favorable and (b) unfavorable magnetic configurations in terms of the exchange energy given by Eq. 1.15.

1.2.2 ZEEMAN ENERGY

The Zeeman energy arises whenever there is an external applied magnetic field $\mathbf{H}_{\text{ext}}(\mathbf{r})$ acting on the magnetization $\mathbf{M}(\mathbf{r})$ of a material. The response of the magnetization, which tends to align with the field direction, can be expressed as follows:

$$F_Z = -\mu_0 \int_V \mathbf{H}_{\text{ext}}(\mathbf{r}) \cdot \mathbf{M}(\mathbf{r})\, \mathrm{d}V\,. \tag{1.16}$$

The Zeeman contribution to the total energy of the system in Eq. 1.14 is minimal when the local magnetization $\mathbf{M}(\mathbf{r})$ is aligned to the local external magnetic field $\mathbf{H}_{\text{ext}}(\mathbf{r})$ everywhere within the magnetic volume, as illustrated in Fig. 1.7.

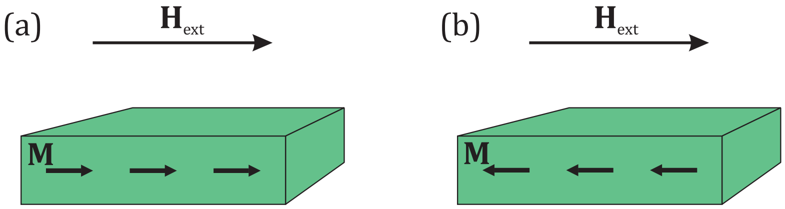

Figure 1.7: (a) Energetically favorable and (b) unfavorable magnetic configurations in an external magnetic field.

1.2.3 MAGNETOSTATIC ENERGY

The *magnetostatic* energy is the energy of the magnetization in a field created by the magnetization itself. In other words, a single magnetic moment in a material creates a dipolar magnetic stray field, which interacts with the other magnetic moments in the material. Note that outside of the material this field is called the stray field and the *demagnetizing* field - inside the material. Thus, the energy associated with it is also known as the *demagnetizing* or *stray field*

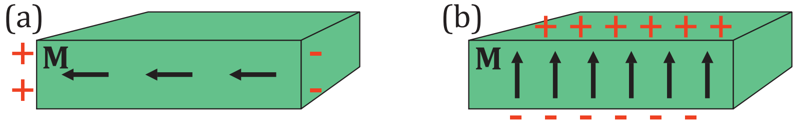

Figure 1.8: (a) Energetically favorable and (b) unfavorable magnetic configurations in terms of the magnetostatic energy given by Eq. 1.21. The magnetic moments in (a) aligned with the stray field created by the neighboring moments produce fewer effective magnetic charges than in (b).

energy. This stray field in the absence of external magnetic fields is governed by the following equations:

$$\nabla \times \mathbf{H}_{\mathrm{str}} = 0\,, \tag{1.17}$$

$$\nabla \mathbf{B} = \mu_0 \nabla(\mathbf{H}_{\mathrm{str}} + \mathbf{M}) = 0\,. \tag{1.18}$$

The stray field then can be derived from a scalar potential $\mathbf{H}_{\mathrm{str}} = -\nabla U$. Substituting this into Eq. 1.18 yields

$$\nabla^2 U = \nabla \mathbf{M}\,. \tag{1.19}$$

Because of its analogy with Poisson's equation in electrostatics, Eq. 1.19 leads to the definition of a magnetic charge density

$$\rho_{\mathrm{M}} = \nabla \mathbf{M}\,. \tag{1.20}$$

Thus, the stray field can be thought of as generated by these magnetic charges (Fig. 1.8). When interacting with other magnetic dipoles in the system, the stray field gives rise to the following contribution to the total energy [55]:

$$F_{\mathrm{str}} = \frac{\mu_0}{2} \int_{\mathbb{R}^3} |\mathbf{H}_{\mathrm{str}}|^2 \,\mathrm{d}V\,, \tag{1.21}$$

where the integration is calculated across the entire $\mathbb{R}^3$ space and a factor of $\frac{1}{2}$ accounts for the double counting of each volume element.

SHAPE ANISOTROPY

The result of the magnetostatic interactions between magnetic dipoles is the shape anitoropy. If macroscopically the magnetization in a material is aligned uniformly, the associated magnetic charges appear at the surfaces (see Fig. 1.8). These magnetostatic surface charges give rise to a demagnetizing field, $\mathbf{H}_{\mathrm{D}} = -N\mathbf{M}$, acting in the opposite to the magnetization direction, were $N > 0$ is a shape-dependent demagnetizing factor. Similarly to Eq. 1.21 the magnetostatic energy due to the demagnetizing field is $\frac{1}{2}\mu_0 \int \mathbf{M}(\mathbf{r}) \cdot \mathbf{H}_{\mathrm{D}}(\mathbf{r})\,\mathrm{d}V$.

By considering the magnetostatic energy of an ellipsoid of revolution [34, 35], it is straightforward to show that the additional contribution to the energy density due to the shape anisotropy reads

$$K_{\mathrm{sh}} = \frac{\mu_0}{4}(1-3N)M_{\mathrm{S}}^2\,. \tag{1.22}$$

For a thin film $N = 1$, which results in shape anisotropy of $-\frac{1}{2}\mu_0 M_{\mathrm{S}}^2$, that is the gain of the magnetostatic energy when the magnetization is in-plane. Therefore, the shape anisotropy is known to induce the well-known in-plane easy magnetization of thin films. Furthermore, the shape anisotropy leads to formation of magnetic domains as will be discussed in the following.

1.2.4 ANISOTROPY ENERGY

Before we consider other sources of the magnetic anisotropy than the sample shape considered above (e.g. related to the sample crystal structure and the micro-scale texture), we briefly discuss the macroscopic meaning of the magnetic anisotropy.

Magnetic anisotropy means that the magnetization $\mathbf{M}$ tends to lie along some fixed direction(s) in a magnetic solid. It costs energy to turn it into any direction other than the preferred axes, known as the *easy axes*. For the simplest case of a *uniaxial anisotropy*, i.e. with only one easy axis, this tendency is represented by the energy density term

$$f_{\mathrm{ani}} = K_1\sin^2\theta + K_2\sin^4\theta + K_3\sin^6\theta + \dots\,, \tag{1.23}$$

where $K_i\,(i = 1,2,3,\dots)$ are the anisotropy constants and θ is the angle between the volume magnetization $\mathbf{M}$ and the anisotropy axis.

Often it is convenient to represent the magnetic anisotropy by an anisotropy field $\mathbf{H}_{\mathrm{K}}$. It is constructed to simulate the effect of magnetic anisotropy and, thus, must be parallel to the easy axis to keep the magnetization and change the sign when $\mathbf{M}$ changes sign. In the simplest case of uniaxial anisotropy, where only $K_1 \neq 0$ in Eq. 1.23, the anisotropy field reads

$$H_{\mathrm{K}} = \frac{2K_1}{\mu_0 M_{\mathrm{S}}}\cos\theta\,, \tag{1.24}$$

where M_{S} is the saturation magnetization.

MAGNETOCRYSTALLINE ANISOTROPY

Magnetocrystalline anisotropy arises because generally non-spherical atomic orbitals prefer to lie in certain crystallographic directions. Then, it is the SOC that assures a preferred direction for the magnetization. For materials which are characterized by certain symmetries (hexagonal, cubic, etc), the magnetocrystalline anisotropy tends to restrict the magnetization to certain direction(s).

For example, the *uniaxial anisotropy*, occurring in e.g. hexagonal crystals such as Co, tends to align all magnetic moments along one easy-axis. In this case, higher order terms in Eq. 1.23 are small and, thus, can be neglected. Hence, the sign of the first order anisotropy constant $K_1 = K_\mathrm{u}$ determines whether the direction is defined as an easy ($K_\mathrm{u} < 0$) or hard ($K_\mathrm{u} > 0$) axis. Systems with so-called perpendicular magnetic anisotropy (PMA), investigated in this thesis, also exhibit a uniaxial anisotropy. In this case the easy-axis is in the out-of-plane (OOP) direction.

To account for other examples of the systems with the magnetocrystalline anisotropy the reader is refereed to e.g. Refs. [35, 36].

MAGNETOELASTIC ANISOTROPY

Magnetoelastic anisotropy in a crystal arises due to the interaction between the magnetization and the mechanical strain of the lattice. The corresponding energy term is defined to be zero for an unstrained lattice [56]. The mechanical strain can be either naturally imposed on the magnetic material during its growth or intentionally to control the magnetic anisotropy, as will be described in this thesis.

Microscopically, the ME anisotropy originates primarily from the SOC [34, 35]. In a general case, the expression for the phenomenological ME energy can be derived from the expansion of the free energy of the crystal in terms of the strain components [56, 57]. Here, for simplicity we show the expression for the uniaxial magneto-elasticity of a polycrystalline system, which reads [34]

$$f_\mathrm{ME} = -\frac{\lambda_\mathrm{s} Y}{2}\left(3\cos^2\theta - 1\right)\epsilon + \frac{Y}{2}\epsilon^2 , \tag{1.25}$$

where Y is Young's modulus, θ is the angle between the magnetization and strain axis, $\epsilon = \Delta l / l$ denotes the elongation along the stress axis and the saturation magnetostriction constant, λ_s, describes the strength of the ME coupling. We can compare the angular dependent term in Eq. 1.25 with the usual expression for uniaxial anisotropy energy density $f_\mathrm{ani} = K_\mathrm{u}\sin^2\theta$, which yields

$$K_\mathrm{ME} = \frac{3}{2}\lambda_\mathrm{s} Y \epsilon , \tag{1.26}$$

which is the additional contribution to the magnetic anisotropy due to strain. Thus, the effect of a tensile strain on a material with a negative magnetostriction coefficient λ_s, such as Ni discussed in Chapter 3, is that the magnetic anisotropy decreases along the direction of the applied strain, while it increases for a material with a positive λ_s, such as CoFeB discussed in Chapters 4, 5 and 6 [34].

INDUCED PERPENDICULAR MAGNETIC ANISOTROPY

Some thin FM films have a normal magnetic easy axis which emerges due to so-called interface anisotropy [58, 15, 59, 60]. The interface anisotropy, resulting from the broken inversion symmetry at the interface, generates giant magnetic anisotropies, able to overcome the shape anisotropy and induce a stable perpendicular magnetization axis in thin films and multilayers. The phenomenological expression for the anisotropy, in this case, reads [34]

$$K_{\mathrm{eff}} = K_{\mathrm{V}} + \frac{K_{\mathrm{i}}}{t_{\mathrm{FM}}}, \tag{1.27}$$

with t_{FM} being the thickness of the ferromagnet. The volume anisotropy, K_{V}, contains the magnetocrystalline anisotropy, which is zero for amorphous ferromagnets, and the shape anisotropy $-\frac{1}{2}\mu_0 M_{\mathrm{S}}^2$.

The experimental and theoretical studies of the interface-induced PMA report that it occurs only for limited combinations of the FM film and the non-magnetic underlayers, suggesting the important role of non-magnetic layer as well as the band structure in producing the PMA [61]. Now, the interfacial anisotropy is thought to originate from the interface hybridization of the orbitals of the magnetic and the non-magnetic metals, which is further supported by the existence of an enhanced PMA in thin polycrystalline HM/FM/oxide multilayers [15, 28, 60, 62, 63, 64]. One of these PMA systems, namely W/CoFeB/MgO, will be considered in Chapters 4, 5 and 6.

The origin of the interfacial PMA in the FM/oxide interface is partially attributed to the interfacial symmetry break and the hybridization between the $3d$-orbitals of the FM and O $2p$-orbitals [65, 66]. The OOP $3d_{z^2}$-orbitals of the FM strongly bond with the OOP $2p_z$-orbitals of the oxygen resulting in a significant charge transfer from $3d_{z^2}$-orbitals to $2p_z$-orbitals. This, in combination with the hybridization of d_{z^2} orbitals with non-degenerate d_{xz} and d_{yz} orbitals due to the SOC, is at the origin of the PMA [67].

Similarly, for the HM/FM interface, the induced PMA is attributed to both the d- and p-orbitals at the interface, as well as to the SOC [61, 62, 68, 65]. Due to the strong SOC and the hybridization-induced charge transfer, the electronic orbitals with the OOP magnetic moment become energetically more favorable than the in-plane [62].

SPIN-REORIENTATION TRANSITION

Generally, the easy axis of the magnetization in magnetic films is determined by the competition between the interface and shape anisotropies as follows from Eq. 1.27. As the shape anisotropy contribution in Eq. 1.27 is independent of the thickness of the FM layer (assuming no change of M_{S} with t_{FM}), at a certain thickness K_{eff} takes positive (negative) values favoring the perpendicular (in-plane) magnetic anisotropy. At the thickness, when the two contributions become comparable, a so-called spin-reorientation transition (SRT) occurs [69, 70], and the magnetization slants towards an intermediate canted state. The SRT observed in W/CoFeB/MgO system will be discussed in Chapter 6.

1.2.5 BROWN'S EQUATION FOR STATIC EQUILIBRIUM

The final step in classical micromagnetics is to minimize the magnetic free energy F given by Eq. 1.14 with respect to $\mathbf{M}$ to find the equilibrium magnetization $\mathbf{M}_{\mathrm{eq}}$ of the system. The condition for the equilibrium magnetization can be calculated by applying the standard variational principles, which yield the expression for the equilibrium condition as a function of an effective magnetic field $\mathbf{H}_{\mathrm{eff}}$ arising from the magnetic free energy F. The effective field $\mathbf{H}_{\mathrm{eff}}$ reads

$$\mathbf{H}_{\mathrm{eff}} = \frac{2A}{M_{\mathrm{s}}}\nabla^2\mathbf{M} + \mathbf{H}_{\mathrm{d}} + \mathbf{H}_{\mathrm{ext}} + \mathbf{H}_{\mathrm{ani}}\,. \tag{1.28}$$

With $\mathbf{H}_{\mathrm{eff}}$ the equilibrium conditions for the magnetization can be expressed as

$$\mathbf{M}_{\mathrm{eq}} \times \mathbf{H}_{\mathrm{eff}} = 0\,, \tag{1.29}$$

$$\mathbf{M}_{\mathrm{eq}} \times \nabla_{\Sigma}\mathbf{M}_{\mathrm{eq}} = 0\,, \tag{1.30}$$

where $\nabla_{\Sigma}\mathbf{M}_{\mathrm{eq}}$ denotes the gradient of $\mathbf{M}$ along the surface Σ of the magnetic material. Equations 1.29 - 1.30 are known as Brown's equations and form the basis for the classical micromagnetic.

1.2.6 FERROMAGNETIC DOMAINS AND DOMAIN WALLS (DWS)

As we have discussed the energy terms that make up the total free energy of a system, it becomes clear that the detailed magnetic behavior of a given material is determined by the balance between these energy terms. It is important to notice that the exchange (Eq. 1.16) and anisotropy (Eq. 1.23) alone would favor a ferromagnetic alignment with the magnetization along the existing easy axes. Clearly, this configuration would create large, long-range stray fields. On the other hand, Eq. 1.21 implies that the energy can be decreased by reducing $\mathbf{M}$. Thus, instead of aligning itself ferromagnetically, the system spontaneously breaks down into *magnetic domains* separated by a magnetic *domain wall (DW)* [35]. Within these domains, the magnetization remains aligned to one of the easy axes, and the spatial confinement reduces the stray field energy.

Figure 1.9 shows two examples among several existing stable magnetic structures, arising from the aforementioned competition of the energy terms, which will be considered in this thesis. A *magnetic vortex state*, shown in Fig. 1.9 (a), is formed in confined lateral structures,

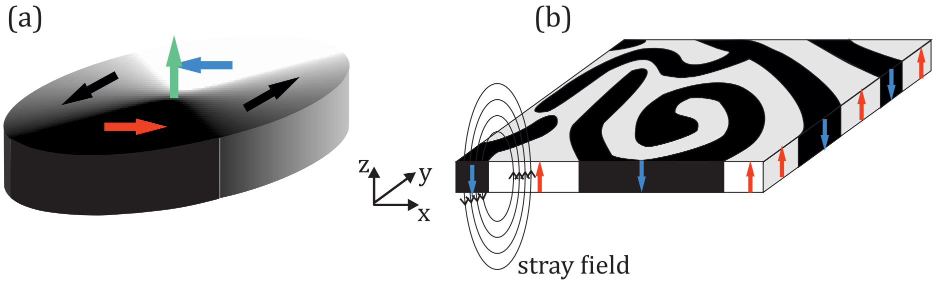

Figure 1.9: Simplified sketch of magnetic domains in (a) a magnetic disc and (b) a PMA material. The local magnetization direction within the domains is indicated by arrows.

where the magnetization curls in-plane following the edges of the structure. The center of the structure, where the magnetization points out of the plane, is known as a *vortex core (VC)*, which typically is small in the order of tens of nm depending on the material [71, 72]. The thermodynamic ground state of PMA films is a labyrinth of stripe domains, as shown in Fig. 1.9 (b). Such a multidomain state becomes favorable due to partial cancellation of the demagnetizing fields of adjacent stripe domains [73].

Within DWs, there can be various configurations which are dictated by the combined contribution of exchange, magnetostatics and anisotropy. In materials with an OOP easy axis, there are two types of DWs depicted in Fig. 1.10, namely a *Bloch wall* and a *Néel wall*.

In a Bloch wall [Fig. 1.10 (a)] a continuous rotation of the magnetization occurs within the planes parallel to the plane of the wall. This wall type provides low bulk stray field contributions and is, therefore, more common for thick films and bulk materials. Néel walls [Fig. 1.10 (b)] are generally more energy expensive due to the non-zero divergence of magnetization. The energy penalty for Néel walls is given by the shape anisotropy constant $K_\mathrm{D} = \frac{1}{2}\mu_0 M_\mathrm{S}^2 N$, where $N = \frac{4t\ln 2}{\pi\Delta_\mathrm{DW}}$ is the wall's demagnetizing factor [30], which depends on the thickness of the FM material, t, and the DW width Δ_DW.[6] Thus, the energy cost for Néel walls is less for thinner films and lower saturation magnetization. Furthermore, the formation of the Néel walls is strongly supported in the presence of the interfacial DMI. This is because the sense of rotation of the magnetization within the Néel wall matches the one set by the DMI terms (see Eq. 1.12 in Section 1.1.2).

---

[6] In the case of PMA materials with large values of the magnetic anisotropy, however, the DW of both types are narrow with the width ($\Delta_\mathrm{DW} \propto \sqrt{A/K}$, where A and K are the exchange and the anisotropy constants, respectively) of the order of a few nm [14].

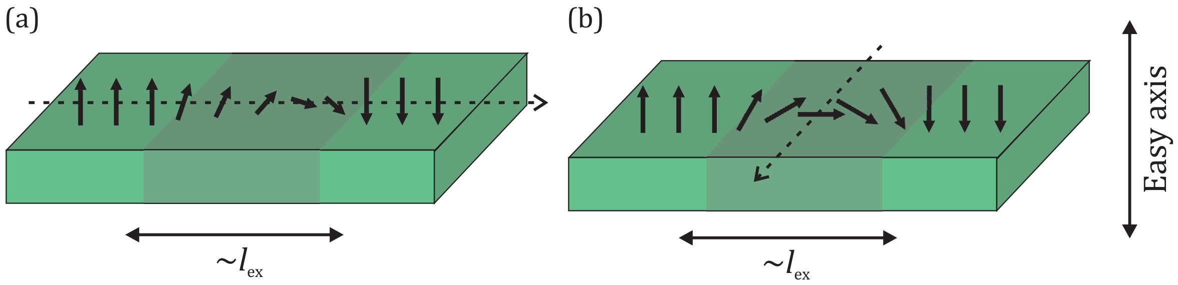

Figure 1.10: Two magnetic domains in a PMA film separated by (a) Bloch type and (b) Néel type DWs (darker region). The dashed lines indicate the axes of rotation of the magnetization inside the DW.

CHIRAL DOMAIN WALLS IN PMA MATERIALS WITH INTERFACIAL DMI

The interfacial DMI favors the Néel type of DWs when it is larger than a certain critical value, D_{c}. D_{c} can be defined by considering the competing magnetostatic energy and the DMI, which yields $D_{\mathrm{c}} = 4\Delta_{\mathrm{DW}}K_{\mathrm{D}}/\pi$, where K_{D} is a parameter defining the magnetostatic anisotropy that favors the Bloch wall as described above [30]. When $D \geq D_{\mathrm{c}}$, the domain wall adopts the Néel configuration, while for $D \leq D_{\mathrm{c}}$ the Bloch configuration is more favorable.

Furthermore, the DMI lifts the degeneracy between the two chiralities of the DWs. The chirality is defined as the sense of rotation of the magnetization within the DW: for a *right-handed* (*left-handed*) Néel type the magnetization rotates clockwise around the direction of the DMI vector **D** (see Section 1.1.2). Thus, following the established convention, a positive DMI constant results in a right-handed rotation of the wall while a negative sign favors a left-handed rotation [48].

The lifted degeneracy manifests itself in the presence of so-called chiral domain walls, i.e. when the magnetic moments within all DWs rotate with the same orientation. This results in a rich variety of topological spin textures, such as spin spirals [48, 49], skyrmions [51, 52] etc., which fall outside of the scope of this thesis, and in the remarkable response of the magnetic domains to the electric currents as we will discuss in the next Section 1.4.2.

1.3 STONER-WOHLFARTH MODEL

The Stoner-Wohlfarth model gives a simple description of the angular dependence of the energy of a magnetic particle where the magnetization rotates coherently as if it were one macroscopic spin. The model gives a limited description of hysteresis loops and can be applied for the analysis of magnetic anisotropy measurements [34] which we will employ in Chapter 4. According to the Stoner-Wohlfarth model, the magnetic free energy density is given by

$$f = K_{\mathrm{eff}}(\sin\theta)^2 - \mu_0 M_{\mathrm{S}} H_{\mathrm{ext}} \cos(\phi_{\mathrm{h}} - \theta). \tag{1.31}$$

The first term is the effective anisotropy constant $K_{\mathrm{eff}} = (K_1 - \frac{1}{2}\mu_0 M_{\mathrm{S}})$ comprising the first order anisotropy constant and the magnetostatic energy, the second term is the interaction of the magnetization with the applied field H_{ext}. The angle of the magnetization relative to the film normal is θ, ϕ_{h} defines the angle from the film normal to the applied field and M_{S} is the saturation magnetization. The Stoner-Wohlfarth model allows one to derive the shape of magnetic hysteresis loops. The field needed to rotate and saturate the magnetization along the hard axis, thus, gives the anisotropy field as defined in Eq. 1.24:

$$H_{\mathrm{K}} = \frac{2K_{\mathrm{eff}}}{\mu_0 M_{\mathrm{S}}}. \tag{1.32}$$

The anisotropy field can be measured in a film with dominating PMA ($K_{\mathrm{eff}} > 0$) by first saturating the magnetization along the easy axis and then applying a field along the hard axis. As long as the magnetization rotates coherently, the Stoner-Wohlfarth model can be applied to extract H_{K}.

1.4 MAGNETIZATION DYNAMICS

1.4.1 FIELD-INDUCED MAGNETIZATION DYNAMICS: LLG EQUATION

The thermodynamic description considered above is employed to define the magnetic configuration in its static equilibrium. However, it does not provide details of the dynamical processes leading to the final state. The LLG equation is typically used to describe the magnetization dynamics [17]:

$$\frac{\mathrm{d}\mathbf{M}}{\mathrm{d}t} = -\gamma \mathbf{M} \times \mathbf{H}_{\mathrm{eff}} + \frac{\alpha}{M_{\mathrm{S}}} \mathbf{M} \times \frac{\mathrm{d}\mathbf{M}}{\mathrm{d}t}, \tag{1.33}$$

where γ is the gyromagnetic ratio and α is the *Gilbert damping* constant. $\mathbf{H}_{\mathrm{eff}}$ is the effective field acting on the magnetization $\mathbf{M}$, which comprises external fields, anisotropy fields etc.

As illustrated in Fig. 1.11, the dynamics of the magnetization subject to the effective field is a combination of an un-damped precession of $\mathbf{M}$ around $\mathbf{H}_{\mathrm{eff}}$ at a fixed angle θ, expressed by $-\gamma \mathbf{M} \times \mathbf{H}_{\mathrm{eff}}$, with the damping term expressed by $\frac{\alpha}{M_S} \mathbf{M} \times \frac{\mathrm{d}\mathbf{M}}{\mathrm{d}t}$, which leads to the relaxation of the magnetization to the equilibrium position, when $\mathbf{M}$ is along $\mathbf{H}_{\mathrm{eff}}$. Note that both the precession and damping terms rotate the magnetization, but do not change its length, which is consistent with treating the magnetization as having a fixed length, as defined earlier.

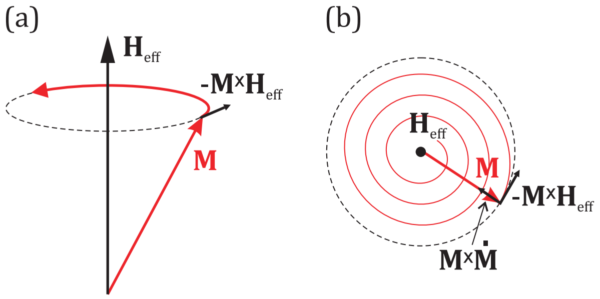

Figure 1.11: Schematic illustration of the magnetization dynamics in an effective magnetic field $\mathbf{H}_{\text{eff}}$. The precession only leads to a continuous rotation (a), the damping slowly aligns the magnetization with the field, resulting in a spiraling motion (b).

From Eq. 1.33 it follows that being one of the contributions to the effective field $\mathbf{H}_{\text{eff}}$, an external magnetic field can be used to excite the magnetization dynamics by tilting it away from its equilibrium direction. Globally, it could lead to movement of the magnetic DW and re-distribution of the magnetic domains, or magnetization reversal. In Chapter 3 of this thesis, we will consider the steady-state magnetization dynamics within a magnetic disc, excited by an alternating Oersted magnetic field, generated by the flow an AC electric current through an underlying non-magnetic wire. In this case, however, the formal description is most conveniently done with the Thiele equation, which we describe below.

THE THIELE EQUATION

The Thiele equation is used to describe the dynamics of complex systems [74], where the magnetization as a continuous vector field is defined by an infinite number of parameters. The Thiele equation can be derived from the LLG equation assuming the magnetization pattern performs a rigid motion without deformations, hence, the current state of the whole magnetization can be described by the current position of one characteristic feature of the pattern. It can thus be applied to describe the dynamics of DWs [74], magnetic vortices [75] and skyrmions [76]. Following the arguments from Refs. [77, 78, 79], we briefly discuss the Thiele equation for the case of steady-state field-induced dynamics of a magnetic vortex (see Section 1.2.6).

The magnetization at the position $\mathbf{r} = (x, y)$ can be expressed by $\mathbf{M}(\mathbf{r} - \mathbf{R}(t))$, where $\mathbf{R} = (X, Y)$ is the position of the vortex core.[7] The equation of motion can be derived by expressing the time derivative at each point by the according spatial derivative and the velocity, $\dot{\mathbf{r}} = \left(\dot{x}, \dot{y}\right)$,

---

[7] Note that we assume 2D magnetization distribution within a disc, which does not depend on z coordinate along the disc thickness.

of the whole pattern:

$$\frac{\mathrm{d}}{\mathrm{d}t}\mathbf{M}(\mathbf{r}) = -\left(\dot{\mathbf{r}}\cdot\nabla\right)\mathbf{M}(\mathbf{r})\,. \tag{1.34}$$

With this expression we can substitute the corresponding terms in the LLG equation 1.33 as:[8]

$$0 = \mathbf{H}_{\mathrm{eff}} + \frac{1}{M_{\mathrm{S}}^{2}}\mathbf{M}\times\left(\mathbf{r}\cdot\nabla\right)\mathbf{M} - \frac{\alpha}{\gamma M_{\mathrm{S}}}\left(\dot{\mathbf{r}}\cdot\nabla\right)\mathbf{M}\,. \tag{1.35}$$

Eq. 1.35 can be re-written in a more familiar form[9] of the Thiele equation describing the vortex core position $\mathbf{R}$ as it moves with a constant velocity in response to continuous external stimuli (due to e.g. applied field) assuming the spin structure of the vortex core is fixed:

$$\mathbf{G}\times\dot{\mathbf{R}} - \nabla W(\mathbf{R}) = 0\,, \tag{1.36}$$

where $W(\mathbf{R})$ is the potential energy of the shifted vortex and $\mathbf{G}$ is the gyrovector, associated with a topological charge of the vortex [78]. The gyrovector for vortices in a disc with the thickness L is a vector pointing perpendicular to the disc plane, $\mathbf{G} = G\mathbf{z} = 2\pi pqLM_{\mathrm{S}}\mathbf{z}/\gamma$, in a direction determined by the magnetization at the vortex core. $q = +1$ for vortices ($q = -1$ for antivortices) and there are two possible values for $p = \pm 1$ defined by the vortex core polarity. The second term in Eq. 1.36 describes the dynamic restoring force acting on the vortex core shifted from the disc center. In the general case, it is calculated by considering exchange, magnetostatic, Zeeman and anisotropy contributions to the total vortex magnetic energy $W(\mathbf{R})$ within the disc, but for sub-micron disc radii, the disc magnetostatic energy gives the main contribution [79]. The restoring force is directed towards the center of the disc.

1.4.2 CURRENT-INDUCED MAGNETIZATION DYNAMICS: SPIN-TORQUE EFFECTS

SPIN-TRANSFER TORQUE

When an electric current is flowing through a magnetic material, interaction between the spin of the electrons and the local magnetization occurs. As we will see later, in this case, the spins are affected by the local magnetization of the material, as well as the magnetization by the spins. The result of the former is a magnetization-dependent response of the electrical properties of the material, such as its resistance (e.g. anisotropic magnetoresistance (AMR) [82], GMR [12]). The latter, on the other hand, can be employed to manipulate the local magnetic configuration of the material via the so-called *spin-transfer torque (STT)* [14, 17, 83].

---

[8] The derivation of the Thiele equations for the case of the current-induced dynamics, which requires the corresponding spin torques terms in the LLG equation (see Section 1.4.2) is discussed in Ref. [80].

[9] Note that in the general case, the Thiele reads [81]: $\tilde{M}\ddot{\mathbf{r}} - \mathbf{G}\times\dot{\mathbf{r}} - D\dot{\mathbf{r}} + \nabla W(\mathbf{r}) = 0$, where D is the dissipation term proportional to the Gilbert damping α introduced in Chapter 1, and $\tilde{M}$ is the vortex core effective mass tensor, which is usually neglected in calculations [79].

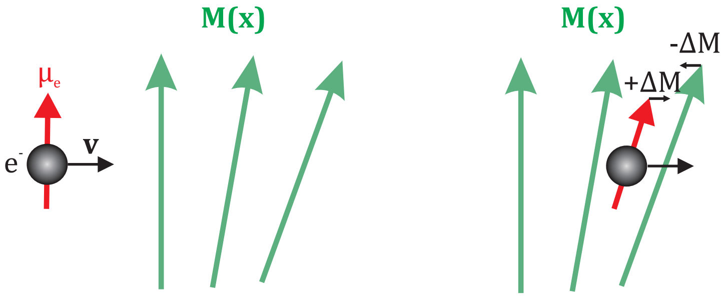

Figure 1.12: Adiabatic STT effect. An electron flowing through a magnetic material will align its spin with the direction of the magnetization. Once the electron flows in a region with a gradient of the local magnetization, the electronic spin will align adiabatically to the direction of the local magnetization, giving rise, due to the conservation of angular momentum, to a torque on the local magnetization.

The mechanism of the STT effect is illustrated schematically in Fig. 1.12. Upon flowing into the area with a magnetization gradient, for example, a DW, the electrons' spins tend to align to the local magnetization vector. This alignment gives rise to a torque on the local magnetization, leading to a rotation of the magnetization towards the spin polarization of the electric current, as a consequence of the angular momentum conservation. Per each electron moving from one domain to the next, the angular momentum transfer amounts to $\frac{1}{2}\hbar$ [84].

Formally, the spin-torque effect can be described by adding two terms in the LLG equation 1.33, which then reads

$$\frac{\mathrm{d}\mathbf{M}}{\mathrm{d}t} = -\gamma \mathbf{M}\times\mathbf{H}_{\mathrm{eff}} + \frac{\alpha}{M_S}\mathbf{M}\times\frac{\mathrm{d}\mathbf{M}}{\mathrm{d}t} - \underbrace{(\mathbf{u}\cdot\nabla)\,\mathbf{M}}_{\text{adiabatic}} + \underbrace{\beta\mathbf{M}\times(\mathbf{u}\cdot\nabla)\,\mathbf{M}}_{\text{non-adiabatic}}, \tag{1.37}$$

where $\mathbf{u} = \frac{gP\mu_B}{2eM_S}\mathbf{j}$, with P being the spin-polarization of the material, and $\mathbf{j}$ the current density vector, is called the *spin drift velocity*. This corresponds to the maximum velocity when all of the changes in the angular momentum of the conduction electrons is transferred to the local magnetization. β is known as the non-adiabaticity parameter [14]. The past two terms in Eq. 1.37 are called the *adiabatic*[10] and *non-adiabatic*[11] contributions of the STT.

---

[10] The adiabatic torque describes the effect of the spin-polarized flow of electrons on the local magnetization direction under the assumption that the spin of the electrons aligns itself instantly to the magnetization due to so-called s-d exchange interaction J_{ex}^{s-d} [14]. This adiabatic limit holds when the magnetization gradient in the direction of the electrons motion is much smaller than the spin precession length, i.e. for wide domain walls (~ 100 nm) which occur in low anisotropy materials [14]. In this case, the electrons have enough time to exchange their angular momentum with the local magnetization.

[11] The non-adiabatic contribution arises when the electrons flow into a region with a large gradient of the local

From Eq. 1.37 we can see that the adiabatic and non-adiabatic torques are directed perpendicularly to each other and have different symmetries. The former has the symmetry of a torque generated by a magnetic field applied along the easy-axis of the system. Accordingly, the adiabatic torque is defined as *field-like (FL)* torque, while the non-adiabatic torque is defined as *damping-like (DL)* torque.

SPIN-ORBIT TORQUE

A few decades after the discovery of the STT effect, another mechanism to excite magnetization dynamics was proposed, namely the SOT, which has a fundamentally distinct origin from the STT. Most commonly the SOTs occur in HM/FM systems, i.e. systems with the broken inversion symmetry, upon sending an electric current in the in-plane geometry [29].

The two model scenarios, schematically illustrated in Fig. 1.13, which we will describe in the following, are known to contribute to the SOTs.

In the first model, the charge current through the HM is converted into a pure spin current due to the *spin Hall effect (SHE)* [85], which propagates towards the interface and is absorbed by the adjacent FM in the form of torque acting on the magnetization [15, 86]. In some sense the SHE-SOT acts similarly to the conventional STT, i.e., the angular momentum transfer from the spin current to magnetization torque. Therefore, the dominant symmetry component of the SHE-SOT is the DL torque [87] which takes the form

$$\mathbf{T}_{\mathrm{DL}} = \frac{\gamma J_s^{\mathrm{SHE}}}{V} \mathbf{m} \times (\mathbf{m} \times \boldsymbol{\xi}) \,. \tag{1.38}$$

Here γ is the gyromagnetic ratio, $\mathbf{m} = \mathbf{M}/M_{\mathrm{S}}$ is the unit magnetization vector of a FM of volume V with the saturation magnetization M_{S}, and $\boldsymbol{\xi}$ is a unit vector of the in-plane spin-polarization due to the OOP spin current. The magnitude of the spin current injected into the FM is determined by the *spin Hall angle (SHA)*, $\theta_{\mathrm{SH}} = (2e/\hbar)\sigma_{\mathrm{sh}}/\sigma_0$, and the driving electric field, E, as $J_s^{\mathrm{SHE}} = \eta\theta_{\mathrm{SH}} A(\hbar/2e)\sigma_0 E$. Here η is the spin injection efficiency across the HM/FM interface of area A, σ_0 and σ_{SH} are the electrical and spin Hall conductivities, respectively [85]. In this case $\mathbf{E} \perp \boldsymbol{\xi}$ and the SHE-SOT competes with the damping term in the LLG equation. However, the spin current in the SHE can also generate spin accumulation at the edges of the HM where the inversion-symmetry is broken. Consequently, the SHE can also contribute to the FL SOT [88].

In relation to the second of these models, a few effects are typically named, such as the *Rashba-Edelstein effect* [89] or *iSGE* [90], the result of which is the conversion of an electric current to spin-accumulation [Fig. 1.13 (b)] at the HM /FM interface due to the SOC and broken

---

magnetization, where the spins do not fully align [80]. Note that $\beta = 0$, implies that the electrons spins align instantly with the magnetization, leaving only the adiabatic torque contribution.

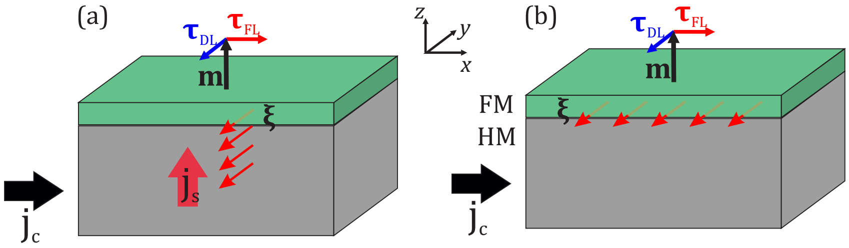

Figure 1.13: Two main model of spin-charge conversion mechanisms at the HM/FM interface. (a) SHE: an electric current through the bulk of the HM layer results in the generation of a transverse spin current, with the spin being perpendicular to the plane of both current. (b) iSGE: an electric current through the interface between HM and FM layer experiences a Rashba field via the SOC under the structural inversion asymmetry, which results in a spin accumulation near the interface. $\boldsymbol{\xi}$ indicates the spin polarization direction. Both mechanisms produce DL and FL torques acting on the magnetization $\mathbf{m} = \mathbf{M}/M_S$ of the FM layer. Adapted from [29].

inversion symmetry at this interface. The non-equilibrium spin density then exerts an effective FL torque, $\mathbf{T}_{\mathrm{FL}} = \eta_{\mathrm{FL}}(\boldsymbol{\xi} \times \mathbf{m})$, on the magnetization in the FM layer via the exchange coupling [88]. $\boldsymbol{\xi}$ gives the direction of the spin accumulation and η_{FL} is a coefficient reflecting the strength of the iSGE induced FL torque. In addition, the non-equilibrium spin density can also precess around the magnetization, leading to an accumulation of $\mathbf{m} \times \boldsymbol{\xi}$, which can generate an effective DL torque on the magnetization [15, 91].

Moreover, it is known that both the SHE-SOT and iSGE-SOT can act simultaneously in a system. In the commonly used bilayers with a nm-scale spin-diffusion length in the HM material and a (sub)nm-thick FM layers, it becomes impossible to distinguish between the SOTs generated by "bulk" SHE or "interface" Rashba-type fields [29, 92, 93]. On the other hand, both models provide qualitatively equivalent expressions for the FL and DL SOTs.

While for detailed theoretical accounts of the Rashba-type effects and SHE, the reader is referred to Ref. [94] and Ref. [85], respectively, in this thesis, we will limit the discussion to the qualitative description of the SOTs based on the symmetry arguments employed in Ref. [93].

In Fig. 1.14 the current $\mathbf{j}_c$, injected along the x direction, generates transverse spin accumulation $\boldsymbol{\xi} || \mathbf{z} \times \mathbf{j}_c$ at the HM/FM interface. As discussed above, this spin-accumulation induces two components of the SOT (see Fig. 1.14), $\mathbf{T}$, (the third component parallel to $\mathbf{m}$ is ineffective), which formally is expressed as

$$\mathbf{T} = \tau_{\mathrm{FL}} \mathbf{m} \times \boldsymbol{\xi} + \tau_{\mathrm{DL}} \mathbf{m} \times (\mathbf{m} \times \boldsymbol{\xi}), \tag{1.39}$$

with $\boldsymbol{\xi}$ being independent of the magnetization. Here, the factors τ_{FL} and τ_{DL} can also depend on the angle of $\mathbf{m}$, which makes the phenomenological description of the SOT more complex [93]. Also note that, although the torque $\mathbf{T}$ is formally decomposed into the $\mathbf{T}_{\mathrm{FL}}$ and $\mathbf{T}_{\mathrm{FL}}$ components, this representation does not allow one to necessarily disentangle the microscopic iSGE and SHE mechanisms of the SOT. [12]

For experimental purposes, it is convenient to employ the effective magnetic fields $\mathbf{B}_{\mathrm{DL,FL}}$ corresponding to the DL and FL torques, which are defined as $\mathbf{T}_{\mathrm{DL,FL}} = \mathbf{m} \times \mathbf{B}_{\mathrm{DL,FL}}$. The advantage of this representation is that the effect of the SOT fields on the magnetization can be directly compared to that of the external magnetic fields of known direction and magnitude. Also note that in PMA systems, such as that considered in Chapter 4 of this thesis, $\mathbf{B}_{\mathrm{FL}}$ and $\mathbf{B}_{\mathrm{DL}}$ are commonly referred to as “transverse field” ($\mathrm{H_T}$) and “longitudinal field” ($\mathrm{H_L}$), respectively [95]. This convention, emphasizing the direction of the effective fields, will be followed in Section 2.4 where the second harmonic spin-torque magnetometry technique will be discussed.

We can now re-write Eq. 1.39 in terms of the effective SOT fields for a current $\mathbf{j}_{\mathrm{c}}||\mathbf{x}$, which, to the lowest order in the magnetization, gives

$$\mathbf{B}_{\mathrm{FL}} = B_{\mathrm{FL}}\mathbf{y}, \tag{1.40}$$

$$\mathbf{B}_{\mathrm{DL}} = B_{\mathrm{DL}}\mathbf{m} \times \mathbf{y}. \tag{1.41}$$

Note also that the Oersted field due to the current flowing in the HM layer produces an additional contribution $B_{\mathrm{Oe}} \approx \mu_0 j_{\mathrm{c}} t_{\mathrm{HM}}/2$ antiparallel to $\mathbf{y}$.

Equations 1.40 and 1.41 correspond to the lowest order terms of the SOT, which are sufficient to qualitatively describe many experimental results. However, generally higher order terms in the magnetization are allowed by symmetry.[13] The typical polycrystalline HM/FM bilayers exhibit C_v symmetry, corresponding to the broken inversion symmetry along the z-axis due to the interface and in-plane rotational symmetry. For such systems, the torques can be decomposed into the following terms expressed in spherical coordinates [see Fig. 1.14 (b)] [93]

$$\mathbf{B}_{\mathrm{DL}} = B^{\theta}_{\mathrm{DL}} \cos\phi\,\mathbf{e}_{\theta} - B^{\phi}_{\mathrm{DL}} \cos\theta \sin\phi\,\mathbf{e}_{\phi}, \tag{1.42}$$

$$\mathbf{B}_{\mathrm{FL}} = B^{\theta}_{\mathrm{FL}} \cos\theta \sin\phi\,\mathbf{e}_{\theta} - B^{\phi}_{\mathrm{FL}} \cos\phi \sin\mathbf{e}_{\phi}, \tag{1.43}$$

where $\mathbf{e}_{\theta}$ and $\mathbf{e}_{\phi}$ are the polar and azimuthal unit vectors, respectively. The coefficients $B^{\theta}_{\mathrm{FL,DL}}$ and $B^{\phi}_{\mathrm{FL,DL}}$ are functions of the magnetization orientation, defined by the polar, θ, and azimuthal, ϕ, angles.

---

[12] Alternatively, the torque $\mathbf{T}$ can be decomposed into the even, $\mathbf{T}_{\mathrm{even}}$, and odd, $\mathbf{T}_{\mathrm{odd}}$, contributions reflecting the symmetry of the DL and FL torques under magnetization reversal, respectively. This representation will be used in Appendix C during the discussion of the linear-response theory employed for calculation of the SOTs.

[13] For example, higher-orders are required to describe the anisotropy of SOTs as shown AlOx/Co/Pt [93].

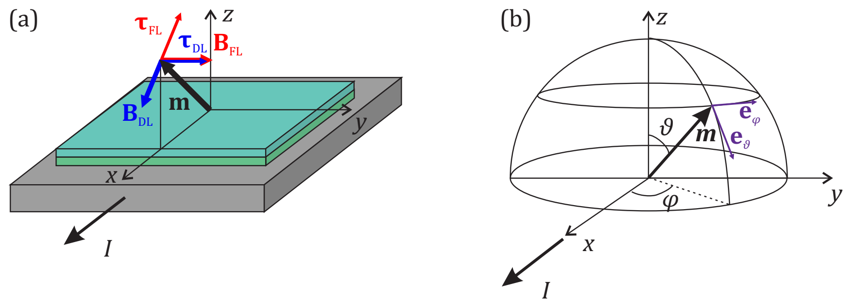

Figure 1.14: (a) Illustration of the SOTs and the corresponding effective fields acting in a model HM/FM system when the magnetization is tilted parallel to the current direction. (b) Schematic of the coordinate system showing $\mathbf{m} = (\sin\theta\cos\phi, \sin\theta\sin\phi, \cos\theta)$. Adapted from [93]

CURRENT-INDUCED SPIN TORQUE MAGNETIZATION SWITCHING

The current-induced spin torques described above are of fundamental as well as of technological importance because they are seen as an alternative to using magnetic fields for manipulating magnetization [62]. For a sufficiently large current, the magnetic layer can respond by reorienting its magnetic moment, allowing for efficient control of the magnetization in nanoscale ferromagnets. In optimized systems, the STT strength can approach a value on the scale of $\hbar$ of the angular momentum transferred per electron. This corresponds to the torque per unit current much larger than that produced by the current-induced Oersted field acting on the magnetization. Furthermore, in the case of the SOT, the net transfer per electron is no longer limited by one $\hbar$ of spin angular momentum, which can make it significantly more energy-efficient.

Another advantage of the spin-torques, and in particular the SOT, is that the switching condition is given by the applied current density and not by the absolute current, which makes the mechanism scalable and, therefore, suitable for high-density memories [62]. Of added benefit is that, unlike magnetic fields, the spin torques can act very locally down to the atomic scale. This makes it easier to manipulate one magnetic element within a dense array, without disturbing neighboring elements. The SOTs in the PMA multilayer system W/CoFeB/MgO and the possibility of their energy-efficient manipulation will be discussed in Chapter 4.

Moreover, in a PMA multilayer system which also exhibits the interfacial DMI, the SHE-induced SOT can move the Neél DWs similarly to an applied OOP magnetic field, which depends on the DW chirality. Such SHE+DMI scenario for a homo-chiral DW is illustrated in Fig. 1.15. The spin current generated due to the SHE in the HM layer acting on a Neél type

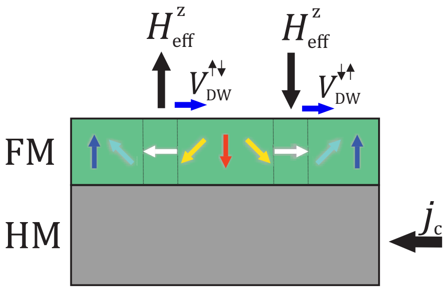

Figure 1.15: Schematic of current-induced motion of homo-chiral DWs in a PMA multilayer system in the absence of external magnetic field, with $\mathbf{H}^z_{\text{eff}}$ being the SHE-induced effective field acting upon the Néel-type chiral DW.

DW gives rise to an effective field [30, 96]

$$\mathbf{H}^z_{\text{eff}} = \frac{\hbar\theta_{\text{SHE}}}{2e\mu_0 M_S t_{\text{FM}}} \cos\Phi \left(\mathbf{j}_c \times \mathbf{e}_y\right), \tag{1.44}$$

where Φ is the angle between the DW moment and the x axis, for $j_c || x$.

One can see from Fig. 1.15 (a) that in the case when the chirality of the DWs is the same, set by the DMI as discussed in Section 1.2.6, this $\mathbf{H}^z_{\text{eff}}$ can lead to parallel DW motion of both walls instead of the domain expansion. This is attributed to the opposite signs of $\mathbf{H}^z_{\text{eff}}$ for up-down ($\cos\Phi = 1$) and down-up ($\cos\Phi = -1$) DWs [96]. Such a remarkable consequence of the interplay between the DMI and SOTs has a potential to make recently proposed race-tack memory concept [97] more efficient [53, 54, 98].

1.5 ELECTRIC FIELD CONTROL OF MAGNETISM VIA THE MAGNETOELASTIC EFFECT

In recent years controlling magnetism on the nanoscale using electric fields has attracted significant attention [99]. Among a number of mechanisms known to facilitate the electric field control of magnetic properties of various systems,[14] mechanical strain, acting via the ME effect on the magnetic anisotropy of a FM, is of interest for this thesis.

The schematic of a typical system to realize the electric field control of magnetic properties via electrically controlled strain is depicted in Fig. 1.16 (a). In this case, an electric field is applied across a piezoelectric substrate, such as $[\text{Pb}(\text{Mg}_{0.33}\text{Nb}_{0.66}\text{O}_3)]_{0.68}$-$[\text{PbTiO}_3]_{0.32}$ (PMN-PT),

---

[14] E.g. the exchange bias in composite FM/antiferromagnet systems or the voltage-induced magnetic anisotropy (VCMA) in magnetoelectric oxides [100, 18].

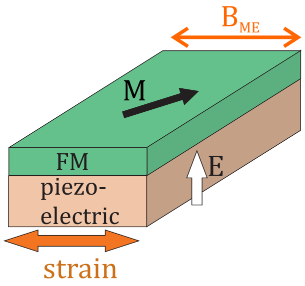

Figure 1.16: Schematic realization of the electric field control of magnetic anisotropy via ME effect. An electric field applied across a piezoelectric substrate generates mechanical strain which is transferred to the adjacent FM layer, where it acts on the magnetization via the strain-induced ME anisotropy. Adapted from [100].

Pb(Zr,Ti)O_3 (PZT), $BaTiO_2$ (BTO), which generates a strain as will be discussed in the next chapter. The strain is transferred to the adjacent FM layer and changes its magnetic anisotropy via the ME effect, as discussed in Section 1.2.

The induced change can be large enough to rotate the direction of the magnetization easy axis by 90° and modify the in-plane magnetic domain pattern [101, 102]. Of particular importance is that the magnetization state of small magnetic elements can be switched by strain [103, 104, 105, 106], which may be useful for data storage applications [107]. The most relevant to this thesis works will be reviewed in more details in the introduction parts of the chapters reporting the studied here impact of a mechanical strain on magnetic properties of in-plane (IP) and OOP magnetized systems. Other experimental and theoretical/computational studies of the impact of mechanical strain on magnetic properties of various systems are described in great details in comprehensive reviews, e.g. Refs. [3, 108].

CHAPTER 2

EXPERIMENTAL TECHNIQUES

> I did not have to taste the soup in order to know the recipe, nor did I have to get an electric shock in order to know about electricity.
>
> A Separate Reality - Carlos Castaneda

This Chapter offers an introduction to the experimental techniques used in this thesis. We will start with a discussion of the most relevant properties of the piezoelectric PMN-PT substrates used for the electrical generation of strain. Then, electron beam lithography (EBL) technique used for the fabrication of microstructures on top of the piezoelectric substrates will be introduced. Furthermore, this Chapter introduces the basics of magneto-optic effects with particular emphasis on the magneto-optical Kerr effect (MOKE) and x-ray magnetic circular dichroism (XMCD) which are widely used for the characterization of magnetic structures. The latter in combination with high spatial and temporal resolution photoemission electron microscopy (PEEM) is known to be a powerful tool for the investigation of magnetization dynamics on the nanoscale. Finally, transport magnetometry techniques will be introduced, which allow one to quantitatively assess the SOTs and DMI in thin film multilayer systems.

2.1 SAMPLE FABRICATION

2.1.1 PIEZOELECTRIC PMN-PT SUBSTRATES

For the generation of electric field-induced mechanical strain, a commercial relaxor ferroelectric substrate $[\mathrm{Pb(Mg_{0.33}Nb_{0.66}O_3)}]_{0.68}$-$[\mathrm{PbTi_3}]_{0.32}$ (PMN-PT) was used [109]. In this Section, we

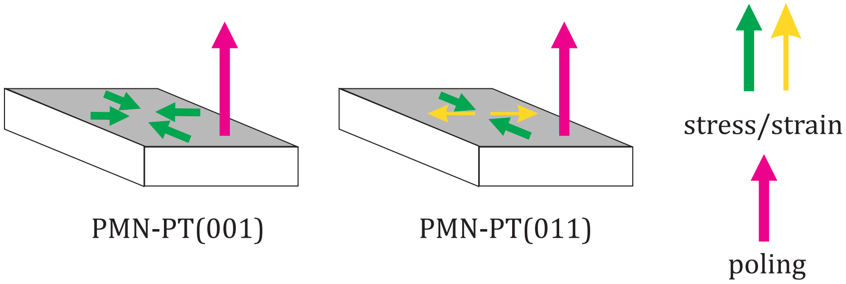

Figure 2.1: Relative orientation of the poling direction (magenta arrows) and the generated tensile (yellow arrows) and compressive (green arrows) strain in piezoelectric PMN-PT (001) and PMN-PT (011) single crystals. Poling direction is set by the applied OOP electric field. Adapted from Ref. [118].

discuss the properties that promote PMN-PT as the best choice of piezoelectric material for the purposes of this work. Primarily, this is because, for similar dimensions, PMN-PT can generate strain close to an order of magnitude larger [110, 111].

Commercially available PMN-PT substrates, grown by Bridgeman method [109, 112], have a rhombohedral crystal structure [109], however, it is known that coexistence of rhombohedral, monoclinic, orthorhombic or tetragonal phases may be observed in a so-called morphotropic phase boundary (MPB) [113, 114]. This close proximity and coexistence of several crystal symmetries is believed to be the origin of very large piezoelectric coefficients of PMN-PT [114].

Moreover, it was shown previously that the character of strain depends on the crystallographic orientation of PMN-PT [115, 116]. The (100) oriented and poled rhombohedral crystal produces an isotropic in-plane piezoelectric response while the (011)oriented and poled crystal produces an anisotropic in-plane piezoelectric response, as schematically depicted in Fig. 2.1. The latter has two orthogonal axes corresponding to tensile and compressive strain [114]. This behavior originates in the ferroelectric polarization associated with the movement of the Ti atoms in the unit cell upon application of an electric field along a certain direction, [001] and [011] in Fig. 2.1 (a) and (b), respectively [117].

Here we consider the mechanism of strain generation in PMN-PT(011),[1] of which the rhombohedral unit cell structure is presented in Fig. 2.2 (a). The coordinate system depicted in this figure shows eight possible directions of the spontaneous electrical polarization along the body diagonals ⟨111⟩. The top view of the (011)-cut of PMN-PT with spontaneous polarization pro-

---

[1] Note that the in-plane $[01\bar{1}]$ and [100] directions of the commercial PMN-PT substrate, when not marked by the provider, can be found by x-ray reflectivity measurement.

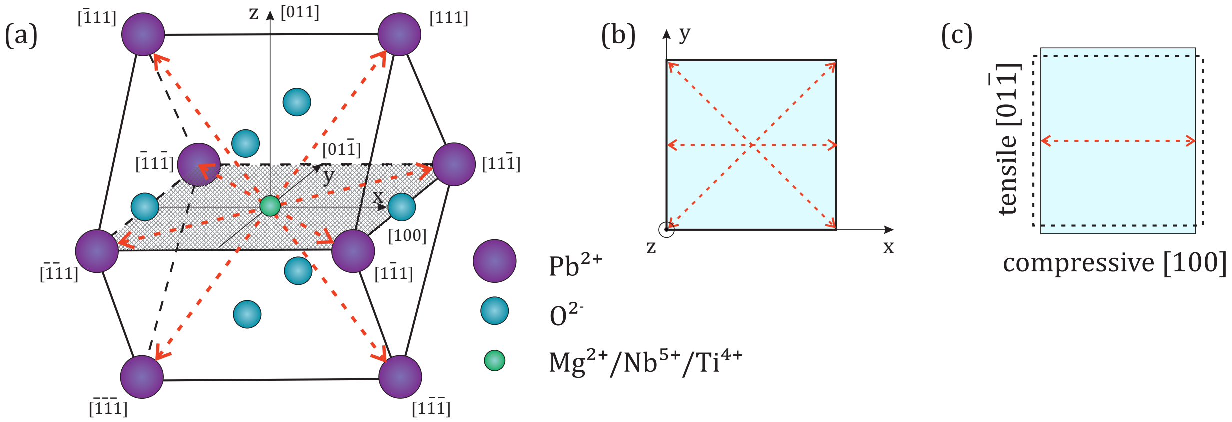

Figure 2.2: (a) The unit cell and spontaneous polarizations of PMN-PT (011). Top view of the polarizations and deformation of the (011) crystal plane of PMN-PT substrate for (b) the virgin state and (c) under an electric field along [011] direction poling only 2 of the 8 possible polarizations.

jections in a virgin state onto the (011) plane in Fig. 2.2 (b). Application of a positive electric field, i.e. along $+z$, with a magnitude larger than the *coercive field* of the substrate (ca. ±200 kV m^{-1}) poles the substrate. As a result, the eight possible polarization directions are switched leaving only two of them along the $[\bar{1}11]$ and [111] directions. The projection of these two polarizations onto the $x-y$ plane lies in the x direction, as shown in Fig. 2.2 (c). Further increase of the electric field rotates these two polarizations toward the z direction, which induces a contraction along x and an extension along y. Note that the extension along y may be the result of a small rotation of the polarization about the z-axis such that a finite y-component of the polarization projection onto the $x-y$ plane is developed under applied field [114].

Thus, as the electric field increases, the polarizations tend to further align with the field direction, resulting in even stronger contraction and extension of the unit cell. This behavior corresponds to the linear part of the strain response to the applied field, shown in Fig. 2.3. When the electric field is removed the polarizations relax to the poled state with only two polarizations along the $[\bar{1}11]$ and [111] directions, but the virgin state, such as that shown in Fig. 2.2 (b), is not be recovered. Note that in Fig. 2.3 the strain response was measured along the x and y directions with the zero reference set to an unpoled state [114].

A negative electric field smaller than the coercive field first causes the two OOP polarizations to rotate to four possible in-plane directions, i.e. along the ⟨111⟩ directions. Each of these has a projected component along both the y and the x directions, which produces a large jump in the strain along the y direction, as seen in Fig. 2.3. Further increase of the negative electric field

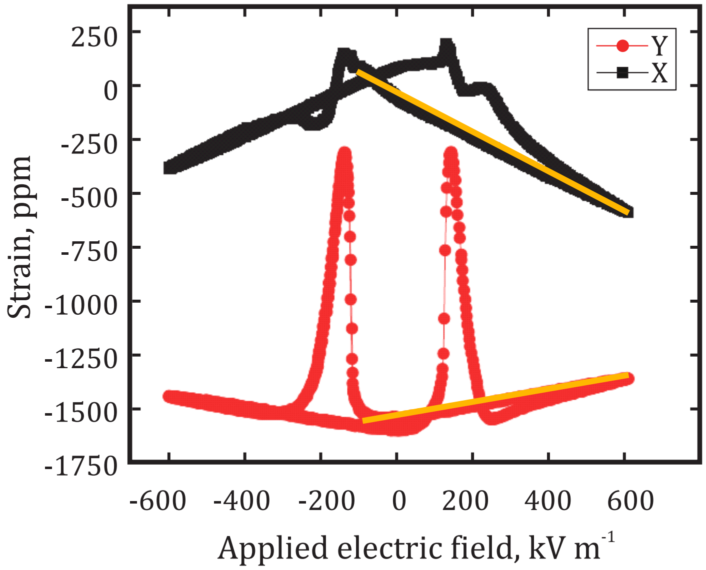

Figure 2.3: Piezoelectric response of a PMN-PT (011) crystal as a function of the applied electric field applied in the [011] direction. The strain is measured along the [100] and $[01\bar{1}]$ directions, defined as x and y, respectively. The yellow lines indicate the linear regime (see text). Adapted from Ref. [114].

leads to another non-180° reorientation of the polarization from the in-plane to the other two directions, i.e. $[1\overline{11}]$ and $[\overline{111}]$, see Fig. 2.2 (a). As a result, the strains along the x and y directions return to a normal poled piezoelectric response and follow the linear trend upon increasing the negative electric field. A similar strain jump occurs upon crossing the positive coercive field which indicates that the tensile and compressive strain directions are determined by the crystallographic directions of PMN-PT and are invariant under the sign of the applied electric field.

As can be seen from the strain hysteresis loop in Fig. 2.3 there are two regimes. By operating in the vicinity of the coercive field, it is possible to take advantage of the first non-180° polarization rotation to produce two distinct, permanent and reversible strain states. It was reported that in this case, ultra-high in-plane piezoelectric coefficients with $d_{31} \sim 1800\ \mathrm{pC\,N^{-1}}$ along the $[01\bar{1}]$ direction can be achieved for an optimized PMN-PT(011) single crystal [119]. Note that for the strain along the x direction, there is no clear conclusion because the strain response, in this case, is quite random.

The second regime is more favorable for the purpose of this thesis as it allows for a reproducible and reliable control of the generated strain by electric fields. Operating in the linear

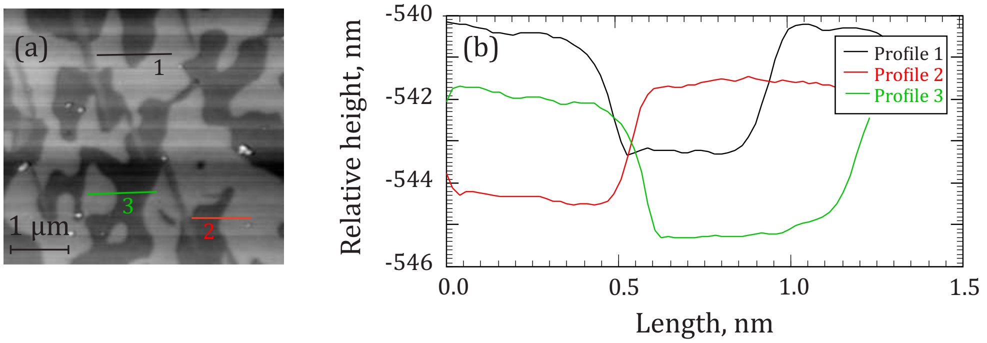

Figure 2.4: (a) AFM images of the surface of an unpoled PMN-PT (011) single crystal. (b) Surface line profiles along the selected paths shown in (a).

region (indicated be yellow lines in Fig. 2.3), the PMN-PT substrate exhibits highly anisotropic behavior, with tensile strain along the $[01\bar{1}]$ and compressive strain along the [100] directions. The piezoelectric coefficients, in this case, are ~ -890 pC N^{-1} along x and $\sim +290$ pC N^{-1} along y, respectively.

The roughness of commercial PMN-PT substrates is declared to be <10 Å [109], however, the atomic force microscopy (AFM) scans of new substrates, presented in Fig. 2.4, demonstrate the existence of surface steps of ca. 3 nm height. As seen in Fig. 2.4 (a), PMN-PT has many domains of two heights in the level of 3 nm even though it is polished. Moreover, the height changes sharply at the domain boundary and remains constant within the domain. Therefore, this height difference is directly related to the ferroelectric multi-domain structure at the surface of unpoled PMN-PT as concluded in e.g. Ref. [120]. Importantly, by AFM we discovered that the roughness of the PMN-PT substrates after ion beam etching (IBE) does not become worse, and nominally similar FM materials, deposited on a brand new PMN-PT substrate and the one etched with the IBE tool, show similar magnetic hysteresis loops. Thus, the substrates can be reused following the IBE for further depositions with a negligible effect on the magnetic properties of the overlaid material.

2.1.2 ELECTRON BEAM LITHOGRAPHY (EBL)

The experiments presented in this thesis were carried out on nanosized magnetic structures, which were fabricated by EBL technique. The basic principle of EBL patterning is as follows. First, a polymeric *resist* is spin-coated on the sample surface, to ensure the resist is of the desired thickness. The solvent in the resist is then evaporated on a hot plate at optimized temperatures. A pre-defined pattern is transferred on the sample by exposing certain areas of the surface with a focused electron beam (e-beam). Depending on the chemical and physical properties of

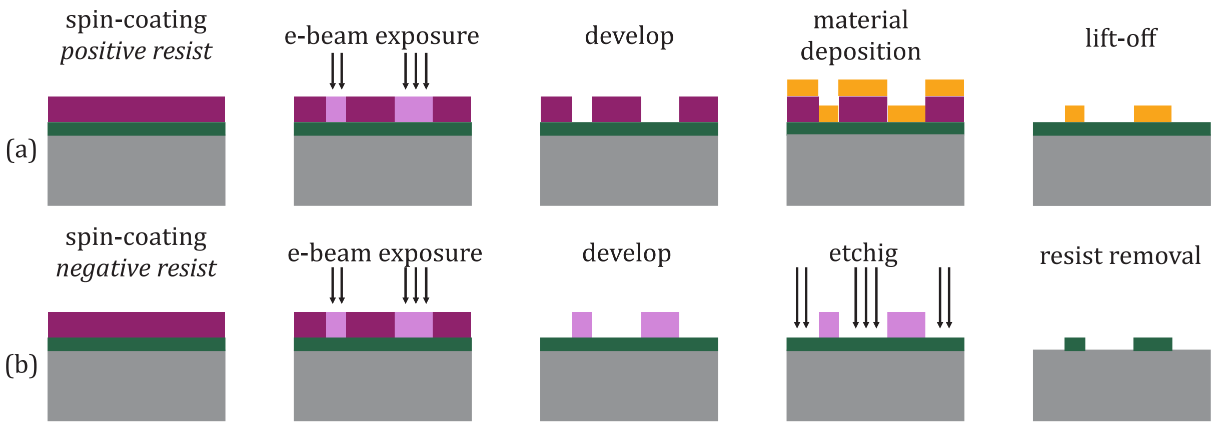

Figure 2.5: Schematic principle of EBL patterning showing subsequent steps of the fabrication processes using a positive (a) and a negative (b) resist.

the resist (classified as positive and negative, see Fig. 2.5), the interaction of the e-beam with the polymer molecules renders the exposed material either soluble for positive resists, Fig. 2.5 (a), or insoluble for negative resists, Fig. 2.5 (b), by a specific chemical, called developer. After the development process, i.e. removing the exposed/unexposed parts of the resist, the sample surface is ready for further processing steps, which can involve etching (either chemical or ion-beam) or a material deposition, as summarized in Fig. 2.5. In this thesis *magnetron sputtering* deposition [121] and Ar-ion etching (in the following, IBE) were employed for thin film deposition and removal of the unnecessary material, respectively.

The EBL exposure is performed by laterally scanning the sample and it allows for defining structures with a spatial resolution down to 10 nm [122]. Besides the electron optics the spatial resolution is also influenced by the resist properties and e-beam characteristics. While scanning, the e-beam is deflected by electron lenses and the maximum deflection achieved defines the writing field (WF). To do the exposure in the next WF, the sample stage is mechanically moved to a new position, so that the undeflected e-beam hits the center of the new field. Eventually, the whole patterned area is scanned by subsequently changing the WF one by one. Note, however, that if the WF alignment procedure, which is generally required prior to any exposure step, is not performed perfectly, stitching errors due to the misalignment between adjacent WF may occur [123]. The choice of the WF area is governed by the size of the area to be patterned, i.e. to pattern a coplanar wave guide (CPW) (see, for instance, Chapter 3) the use of a larger WF is sensible. On the other hand, for patterning small structures on a small area, a smaller WF is preferred as it involves shorter deflection distances and results in a better e-beam quality.

Moreover, if a multiple-step lithography process is needed, a layer to layer WF alignment is crucial [124]. For that, each writing field is designed to contain at least three alignment markers, which are used to align the layers of subsequent steps.

Fabrication of the structures investigated in this thesis was done using a Raith Pioneer dedicated EBL system. As the samples studied in Chapters 3 and 4, 5 were fabricated using two distinct processes the fabrication details for each of them are given in Appendix A.

2.2 MAGNETO-OPTICAL (MO) EFFECTS

The field of magneto-optics started with the observation of rotation of the polarization plane of linearly polarized light upon transmission through a piece of lead-borosilicate glass in a magnetic field by Faraday [125] and the discovery of a similar effect for linearly polarized light reflecting from a piece of iron, known as Kerr effect [126]. Interestingly the microscopic origin of these two effects was only understood long after with the development of quantum mechanics. The basic origin of the magneto-optic (MO) effects is known to be the SOC, which establishes the coupling between the magnetic field interacting with the spins and the photons, which interact with the orbital degrees of freedom [127]. Practical interest was triggered by the discovery that magnetic domains could be observed using Kerr effect [128, 129], after which also the technological relevance of the MO effects was realized [130].

Early research in magneto-optics involved optical transitions within the energy range corresponding to intra-band transitions, thus involving the electronic states of the valence band. Later it was proposed that the MO effects should also occur upon x-ray excitations from core levels to valence states, which was then confirmed by the discovery of x-ray magnetic dichroism (XMD) [131, 132]. Using x-rays provided a way to examine the magnetic properties of solids on an atomic scale. Moreover, with an understanding of the sum rules, it became possible to use XMD as a quantitative measure of spin and orbital moments of a particular element in the material.

Nowadays a number of MO effects is widely used to probe properties of magnetic materials. Below we consider in more detail two examples relevant to this thesis.

2.2.1 MAGNETO-OPTIC KERR EFFECT (MOKE)

Magneto-optic Kerr effect (MOKE) occurs when linearly polarized light is reflected from a magnetic medium. The polarization of the reflected light undergoes a two-fold modification: *(i)* tilt of the polarization plane with respect to that of the incoming beam, known as *Kerr rotation,* θ_K, *(ii)* the new polarization becomes elliptical, referred to as *Kerr ellipticity,* ϵ_K. These two

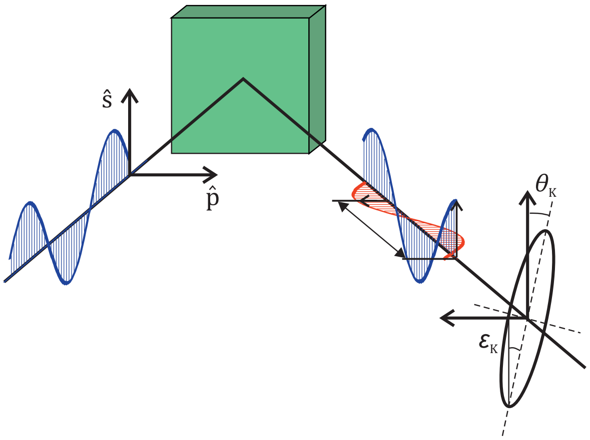

Figure 2.6: Illustration of the MOKE with the geometrical representation of the complex Kerr angle Φ_K. Kerr rotation, θ_K, is related to the orientation of the ellipse's major axis whereas Kerr ellipticity, ϵ_K, is related to the minor to major axis ratio.

consequences of MOKE are depicted in Fig. 2.6. Together the Kerr rotation and ellipticity are combined into the *complex Kerr angle* $\Phi_K = \theta_K + i\epsilon_K$ which in the case of MOKE is a function of the magnetization.

For a detailed quantum mechanical description of the Kerr effect in FM materials, the reader is referred to e.g. Refs. [127, 133]. Here, we will follow an alternative description of MOKE based on the classical *dielectric tensor theory* [133, 134], where the reflected E^{r} and the incident E^{i} amplitudes are related through the reflectivity tensor $\hat{r}$ as

$$\begin{bmatrix} E_s^{\mathrm{r}} \\ E_p^{\mathrm{r}} \end{bmatrix} = \begin{bmatrix} r_{ss} & r_{sp} \\ r_{ps} & r_{pp} \end{bmatrix} \begin{bmatrix} E_s^{\mathrm{i}} \\ E_p^{\mathrm{i}} \end{bmatrix} . \tag{2.1}$$

Here p and s are the standard notations for the electric field oscillating in the plane of incidence and perpendicular to it, respectively (Fig. 2.6). The presence of non-vanishing off-diagonal components $r_{sp}(r_{sp})$ which are zero in a non-magnetic medium leads to the mixing of the two orthogonal components of the electric field.

For example, for s-polarized incident light, the reflected electric fields from Eq. 2.1 are $E_s^{\mathrm{r}} = r_{ss}E_s^{\mathrm{i}}$ and $E_p^{\mathrm{r}} = r_{ps}E_s^{\mathrm{i}}$. For small changes in the incident polarization, θ_{K} is related to the component of E_p^{r} that is in phase with E_s^{r}, leading to the rotation of the polarization upon reflection. ϵ_{K} is related to the component of E_p^{r} that is $\pi/2$ out of phase with E_s^{r}, leading to ellipticity.

Thus, MOKE arises due to the non-zero off-diagonal reflectivity components as well as modulation of the diagonal components in Eq. 2.1 in the presence of a magnetic field [134]. There-

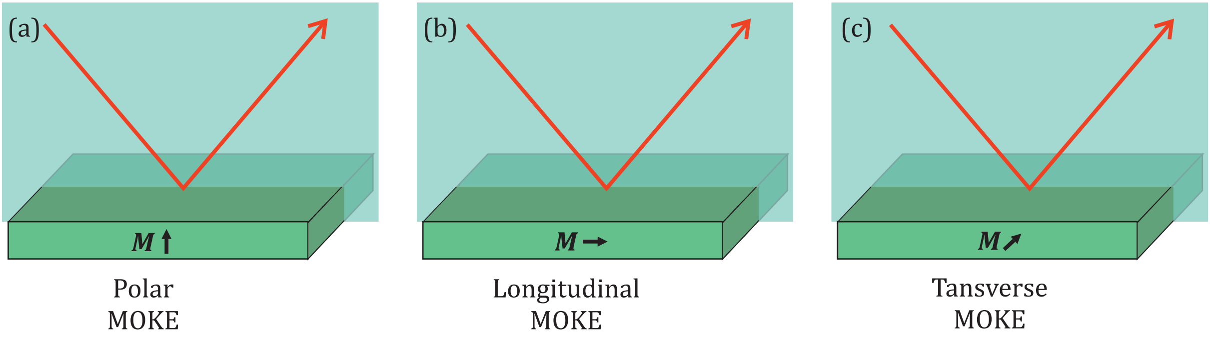

Figure 2.7: Schematics of (a) polar, (b) longitudinal and (c) transverse MOKE configurations, depending on the relative orientation of the plane of incidence of the probing light and the magnetization direction within the sample.

fore, the Kerr effect has become widely used to probe the magnetization of materials as a function of different parameters such as temperature, magnetic field and composition.

There are three main MOKE configurations differing in the relative orientation of the magnetization direction **M** (or the external magnetic field **H**) and the plane of incidence of the probing beam. These three configurations are schematically depicted in Fig. 2.7:

- *Polar MOKE* - when the magnetization of the sample is pointing in the direction perpendicular to the sample plane, called OOP magnetization.
- *Longitudinal MOKE* - when the magnetization is in the plane of the sample (*in-plane* magnetization) and in the plane of incidence.
- *Transverse MOKE* - when the in-plane magnetization is perpendicular to the plane of incidence.

For the experiments described in this thesis, the longitudinal MOKE and polar MOKE configurations are used to detect the IP or OOP magnetization components, respectively. The schematic of the longitudinal MOKE[2] setup used in this thesis is presented in Fig. 2.8 with the indicated components. Linearly (*s*-) polarized light from the laser passing through the polarizer P_1 is focused on the sample surface by a lens. The magnetization of the sample causes changes in the polarization of the reflected light, which after the collimation lens passes through the photo-elastic modulator (PEM) and a linear polarizer P_2, oriented at 0° and 45° with respect

---

[2] The schematic of the polar MOKE setup differes only by the orientation of the magnetic field, which in this case, is directed perpendicular to the sample plane.

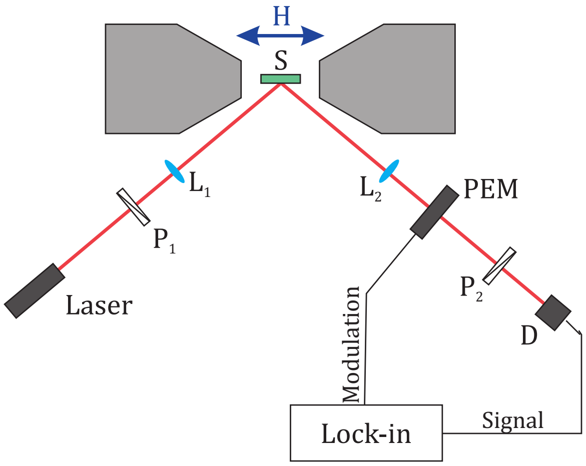

Figure 2.8: Sketch of a basic longitudinal MOKE setup showing the laser, the sample (S), two polarizers P_1 and P_2, two lenses L_1 and L_2 employed to focus the beam onto the sample and re-parallelize the beam after the reflection, PEM is a modulator and D is a photon detector. The polarization of the laser light lies in the direction perpendicular to the page.

to vertical, respectively. The signal arriving at the detector at given harmonics of the PEM frequency is then analyzed by a lock-in amplifier is proportional to the complex Kerr angle Φ_K:

$$\begin{aligned} \theta_\mathrm{K} &\propto I_{1\omega_\mathrm{PEM}} \\ \epsilon_\mathrm{K} &\propto I_{2\omega_\mathrm{PEM}}\,. \end{aligned} \tag{2.2}$$

We also note that in order to measure the absolute values of θ_K and ϵ_K it is necessary to measure the initial intensity illuminating the sample. However, typically in MOKE experiments, one is only interested in qualitative changes of these quantities as a function of applied magnetic field.

The information depth of the reflective MOKE technique is determined as $l_\mathrm{prob} = \lambda/4\pi\beta$, where β is the imaginary part of the refractive index of the material [135]. For typical metallic systems investigated in the framework of this thesis, l_prob amounts to ~ 20 nm. It is important to note that although this technique can be very sensitive, it does not provide a quantitative measure of the magnetization. However, from the shape of the obtained hysteresis loop, the magnetization reversal processes can be investigated in detail.

2.2.2 X-RAY MAGNETIC CIRCULAR DICHROISM (XMCD)

As mentioned above, x-ray magneto-optics makes use of excitations from deep atomic core levels onto unoccupied valence states. In the following, we will focus on XMCD on the example of $L_{2,3}$ edges of transition metals as schematically sketched in Fig. 2.9, as it is used to probe the magnetic properties of $3d$ materials, such as Ni, Co and Fe used in this thesis.

In the simplest picture of x-ray absorption, a photon transfers its energy to a core electron and the electron is excited into an unoccupied electronic state. Formally this process is described by the transition probability $T_{\mathrm{i}\to\mathrm{f}}$, also known as *Fermi's Golden rule* [136]:

$$T_{\mathrm{i}\to\mathrm{f}} \propto \langle f \left|\hat{\mathrm{H}}\right| i\rangle \, \delta\left(E_{\mathrm{f}} - E_{\mathrm{i}} - h\nu\right) \rho\left(E_{\mathrm{f}}\right), \tag{2.3}$$

where E_{f} and E_{i} are the energies of the final and initial states, respectively, $h\nu$ is the photon energy. $\langle f \left|\hat{\mathrm{H}}\right| i\rangle$ is the transition matrix element, with the $\hat{\mathrm{H}}$ being the Hamiltonian that describes the interaction between the photon and the excited electron. $\rho\left(E_{\mathrm{f}}\right)$ is the density of free final states with the energy E_{f}. For a more detailed account, the reader is referred to e.g. Ref. [36].

As a consequence of Eq. 2.3, the absorption of a photon of energy $h\nu$ takes place only if certain conditions, defined as *dipole selection rules*, are simultaneously satisfied. The dipole selection rules[3] for transitions between states of the form $|n, l, m_l, s, m_s\rangle$ are:

$$\Delta l = \pm 1,$$
$$\Delta m_l = 0, \pm 1,$$
$$\Delta s = 0,$$
$$\Delta m_s = 0.$$

From these selection rules, it follows that the electrons from $2p$ core states can be excited to the unfilled $3d$ states of transition metals, as illustrated in Fig. 2.9 (a). As a result of the $2p \to 3d$ transitions, an x-ray absorption spectrum such as that shown in Fig. 2.9 (b) can be obtained. The shape of a typical x-ray spectrum is determined by different order interactions taking place in the system. In particular, *core spin-orbit coupling* is responsible for the separation of $2p_{3/2}$ and $2p_{1/2}$ (L_3 and L_2) peaks. In systems with weak valence band SOC, the integrated absorption intensities of unpolarized x-rays result in a branching ratio $L_3 : L_2 = 2:1$, and their sum is directly proportional to the number of d holes [36, 139], i.e. unoccupied states.

Valence band exchange splitting provides the necessary symmetry breaking for the x-ray MO effect to occur. As discussed in Section 1.1.2 of this thesis, the magnetic properties of the $3d$ transition metals are mainly determined by their valence d-electrons. For the $3d$ ferromagnets the difference between the number of spin-up $N_\uparrow$ and spin-down $N_\downarrow$ d-holes defines the spin magnetic moment due to the exchange interaction, $m_s = \left(N_\uparrow - N_\downarrow\right)\mu_B$. Thus, the use of circularly polarized light allows us to study the magnetic properties of $3d$ materials, such as Ni, Fe and Co used in this thesis.

The underlying mechanism can be explained using the following two-step picture:

---

[3] The dipole selection rules are dictated by the non-vanishing transition matrix elements which are tabulated elsewhere [137, 138].

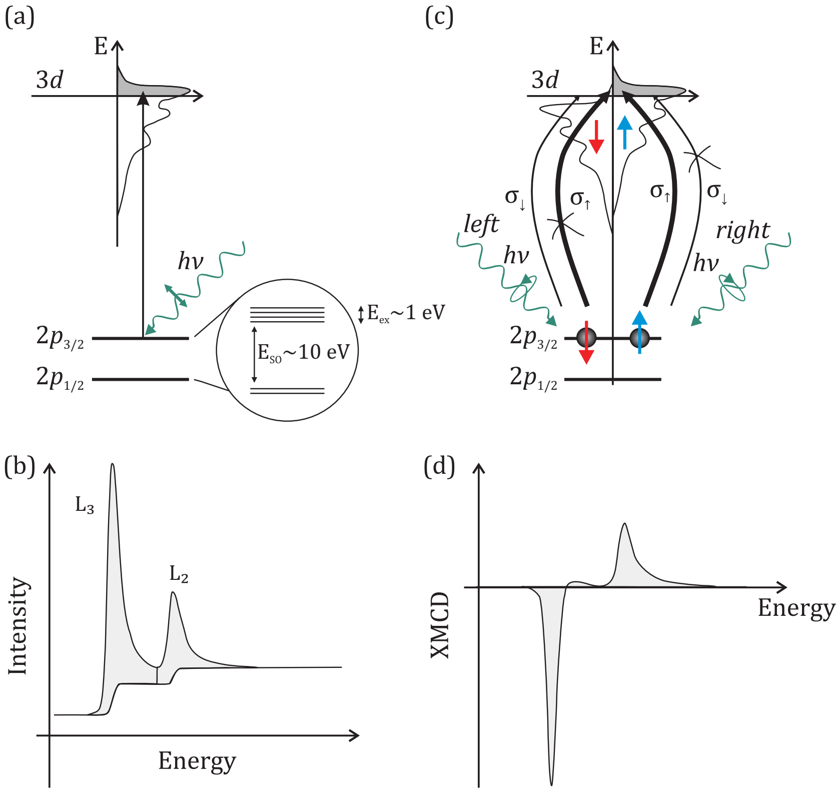

Figure 2.9: (a) Schematic illustration of electronic states with the valence states and the core states assumed to be spin-orbit split into $2p_{3/2}$ and $2p_{1/2}$ states, giving rise to the L_3 and L_2 edges in experimental spectra in (b), respectively. (b) Schematic shape of an L-edge x-ray absorption spectrum for the 3d transition metals, such as Fe, Co, Ni. (c) Electronic states for a transition metal, where the valence band is represented by spin-up and spin-down d sub-bands and the L_3 transition is indicated. Spin-up, $\sigma_\uparrow$ photoelectrons are more readily excited from the $2p_{3/2}$ level with right-handed circularly polarized light to the partially unfilled 3d valence spin-up band because the dipole operator does not allow spin-flips during excitation. (d) Qualitative shape of the XMCD spectrum estimated using Eq. 2.4.

First step. The *right* (*left*) circularly polarized photons transfer the angular momentum $\hbar$ ($-\hbar$) to the excited photoelectron. For the electrons originating from spin-orbit split levels the photon's angular momentum is transferred to the spin via SOC. As a result, in this step, photoelectrons with opposite spins are created upon absorption of left or right circularly polarized light.[4] Thus, excitation of electrons at the $2p_{3/2}$ level (L_3 edge) with right-handed circularly polarized light will preferentially produce spin-up electrons.

Second step. At this point, the magnetic properties enter via the spin-split valence band [see Fig. 2.9 (c)], which acts as a detector for the spin of the excited photoelectron. Since only the transitions within one spin sub-band for a given photon polarization are allowed by the selection rules, the asymmetry in the spin-up and spin-down states at the Fermi level in magnetic materials leads to the asymmetry in the absorption of circularly polarized light.

Thus, by calculating the difference of the normalized intensities recorded with right and left circular polarizations at the L_3 and L_2 edges as:

$$I_{\mathrm{XMCD}} = \frac{I_+ - I_-}{I_+ + I_-}, \tag{2.4}$$

where I_+ and I_- correspond to the absorption yield of circularly polarized photons of positive and negative chiralities, respectively, we can obtain an XMCD spectrum, such as one shown in Fig. 2.9 (d). Note that the quantization axis, in this case, is given by the magnetization direction which needs to be aligned with the photon spin for maximum dichroism effect [36]. It is easy to show that it is equivalent to fix the x-ray polarization and switch the magnetization direction. Moreover, since $p_{3/2}$ and $p_{1/2}$ levels have opposite SOC ($l+s$ and $l-s$, respectively), the sign of the XMCD at the L_3 and L_2 edges is inverted, as can be seen in Fig. 2.9 (d).

Therefore, for transition metals, the core level SOC and d-band exchange splitting together determine the shape of the x-ray spectra in Fig. 2.9 (b,d). In addition to these two interactions, there are also *valence band SOC* and *core exchange splitting*, which are typically weak and therefore can be neglected for a qualitative understanding.

Quantitatively the size of the dichroism depends on three parameters [36]:

- the degree of circular polarization of photons P_{circ},
- the expectation value of the magnetic moment $\langle \mathbf{m} \rangle$ of the $3d$ shell,

---

[4] Note that "spin-up" and "spin-down" are defined with respect to the photon helicity, which is parallel (antiparallel) to the x-ray propagation direction for the right (left) circular polarization [135].

- the angle θ between the magnetic moment $\mathbf{m}$ and the direction of the photon angular momentum $\mathbf{L}_{\mathrm{ph}}$.

This can be summarized in the following expression:

$$I_{\mathrm{XMCD}} \propto P_{\mathrm{circ}} \mathbf{m} \cdot \mathbf{L}_{\mathrm{ph}} \propto P_{\mathrm{circ}} \langle \mathbf{m} \rangle \cos\theta\,. \tag{2.5}$$

2.3 HIGH-RESOLUTION X-RAY-BASED MAGNETIC IMAGING

In order to carry out high-resolution imaging of magnetic samples utilizing the XMCD effect as a contrast mechanism, one requires a source of monochromatic and highly brilliant x-rays. Today's most powerful sources of x-rays are large-scale facilities designed to generate fully polarized, tunable synchrotron radiation, where the x-ray energy can be tuned to the absorption edge of a magnetic atom. The discussion below focuses on the concept of synchrotron radiation and its application to nanoscale magnetism on the example of photoemission electron microscopy.

2.3.1 SYNCHROTRON RADIATION

Originally considered as a waste of energy in high energy physics, today, synchrotron radiation constitutes the best choice for many experiments such as magnetic domain imaging used in this thesis requiring high spatial and temporal resolution.

The synchrotron radiation is created by circulating electrons (or positrons) in a synchrotron storage ring with a constant velocity and energy of a few GeV. The electron beam is first accelerated in a linear accelerator followed by a booster ring and then it is injected into the storage ring as depicted in Fig. 2.10 (b). In the storage ring, the electrons are propelled forward by a microwave field, which is produced by rf-cavities and consists of rf-buckets revolving around the ring. Electrons that are filled into a bucket form a so-called bunch and one bunch contains in the order of 10^{10} electrons. In the stationary frame of an observer, such bunches have a typical length $l = 10$ mm, corresponding to a pulse length of about $\tau = l/c \approx 30$ ps.

In fact, the storage ring is a polygon consisting of tens of linear parts angled together by bending magnets, where the electron bunch travels along a curved path around the vertical magnetic field lines as illustrated in Fig. 2.10 (b). In general, upon deflection in the bending magnet, thus traveling under acceleration, charged particles emit x-ray radiation, so-called *Bremsstrahlung*. In the case of electrons revolving in a synchrotron, this radiation is called *synchrotron radiation*. Furthermore, since the electrons revolving in a storage ring with an energy of several GeV are relativistic, the synchrotron radiation is a result of relativistic effects, which

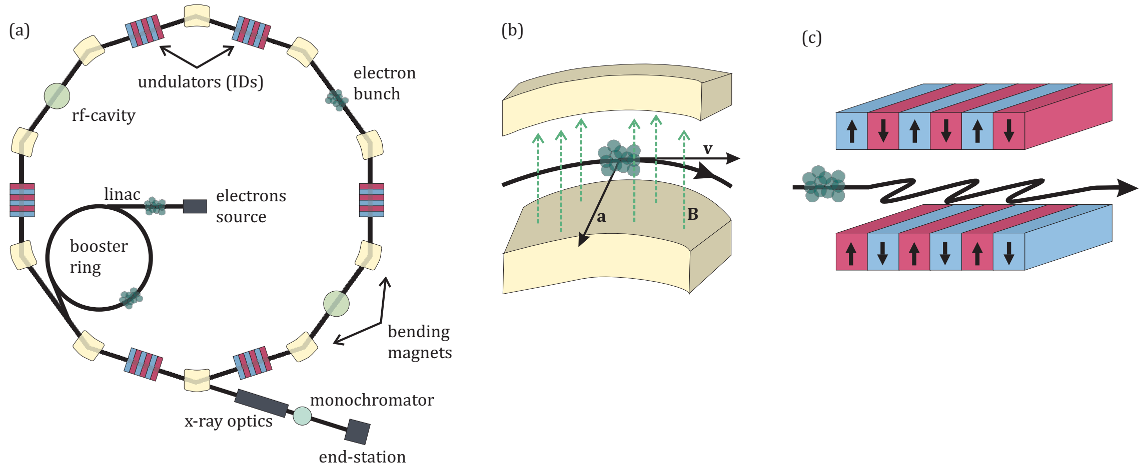

Figure 2.10: (a) Sketch of a synchrotron light source. (b) Schematic of the electrons trajectory within a bending magnet. The velocity **v** is in the tangential direction and the acceleration **a** points toward the center of the circular trajectory. (c) Schematic of an undulator with the electron path depicted.

lead to a distortion of the radiation pattern as shown in Fig. 2.11. The radiation pattern typically emitted by accelerating charged particles, shown in Fig. 2.11 (a), in the case of relativistic electrons, becomes distorted such that, in the laboratory frame, most of the radiation is emitted into a narrow cone of the opening angle $2/\gamma$, as depicted in Fig. 2.11 (b). For the detailed formal description of synchrotron radiation the reader is referred to Ref. [140].

Note that because the primary function of the bending magnets is to keep the electrons in a closed orbit withing the storage ring, the radiation generated by the bending magnets is not optimal. Therefore in the newer generations of synchrotron light sources, other types of devices are employed to generate synchrotron radiation. One example is an *undulator*, inserted into the straight part of a storage ring. Undulators are constructed of an array of magnets with alternating polarity, as seen in Fig. 2.10 (c). Such arrangement of the magnets causes the electron bunch that is passing through it to deflect, similarly to the bending magnets, but in contrast to bending magnets, no deflection or displacement of the electron beam occurs eventually. Constructive interference of the radiation emitted at each of the periodic deflections of the electrons results in the generation of a coherent x-ray beam of much higher brilliance as compared to that produced by a bending magnet.

The emitted synchrotron radiation is extracted into a beamline, where the x-ray beam is further shaped and focused, and a well-defined photon energy is selected by a monochromator with high energy resolution before the x-ray beam arrives at the experimental setup at the end

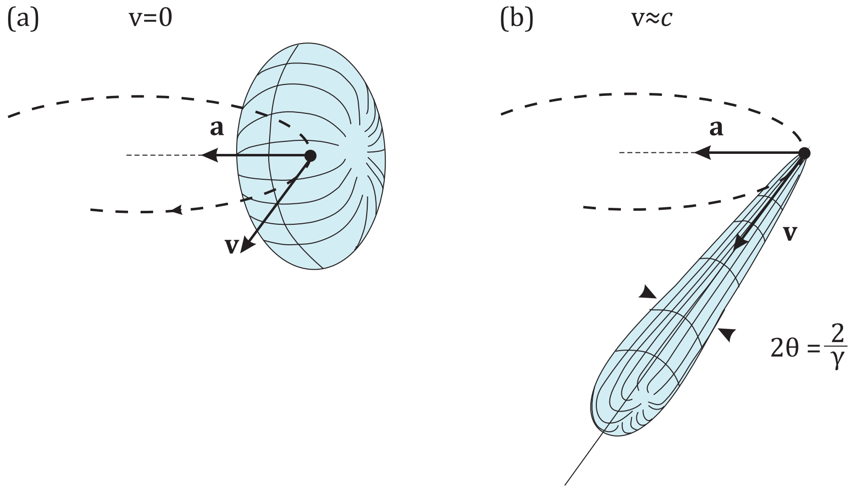

Figure 2.11: Sketch of the radiation pattern emitted by a charge moving along a circular orbit (a) in the rest frame of the charge ($v = 0$) and (b) in the laboratory frame of a stationary observer while the charge is moving with tangential velocity $v \approx c$. The opening angle containing most of the synchrotron radiation is $2/\gamma$.

of the beamline, see Fig. 2.10 (a).

Finally, we address the origin of the polarization of synchrotron radiation, which arises due to the conservation of angular momentum. In the case of bending magnet radiation in the plane of the electrons orbit is linearly polarized, while radiation emitted at finite angles above and below the orbit is left- and right-circular polarized, respectively. Using a suitable aperture to select the radiation it is possible to obtain the desired polarization. In undulators, it is possible to induce different periodic electron trajectories. When the oscillation is confined to a plane the radiation is linearly polarized in that plane. If the path is helical the resulting radiation is purely left- or right-circularly polarized. Undulators installed into the new generation of synchrotron radiation sources allow for full polarization control.

2.3.2 PHOTOEMISSION ELECTRON MICROSCOPY (PEEM)

For direct imaging experiments, PEEM was used in this thesis. PEEM is a photons-in/electrons-out technique where the electrons emitted from a sample upon illumination by a monochromatic ultra-violet (UV) or x-ray light are detected to generate a high-resolution image, as illustrated in Fig. 2.12. In combination with x-ray dichroism PEEM is a widely used technique in surface science, which allows one to study magnetic properties with element sensitivity and high lateral resolution.

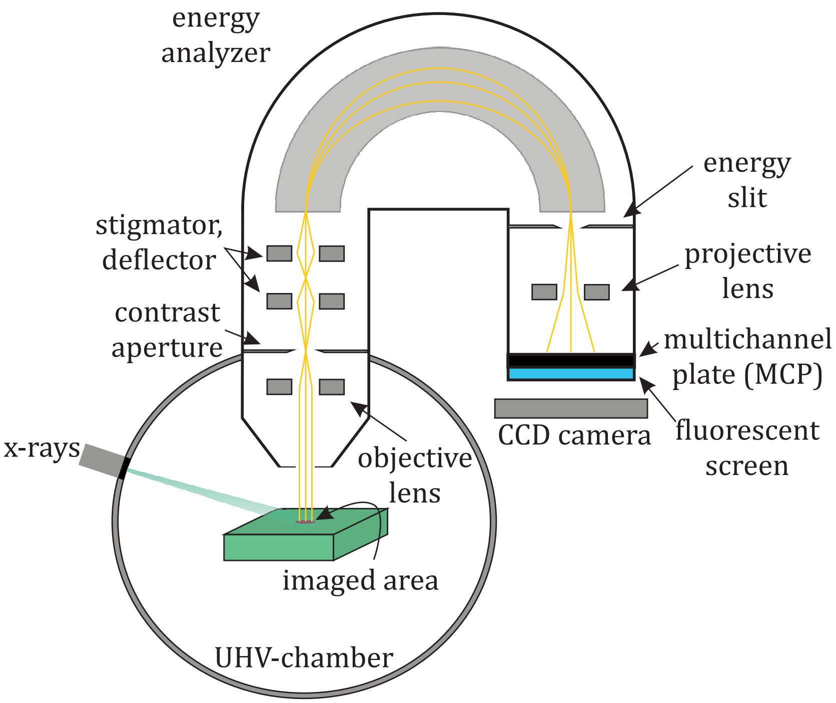

Figure 2.12: Schematic of a PEEM setup. Electrons are emitted from the sample and collected by an objective lens, which conveys the electrons in the imaging section of the microscope where they form an image on a multiplier channel plate combined with a phosphor screen and the image is then acquired with a camera.

The x-ray beam arrives at the sample at an angle of 16° and is focused on the sample surface to match the field of view of the microscope, typically $5-50$ μm. Following the absorption of a photon, a core level electron is excited on to an unoccupied state leaving a core hole, see Fig. 2.13 (a). Upon recombination of the core hole, secondary electrons are generated as illustrated in Fig. 2.13 (b). Due to Auger processes and inelastic scattering of secondary electrons, a cascade of low energy electrons is created with a wide spectrum of energies between the photon energy and the work function of the sample. Therefore, some of these electrons have large enough energy to escape into the vacuum, where they are accelerated by a $10-20$ kV voltage applied between the objective lens and the sample, see Fig. 2.12. The collected electrons are then conveyed into the PEEM column, where they are projected with magnification onto a phosphor screen by a set of electrostatic or magnetic lenses and the image can be viewed in real-time at video rates.

The energy resolution of the x-ray beam is determined by a monochromator in the beamline, while the spatial resolution is determined by the microscope itself, i.e. electron optics, the size of the aperture, and the operation voltage. The main contributions to the resolution come from spherical aberration (electrons with different angles), chromatic aberration (electrons with different kinetic energies), and diffraction [141]. In fact, for x-ray excitation of electrons, chromatic aberrations dominate, arising from the fact that chromatic electron lenses focus the electrons with different kinetic energies differently. Therefore, wide energy distribution of secondary electrons leads to blurring of the PEEM image. Advanced PEEM setups are equipped with energy analyzers and energy slits, allowing to select the electrons with well defined kinetic energy, thus, minimizing chromatic aberration effects and improving the image quality. A spatial resolution of up to 20 nm can be achieved in these setups [142, 143].

Because the secondary electron intensity closely follows the x-ray absorption spectrum of the sample, element sensitivity is also offered by x-ray PEEM. In addition to the spectroscopic contrast, other basic contrast mechanisms exist. For example, the electron yield from different sample areas is determined by the local work function and topology [36].

Finally, we note that PEEM is a surface-sensitive technique because the emitted electrons originate from a very shallow layer associated with the electron's mean free path. Although x-rays penetrate much deeper into the material, most of the signal is generated in the top $2-5$ nm, according to the universal curve [144].

2.3.3 STATIC AND TIME-RESOLVED XMCD-PEEM IMAGING

To study the magnetic domain structure of ferromagnets and its dynamics high-resolution static and time-resolved PEEM imaging in combination with the XMCD effect is often used.

STATIC XMCD-PEEM

First, a PEEM image is acquired using, one circular polarization of x-rays of the energy tuned to the absorption edge of the studied material (in this case the L_3 edge), see Fig. 2.14 (a). This image shows a circular field of view (FOV) of 10μm with micron-sized Ni discs. As the magnetic contrast is weak the second image acquired with the opposite circular polarization is required, see Fig. 2.14 (b). After the two images are aligned to each other the dichroism image (later referred to as *XMCD-PEEM image*) is constructed by calculating the XMCD for each pixel individually according to the relation in Eq. 2.4. The calculated XMCD-PEEM image, shown in Fig. 2.14 (c), reveals the magnetic domain structure of the Ni discs which is barely visible in the images taken with only one circular polarization. Domains with the magnetization pointing along the x-ray propagation direction are seen white, while domains with the opposite magne-

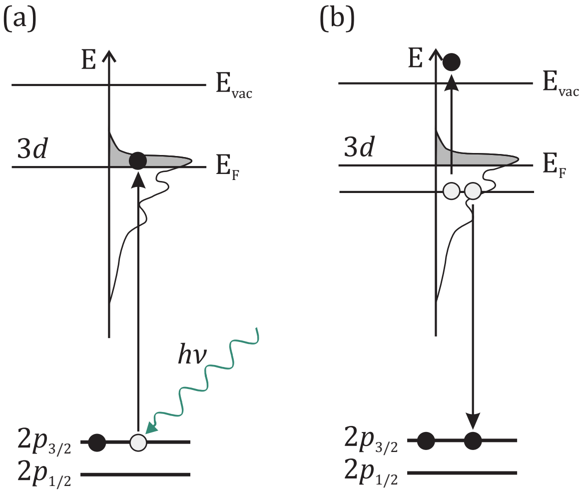

Figure 2.13: Sketch of the photoexcitation process leading to the generation of the secondary electrons in PEEM. (a) Absorption of an energetic x-ray photon leads to the transition of one electron to the Fermi level, leaving a core hole. (b) An electron from the Fermi level recombines with the core hole causing a cascade of Auger and secondary electrons which may escape to the vacuum and can then be detected by PEEM.

tization direction are seen black.[5] Also note that domains with the magnetization orthogonal to the x-ray beam direction are seen gray, i.e. showing zero XMCD effect according to Eq. 2.5.

Thus, magnetic structures of different sizes and shapes can be imaged at once, because PEEM is a direct imaging method that simultaneously images all structures within the FOV (10 μm in Fig. 2.14). We also note that due to the nearly grazing angle of incidence of x-ray beam XMCD-PEEM is more sensitive to the in-plane magnetization, however PMA materials with a strong OOP contrast can also be successfully investigated.

Note that because the number of photons within one x-ray bunch is insufficient to form a PEEM image with adequate statistics (especially at small FOV), an image is formed as an average of a series of frames acquired with certain exposure time (typically $1-3$ s). There are, however, several aspects that can influence the quality of XMCD-PEEM images. Besides the instrumental resolution, discussed above, these are the effects associated with instrument vibrations and thermal drift.

The vibration of the sample stage with respect to the electron imaging optics leads to an increased noise level resulting in blurred edges in the image. The timescale of these vibrations is comparable to the exposure time of a single frame and limited corrections can be made to

---

[5] Note that the sign of the XMCD contrast reverses for the L_2 edge, as discussed in the previous section.

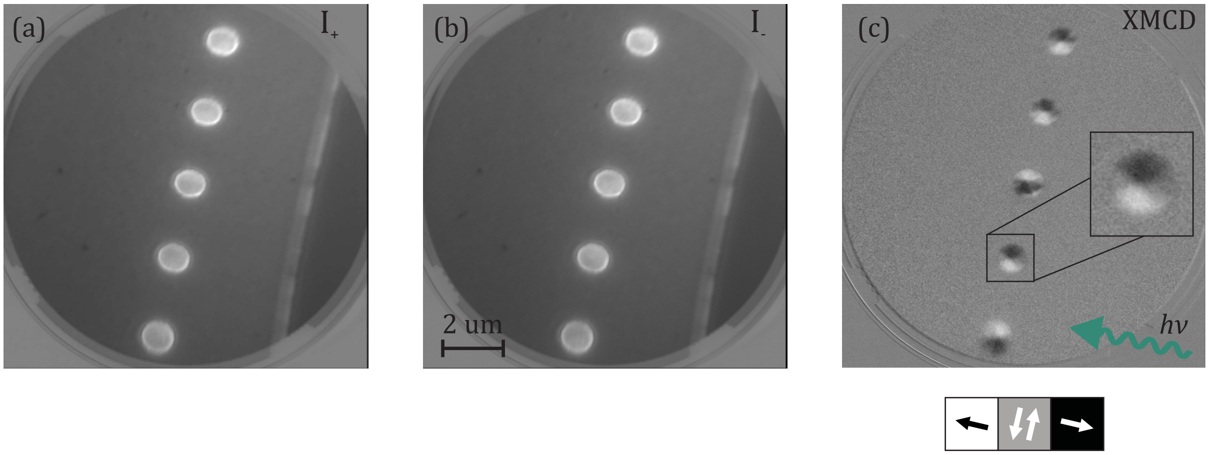

Figure 2.14: PEEM images of Ni microstructures acquired with photon energies of 852.5 eV corresponding to the L_3 edge of Ni using positive (a) and negative (b) polarization of light, respectively. (c) XMCD-PEEM image of Ni microstructures constructed from (a) and (b) after the drift-correction procedure. The inset shows the zoomed-in image of one Ni microstructure.

improve the quality (e.g. Gaussian de-blurring filter). Disabling mechanical pumps operating on the microscope chamber can lead to a reduction of noise, thus, providing an improved image quality.

Thermal drifts occur due to cooling or heating of the sample and due to illumination of the sample with high brilliance x-rays (or other light sources), which also leads to heating. They manifest themselves in a rigid translation of the image through the acquired frames. Under normal conditions, the timescale of thermal drifts is much larger than the typical exposure time. Therefore, a *drift correction* procedure can be employed prior to averaging of the acquired frames to form the final image. Such drift correction procedures, based on an algorithm described e.g. in Ref. [145], are available at PEEM beamlines and are individually adapted to the data acquisition routines.

Moreover, before drift correction, the acquired images need to be normalized to remove features related to the PEEM imaging section, i.e. multiplier channel plate, the phosphor screen and the camera. The normalization image is acquired with a de-focused objective lens, such that only the artifacts remain visible in the image, while the morphological structure of the sample is smeared out.

In order to obtain the XMCD-PEEM image in Fig. 2.14 (c), the drift correction procedure following the normalization of the acquired images for each polarization was carried out prior to averaging and calculation of the XMCD image. As a result, a high-resolution image of the

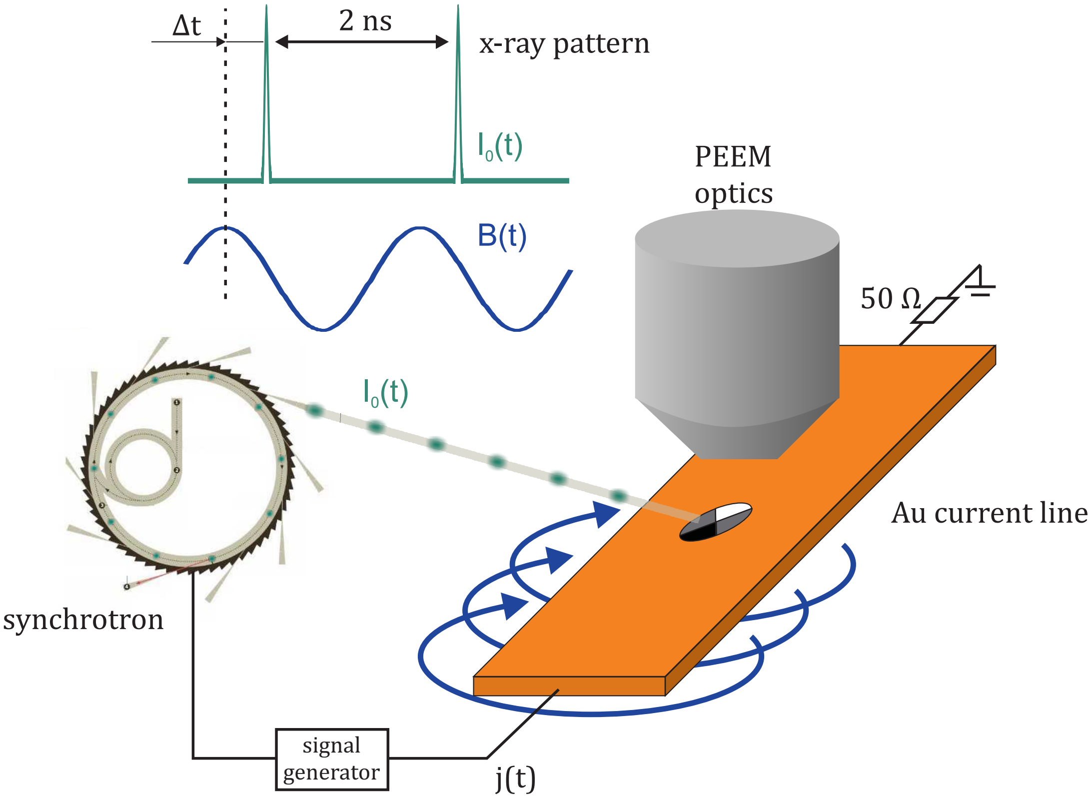

Figure 2.15: Schematic of time-resolved pump-probe PEEM. An oscillating magnetic field is generated by an AC current in a stripline on top of which magnetic structures are fabricated. A phase relation is maintained by synchronizing the excitation signal with the x-ray pulses by a timing signal from the synchrotron clock. By varying the phase shift, Δt, between the x-ray pulses and the phase-locked excitation signal, the time evolution of the magnetic configuration of the sample can be mapped. Adapted from Ref. [146].

projection of the local magnetization along the beam propagation direction is generated.

TIME-RESOLVED XMCD-PEEM

Pulsed nature of the synchrotron radiation, as discussed above, allows one to probe also magnetization dynamics as the pulse width ranging from 50 to 200 ps,[6] naturally provides a high temporal resolution necessary to study processes on a few ns-timescale.

In time-resolved XMCD-PEEM experiments, such as that schematically shown in Fig. 2.15, imaging is accomplished in a so-called *"pump-probe"* technique, where an excitation signal is synchronized with incoming x-ray pulses and is applied to the sample with various delays. By

---

[6] Pulse width varies between facilities and operating modes.

varying the delay and integrating over many repetitions for a given delay, the average response of the sample to the excitation can be mapped out in time.

Because the pump-probe technique requires the system to arrive at the exact same state at each time delay between the pump and the probe, it is important that the studied process is reproducible at the probing frequency. Since this frequency is set by the temporal structure of the x-ray beam, i.e. the synchrotron clock, the electronics employed in the experiment should be in sync with the synchrotron.

As an example, we consider the time-resolved PEEM setup available at CIRCE beamline at the ALBA synchrotron (Barcelona, Spain). Upon receiving a digital master clock signal from the synchrotron clock, an analog (500 MHz for ALBA) [147] signal is generated by a commercial signal generator. This electrical signal (phase-locked to the synchrotron master timing signal) is then converted to optical and passed by optical fiber into the high voltage (HV)-rack, thus, providing a complete galvanic separation. In the next step, the signal, converted back to electrical, is amplified by an rf-amplifier and passed to the sample via a coaxial cable.

This scheme allows one to vary the power of the generated rf-signal as well as the phase shift with respect to the synchrotron clock. The resulting total time resolution is in the order of 80 ps (corresponding to the sum of the x-ray bunch length, the electronic jitter, and the de-phasing over the storage ring) [148].

Thus, time-resolved XMCD-PEEM imaging with high spatial and temporal resolution is an excellent tool to study spin dynamics in nanomagnetic structures. In Chapter 3 of this thesis, we describe the experiment that demonstrates a significant role of XMCD-PEEM imaging in providing fundamental information in understanding the control of vortex core gyration dynamics. In this experiment an oscillating magnetic field was used as an excitation to constantly maintain the steady-state gyration of a vortex core. In order to generate such field, an AC current from a signal generator was flowing through a stripline. As a result, the induced field above the stripline influences the magnetic structures placed on top, but extends only several micrometers above them, thus, minimizing the effect on the emitted electrons. It is important to note that at high frequencies such as those typical for synchrotrons (hundreds of MHz), an impedance matching should be taken into account to prevent significant losses of the excitation signal before it arrives at the sample. Therefore a coplanar wave-guide geometry is required to match the impedance of the stripline with respect to the rest of the electrical circuit.

PEEM SAMPLE ENVIRONMENT

Standard commercial PEEM sample holders are equipped with a filament for heating and a thermocouple for reading the temperature and have four spring contacts (two for the thermo-

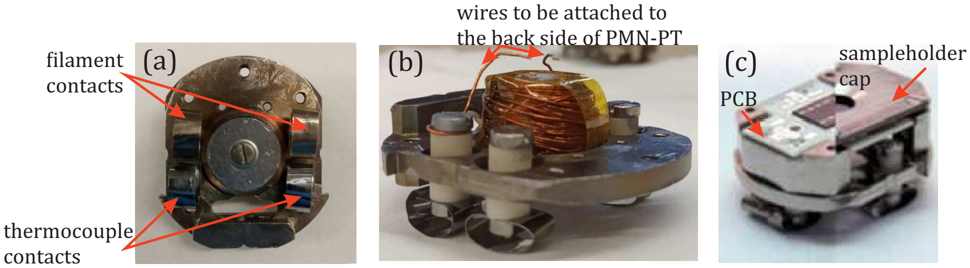

Figure 2.16: PEEM compatible sample holders. (a) Spring contacts of the sample holders designed for a connection to a filament and a thermocouple. (b) Custom sample holder with an OOP electromagnet and two wires for poling a PMN-PT substrate. (c) Custom sample holder with a PCB, available at ALBA synchrotron [149].

couple, two for the filament), as shown in Fig. 2.16 (a). The sample is placed in the central part and is fixed with a sample holder cap, such that the sample surface and the cap are in good electrical contact. The four spring contacts are electrically isolated from the sample holder body and the cap, while the body and the cap, thus the sample surface, are kept at local ground, also known as “start voltage (STV)”, because it is a reference potential for the emitted electrons. However, certain experiments can require modifications of the PEEM sample holders in order to enable the application of electric currents, voltages and magnetic fields.

Modification of the PEEM sample holder to connect two of the four feet (originally connected to the thermocouple) to a voltage generator, allows one to pole a piezoelectric substrate *in situ*. This can be realized by using a ultra-high vacuum (UHV) compatible wire which connects the spring contacts to the bottom surface of the substrate, as shown in Fig. 2.16 (b). It is important to keep the bottom surface electrically isolated from the sample holder body, which can be achieved by an insulating spacer below the sample. Thus, the sample surface connected to the sample holder cap is at STV while the backside of the sample can be kept at another voltage. The conductive silver paste can be used to ensure good electrical contact of the wire to the bottom electrode.[7]

If the sample surface contains patterns, e.g. a stripline to send electric currents, the sample is placed on a UHV-compatible PCB [149] in order to facilitate the electrical contact of the stripline to the signal generator inside the HV-rack. The contacts from the PCB, attached to a PEEM sample holder, to the sample are made using a wire-bonder. When using a PCB, the sample holder cap is mounted with some distance to the sample surface to avoid short circuits

---

[7] It is recommended to use a small drop to attach the wire to the substrate only in one place in order to prevent possible clamping and damage of the substrate during poling.

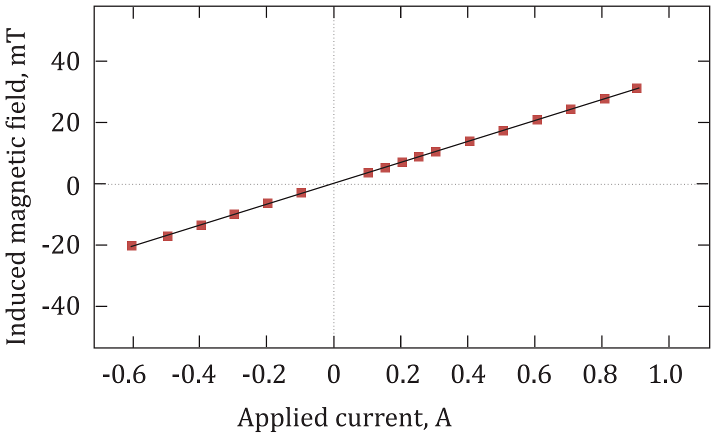

Figure 2.17: Measured magnetic field produced by the OOP sample holder, such as that shown in Fig. 2.3.3 (b) in the sample surface position, in the center of the yoke as function of current.

with the electrical contacts [Fig. 2.16 (c)]. This approach, however, limits the imaging area of the sample to a few mm. This is due to the shadowing effect, because of the near-grazing incidence angle of x-rays, as well as an additional electrostatic lens effect of the raised cap [149]. Moreover, it is important to keep the wires to the stripline hidden under the sample holder cap to avoid electrical discharges.

To study magnetic materials with an OOP easy axis a PEEM sample holder with an integrated OOP electromagnet can be necessary. This can be realized by using a single cylindrical yoke and a coil as shown in Fig. 2.16 (b). The magnetic field characteristics provided by such a custom-built sample holder with a 5 mm diameter yoke, using 750 turns coil with 0.125 mm Kapton insulated Cu wire is shown in Fig. 2.17. It can be seen that the magnetic field of ca. 40 mT can be generated at 1 A with a good homogeneity in the center of the yoke.

Note that the maximum generated magnetic field is limited on the one hand by the current source and heating of the wire (max 0.3 – 0.4 A can be applied for longer times, while up to 1 A could be applied for short pulses) [149], and on the other hand by image distortions due to electron deflection by the field. However, because the velocity of the emitted electrons in this configuration is almost parallel to the magnetic OOP field, non-significant distortions of the electron beam can be expected, according to the Lorentz force. Therefore, it is still possible to obtain a high-resolution XMCD-PEEM image when using a moderate OOP magnetic field.

2.4 SECOND HARMONIC SPIN-TORQUE MAGNETOMETRY

2.4.1 ANOMALOUS HALL EFFECT MAGNETOMETRY

The anomalous Hall effect (AHE), as a transport manifestation of magnetism, is a powerful tool for studying magnetic properties of ultrathin magnetic films and multilayers [150]. In a typical Hall effect measurement scheme, the Hall voltage (V_H) comprises three contributions:

$$V_\mathrm{H} = \frac{R_\mathrm{H}}{t} B\cos(\alpha) + \frac{\mu_0 R_\mathrm{S} I}{t} M\cos(\theta) + \frac{kI}{t} M^2 \sin^2(\theta)\sin(2\phi)\,, \tag{2.6}$$

where t is the film thickness, R_s is the anomalous Hall coefficient and k is the planar Hall coefficient and the angles α, θ and ϕ are defined in Fig. 2.18. The first term in Eq. 2.6 is the ordinary Hall effect (OHE) and arises due to the Lorentz force acting on the conduction electrons. The OHE depends on the z-component of the magnetic field, and produces an electric field perpendicular to B_z and the current density. The second term is the AHE and arises due to spin dependent scattering mechanisms [151]. The AHE depends on the perpendicular component of **M**, and produces an electric field perpendicular to M_z and the current density. The last term in Eq. 2.6 is the planar Hall effect (PHE). The PHE is proportional to the square of the planar component of **M**, and produces an electric field parallel and perpendicular to the current.

Since R_s and k are usually unknown, one does not need to calculate the magnetization using Eq. 2.6 to obtain a hysteresis loop [152]. For this, one plots the second term (AHE) as a function of the field to get the OOP magnetization ($M\cos(\theta) = M_z$) hysteresis loop with a constant multiplicative factor. Similarly, a plot of the PHE term vs B field gives the in-plane magnetization ($M^2\sin^2(\theta)\sin(2\phi) = M_x M_y$) hysteresis loop modified by a different constant multiplicative factor.

One can also see that all three terms in Eq. 2.6 are inversely proportional to the film thickness t, which renders AHE magnetometry ideal for studying magnetization processes (e.g. hysteresis loop) in ultra thin magnetic films.

2.4.2 HARMONIC HALL MEASUREMENTS

Furthermore, low-frequency harmonic Hall voltage measurement is one of the commonly used techniques to quantify current-induced SOTs [153, 154]. This approach relies on measuring the effect of an electric current on the orientation of the magnetization acting via the FL and DL SOTs, as described in Section 1.4.2 and schematically shown in Fig. 2.19 (a). More specifically, the effective magnetic fields associated with the SOTs can be extracted by analyzing the magnetization angle as a function of the amplitude and phase of the applied current. In this case, the harmonic Hall voltage arises due to the mixing of the AC current with the Hall resistance, which

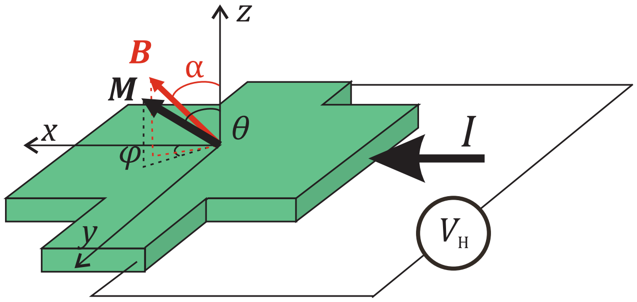

Figure 2.18: Geometry of the AHE measurement. α is the angle between the applied field and the normal to the sample, θ is the angle between the magnetization and the normal and ϕ is the angle between the current, I, and the in plane component of the magnetization.

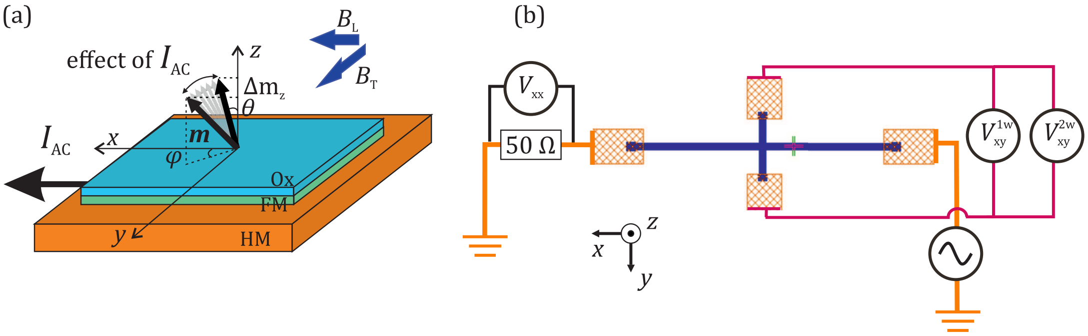

Figure 2.19: (a) Schematic of the effect of an AC current on the magnetization in a HM/FM multilayer with PMA. The current-induced SOTs fields and Oersted field (see text) tilt the magnetization of the FM layer from the OOP direction. Adapted from Ref. [29]. (b) Experimental setup for 2ω Hall measurements of the SOTs. A low frequency AC current is applied to the nanowire, and the Hall signal is measured at the patterned Hall bar contacts and analyzed for the first and second harmonics using two lock-in amplifiers.

is modulated by the change of the magnetization. Note that since the magnetization dynamics are much faster than the current frequency used in such experiments (typically a few kHz), the magnetization tilted by the anisotropy field, external magnetic field and current-induced effective fields is assumed to be in static equilibrium.

Below, we describe the approach to evaluate the harmonic Hall voltages following the derivations in Ref. [154]. Formally, the time-dependent Hall resistance $R_{xy}(t)$ can be expressed to the first order in current by

$$R_{xy}(\mathbf{B}_{\text{ext}} + \mathbf{B}_I(t)) \approx R_{xy}(\mathbf{B}_{\text{ext}}) + \frac{\mathrm{d}R_{xy}}{\mathrm{d}\mathbf{B}_I} \cdot \mathbf{B}_I \sin(\omega t)\,, \tag{2.7}$$

with $\mathbf{B}_{\text{ext}}$ and $\mathbf{B}_I = \mathbf{B}_{\text{DL}} + \mathbf{B}_{\text{FL}} + \mathbf{B}^{\text{Oe}}$ being the external and the current-induced effective magnetic field, containing the DL sand FL SOTs contributions and the current-induced Oersted field. Rewriting Eq. 2.7 in terms of Hall voltage according to $V_{xy} = R_{xy} I_0 \sin(\omega t)$, where I_0 is the current amplitude, we obtain

$$V_{xy}(t) = I_0 \left[R^0_{xy} + R^{\omega}_{xy} \sin(\omega t) + R^{2\omega}_{xy} \cos(2\omega t) \right]. \tag{2.8}$$

Here

$$R^0_{xy} = \frac{1}{2} \frac{\mathrm{d}R_{xy}}{\mathrm{d}\mathbf{B}_I} \cdot \mathbf{B}_I\,,$$

$$R^{\omega}_{xy} = R_{xy}(\mathbf{B}_{\text{ext}})\,,$$

and

$$R^{2\omega}_{xy} = -\frac{1}{2} \frac{\mathrm{d}R_{xy}}{\mathrm{d}\mathbf{B}_I} \cdot \mathbf{B}_I + R^{2\omega}_{\nabla T}\,.$$

are the zero, first, and second harmonic components of R_{xy}, respectively.

The first harmonic term is analogous to the DC Hall signal introduced in Eq. 2.6 and is given by

$$R^{\omega}_{xy} = R_{\text{AHE}} \cos\theta + R_{\text{PHE}} \sin^2\theta \sin 2\phi, \tag{2.9}$$

where R_{AHE} and R_{PHE} are the anomalous and planar Hall signals, respectively. Note that the contribution of the OHE in negligibly small compared to the other contributions, hence it is omitted [152]. The second harmonic term includes modulation of the Hall resistance due to the SOTs and an additional contribution due to the Joule heating. The latter can be assumed negligible (or subtracted) [155], and $R^{2\omega}_{xy}$ can then be expressed as

$$R^{2\omega}_{xy} = A_\theta \mathbf{B}_I \cdot \mathbf{e}_\theta + A_\phi \mathbf{B}_I \cdot \mathbf{e}_\phi\,, \tag{2.10}$$

where $\mathbf{e}_\theta$ and $\mathbf{e}_\phi$ are the polar and azimuthal unit vectors, respectively. The coefficients A_θ and A_ϕ are the parameters of the applied magnetic field and their detailed expression can be found elsewhere [29, 154]. Using the analytical expressions for A_θ and A_ϕ, Eq. 2.10 allows one to determine the azimuthal and polar components of B_{FL} and B_{DL} for different magnetization angles by measuring $R^{2\omega}_{xy}$ as a function of the external field B_{ext}. However, for the purpose of this thesis, it is sufficient to use a simplified model, which is valid for systems with a uniaxial magnetic anisotropy, such as PMA films.

In uniaxial (and easy plane) systems the number of independent measurements, required to extract the SOTs can be reduced to two [93, 155]. Furthermore, a small angle approximation can be applied when the magnetization deviates from the z-axis only very little, which is the case for PMA systems [95, 154]. Under these assumptions, $R_{xy}^{2\omega}$ varies linearly with the external field and the SOTs can be extracted by performing two sets of measurement, i.e. for longitudinal and transverse external magnetic fields.

The measurement schematic implemented for the experiment in this thesis is shown in Fig. 2.19 (b). An AC voltage is applied to the current line, so that the AC current is flowing along the x direction and the voltage drop across a 50 Ω resistance is measured by a lock-in amplifier to extract the current amplitude. The in-phase first harmonic ($V_{xy}^{1\omega}$) and the out-of-phase (90° off) second harmonic ($V_{xy}^{2\omega}$) of the anomalous Hall voltage are measured simultaneously using two lock-in amplifiers across the Hall bar.

By measuring $V_{xy}^{1\omega}$ and $V_{xy}^{2\omega}$ as a function of the in-plane magnetic fields, transverse (B_T, along y) or parallel (B_L, along x) to the current direction, we can obtain the transverse ($\mu_0\Delta H_\mathrm{T}$) and the longitudinal ($\mu_0\Delta H_\mathrm{L}$) components of the SOT effective field by using the following expression [154, 153]:

$$\mu_0\Delta H_{\mathrm{L(T)}} = -2\frac{\left(B_{x(y)} \pm 2\xi B_{y(x)}\right)}{1-4\xi^2}, \tag{2.11}$$

where the ± sign corresponds to the magnetization direction along $\pm z$, and $B_x \equiv \left(\frac{\partial V_{xy}^{2\omega}}{\partial B_\mathrm{L}} / \frac{\partial^2 V_{xy}^{1\omega}}{\partial B_\mathrm{L}^2}\right)$ and $B_y \equiv \left(\frac{\partial V_{xy}^{2\omega}}{\partial B_\mathrm{T}} / \frac{\partial^2 V_{xy}^{1\omega}}{\partial B_\mathrm{T}^2}\right)$. In Eq. 2.11, $\xi = \frac{R_\mathrm{PHE}}{R_\mathrm{AHE}}$ is defined as the ratio of the PHE and the AHE resistances.

As the last step the $\mu_0\Delta H_{\mathrm{L(T)}}$ are plotted as a function of the current density j_c for both magnetization directions $\pm\mathbf{m}$. The resulting linear dependencies of $\mu_0\Delta H_\mathrm{L}$ and $\mu_0\Delta H_\mathrm{T}$ should be odd and even with respect to the magnetization reversal, reflecting the different symmetry the DL and FL SOTs, respectively. Linear fits to these dependencies, i.e. $\mu_0\Delta H_\mathrm{L}/j_\mathrm{c}$ and $\mu_0\Delta H_\mathrm{T}/j_\mathrm{c}$ determine the DL ($\mu_0 H_\mathrm{DL}^\mathrm{eff}$) and FL ($\mu_0 H_\mathrm{FL}^\mathrm{eff}$) SOT effective fields.

Note that the approximation used above provides only the lowest order contribution to the SOTs. However, owing to its simple implementation, it is widely used to characterize the SOTs in PMA systems. The generalization of this technique to e.g. in-plane magnetized systems is described by Hayashi et al. in Ref. [154].

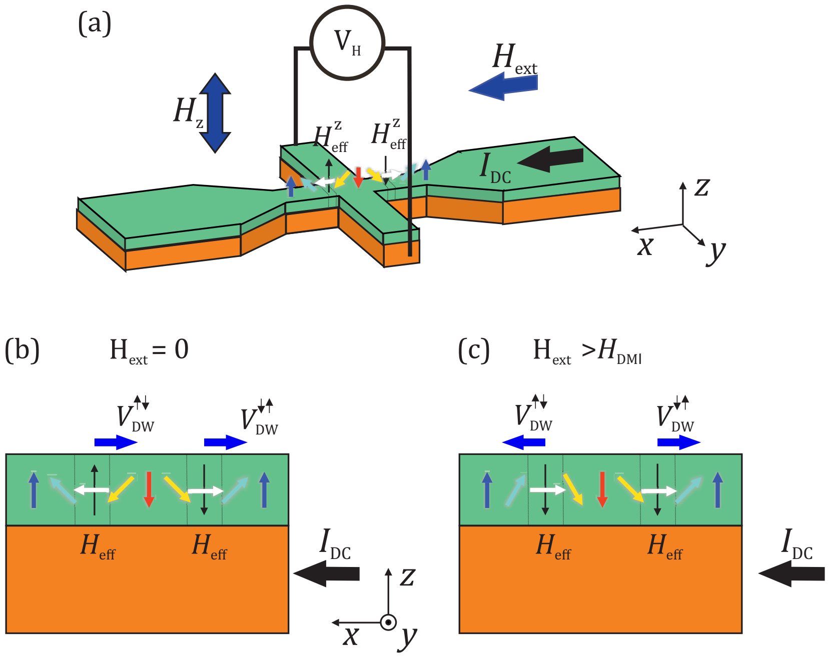

Figure 2.20: (a) Schematic of AHE measurement of hysteresis loops in a magnetic heterostructure with PMA with the in-plane bias field H_{ext}. H_{eff}^{z} is the SHE-induced effective field acting on the chiral Néel DWs. Schematic illustration of the DW motion in the central region of the Hall-cross in (a) due to H_{eff}^{z} (b) in the absence of external magnetic field and (c) when $H_{\mathrm{ext}} > H_{\mathrm{DMI}}$. $v_{\mathrm{DW}}^{\uparrow\downarrow}$ and $v_{\mathrm{DW}}^{\downarrow\uparrow}$ indicate the motion of the up-down and down-up DW, respectively. Thin black arrows in (b,c) indicate the direction of the SHE-induced H_{eff}^{z}.

2.5 DMI MEASUREMENTS BY CURRENT-INDUCED HYSTERESIS LOOP SHIFT

In magnetic PMA systems, the SHE-induced spin torque can drive the Néel DWs similarly to an applied OOP magnetic field, as discussed in Section 1.4.2. Based on this effect, the recently proposed measurement scheme of current-induced shift of the OOP hysteresis loop as a function of the in-plane bias field allows one to simultaneously quantify the SOTs and the DMI effective field. Below, we will describe this measurement protocol introduced in Ref. [96].

As illustrated in Fig. 2.20 (a), the H_{eff}^{z} generated due to the SHE in the HM upon sending a DC current j_{c}, leads to the motion of chiral DWs in the same direction in the absence of an external magnetic field. This is attributed to the different signs of H_{eff}^{z} for up-down and down-up DWs [see Fig. 2.20 (b)]. On the contrary, upon application of an in-plane field, H_{ext}, that is

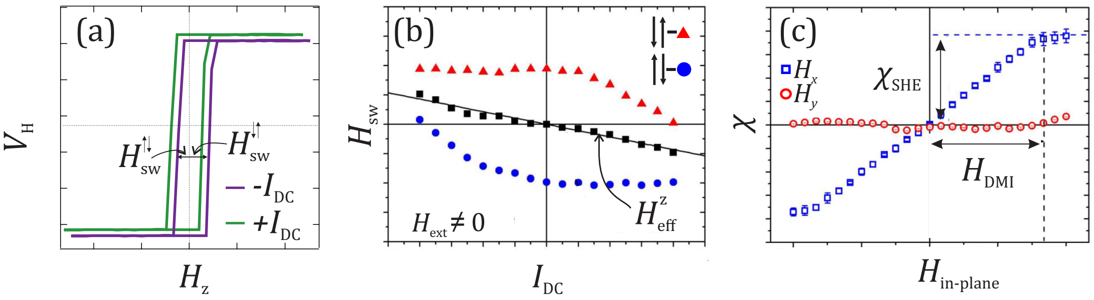

Figure 2.21: (a) Schematic AHE loops corresponding to opposite DC currents. Vertical shift is introduced for clarity. (b) Schematic dependence of the switching fields H_{SW} for down-to-up and up-to-down magnetization reversals as functions of I_{DC} for a non-zero H_{ext}. (c) Schematic dependence of the effective $\tau = H^z_{eff}/j_c$ as a function of applied in-plane field used to extract the DL SOT, indicated as τ_{SHE} and the effective DMI field, H_{DMI}. Adapted from Ref. [96].

strong enough to overcome the DMI effective field, H_{DMI}, the direction of the magnetic moments within the DWs is reversed. This results in the current-induced domain expansion or contraction depending on the current polarity, rather than the DWs motion, because the H^z_{eff} is now pointing along the same direction for both types of the DWs as depicted in Fig. 2.20 (c). Therefore, the applied current j_c and the in-plane bias field play a significant role not only for the magnetization switching via current-induced DW motion, but also for the OOP magnetic field-driven switching process. This can be utilized for measuring the DMI effective field and the DL SOT on a Hall-cross device, as shown in Fig. 2.20 (a).

For this, the AHE voltage OOP loops are measured to characterize the magnetization switching in the Hall-cross devices as a function of an applied DC current and in-plane bias field. Examples of the resulting AHE hysteresis loops are schematically shown in Fig. 2.21 (a). It can be seen that the AHE loops exhibit a shift along the H_z axis for the opposite polarities of I_{DC} which indicates the existence of a current-induced H^z_{eff} due to the DL SOT. By plotting the switching fields, H_{SW}, for both down-up and up-down transitions vs. I_{DC} one obtains a switching diagram, as qualitatively shown in Fig. 2.21 (b).

The variation of the switching field with the DC current is explained by two contributions: *(i)* linear tilt due to the current-induced $H^z_{eff}(I_{DC})$; *(ii)* reduction of coercivity due to the Joule heating ($\propto I^2_{DC}$). Hence, $H^{\uparrow\downarrow}_{SW} = H^z_{eff}(I_{DC}) - H_c(I^2_{DC})$ and $H^{\downarrow\uparrow}_{SW} = H^z_{eff}(I_{DC}) + H_c(I^2_{DC})$. The Joule heating contribution can be eliminated by considering only the horizontal shift of the hysteresis loop center, i.e. $H^z_{eff} \equiv (H^{\downarrow\uparrow}_{SW} + H^{\uparrow\downarrow}_{SW})$. Thus, the linear variation of H^z_{eff} with I_{DC} determines $\tau = H^z_{eff}/j_c$, where j_c is the current density, which is plotted as a function of the in-plane bias field, as schematically shown in Fig. 2.21 (c).

The estimated τ increases linearly with H_x until it saturates when the bias field reaches the H_{DMI}, i.e. when the DW orientations in the device align to the external field. On the contrary, there should be no variation of τ with H_y, because this only reorients the magnetic moments within the DWs to the Bloch-type configuration.

From this measurement protocol we can, thus, extract the DL SOT efficiency, τ_{SHE}, and the DMI effective field, H_{DMI}, which correspond to τ and the in-plane field at the saturation, respectively, as indicated in Fig. 2.21 (c).

CHAPTER 3

ELECTRIC FIELD CONTROL OF MAGNETIZATION DYNAMICS IN MAGNETIC VORTICES

3.1 INTRODUCTION

This Chapter focuses on magnetic vortex structures and their control by electric field-induced strain. Due to the high stability and unique gyration dynamics [71, 156], magnetic vortices are considered as promising candidates for information carriers in potential spintronic applications like data storage [25] or nano-oscillators [157].

Motivated by the technological relevance, the stability and the dynamical behavior of the magnetic vortices under external excitations are well studied [79]. Now, the research interest is focused on exploring novel energy-efficient approaches to manipulate the structure and the dynamics of the vortices, as this is a key requirement for applications. While conventionally manipulation of the magnetic vortices [158, 159] was done by magnetic fields and spin-polarized currents [160, 161, 162, 163], using mechanical strain is seen as a promising alternative because it avoids electrical currents with the associated ohmic losses [20]. Furthermore, the possibility of generating the strain locally and, hence, to realize the control on the nanoscale is particularly advantageous for the development of high-density storage devices.

In this Chapter, following the review of the fundamental properties which make magnetic vortex structures attractive for practical applications, we will discuss the recent progress in the investigation of the impact of strain on the magnetic vortices, which via the ME coupling, can influence their stability, reversal, and dynamics. Then, based on our time-resolved XMCD-PEEM experiments and micromagnetic simulations, we will demonstrate the possibility of using electric field-induced strain as a low-power approach to tune the dynamical response of magnetic vortices.

In Chapter 1, we discussed that under certain conditions the formation of a flux-closure state is energetically favorable. In particular, when the magnetization is confined into a thin structure with small lateral dimensions a magnetic vortex can be formed [35, 164]. Due to the demagnetization effect, which is responsible for the shape anisotropy, the magnetization distribution in these magnetic structures is such that the formation of magnetic charges at the surfaces is minimized, which otherwise would increase the total energy of the system. As a result, the local magnetization $\mathbf{M}(\mathbf{r})$ as a function of position $\mathbf{r}$ has a tendency: (*i*) to point within the plane of the structure, except the vortex core (VC) region (see Chapter 1); (*ii*) to follow the curved edge of the confined structure, thereby completely avoiding the generation of any significant magnetic charges at the edge [165]. In the center, the magnetization is forced OOP to avoid large angles between magnetic moments that would drastically increase the exchange energy.

A stable vortex state configuration for different dimensions, i.e. thickness, L, and radius, R, defining the aspect ratio, L/R, of a cylindrical structure, can be calculated using micromagnetic simulations taking into account the aforementioned energy considerations [166]. From such calculations as well as from experimental observations [156, 167] it is known that generally at remanence, the vortex state is stable in soft magnetic cylindrical dots with lateral dimensions greater than the material specific exchange length and the thickness of the structure [166]. However, if the aspect ratio is too small and if the radius is larger than the core radius, the magnetization is saturated in the plane, thus forming an IP single domain state. On the other hand, if the disc is too thick, the magnetization is saturated along the OOP axis. Finally, for very large lateral sizes where the magnetostatic energy contribution dominates, multiple domains can appear due to the defects at which the DWs can be pinned.

Besides the stability over a wide range of dimensions, magnetic vortices exhibit a four-fold degenerate ground state, as schematically depicted in Fig. 3.1. The chirality of a vortex, i.e. the in-plane curl direction, can be clockwise or counterclockwise. Furthermore, the polarity of the VC, i.e. the direction in which the magnetization at the center is pointing, can be upwards or downwards. Therefore, magnetic vortices can be potentially used to store two bits in one nanostructure [25], which is another practical advantage of magnetic vortices.

Furthermore, while in relaxed laterally confined structures, the magnetic VC can be seen as

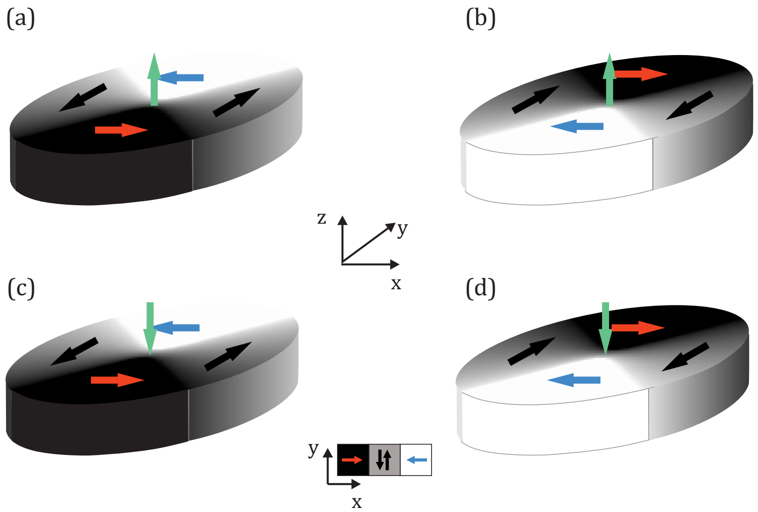

Figure 3.1: The four basic magnetic vortex configurations classified by the in-plane curl direction (a,c) clockwise and (b,d) counterclockwise and the OOP direction of the VC. The in-plane magnetization direction within the black, white and gray domains is indicated by red, blue and black arrows, respectively. The OOP component of the magnetization of the VC is depicted by green arrow.

trapped in a potential well, strongly determined by the shape anisotropy of the disc, that forces it to stay at the center, it is also possible to move the VC around by external stimuli. For example, due to the excitation with an oscillating magnetic field,[1] the VC experiences a restoring force against this motion. As a result, the core gyrates at a given frequency in an iso-energy orbit around its equilibrium position, which is called a gyrotropic mode. When the field is turned off, the core relaxes back to its equilibrium position in a spiral motion due to a damping process. The gyrotropic eigenfrequency, f_0, of the VC is proportional to the aspect ratio of the structure $f_0 \sim \frac{L}{R}$ [159, 168, 169] and, hence, can be tuned by adjusting the geometrical dimensions.

As discussed in Chapter 1, the vortex steady-state gyrotropic orbits can be described using the Thiele equation [74, 81]

$$\mathbf{G} \times \dot{\mathbf{R}} - \nabla W(\mathbf{R}) = 0\,, \tag{3.1}$$

where $\mathbf{R}$ is the position of the vortex core, and $\mathbf{G}$ the gyrovector, describing the precessional motion of the vortex core, $W(\mathbf{R})$ is the potential energy of the vortex core giving rise to the restoring forces with its minimum at the equilibrium position of the VC.

---

[1] Since in this Chapter the excitation by an AC magnetic field is considered, the discussion of the other approaches to excite the VC dynamics, e.g. using spin-polarized currents [160, 161], are left out. For more details, see the corresponding references.

For magnetic vortices excited resonantly, the VC follows a circular path for square /circular shapes [159, 170]. However, for the off-resonant excitation, the gyration orbit becomes elongated perpendicular to the excitation field direction, if the excitation frequency is smaller than the eigenfrequency of the system. Vice versa, if the excitation frequency is larger than the eigenfrequency, the orbit is elongated along the oscillating magnetic field direction [171, 172].

Resonant excitation of magnetic vortices has another remarkable consequence, reported in Ref. [158]. Exciting resonantly the gyration of a VC with a continuous sinusoidal field enables switching of the VC polarity using a drastically decreased amplitude of the external magnetic fields. In this case, the amplitudes can be reduced down to 1.5 mT, while conventionally, the OOP magnetic fields of the order of 0.5 T were required to reverse the z-component of the magnetization of the VC [173, 174].

As discussed in Chapter 1, the effect of strain on magnetic structures can be described by including an additional magnetic anisotropy term arising due to the ME coupling. Besides the strain-induced modifications of static vortex structures reported in, e.g. Refs. [101, 104], a reversal of both vortex polarity and chirality can be generated by strain. Numerical simulations show that the non-uniform strain can be used to reverse the VC polarity by modulating the phase difference between the electrodes employed for the strain generation [175]. Also, shear strain generated by torsion can switch the polarity when the direction of torsion is opposite to the in-plane curl of the magnetization [176]. The strain-mediated switching of the vortex chirality between clockwise and counterclockwise can be achieved by applying strain pulses of appropriate magnitude and length, as demonstrated in the recent experimental study [177].

Furthermore, the additional anisotropy gives rise to a modification of the aforementioned potential energy landscape $W(\mathbf{R})$ in Eq. 3.1, which, in turn, can impact the vortex dynamics. To illustrate the effect of strain, it is convenient to consider the potential $W(\mathbf{R})$ in terms of the effective restoring force spring constants κ_x and κ_y along the x and y directions, respectively [170, 178], which for small displacements of the VC is

$$W(\mathbf{R}) = W(0) + \frac{1}{2}\left[\kappa_x X^2 + \kappa_y Y^2\right], \tag{3.2}$$

where $\mathbf{R} = (X, Y)$ is the VC position and the spring constants comprise various energy contributions, e.g. the magnetostatic, exchange and ME energies. With this representation, which describes a harmonic potential well, and assuming the negligible effect of damping on the magnitude of f_0, i.e. when $G \gg |D|$, the gyration eigenfrequency f_0 and the orbit eccentricity ϵ are given by

$$f_0 \approx (2\pi G)^{-1}\sqrt{\kappa_x \kappa_y}, \tag{3.3}$$

$$\epsilon \approx \sqrt{\frac{|\kappa_y - \kappa_x|}{\max[k_y, k_x]}}. \tag{3.4}$$

As extracted from the dynamical vortex potential-well[2] [161, 178] the spring constants $\kappa_x = \kappa_y$ and the eccentricity $\epsilon = 0$ for the case of zero ME anisotropy, as expected [170]. However, the in-plane magnetic anisotropy along the x-axis leads to the softening of both κ_x and κ_y as shown in Ref. [170]. As a result, the ME contribution acts as to push the VC out of the system along the direction of the induced easy axis, leading to the elliptical VC trajectories with the major axis being oriented along the applied anisotropy axis. Furthermore, the softening of the spring constant is always associated with the reduction of f_0 with increasing magnitude of the imposed magnetic anisotropy. Thus, the mechanical strain can be employed to control the VC gyration orbit as well as the gyrotropic eigenfrequency of magnetic vortices, as shown numerically [170, 179] and experimentally by straining rectangular microstructures [180] using pressured gas cells.

Besides using the static strain to modify the static domain configuration and dynamic properties of magnetic vortices, one can also employ time-varying strain to excite the vortex dynamics. As shown based on micromagnetic simulations, the VC oscillations can be induced in a system where the circular symmetry of the flux-closure state is broken due to the imposed strain gradient and the vortex polarity can reverse [181]. Furthermore, periodically modulated by surface acoustic waves strain can induce the vortex dynamics in the picoseconds scale, as demonstrated experimentally in Ref. [148].

From the above discussion, it is evident that the existing studies predict fundamentally the feasibility of using strain to control the magnetic vortices and their dynamics. Moreover, as the strain can be generated locally and tuned electrically [182], this approach is potentially very attractive for future vortex-based technologies. Despite many numerical works, there are only a few experimental realizations of this approach [148, 180]. Furthermore, full electrical control of the dynamical response of magnetic vortices is desired for potential device application.

3.2 SAMPLE CONFIGURATION

To induce and electrically control the strain, a PMN-PT (011) substrate was employed, as discussed in Section 2.1.1, on top of which a 55 nm thick CPW was fabricated in order to generate an oscillating Oersted field by applying an AC current to the current line. An array of cylindrical microstructures of various lateral dimensions ranging from 0.4 μm to 0.7 μm in radius was

---

[2] The effective κ_x and κ_y can be determined from the slopes of the linear fits to W vs. $(X, 0)^2$ and $(0, Y)^2$.

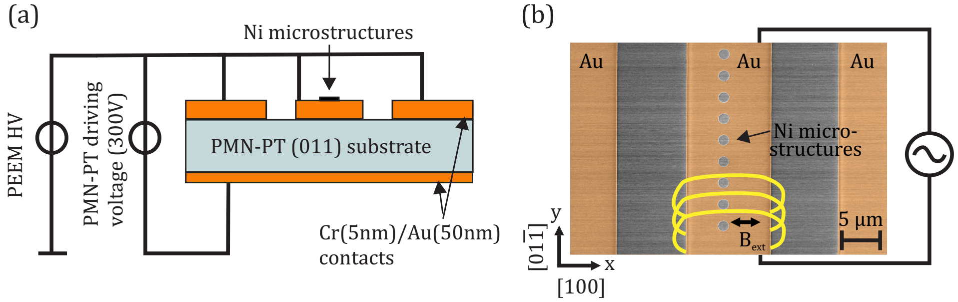

Figure 3.2: (a) Schematic of the side view of the sample used for the observation of vortex core gyration dynamics modulated by the ME coupling. (b) SEM image of the sample surface showing the magnetic microstructures fabricated on top of a stripline, which in turn generates an oscillating magnetic field due to the injected AC current with 500 MHz frequency. The CPW together with the stripline and the magnetostrictive microstructures are fabricated on top of the PMN-PT substrate with an additional electrical contact at the bottom to generate uniaxial in-plane strain upon application of an OOP electric field across the substrate. Adapted from [183].

fabricated from a 50 nm thick magnetostrictive Ni film. In Fig. 3.2, we demonstrate the sample environment designed to study the impact of electric field-induced strain on the properties of a magnetic vortex state. A scanning electron microscopy (SEM) image, showing the resulting Ni microstructures on top of the current line, is presented in Fig. 3.2 (b). The details of the sample fabrication process are given in Appendix A.

The piezoelectric substrate was attached to a UHV-compatible PCB holder by a single drop of a silver conductive paste on the bottom of the substrate to ensure good electrical contact and also prevent possible clamping and damage of the substrate during its expansion. This arrangement allowed us to use the full strain generated by the application of the electric field. The electric field generated by a floating voltage generator inside the high voltage environment of the PEEM control unit (see Section 2.3.2) was applied between the top and the bottom electrodes of the PMN-PT substrate, as schematically shown in Fig. 3.2 (a).

After the fabrication of the Ni microstructures and before the measurements, the PMN-PT substrate was poled by applying a positive electric field of 500 kV m^{-1}, which promoted the linear regime of the strain response (see Section 2.1.1). Later on, we used the electric field in the rage from -100 to 600 kV m^{-1}, which enabled full and reliable control of the generated strain by varying the applied field in this range [114]. Furthermore, as the total thickness of the layers between the PMN-PT and the magnetic nanostructures was limited to 55 nm, the complete transfer of the generated strain was expected [101]. The stripline was aligned with respect to the crystallographic $[01\bar{1}]$ and [100] directions of the PMN-PT crystal, defining the directions of the tensile and compressive strain, as indicated in Fig. 3.2 (b).

The electrical contact between the stripline and the PCB was made by a wire bonder and other details of the sample mounting on the cartridge were similar to those, described in Section 2.3.2. One end of the stripline was electrically connected to the STV by silver paste together with the ground plates of the CPW. As a result, the DC resistance of 134 Ω was measured between the stripline and the STV at zero electric field applied to the PMN-PT substrate.[3]

3.3 XMCD-PEEM IMAGING OF STATIC DOMAIN STRUCTURE IN NI DISCS AS A FUNCTION OF STRAIN

First, we carried out static imaging of the Ni microstructures as modified by the electric field-induced strain to ensure that our rather complex system had the expected robust properties in the static regime. The magnetic configuration of the discs was investigated by means of XMCD-PEEM using circularly polarized light at the energy of 852.5 eV, corresponding to the Ni L_3 absorption edge. The imaging was carried out at room temperature at the CIRCE beamline (ALBA, Barcelona) equipped with an Elmitec PEEM setup [185].

Prior to XMCD-PEEM imaging, we *ex situ* de-magnetized the system by applying an alternating magnetic field with an exponentially decreasing amplitude using an electromagnet. As can be seen in Fig. 3.3, for a wide range of lateral dimensions of the Ni microstructures (0.8 – 1.4 μm), a vortex state was initially formed with the in-plane magnetization curling around the VC. Here, we can observe that the domain configuration has a nearly equivalent contribution from black/white and gray domains, i.e. the domains with orthogonal to each other magnetization directions. Such symmetric distribution of the vortex magnetization corresponds to an unstrained, shape anisotropy dominated state [71, 156].

The application of an electric field leads to a change of the magnetic domain distribution, as can be seen by comparing Fig. 3.4 (a-d). More specifically, while the domain structure of a 1 μm vortex measured at 250 kV m^{-1} is symmetric, the black and white domains contribute more to the domain structure of the same disc at 500 kV m^{-1}, as shown in Fig. 3.4 (d). On the contrary,

---

[3] Indeed, having an impedance matched CPW is important for rf-measurements, however achieving this on a piezoelectric substrate is difficult because of the non-linear dielectric response [184]. On top of it, as the sample is put inside the PEEM, the signal is also attenuated by the cable and the UHV feedthrough, and the spring contacts of the sample holder, which are non-high-frequency components. These factors cannot be easily controlled.

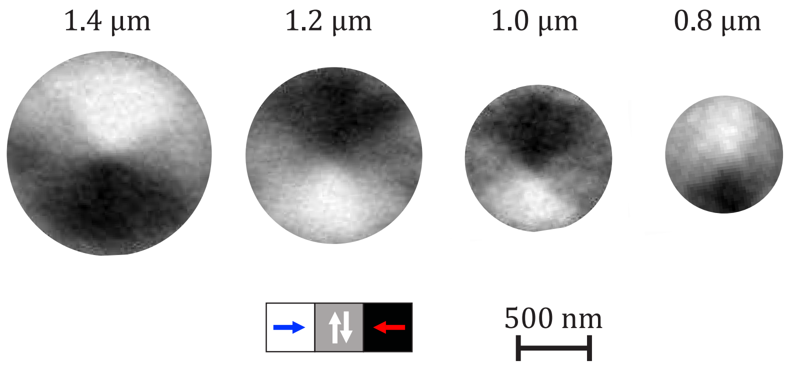

Figure 3.3: XMCD-PEEM images of the magnetization configuration of Ni discs of different sizes measured at 250 kV m^{-1} applied across the PMN-PT substrate. As discussed further in the text, approximately zero strain is exerted on the Ni discs at 250 kV m^{-1}.

as can be seen in Fig. 3.4 (a) and (b), the domains with the magnetization along the y direction (gray domains) grow in size at the expense of the black/white domains, for the electric fields below 250 kV m^{-1}. This indicates that the electric field-induced piezoelectric strain generates a uniaxial anisotropy in the magnetic material, favoring one magnetic domain direction over the perpendicular domain.

We also note that the symmetric domain distribution corresponds to an applied electric field of about 250 kV m^{-1}, shown in Fig. 3.4 (c). This is attributed to the additional uniaxial anisotropy contribution at zero applied electric field, as observed previously [101]. A possible explanation stems from the substrate, which, in its virgin state, falls into a piezoelectric multidomain state [114]. When the substrate is electrically poled, regions with different ferroelectric domains may give rise to regions with a different pre-strain, which can then influence the magnetization of the Ni microstructures, fabricated on an unpoled substrate [101]. Therefore, the application of the electric field of 250 kV m^{-1} compensates for the pre-strain and leads to an unstrained domain distribution in the Ni disc. The compressive strain of a larger magnitude along the x direction is generated upon increasing the electric field above 250 kV m^{-1}. Consequently, the areas of the black and white domains in Fig. 3.4 (d) each increase by ca. 11%, see Fig. 3.5 (a). On the other hand, for the electric fields below 250 kV m^{-1}, the compression (extension) along the x (y) -axis is weaker (stronger) than that at 250 kV m^{-1}, as suggested by the approximately linear response of the generated strain on the electric field in this field range (see Fig. 2.3 in Section 2.1.1). Therefore, the effective compressive and tensile strain acting on the Ni microstructures invert when the electric field crosses 250 kV m^{-1}, as indicated by green and yellow arrows in Fig. 3.4 (a-d).

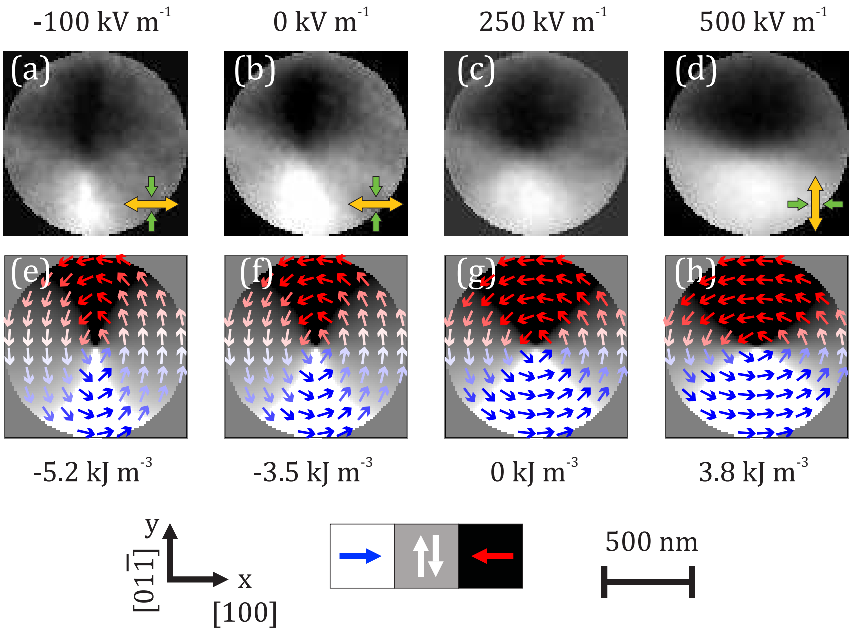

Figure 3.4: (a)-(d) XMCD-PEEM images of the magnetization configuration of a 1-μm Ni disc as a function of different applied electric fields across the piezoelectric substrate. (e)-(h) Magnetization configuration of a 1-μm Ni disc with different magnitudes of the ME anisotropies introduced into the micromagnetic simulations. The gray scale indicates the magnetic contrast and the colored arrows indicate the magnetization direction. Reproduced from Ref. [183] with the permission of AIP Publishing.

Thus, one can see that the domains with the magnetization along the effective compressive strain direction grow in size, which is in qualitative agreement with the expected behavior of Ni with its negative magnetostriction constant (for bulk Ni, $\lambda_s \sim -32$ ppm) [186, 187] and agrees well with the results reported earlier for microstructured Ni squares [101].

To quantify the induced ME anisotropies we carried out micromagnetic simulations in the MicroMagnum framework [188] using the following parameters for Ni: exchange constant, A $= 8\cdot10^{-12}$ J m^{-1}, saturation magnetization, $M_s = 4.8\cdot10^5$ A m^{-1} and the Gilbert damping parameter $\alpha = 0.01$. The numerical discretization used a cell size of 3 nm in the in-plane direction, which is well below the exchange length $l_{ex} \approx 7.4$ nm for the given parameters. In the OOP direction, the discretization was 50 nm, corresponding to the thickness of the Ni microstructures. The effect of the electric field-induced strain was introduced into the simulations as an additional uniaxial anisotropy term, K_{ME}. For every value of the ME anisotropy, the magnetic configuration was initialized in the vortex state and relaxed into its equilibrium state. Note that

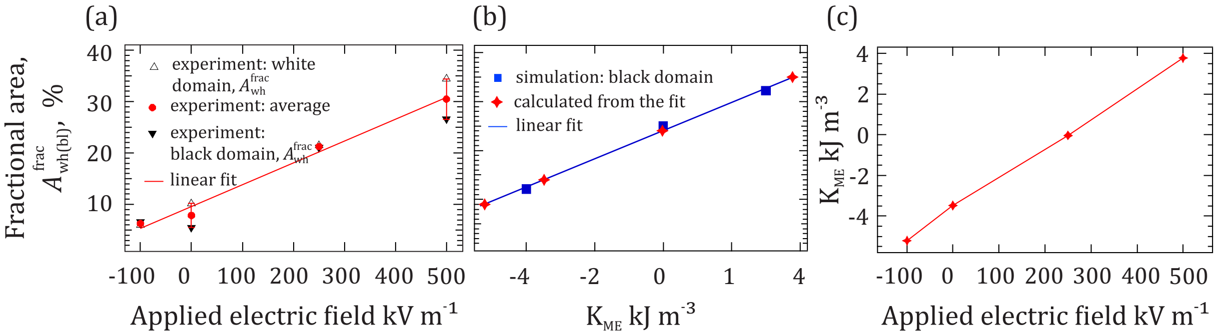

Figure 3.5: (a) Fractional areas of black, $A^{\mathrm{frac}}_{\mathrm{bl}}$, or white, $A^{\mathrm{frac}}_{\mathrm{bl}}$, magnetic domains within a disc as a function of the applied electric field (for experimental values) or effective ME anisotropy (for micromagnetic simulations). Open and filled black triangles correspond to experimental white and black domains fractional areas. Red circles correspond to their average. (b) Blue squares correspond to fractional areas of the black domain extracted from the images simulated for selected values of ME anisotropy, namely, -4 kJ m^{-3}, 0 kJ m^{-3}, 3 kJ m^{-3}. The data was fitted using a linear function, shown by a blue line. The red markers correspond to the required ME anisotropies to obtain the same change in the fractional areas as in the experiment. (c) Electric fields vs. ME anisotropies resulting in the same relative change of the magnetic domain distribution. Reproduced from Ref. [183] with the permission of AIP Publishing.

due to the polycrystalline nature of the Ni film, no other anisotropy contribution besides the one arising from the applied strain was included into the micromagnetic simulations.

To quantitatively compare the experimental XMCD-PEEM images with the micromagnetic simulations and, thus, understand what ME anisotropy was induced in the system for a given electric field, we estimated fractional areas occupied by a domain of one type and plotted them as a function of the applied electric field for experimental images and the ME anisotropy for simulated images. First, a region of interest (ROI) containing the vortex core at the center was defined. To estimate the areas of the black, A_{bl}, or white, A_{wh}, domains we calculated the area taken up by the pixels with a value below or above a certain threshold, respectively. Note that the threshold pixel value was kept the same for all the images acquired at various applied electric fields. The fractional areas, $A^{\mathrm{frac}}_{\mathrm{bl}} = A_{\mathrm{bl}}/A_{\mathrm{tot}}$ and $A^{\mathrm{frac}}_{\mathrm{wh}} = A_{\mathrm{wh}}/A_{\mathrm{tot}}$, presented in Fig. 3.5 (a), were then determined as a ratio of the estimated areas of black and white domains to the total area of the ROI, A_{tot}.

These results for the white and black magnetic domains are presented by the black open up-triangular and filled down-triangular markers in Fig. 3.5 (a), respectively. We also show the averaged values between the black and the white domains' fractional areas, indicated by red circular markers in the same graph. This can be done, assuming a symmetric vortex state, i.e. that the black and the white domains in this representation occupy equal areas. Doing so gives us an estimate for the error of the values of the fractional area for the XMCD-PEEM images, which we show in Fig. 3.5 (a). We also observe that $A_{\mathrm{wh}}^{\mathrm{frac}}$ and $A_{\mathrm{bl}}^{\mathrm{frac}}$ change linearly with the electric field, which is provided by the linear response of the generated strain to the applied electric field.

We followed the same procedure to estimate the fractional areas of the black domains in the images obtained by micromagnetic simulations for selected values of the ME anisotropy, -4 kJ m^{-3}, 0 kJ m^{-3}, 3 kJ m^{-3}. The results are presented in Fig. 3.5 (b) by blue square markers. Note that positive K_{ME} corresponds to the easy axis along the x direction, i.e. favoring the black/white domains over the gray ones. Negative K_{ME} induces an easy axis along the y direction, thus favoring the magnetization alignment in the y direction. We then analogously fit the data with a linear function to obtain the dependence of the domain fractional area on the induced ME anisotropy. This enables us to determine which values of ME anisotropy lead to the relative changes in the domain structure observed in the experiment. For example, when the applied electric field is changed from 250 kV m^{-1} to 500 kV m^{-1}, the black/white domain fractional area is increased by ca. 11 %. From the fit in Fig. 3.5 (b), we find that in order to obtain the 11 % black/white domain growth, a ME anisotropy of 3.8 kJ m^{-3} is required. Similarly, we obtain that the ME anisotropies of -3.5 kJ m^{-3} and -5.2 kJ m^{-3} for 10 % and 15 % decrease in the fractional area of the black/white domain, respectively. The resulting required values of the ME anisotropy are shown in Fig. 3.5 (b) and one to one conversion of the applied electric field to the induced ME anisotropy is shown in Fig. 3.5 (c).

3.4 TIME-RESOLVED XMCD-PEEM IMAGING OF VORTEX CORE GYRATION DYNAMICS IN STRAINED DISCS

To excite the gyrotropic motion of the VC, a continuous sinusoidal signal was applied to the stripline, which was synchronized with the x-ray bunches illuminating the sample, the latter having 499.654 MHz (in the text referred to as 500 MHz) repetition rate. For each phase delay between the rf-excitation and the x-ray bunches, PEEM images were acquired in a stroboscopic mode, as described in Section 2.3.2.

The amplitude of the AC voltage arriving at the stripline was estimated based on the analysis of the STV maximum shift for different phases of the rf-signal [189]. Figure 3.6 (a) shows the analyzed STV scans each exhibiting a characteristic inelastic secondary electrons peak. As any

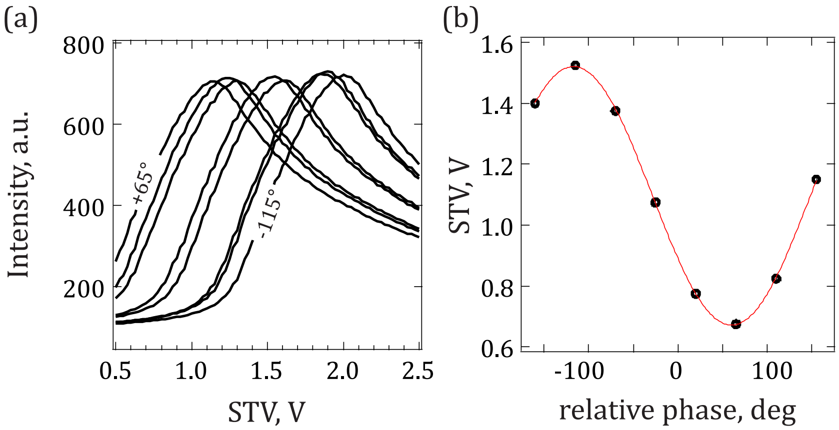

Figure 3.6: (a) STV scans taken at the stripline at various phases of the rf-signal. (b) Shift of the maxima of the STV spectra in (a) as a function of the phase. Red line shows the sin fit to the data.

local surface potential leads to the change of the kinetic energy of the photoelectrons, which is scanned with the STV, the observed variation of the STV can be directly correlated with the voltage at the stripline [189]. From the fit of the STV dependence on the relative phase shown in Fig. 3.6 (b), we estimate the AC voltage of 420 mV to arrive at the stripline. Therefore, it can be expected that despite the impedance mismatch to the stripline, a sizeable rf-signal was able to reach the sample. On the basis of Ampere's law, we can estimate the resulting Oersted field of 12 mT at the center of the Ni discs, i.e. 50 nm from the center of the stripline.

To determine the resolution of the images, we show in Fig. 3.7 (a) an XMCD-PEEM image acquired using a FOV of 10 μm, i.e. with similar conditions to the images in Fig. 3.4 and consider an intensity line profile taken along the red line. The Gaussian fit of this intensity change, shown in Fig. 3.7 (b), yields 5.5 ± 0.6 pixels for the half-width at half-maximum (HWHM), resulting in ca. 60 nm of spatial resolution of the images in XMCD mode.

In order to reconstruct the VC gyration orbit and study the effect of the electric field-induced strain, we determined the VC position for every XMCD-PEEM image acquired at various phases of the excitation and various poling voltages. To extract the xy position of the VC during its gyration motion, we used the following algorithm. First, a ROI of a central part of the disc, including the VC, was selected, as shown in Fig. 3.8 (a). Then, a one-pixel wide line profile along the y direction was analyzed as a function of its x coordinate. The examples of the XMCD signal variation along the line profiles corresponding to three different x positions are plotted in Fig. 3.8 (c). When the contrast showed maximum variation along the line profile, the corre-

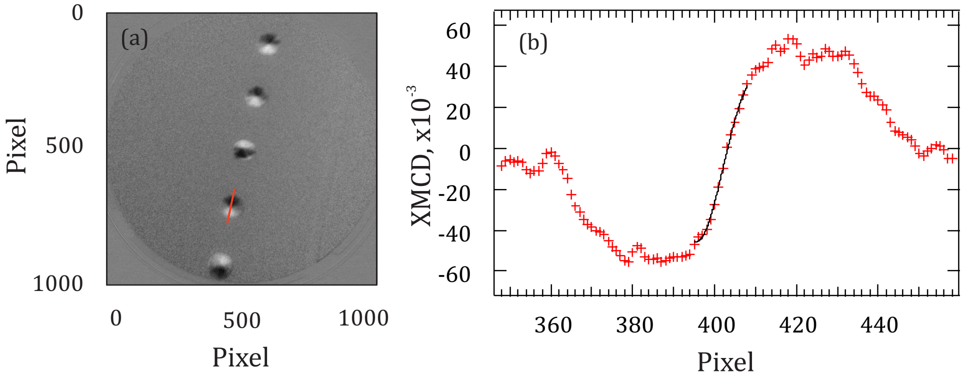

Figure 3.7: (a) XMCD-PEEM image of the Ni microstructures on top of a stripline in a FOV of 10 μm. The red line indicates the region where a line profile was taken. (b) Line profile of the XMCD intensity as fitted by a Gaussian function. Reproduced from Ref. [183] with the permission of AIP Publishing.

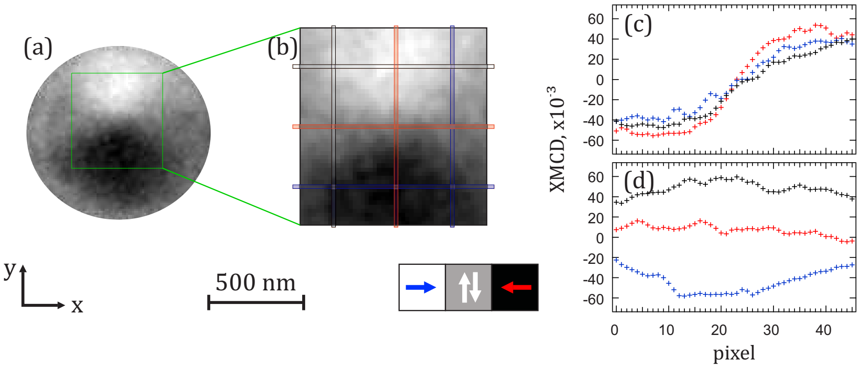

Figure 3.8: (a) XMCD-PEEM image of the vortex state in the disc. (b) Zoomed-in XMCD-PEEM image of the VC area, marked by the green square in (a). The black, red and blue vertical and horizontal lines indicate where the line profiles shown in (c) and (d) were taken. (c) Vertical and (d) horizontal one-pixel wide line profiles taken along the corresponding lines indicated in (b). Reproduced from Ref. [183] with the permission of AIP Publishing.

sponding x position was assigned to the x coordinate of the VC.

Analogously, a one-pixel wide line profile along the x direction was taken and analyzed as a function of its y coordinate. The examples of these profiles corresponding to three different y coordinates are shown in Fig. 3.8 (d). The y position yielding a minimal variation of the XMCD signal within the line profile was taken as the y coordinate of the VC.

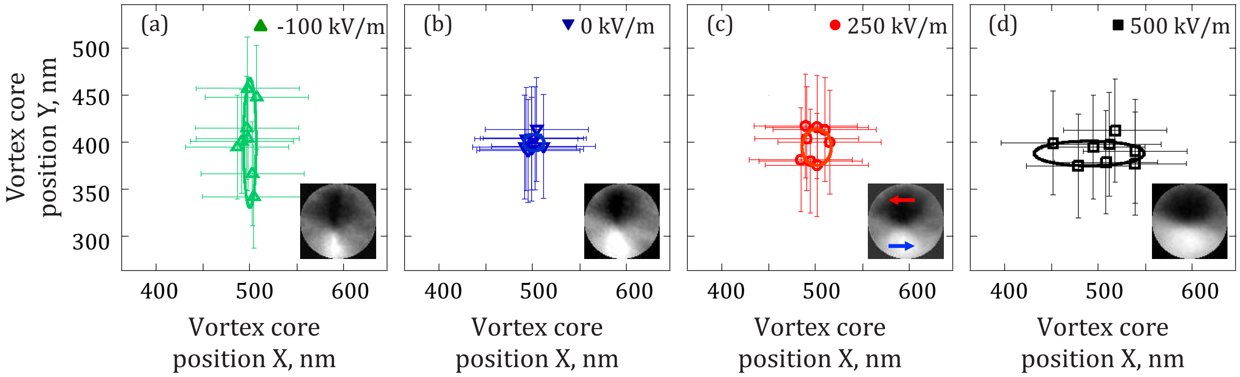

Figure 3.9: Experimentally determined distribution of *xy* positions of the VC during its gyration measured as a function of an electric field applied to the piezoelectric substrate. The *xy* positions were extracted from the time-resolved XMCD-PEEM images using the algorithm described in the text. The insets show the domain configurations at each amplitude of the electric field as shown in Fig. 3.4. Adapted from Ref. [183].

The results of the VC dynamics excited by an alternating magnetic field are summarized in Fig. 3.9. Here, the phase-dependent xy positions of the VC, as extracted using the algorithm described above, are plotted for selected amplitudes of the electric field applied across the PMN-PT substrate. The orbit shown in red dots in Fig. 3.9 (c), measured at 250 kV m^{-1}, is nearly circular, which corresponds to an unstrained vortex state as discussed earlier and agrees with the predicted behavior [159, 170, 171, 172, 190].

When the strain-induced uniaxial anisotropy sets in, the orbit deviates from the circular shape. At 500 kV m^{-1} applied to the substrate, which results in the ME anisotropy easy axis along the x direction, the VC displacement along the x direction reaches $\sim$ 90 nm, while in the y-axis direction it moves within $\sim$ 40 nm [Fig. 3.9 (d)]. For negative and zero applied electric fields, shown in Fig. 3.9 (a) and (b), respectively, the VC movement becomes more confined in the x direction, i.e. the gyration amplitude along x does not exceed a few tens nm, which is below the resolution limit. Furthermore, as seen in Fig. 3.9 (a), the orbit measured at -100 kV m^{-1} is strongly elongated in the y-axis direction, with the spread of more than 100 nm.

Thus, we show experimentally that the application of an electric field, and as a consequence piezoelectric strain, strongly deforms the VC gyration orbit. The ME anisotropy confines the VC so that it moves along the easy axis set by the induced anisotropy. This observation agrees with the behavior previously obtained numerically [170], which explains the increase in ellipticity of the VC gyration orbit by the softening of the restoring force due to the uniaxial anisotropy.

However, as mentioned earlier, this softening has another consequence on the VC gyration dynamics. Specifically, the additional uniaxial anisotropy leads to a decrease of the VC eigenfrequency for the distorted vortex state compared to the undistorted state [170, 180]. In general, both these effects need to be taken into account to understand the observed modification of the VC gyration orbit under the application of an electric field-induced strain.

3.5 MICROMAGNETIC SIMULATIONS OF THE VORTEX CORE GYRATION DYNAMICS UNDER MAGNETOELASTIC ANISOTROPY

In order to understand our experimental observations, we address the effect of strain-induced ME anisotropy on the VC gyration orbit by means of micromagnetic simulations. The simulations were carried out on a 20 nm thick disc of 200 nm in radius, which was relaxed into a vortex state. Note that in order to be able to carry out simulations in realistic computational times with sufficient accuracy, we considered a disc of smaller dimensions but the same aspect ratio. To excite the vortex core gyration in simulations, we imposed an in-plane oscillating magnetic field with an amplitude of 3 mT along the x direction. The VC position was extracted from the simulations by finding the xy coordinates where the absolute value of the OOP component of the magnetization was maximum.

Note that the magnitudes of the ME anisotropy used for dynamics simulations are different because of the different dimensions of the structure which result in a larger shape anisotropy for smaller discs. The ME anisotropy magnitudes were chosen to give rise to similar changes of the static magnetic configuration, analogous to the ones presented in Fig. 3.4.

It is worth mentioning that we assume the material to be homogeneous in the z direction, as the thickness of the sample was much smaller than the radius of the microstructure. Moreover, the frequency regime that we worked in suggested that only a uniform gyration mode was excited [54, 191]. The higher excitation modes were not expected to occur for such geometries and frequencies, which made the discretization in the z direction irrelevant for our purposes. We also note that we did not consider vortex core switching. Therefore, for the purposes of this thesis, it was sufficient to consider one cell in the z direction.

The micromagnetic simulations not only allowed us to vary the induced ME anisotropy in the system to mimic the effect of strain, but also to change the excitation frequency, which was not possible in the present experiments. In particular, we are interested in the excitation frequencies well above and below the gyration eigenfrequency of the undistorted vortex state.

First, we set the frequency of the excitation $f_{\text{ex}} = 256$ MHz in the simulations to match the gyration eigenfrequency for the undistorted vortex state of the given geometry. The resulting VC gyration orbits for selected magnitudes of the ME anisotropy are shown in Fig. 3.10 (b). One can

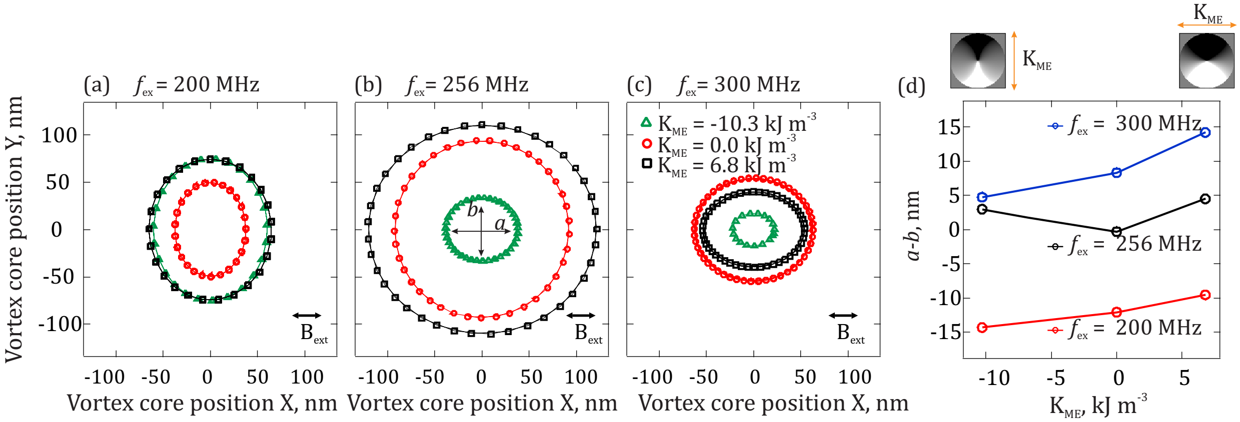

Figure 3.10: Micromagnetically simulated VC gyration orbits in a 20 nm thick Ni disc of 200 nm in radius excited with a sinusoidal magnetic field in the x direction at (a) 200 MHz, (b) 256 MHz and (c) 300 MHz with an amplitude of 3 mT for selected values of K_{ME}. Reproduced from Ref. [183] with the permission of AIP Publishing. (d) Difference of the major and minor axes of the elliptical VC gyration orbits as a function of K_{ME} for three excitation frequencies. Insets show the domain configurations of the vortex state corresponding to $K_{\mathrm{ME}} = -10.3$ kJ m^{-3} and $K_{\mathrm{ME}} = 6.8$ kJ m^{-3} with indicated direction of the ME easy axis.

see that without the contribution of the ME anisotropy, red circular markers in Fig. 3.10 (b), the VC gyration orbit has a circular shape, as the excitation occurs at resonance. For the non-zero ME anisotropies, the orbit's shape is deformed. Modifications of the VC gyration orbits with the ME anisotropy are observed also for the off-resonant excitation, i.e. at $f_{\mathrm{ex}} = 200$ MHz and $f_{\mathrm{ex}} = 300$ MHz as demonstrated in Fig. 3.10 (a) and (c), respectively. Quantitatively, the trends of the induced modifications are summarized in Fig. 3.10 (d). Here we plot the difference of the major and minor axes of the ellipses fitted into the VC gyration orbits, $a-b$, as a function of the ME anisotropy, where a (b) is the axis along the x (y) -axis directions, as indicated in Fig. 3.10 (b).

3.6 DISCUSSION

Before we go into the discussion of the observed behavior we emphasize once more that the effect of the ME anisotropy on the VC gyration dynamics is two-fold: (*i*) the elongation of the orbit in the direction of the induced uniaxial anisotropy and (*ii*) the eigenfrequency reduction due to the ME anisotropy. We schematically illustrate these two effects separately in Fig. 3.11.

As described analytically [171] and demonstrated numerically [192], the gyration orbit is elongated perpendicular to the excitation field direction when $f_{\mathrm{ex}} < f_0$, i.e. if the excitation frequency is smaller than the eigenfrequency of the system. On the contrary, if the excitation frequency is larger than the eigenfrequency ($f_{\mathrm{ex}} > f_0$), the orbit is elongated in the direction of the oscillating magnetic field, as shown in Fig. 3.11 (a).

In Fig. 3.11 (b), we depict the effect of the ME anisotropy itself, by schematically indicating one ring down[4] of the VC spiral motion back to the center after the excitation with a magnetic field pulse, in analogy to Ref. [170]. Due to the softening of the restoring force mainly along the anisotropy direction, the movement of the VC along this direction becomes more favorable and the orbit more extended.

Since these two effects always act in combination in the case of a continuous excitation with an AC magnetic field, they can add up or compensate each other depending on the frequency range, as we discuss below.

Indeed, by comparing the orbits represented by red circular markers in Figs. 3.10 (a-c), we can clearly see the sole effect of the off-resonant excitation. For the excitation frequency larger (smaller) than the gyration eigenfrequency of the undistorted vortex, the VC gyration orbit is elongated along (perpendicular) to the oscillating field direction, i.e. the x-axis.

The deformations due to the ME anisotropy can be observed clearer in Fig. 3.10 (d). The circular gyration orbit at $K_{\mathrm{ME}} = 0$ kJ m^{-3} and $f_{\mathrm{ex}} = 256$ MHz with $a = b$ due to the resonant excitation becomes deformed along the x direction, so that $a > b$ for both $K_{\mathrm{ME}} = -10.3$ kJ m^{-3} and $K_{\mathrm{ME}} = 6.8$ kJ m^{-3}, see black markers in Fig. 3.10 (d). This is a result of the ME anisotropy-induced reduction of f_0, which reduces to 230 MHz and 208 MHz at $K_{\mathrm{ME}} = 6.8$ kJ m^{-3} and $K_{\mathrm{ME}} = -10.3$ kJ m^{-3}, respectively. As follows from the model depicted in Fig. 3.11, the anisotropy of $K_{\mathrm{ME}} = 6.8$ kJ m^{-3} leads to the elongation of the VC gyration orbit in the x direction both due to the induced easy axis along x and the decreased f_0 for the deformed vortex state. On the contrary, at $K_{\mathrm{ME}} = -10.3$ kJ m^{-3} these two contributions counteract, because the ME anisotropy sets the easy axis in the y direction, while the frequency mismatch favors gyration along the x-axis. As a result of this interplay, the elongation of the VC gyration orbit is more pronounced in the x direction for $K_{\mathrm{ME}} = 6.8$ kJ m^{-3} as compared to $K_{\mathrm{ME}} = -10.3$ kJ m^{-3}.

Analogous trends can be observed in Fig. 3.10 (d) for the off-resonant excitation with $f_{\mathrm{ex}} = 300$ MHz and $f_{\mathrm{ex}} = 200$ MHz. In the former case, the gyration orbit at $K_{\mathrm{ME}} = 0$ kJ m^{-3} is no longer circular, but elongated in the x direction ($a > b$) because $f_{\mathrm{ex}} > f_0$. The induced ME anisotropy along both the x and y directions leads to a reduction of the vortex eigenfrequency and, as a result, the deformation along the x-axis occurs. In addition, $K_{\mathrm{ME}} = 6.8$ kJ m^{-3} favors the VC gyration along the x-axis, thus, resulting in further elongation of the orbit in the x direction.

---

[4] The orbits are depicted as open circles to account for the damping after the excitation is removed.

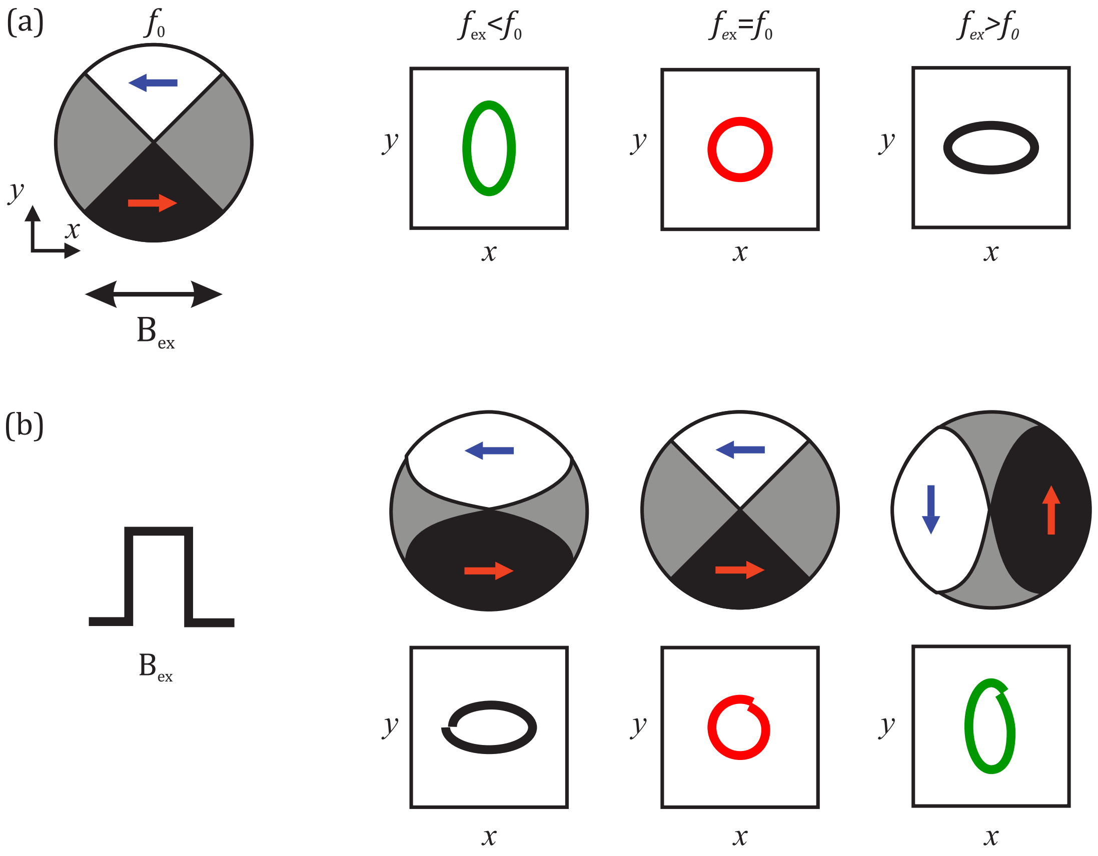

Figure 3.11: Schematic illustration of the VC orbits (a) during gyration when the frequency of the excitation, f_{ex}, does not match the eigenfrequency, f_0, in the absence of the ME anisotropy and (b) during the ring down of the VC spiral motion back to the center after a magnetic field pulse when the ME anisotropy is imposed.

On the contrary, $K_{\mathrm{ME}} = -10.3$ kJ m^{-3} induces the easy axis along y and counteracts the elongation in the x direction. Therefore, for the excitation frequency above the eigenfrequency of the undistorted vortex, the difference $a - b$ is larger at $K_{\mathrm{ME}} = 6.8$ kJ m^{-3} than that at $K_{\mathrm{ME}} = -10.3$ kJ m^{-3}. Hence, it indicates that the VC gyration is more favorable and, thus, extended along the x direction.

Similar arguments can be applied to the case when the excitation frequency is below the eigenfrequency of the vortex state, i.e. $f_{\mathrm{ex}} = 200$ MHz shown in Fig. 3.10 (d) by the red line. Unlike the previous scenario, all orbits tend to elongate along the y direction, i.e. perpendicularly to the magnetic field, see Fig. 3.10 (a). In addition, the uniaxial ME anisotropy along y makes the y-axis even more favorable for the orbit shown by green markers, while for $K_{\mathrm{ME}} = 6.8$ kJ m^{-3}, the ME anisotropy counteracts the frequency mismatch and leads to elongation in the x direction. This results in the green gyration orbit at $K_{\mathrm{ME}} = -10.3\ \mathrm{kJ\ m^{-3}}$ being more elongated in the y direction than the black orbit at $K_{\mathrm{ME}} = 6.8\ \mathrm{kJ\ m^{-3}}$ and the red orbit at $K_{\mathrm{ME}} = 0\ \mathrm{kJ\ m^{-3}}$. It is also reflected in the decreasing difference $a - b$ while the ME anisotropy switches from the easy y-axis to x-axis in Fig. 3.10 (d).

Thus, by looking at the dependencies in Fig. 3.10 (d) we see that addition of the ME anisotropy to the system shifts the resonance such that a circular gyration orbit is achieved at different conditions, i.e. at non-zero ME anisotropies. This demonstrates that one can also tune the magnitude of the ME anisotropy to fully compensate the two contributions leading to the orbit deformations and make the gyration orbit circular even for the off-resonant excitation.

Even though the simulations of the dynamics were performed on a structure with different dimensions than the experimental one, the revealed mechanisms can qualitatively explain the experimental observations. Specifically, the experiments show that the VC gyration orbit becomes elongated in the x (y) direction when $500\ \mathrm{kV\ m^{-1}}$ ($-100\ \mathrm{kV\ m^{-1}}$) is applied across the PMN-PT substrate, as depicted in Fig. 3.9, i.e. the gyration becomes more favorable in the direction of the easy axis induced by the piezoelectric strain. While being also governed by the competition between the frequency mismatch due to the ME anisotropy and the anisotropy-induced deformation of the domain structure, the experimentally observed modifications of the gyration orbit associated with the electrically tunable strain allow us to identify that the effect of the modified domain configuration is dominant for the particular microstructures studied in the experiment.

It is worth noting that the micromagnetic simulations reveal no significant change in the VC profile for the considered range of the ME anisotropy, which is in line with the previously reported behavior of the VC under applied stress [170]. Thus, we attribute the observed effect of strain on the VC gyration dynamics primarily to the modifications of the in-plane magnetization distribution within the vortex due to the ME anisotropy.

To conclude, in this Chapter, we present the study of the dynamics of magnetic vortices hosted in magnetostrictive microstructures on top of a piezoelectric substrate. We demonstrate the modification of the VC steady-state motion due to an electric field-induced strain. We find that the ME anisotropy generated by piezoelectric strain not only modifies the static magnetic configuration of the microstructures but also influences the VC gyration orbit, which we determine by time-resolved imaging of the magnetic configuration of the vortices. Our findings demonstrate that the electrically induced and controlled ME anisotropy allows one to tune the VC gyration orbit in addition to tuning the gyrotropic frequency of the microstructures. We discuss the two underlying mechanisms responsible for the observed modifications of the gyration orbit, namely, the change in the resonance frequency and the change in the potential landscape due to the additional uniaxial anisotropy. The magnetization dynamics behavior observed in the experiment is in good qualitative agreement with the micromagnetic simulations, where we model the effect of the piezoelectric strain by an additional uniaxial anisotropy term.

Our results show that electrically induced strain can be used to tailor the magnetodynamical response of magnetic vortices. Of particular importance is that the VC gyration orbit deformations are accompanied by a modification of the gyration eigenfrequency, which allows for the local tuning of the gyration resonance. This is particularly useful as it allows one to selectively switch the VC polarity of the vortex by a global excitation field for which the gyration eigenfrequency is tuned by electric field-induced strain. Our findings demonstrate an energy-efficient tool to fully electrically control vortex dynamics, which could be a key asset for future vortex applications in microwave devices.

The results presented in this Chapter were published in *Applied Physics Letters* [183].

CHAPTER 4

ELECTRIC FIELD CONTROL OF SPIN-ORBIT TORQUES (SOT)S IN PERPENDICULARLY MAGNETIZED W/COFEB/MGO THIN FILMS

4.1 INTRODUCTION

As discussed in Section 1.4.2, the SOT-induced magnetization switching, generated by the flow of an electric current in the plane of a HM/FM bilayer, offers a promising alternative to the conventional STT mechanism [15, 16, 27, 28, 93, 95]. From the discussion of the origin of the SOTs it follows that their magnitude and the sign can be adjusted by optimizing the parameters of the system such as the thickness and the composition of the layers. In this case, though, the SOTs remain fixed once the multilayer is fabricated. However, for complex switching concepts, i.e. to selectively switch parts of the FM using single pulse lines, which may lead to drastically simplified device architectures, it is necessary to locally and dynamically tune the SOTs in a system.

In this regard, mechanical strain has attracted particular attention because of its potential for local actuation [193] and the possibility of energy-efficient strain generation (see Chapter 1). The strain effect on the spin torque-induced magnetization switching was intensively assessed theoretically and computationally [194, 195, 196]. For example, recent calculations demonstrated that the critical current density required for 180° magnetization switching of a FM layer due to STT is drastically decreased because of the substrate misfit strain [194].

The only previous experimental study addressing the impact of strain on the SOT switching focused on a system with an in-plane (IP) magnetized FM layer [196], thus the effect of strain was found to be primarily on the magnetic anisotropy. The SOT measured for this system by spin-torque ferromagnetic resonance (ST-FMR) showed that the strain-induced magnetic anisotropy rotates the magnetic easy axis and acts as to eliminate the incubation delay in the current-induced switching, thus, reducing the switching time. However, the DL SOT response to the induced strain was negligible and the observed changes in the ST-FMR signal were mainly attributed to the strain-induced changes in the magnetic anisotropy.

Moreover, in the light of potential applications, it is more desirable to optimize the parameters of the SOT switching of FM elements with PMA. These systems are the materials of choice because of their intrinsically higher thermal stability, packing density and better scalability compared to their IP counterparts [66, 197]. Furthermore, in the DL SOT-induced switching geometry of the OOP magnetization, it is possible to realize deterministic switching if the induced uniaxial strain is misaligned with respect to the net spin polarization, as demonstrated in the recent computational study [195].[1]

In this Chapter, we discuss the impact of electrically controlled strain directly on the SOTs in PMA W/$Co_{20}Fe_{60}B_{20}$/MgO film grown on a piezoelectric substrate. First, we assess the change of the magnitude of the SOTs as modified by tensile or compressive strain experimentally. We then go further into the discussion of the nature of the observed strain responses of the SOTs. With the help of theoretical band structure calculations from collaborating colleagues, we reveal the microscopic origin of the observed behavior.

4.2 SAMPLE CONFIGURATION

Experimentally the DL and the FL effective SOT fields were measured by 2ω spin-torque magnetometry (see Section 2.4 for details) on W(5 nm)/$Co_{20}Fe_{60}B_{20}$(0.6 nm)/MgO(2 nm)/Ta(3 nm)

---

[1] We note that generally, the magnetization switching in FM/HM multilayers by DL SOTs is not deterministic. Conventionally, an external IP magnetic field is required to switch an OOP magnetization into a fixed direction [58, 86, 198], that otherwise switches randomly to up or down direction [199]. As an example, in the Pt/Co/AlOx stack, considered in Ref. [15], a positive current pulse induces an effective field B_{DL}, which acting together with an IP field B_x can switch the magnetization direction from “up” to “down” if initially $B_{\mathrm{DL}} || B_x$ [15]. It was also shown that the rotation sense changes upon the reversal of the current polarity, such that bipolar switching is achieved by either current or IP field reversal. As the transferred angular momentum is generally transverse to both the current direction and the normal to the plane, it cannot ensure reversible magnetization switching between the “up” and “down” directions. Hence, only the DL torque acting in combination with e.g. an additional IP field B_x, that breaks the symmetry ensures, the deterministic switching of the OOP magnetization [15, 86].

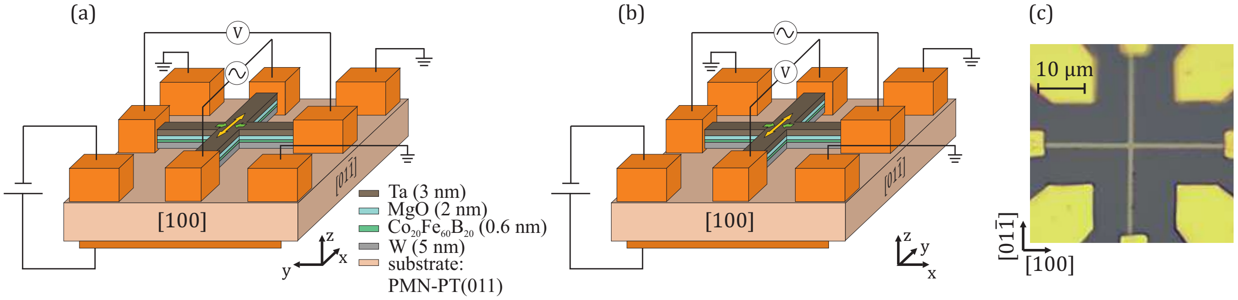

Figure 4.1: Schematic of the Hall bar device of W/$Co_{20}Fe_{60}B_{20}$/MgO/Ta fabricated on top of a bare PMN-PT(011) substrate and the electrical contacts used for the application of the OOP electric field to generate strain as well as the electrical contacts to the Hall bar. (a) The tensile and (b) the compressive strain configuration. (c) Optical microscope image of the Hall-cross structure used for the spin torque measurements. Adapted from Ref. [200].

Hall-cross devices fabricated on top of a PMN-PT (011) substrate. The PMN-PT substrate was employed to electrically generate mechanical strain as discussed in Section 2.1.1 and the Hall-cross devices were fabricated following the procedure described in details in Appendix A. The schematic of the sample configuration is depicted in Fig. 4.1 (a,b) and an optical microscope image of the structure used in the experiment is shown in Fig. 4.1 (c). For convenience, we employed the convention that the current flow was always along the x-axis. Thus, in the configuration shown in Fig. 4.1 (a) the current flow, i.e. the x-axis, was along the $[01\bar{1}]$ direction of the PMN-PT substrate and in the text, it is referred to as tensile strain configuration. For the compressive strain geometry, we used the same Hall-cross device, but the electrical contacts for the current and voltage lines were swept. Thus, the current flow (x-axis) in the compressive strain geometry was along the [100] direction, as shown in Fig. 4.1 (b).

We also note that prior to any measurements, the PMN-PT substrate was electrically poled by applying +400 kV m^{-1}, which allowed us to operate in the linear regime of the strain vs. electric field response (see Section 2.1.1 for more details on the PMN-PT poling).

First, we characterized the magnetic state of the Hall-cross device by measuring the AHE as a function of the OOP magnetic field at 0 kV m^{-1}. The resulting hysteresis loop is shown in Fig. 4.2 (a) and demonstrates an easy-axis switching which is typical for W-based thin CoFeB stacks [201, 202]. The corresponding AHE resistance is observed to be ~ 0.38 Ω, obtained by the measured AHE voltage divided by applied current.

Next, in order to estimate the PHE, we measured the transverse resistance as a function of azimuthal angle, ϕ, by rotating the sample under an IP field of 0.95 T, which was large enough to

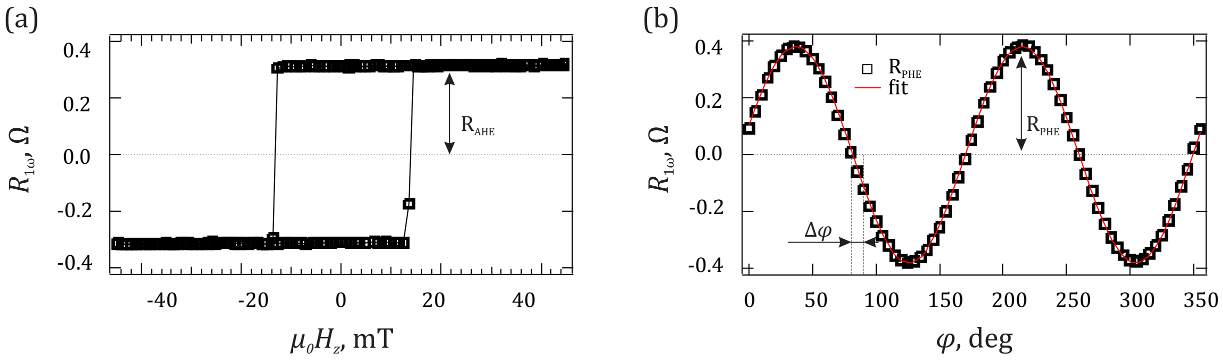

Figure 4.2: (a) Anomalous Hall resistance, R_{AHE}, as a function of an OOP magnetic field ($\mu_0 H_z$). (b) Planar Hall resistance, R_{PHE}, measured using a rotating IP magnetic field of 0.95 T. The measurements were carried out using an applied current of 0.1 mA.

saturate the magnetization in the film plane. In this measurement configuration, there was no AHE contribution to the measured resistance, thus, we probed only the PHE contribution. This was supported by good agreement of the measured azimuthal dependence with the fit by $\sin 2\varphi$ function, shown in Fig. 4.2 (b). Furthermore, we used the PHE angular dependence to align the Hall-cross within the 3D vector magnet. A slight misalignment of the Hall-cross with respect to the coordinate system of the magnet [$\Delta\varphi$ in Fig. 4.2(b)] was compensated by assigning the angles at which the PHE signal was zero to be the x/y directions of the IP vector magnetic field. This ensured that the transverse ($\mu_0 H_y$) and longitudinal ($\mu_0 H_x$) magnetic fields, employed in the 2ω measurements below, were aligned with the arms of the Hall-cross device.

It is also important to note that the system studied here exhibits a large PHE, while in other systems it can be negligibly small compared to the AHE contribution [203]. The large contribution of the PHE in W-based systems is attributed to the large SOC in tungsten [204, 203]. Since the PHE shares the same origin with the AMR [82], it is expected to depend on the SOC in the system, similarly to the AMR. Therefore, in HM/FM multilayers, where the HM, such as tungsten in this case, is a source of the SOC, the PHE can be large and even greater than the AHE, as seen in Fig. 4.2.

4.3 CHARACTERIZATION OF STRAIN

In order to estimate the strain generated upon application of the electric field across the PMN-PT substrate we analyzed the Hall bar resistance change as a function of the DC poling voltage, shown in Fig. 4.4 (a). As illustrated in Fig. 4.3, the Hall-cross arm oriented along the tensile

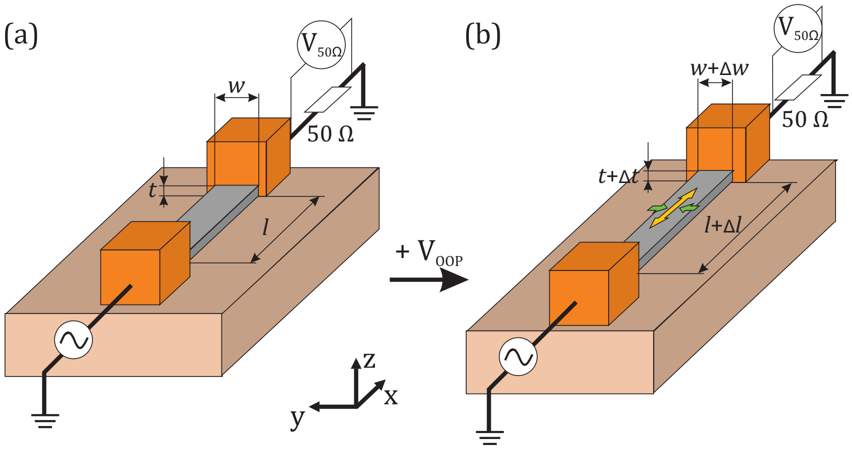

Figure 4.3: Schematic showing the expansion and contraction due to the uniaxial piezoelectric strain when DC voltage, V_{OOP}, is applied in the z direction. The resistance of the wire is estimated by measuring the voltage across 50 Ω resistance knowing the input voltage. Upon poling of the piezoelectric substrate the unstrained wire in (a) is deformed due the piezoelectric strain in (b) and the strain can be estimated by the resistance change.

($[01\bar{1}]$) strain direction, becomes longer and narrower due to the uniaxial strain, which is reflected in the change of its resistance. Vice versa, the Hall-cross arm along the compressive ([100]) strain direction becomes wider and shorter, leading to an increase of the resistance.

It is known, that the resistance of a wire of resistivity ρ, length l and cross-sectional area A, given by $R = \frac{\rho l}{A}$, changes proportionally to the change in the length of the wire upon application of strain. In addition, other geometrical and physical effects arise when the bar is strained: the change in the cross-sectional area by an amount determined by Poisson's ratio ν and the change in resistivity as the structure of the material is distorted.

Formally the resulting change in resistance can be expressed as follows

$$\frac{\delta R}{R} = \frac{\delta l}{l} + \frac{\delta \rho}{\rho} - \frac{\delta A}{A}. \tag{4.1}$$

This can be written in terms of the longitudinal strain $\epsilon_x = \frac{\delta l}{l}$ [205]

$$\frac{\delta R}{R\epsilon_x} = \left(1 - \frac{\delta A}{A\epsilon_x}\right) + \frac{\delta \rho}{\rho\epsilon_x}, \tag{4.2}$$

where the first term on the right is a factor describing the geometrical deformation, C_{geom}, and the second term on the the right is the strain coefficient of the specific resistivity, C_ρ, and can be found in the literature [206].

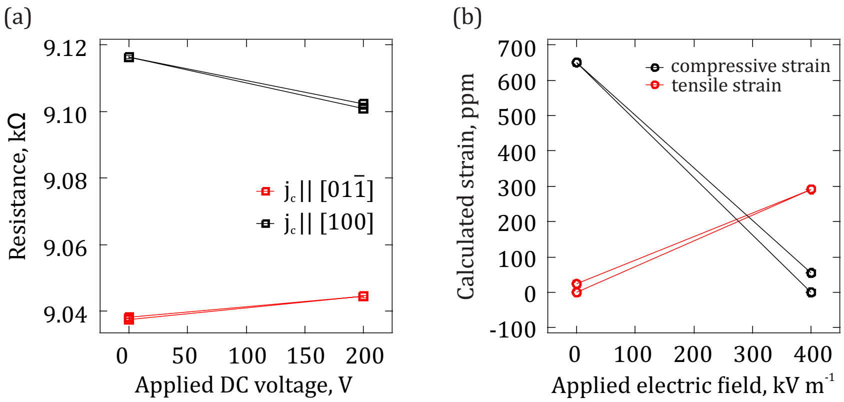

Figure 4.4: (a) The resistance measured for the Hall bar arms along the [01$\bar{1}$] (red) and [100] (black) directions. (b) The strain as calculated from the resistance change plotted as a function of the applied electric field across the 0.5 mm thick PMN-PT substrate.

Thus, the strain in a Hall bar coupled to the PMN-PT substrate can be found from the resistance change using

$$\epsilon_x = \frac{\delta R}{R} \frac{1}{C_{\text{geom}} + C_\rho} \,. \tag{4.3}$$

To calculate the geometrical factor C_{geom} for uniaxial strain we follow the arguments from Ref. [207]:

$$\frac{\delta A}{A} = \frac{\delta t}{t} + \frac{\delta \varpi}{\varpi} = \epsilon_z + \epsilon_y = -\epsilon_x(\nu_z + \nu_y)\,, \tag{4.4}$$

$$C_{\text{geom}} = 1 - \frac{\delta A}{A\epsilon} = 1 + \nu_z + \nu_y \,. \tag{4.5}$$

Assuming the Poisson's ratio of the film $\nu_z = 0.32(7)$ and the strain coefficient of specific resistivity $C_\rho = 0.935$ as the average of the film's constituents[2] and $\nu_x = \nu_y = 0.32$ for the substrate [208], the final relation takes the form

$$\epsilon = \epsilon_x = 0.363 \frac{\delta R}{R} \,. \tag{4.6}$$

The resistance change was calculated from the measured voltage drop across the 50 Ω resistance in series with the Hall bar knowing the input voltage. Fig. 4.4 (a) shows the resistance jump measured for the Hall bar along the tensile (red) and compressive (black) strain directions due the electric field of 400 kV m^{-1} applied to the PMN-PT substrate. The generated strain estimated using Eq. 4.6 is plotted in Fig. 4.4 (b) as a function of the applied electric field. The

---

[2] As taken from Ref. [206] $\nu_{\text{Fe}} = 0.28$, $\nu_{\text{Co}} = 0.33$, $\nu_{\text{W}} = 0.32$, $\nu_{\text{Ta}} = 0.34$, $C_{\rho\text{Co}} = 0.84$, $C_{\rho\text{W}} = 1.16$, $C_{\rho\text{Ta}} = 1.30$, $C_{\rho\text{Fe}} = 0.44$, $C_{\rho\text{W}}$. Here the data for MgO and B were omitted as they are unavailable due to the insulating nature of these materials.

electric field was converted from the applied DC voltage across the 0.5 mm thick PMN-PT substrate. We can see that for the electric field of 400 kV m^{-1} the generated compressive (tensile) strain within the linear regime is ca. $-7 \cdot 10^{-4}$ $(3 \cdot 10^{-4})$, which is close to the values reported in the literature for commercially available PMN-PT (011) substrates [109, 114].

4.4 MEASUREMENTS OF THE SOTS IN W/COFEB/MGO THIN FILMS

Prior to measuring the electric field-induced strain dependence of the SOTs in our system, we characterized the impact of strain on the OOP magnetic hysteresis. Figure 4.5 shows the anomalous Hall voltage sweep with the OOP magnetic field ($\mu_0 H_z$) measured at 0 kV m^{-1} (red line) for W/$Co_{20}Fe_{60}B_{20}$/MgO/Ta. The OOP magnetization loop, measured at 400 kV m^{-1} (black line) in the tensile strain configuration [Fig. 4.1 (a)], is overlaid on top of it and shows no sizeable change due to the generated strain. Hence, we see that the system has always a dominating PMA within the strain regime used in the experiment.

This is in agreement with the measurements of the strain response of the PMA constant for a nominally similar system shown in Fig. 4.5 (b). We followed the technique of measuring the PMA field, H_K, based on the AHE measurements with rotating external magnetic field in a small angle around the easy axis (see Ref. [209] for more details). The anisotropy field was then analyzed employing the Stoner-Wohlfarth theory with small angle deviation to extract H_K at various magnitudes of the electric field applied to the PMN-PT substrate. The anisotropy constant K_{eff} was calculated as $K_{eff} = \frac{\mu_0 H_K M_s}{2}$. As can be seen from the plot of K_{eff} as a function of the applied electric field in Fig. 4.5 (b), the PMA is not varied significantly by the induced strain. Indeed, the typical magnitude of the strain-induced ME anisotropy for CoFeB films is in the order of 10 kJ m^{-3} [180] and, thus, is negligible compared to the PMA in our system [59]. Moreover, the AHE and PHE also do not show any dependence on the applied strain, as can be seen in Fig. 4.5 (c).

To measure the SOT we followed the scheme described in Section 2.4. Figure 4.6 shows the representative IP field dependencies of the first ($V_{1\omega}$) and the second ($V_{2\omega}$) harmonics of the Hall voltage when an AC current with the current density of $j_c = 3.8 \times 10^{10}$ A m^{-2} was applied to the current line. The DC poling voltage was set to zero, thus, no strain was imposed on the Hall cross. One can see, that the 1ω signals dependence on the longitudinal, Fig. 4.6 (b), and transverse, Fig. 4.6 (d), magnetic fields is parabolic and changes sign upon magnetization reversal. On the other hand, the linear dependencies of the 2ω signals demonstrate distinct behavior. The longitudinal field sweep of the 2ω signal, Fig. 4.6 (a), reverses the sign for $\pm M_z$, while the

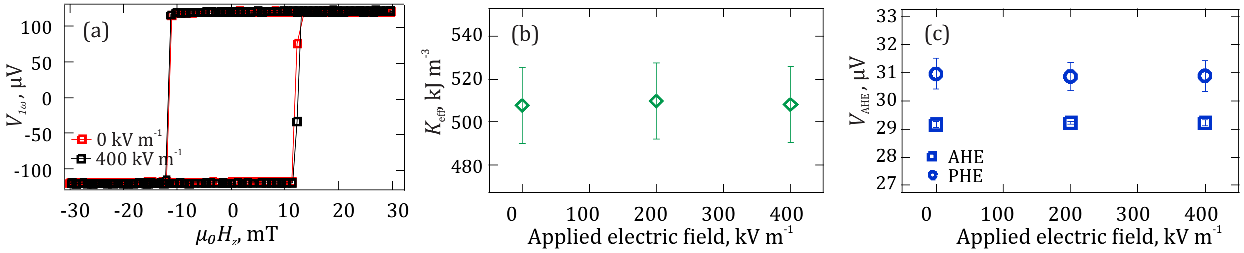

Figure 4.5: 1ω Hall voltage hysteresis loop measured during the OOP magnetic field sweep at 0 kV m^{-1} (red), and 400 kV m^{-1} (black) applied across the PMN-PT substrate using an applied current of 0.33 mA. Adapted from Ref. [200]. (b) PMA constant K_{eff} and (c) AHE and PHE as a function of the electric field applied across the PMN-PT substrate.

sign for the transverse field sweep, Fig. 4.6 (b), remains the same for both magnetization directions. Overall, the trends of the 1ω and the 2ω signal dependencies on the external magnetic field exhibit the expected symmetries [93].

Using Eq. 2.11 we analyzed the transverse ($\mu_0\Delta H_{\mathrm{T}}$) and the longitudinal ($\mu_0\Delta H_{\mathrm{L}}$) components of the SOT effective field for both magnetization directions $\pm M_z$ and plotted them as a function of the applied current density j_{c} in Fig. 4.6 (e) and (f). The resulting linear dependencies were fitted such that the slopes $\left(\mu_0\Delta H_{\mathrm{T(L)}}/j_{\mathrm{c}}\right)$ determined the FL, $\mu_0 H_{\mathrm{FL}}^{\mathrm{eff}}$, and DL, $\mu_0 H_{\mathrm{DL}}^{\mathrm{eff}}$, SOT effective fields. One can notice, that the resulting slopes corresponding to the opposite magnetization directions of both the longitudinal [Fig. 4.6 (e)] and the transverse [Fig. 4.6 (f)] SOT effective fields are slightly different. This can occur due to the misalignment of the Hall-cross device with respect to the external magnetic fields.

Furthermore, parameter ξ in Eq. 2.11, which is typically negligible in other systems [154], is known to be enhanced for W-based multilayers [203], due to the large PHE, as discussed above. In this system we found $\xi \approx 1.25$, showing no dependence on the electric field induced strain, as seen in Fig. 4.5 (c).

The resulting linear slopes from the fitting of the dependencies in Fig. 4.6 (e,f) were averaged to obtain the FL and the DL SOT effective fields for 0 kV m^{-1}. Similarly the effective SOT fields were extracted for different DC electric fields applied to the PMN-PT substrate.

4.5 SOTS AS A FUNCTION OF STRAIN: EXPERIMENT AND THEORY

The results are summarized in Fig. 4.7. As can be seen in Fig. 4.7 (a), for the current flow along the tensile strain direction the magnitude of the FL torque does not change significantly. On

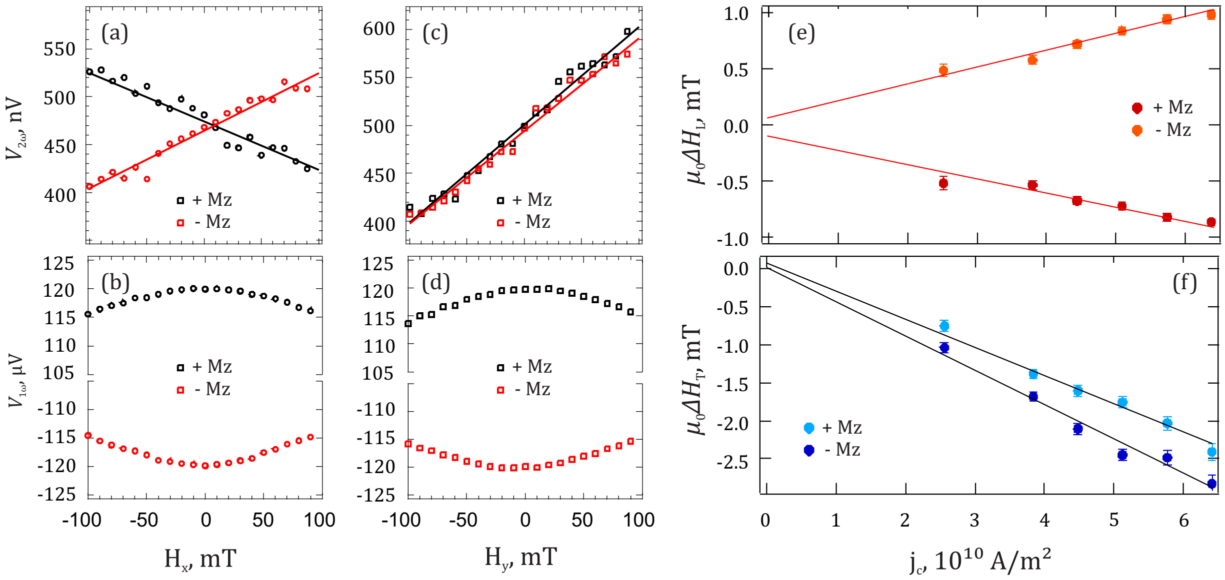

Figure 4.6: (a) $V_{2\omega}$ and (b) $V_{1\omega}$ signals as a function of the IP magnetic field directed along the current flow. (c) $V_{2\omega}$ and (d) $V_{1\omega}$ signals as a function of the IP field directed transverse to the current flow. The data were measured at the current density of 3.8×10^{10} A/m^2. Black and red symbols represent signals for the magnetization pointing along $+z$ and $-z$, respectively. (e) The longitudinal ($\mu_0\Delta H_{\mathrm{L}}$) and (f) the transverse ($\mu_0\Delta H_{\mathrm{T}}$) components of the SOT effective fields plotted as a function of current density j_{c}. Adapted from Ref. [200].

the contrary, the magnitude of the DL torque increases by a factor of 2 upon increasing the DC electric field up to 400 kV m^{-1}, Fig. 4.7 (b).

On the other hand, when the current is flowing along the compressive strain direction, the magnitude of the DL torque decreases with increasing strain, while the FL torque remains mostly unchanged, as can be seen in Figs. 4.7 (d) and (c), respectively. Note that the magnitudes of the torques at zero electric field measured in two orthogonal directions are not equal. This can be attributed to the pre-strain imposed on the Hall-cross at 0 kV m^{-1}, which originates from the ferrolectric domains of the PMN-PT substrate after the initial poling [101, 183, 114], because the Hall-cross devices were fabricated on an unpoled substrate [101].

Thus, we find experimentally that the magnitude of the DL torque increases (decreases) upon application of electrically induced tensile (compressive) strain, while the FL torque remains unchanged for both characters of the strain. We also note that our results for W-based perpendicularly magnetized $Co_{20}Fe_{60}B_{20}$ stack show an opposite trend than that for Pt-based IP magnetized $Co_{40}Fe_{40}B_{20}$, reported in Ref. [196]. The observed opposite behavior can be at-

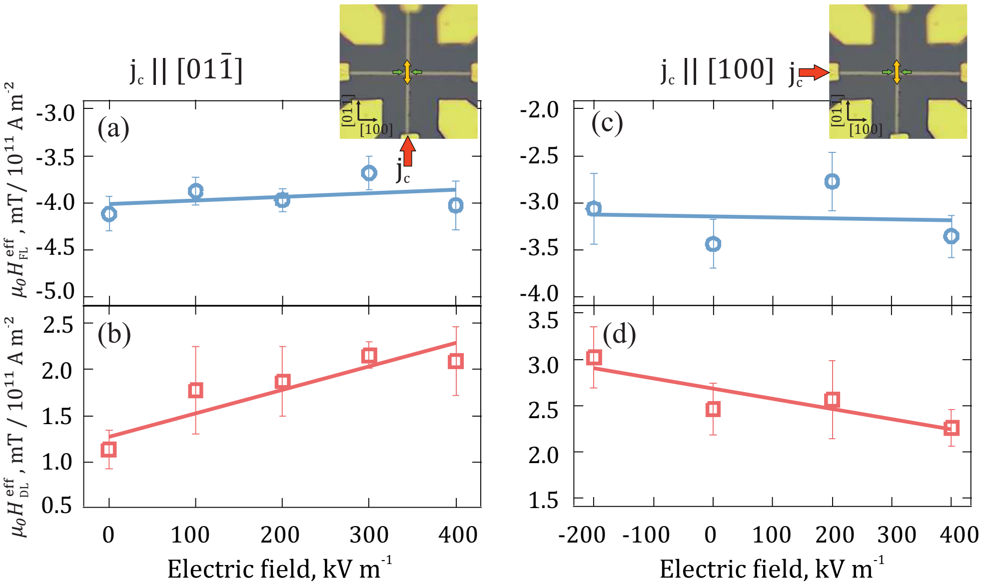

Figure 4.7: (a) Field-like and (b) damping-like SOT effective fields as a function of the electric field applied across the PMN-PT(011) for the current flowing along the tensile ([01$\bar{1}$]) strain direction (see the inset). (c) Field-like and (d) damping-like SOT effective fields as a function of the electric field applied for the current flowing along the compressive ([100]) strain direction (see the inset). The solid lines represent the linear fit to the data as a guide to the eye. Adapted from Ref. [200].

tributed to the difference in the SHAs of Pt and W [210].

In order to understand the microscopic origin of the experimentally observed strain dependence of the FL and DL SOTs, we performed density functional theory (DFT) calculations of the electronic structure of a model system, namely W(001)/Fe$_{0.7}$Co$_{0.3}$, consisting of a perpendicularly magnetized FeCo monolayer and non-magnetic W underlayers. As depicted in Fig. 4.8 (a,b), the crystal structure was expanded or contracted while keeping the IP area of the unit cell constant to mimic the effect of uniaxial strain. We defined the strain by the ratio $\delta = (a'_j - a_j)/a_j$, with a_j and a'_j denoting the lattice constant along the j-th IP direction in the relaxed and distorted case, respectively. As expected from the symmetry point of view, as a result of any finite strain, the original C_{4v} crystal symmetry was reduced to C_{2v}, as shown in Fig. 4.8 (b).

As discussed in Appendix C, within the Kubo formalism [211] the SOT $T_i = \tau_{ij} E_j$ acting on the magnetization is represented as the linear response to the applied electric field E_j, mediated by the torkance τ_{ij}. In the system with the mirror symmetry and the OOP magnetization the torkances τ_{xx} and τ_{yy} characterize the FL SOTs, whereas τ_{xy} and τ_{yx} correspond to the DL

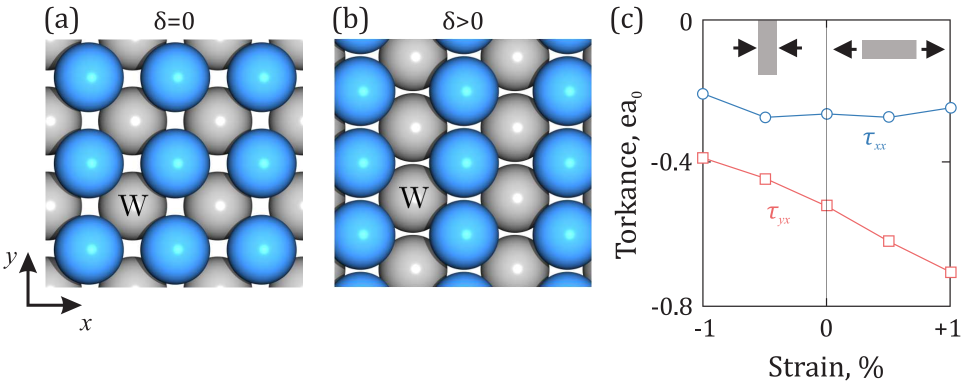

Figure 4.8: (a) The schematic of the relaxed crystal structure of the $Fe_{0.7}Co_{0.3}$/W(001) film used in the calculation. (b) The uniaxial strain δ modifies the equilibrium crystal structure and reduces the symmetry from C_{4v} to C_{2v}. (c) Dependence of the FL (blue) and DL (red) torkances on strain along the direction of the electric field, where a constant broadening of the energy bands by 25 meV is used. Adapted from Ref. [200].

torques. In the following, δ refers to the strain along the orientation of the applied electric field, which points into the x-direction.

Based on the band structure calculations, we obtained the SOTs response to δ shown in Fig. 4.8 (b), which demonstrate similar qualitative trends as found in the experiment. Specifically, the theory results for the FL and the DL torkances also follow distinct dependencies on the strain. The theory predicts the DL torkance to increase (decrease) with increasing tensile (compressive) strain, while the FL torkance is hardly affected by strain. This observation highlights the distinct nature of the FL and the DL torques. Originating from different electronic states, they generally follow distinct dependencies on structural details.

To elucidate this remarkable behavior, we present in Fig. 4.9 (a) the momentum-space distribution of the microscopic contributions to the DL SOT for relaxed and strained films. One can notice that the occupied states around the M-point barely contribute, and the major source of the DL is provided by the states near the high-symmetry points Γ, X, and Y. By comparing these momentum-space maps at $\delta = 0$ and $\delta > 0$ in Fig. 4.9 (a) we see that the tensile strain promotes strong negative contributions around X and Y. As a consequence, it leads to an overall increase of the magnitude of τ_{yx}, as reflected in Fig. 4.8 (c).

To further associate our findings with the underlying electronic structure, we analyzed the orbital polarization of the d-states in the FM layer. Our calculations show that the behavior of d_{xy}, $d_{x^2-y^2}$, and d_{z^2} is independent of the induced strain δ. On the other hand, the states

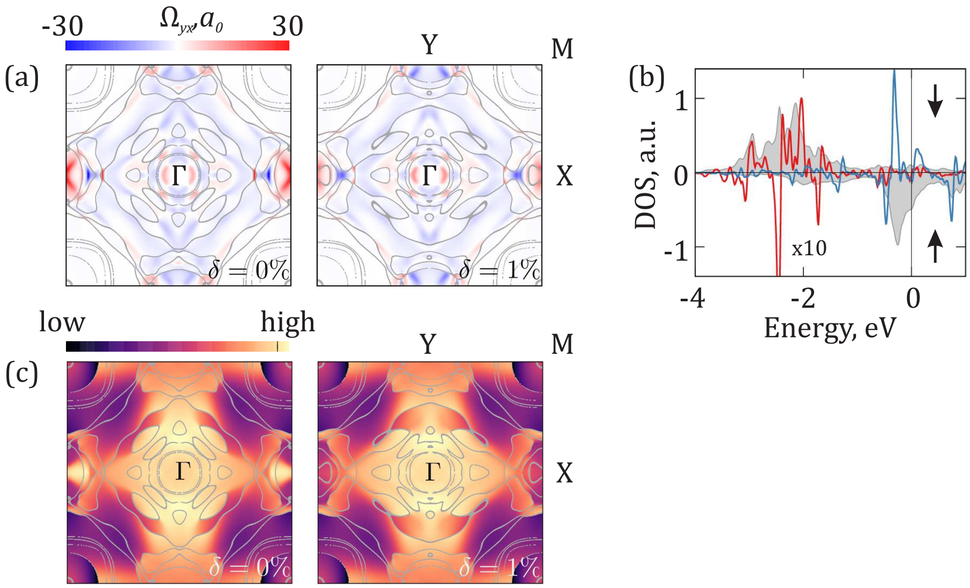

Figure 4.9: (a) Microscopic contribution of all occupied bands to the DL SOT in relaxed and strained crystal structure. Gray lines indicate the Fermi surface. (b) The density of d_{yz}-states in the magnetic layer as compared to the behavior without strain (gray) for majority (red) and minority (blue) spin channels due to the tensile strain of $\delta = 1\%$. The red and blue curves, showing the difference with respect to the unstrained case, are scaled by a factor of 10. (c) Momentum-space distribution of the d_{yz}-polarization of all occupied majority states in the magnetic layer of the relaxed and strained system. Adapted from Ref. [200].

of d_{yz}- and d_{zx}-character transform distinctly with respect to tensile or compressive strain. As discussed in Chapter 1, the d_{yz} and d_{zx} orbitals also mediate the hybridization with the HM substrate, which implies that their dependence on structural details can be reflected in the modification of the SOTs in the studied thin films.

As an example, Fig. 4.9 (b) shows the strain-induced change of the density of d_{yz}-states in the magnetic layer as compared to the unstrained structure. While the density of majority-spin states (red) at the Fermi level is hardly affected by the tensile strain, the minority-spin states (blue) are redistributed rather strongly. As revealed by the momentum-resolved orbital polarization in Fig. 4.9 (c), microscopically, this effect stems from pronounced variations of the d_{yz}-polarization around the X-point due to strain, which correlates with the changes of the DL torkance observed in Fig. 4.9 (a). Thus, the picture that emerges from our first-principles study is that the uniaxial strain modifies symmetry and orbital polarization of the electronic states, which imprints uniquely on the nature of SOTs.

4.6 DISCUSSION

As mentioned earlier, the $Co_{20}Fe_{60}B_{20}$ film considered in this Chapter has the dominating PMA, as revealed by the hysteresis loops [Fig. 4.5 (a)] and the PMA constant behavior [Fig. 4.5 (b)] with strain. Hence, it allows us to probe the direct effect of strain on the SOTs without modifying the magnetic anisotropy, while the previous works focused on systems where the dominating effect of the strain was a change of the anisotropy [194, 195, 196]. In comparison to Ref. [196], where the IP anisotropy and, thus, the energy landscape were altered by strain, in our work, the $Co_{20}Fe_{60}B_{20}$ layer is always magnetized perpendicular to the film plane, keeping the angle between the easy axis and the current direction and, consequently, the energy landscape for the SOTs unchanged. As the strain-induced variation of the energy landscape could be the origin of the SOTs behavior reported in Ref. [196], a fundamentally distinct driving mechanism for the strain response of the SOTs in our system can be expected.

Our theoretical calculations reveal the microscopic origin of the observed behavior of the FL and DL torques. The results show that the uniaxial strain modifies the symmetry and orbital polarization of the electronic states, which imprints uniquely on the nature of SOTs, thus, allowing us to qualitatively reproduce our experimental findings. Beyond revealing the key role of hybridized states at the FM/HM interface, our results suggest a clear scheme for generally engineering spin-orbit phenomena. Utilizing the complex interplay of spin and orbital magnetism, SOC, and symmetry, we can tailor the magnitude of SOTs in multilayer devices by designing the orbital polarization of the states near the Fermi level by strain.

Importantly, our findings demonstrates the possibility to enhance the fundamental spin-orbitronic concepts towards competitive technologies by tuning the magnitudes of SOTs in PMA systems on demand by means of electrically controlled strain. Furthermore, by employing various local strain patterns, one can tune the SOTs in a FM element locally. This opens up roots to design more complex switching sequences of multiple ferromagnetic elements for new device architectures.

For example, when tuning the efficiency of the DL torque, responsible for the switching, by straining some local areas of a FM element, one can achieve the situation when the DL torque is large enough to switch the magnetization direction of the strained parts, while it is too small to switch the unstrained parts, as schematically depicted in Fig. 4.10. As a result, selective switching of the FM element can be realized with a single current density [Fig. 4.10 (b)]. The switching patterns can also be altered by employing various configurations of the electric fields, allowing for an additional level of control, which eventually can lead to the realization of an energy efficient multi-level memory cell capability.

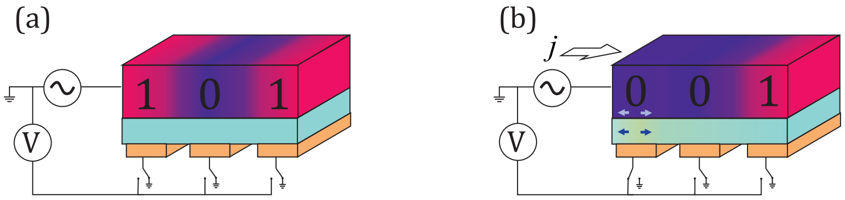

Figure 4.10: Schematic illustration of a device architecture where the piezoelectric strain generated locally is imposed on selected parts of the switching bit to allow for local magnetization direction switching of only selected strained parts with a single current pulse. (a) No current and no local strain (electric field) is applied and "1" and "0" are encoded by the magnetization direction of the bits (blue and red domains). (b) The strain is applied locally to the leftmost "1" area leading to the increased efficiency of the DL torque for the given current density, j, while the other "1" remains unstrained and, thus, unchanged.

In conclusion, in this Chapter, we present the study of the strain response of current-induced SOTs in perpendicularly magnetized W/$Co_{20}Fe_{60}B_{20}$/MgO multilayers grown on a piezoelectric substrate. By application of an electric field to the PMN-PT substrate we generate tensile and compressive strain acting on a Hall-cross device, for which by means of the 2ω Hall voltage analysis we evaluate the SOTs. We find that the strain response of the FL and DL torques is different and that the magnitude of the DL torque enhances approximately by a factor of two if the tensile strain is applied parallel to the current flow. We explain our experimental results by the band structure calculations that uncover the microscopic origin of the observed strain effects on the SOTs. We reveal that the orbital polarization of the electronic states in the FM, dominating the hybridization with the electronic states in the HM underlayer, is modified differently with respect to tensile or compressive strain. This manifests in a sizable variation of the magnitude of the DL torque while the FL torque remains mostly unaffected. The demonstrated possibility to tune the SOTs by means of electric field induced strain paves a novel path towards to the energy-efficient "dynamical" control of the current-driven SOT-switching necessary to enable future spintronics applications.

The results presented in this Chapter were published in *Physical Review Letters* [200].

CHAPTER 5

ELECTRIC FIELD CONTROL OF THE DZYALOSHINSKII-MORIYA INTERACTION IN PERPENDICULARLY MAGNETIZED W/COFEB/MGO FILMS

5.1 INTRODUCTION

Recently, the antisymmetric exchange interaction, the DMI (see Sections 1.1.2, 1.2.6, 1.4.2 for an introduction), has attracted substantial interest due to the novel resulting spin structures and possible applications that can be facilitated by the control of this interaction [212]. As discussed in Chapter 1, in contrast to the Heisenberg interaction, which favors collinear alignment of neighboring spins $\mathbf{S}_i$ and $\mathbf{S}_j$, the DMI prefers an orthogonal orientation of the spins as follows from its formal description $\mathbf{D}_{ij} \cdot \left(\mathbf{S}_i \times \mathbf{S}_j\right)$. Furthermore, the chirality of this interaction is set by the direction of the DMI vector $\mathbf{D}_{ij}$, hence also the resulting spin structures are chiral.

In ultrathin FM layers in contact with a HM with large SOC, the interfacial DMI may lead to the stabilization of such chiral magnetic textures as chiral Néel walls [30] and magnetic skyrmions [31, 98]. Technologically attractive is that by tuning the magnitude of the DMI, one can tailor these magnetic structures [54, 213, 214, 215, 216] as, for instance, the skyrmion stability region is governed by the competition of the DMI with the exchange and magnetic anisotropy [98, 217]. Furthermore, the chirality of the spin configuration introduces new features of the magnetization dynamics. Large DMI stabilizes the DW internal structure against DW transformations (precessional dynamics) [30], so that the DWs can be driven to very large velocities by magnetic fields [218, 219, 220]. Another technologically relevant advantage is that chiral Néel walls and skyrmions can be displaced efficiently when driven by spin polarized currents via SOTs [31, 53, 54, 98]. Furthermore, the DMI is known to govern the skyrmion annihilation field [217], thus, tuning this interaction can potentially assist to effectively "write" or "delete" skyrmions. Therefore, the DMI and the routes for its optimization are being intensively studied, because both kinds of the magnetic textures stabilized by the DMI are predicted to be used as information carriers in future spintronics devices [97, 212, 221].

As already shown in a number of works [54, 213, 214, 215], similarly to the SOTs, the magnitude of the DMI in ultrathin PMA materials can be tuned by judiciously selecting the layer materials, the interfaces and the thicknesses of the constituent layers. This approach does not allow, however, for a "dynamical" control of the DMI, as the magnitude of the DMI is fixed by the choice of the single layer geometries and their interfaces. Therefore, the search for alternative means to tune the DMI, such as by electric fields [222, 223, 224, 225, 226, 227] in HM/FM/Oxide structures and strain [216, 228, 229], is at the center of attention.

In the former case, similarly to voltage controlled PMA (VCMA), voltage is applied perpendicularly to the plane of the interface between the insulator and the metal. The resulting electric field is shown to increase the strength of the Rashba SOC at the FM/Oxide interface [225] and, consequently, the DMI associated with this interface. The efficiency of the electric field control of the DMI is typically characterized by the slope of the DMI change with respect to the electric field, $\beta_{\mathrm{DMI}} = \Delta D/\Delta E$, which is found to be in the order of 10 – 2000 fJ $(\mathrm{V\,m})^{-1}$ for different systems [225, 226, 227].

Using electric fields to modify the DMI, however, limits the kind of systems because it requires an additional insulating layer. The use of strain, on the other hand, first studied experimentally for bulk DMI systems [230, 231], allows one to overcome this limitation. Recent experimental works report on the imact of mechanical strain also on the interfacial DMI in FM/HM multilayers, demonstrating the DMI enhancement with the strain. The strain in these works was generated either by adjusting the growth parameters [228], thus, introducing permanent strain, or by mechanically bending the sample [229]. Therefore, the next step is the experimental realization of the dynamical strain control of the interfacial DMI.

In this Chapter, we discuss the dynamical control of the interfacial DMI in thin film of W/$\mathrm{Co_{20}Fe_{60}B_{20}}$/MgO/Ta by electric field-induced strain. First, we study the strain response of the DMI experimentally. We then compare the experimental results with theoretical DFT calculations carried out on the same model W(001)/$\mathrm{Fe_{0.7}Co_{0.3}}$ system for which the microscopic

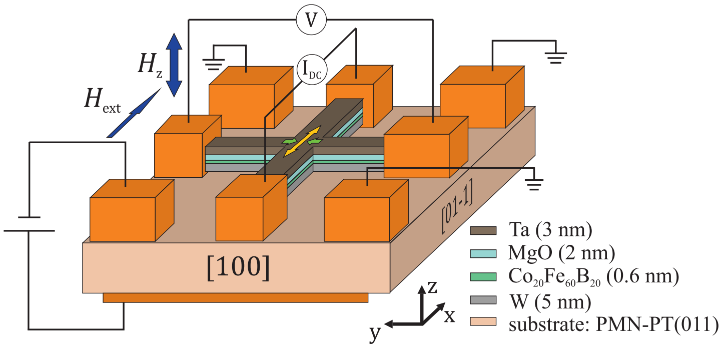

Figure 5.1: Schematic of the sample configuration for the measurements of the DMI in W/$Co_{20}Fe_{60}B_{20}$/MgO/Ta. The DC current is applied to the Hall-cross structure and the AHE hysteresis loop is measured during the OOP magnetic field sweep at various IP bias fields.

origin of the SOTs and their response on the strain was discussed in Chapter 4.

5.2 MEASUREMENTS OF THE DMI IN W/COFEB/MGO

The DMI measurements were carried out on the same Hall-cross device fabricated from a continuous film of W(5 nm)/$Co_{20}Fe_{60}B_{20}$(0.6 nm)/MgO(2 nm)/Ta(3 nm) as that used for the SOTs measurements described in Chapter 4. The fabrication details are given in Appendix A. The measurements scheme used is depicted in Fig. 5.1. We measured the AHE voltage during the OOP magnetic field sweep to characterize the magnetization switching as a function of the applied DC current I_{DC} and the IP bias field. An electric field applied to the piezoelectric PMN-PT substrate in the range of 0 – 400 kV m^{-1} was used to generate strain. In analogy to the strain response of the SOTs measurements, we defined as the tensile strain geometry the configuration where the current flow, i.e. the x-axis, was along the $[01\bar{1}]$ direction of the PMN-PT substrate (see Fig. 5.1). Vice versa, in the compressive strain geometry the current, x-axis, was applied along the [100] direction of the substrate. The measurements in the tensile and compressive geometries were performed on the same Hall-cross device.

To measure the DMI effective field in our system and its modification with strain we followed the measurement protocol described in Section 2.5 of this thesis or in more detail in Ref. [96]. The normalized AHE voltage OOP loops measured at $I_{\mathrm{DC}} = \pm$ 4 mA and an IP bias field $\mu_0 H_x = 180$ mT are shown in Fig. 5.2 (a). Note that the loops are slightly shifted relative to each other for clarity. We can observe an opposite shift of the loops along the $\mu_0 H_z$ axis at opposite polarities of the I_{DC}. This shift can be attributed to the current-induced H^z_{eff} arising due

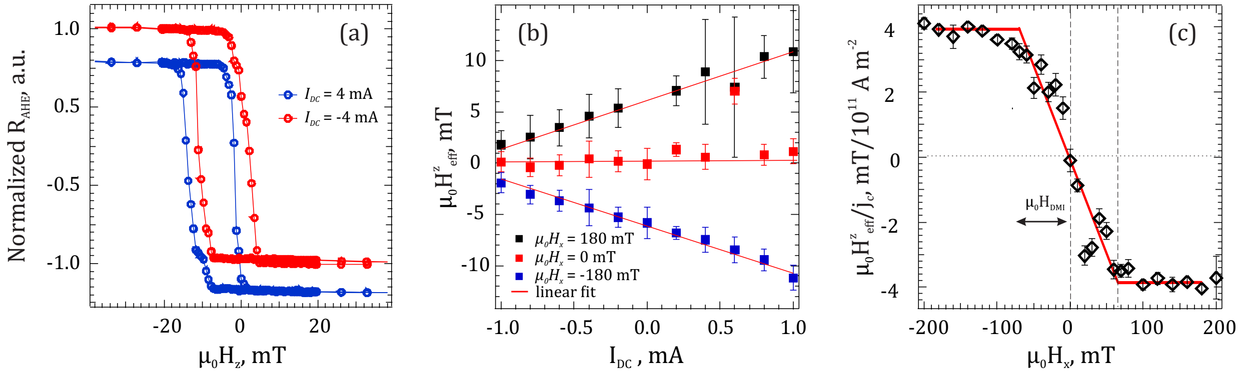

Figure 5.2: (a) AHE loops for W/$\mathrm{Co_{20}Fe_{60}B_{20}}$/MgO/Ta measured at $I_{\mathrm{DC}} = \pm$ 4 mA and an IP bias field $\mu_0 H_x$ = 180 mT. (b) H^z_{eff} as a function of I_{DC} measured at different bias fields $\mu_0 H_x$. The measured $H^z_{\mathrm{eff}}/j_{\mathrm{c}}$ as a function of applied in-plane field used to extract the DMI effective field $\mu_0 H_{\mathrm{DMI}}$.

to the DL SOT in the HM layer [96]. We then determined the switching fields $H^{\downarrow\uparrow}_{\mathrm{SW}}$ and $H^{\uparrow\downarrow}_{\mathrm{SW}}$ for both down-to-up and up-to-down transitions, respectively, defined as the zero-crossing fields of the normalized Hall voltage signal. To eliminate the Joule heating effect we calculated $H^z_{\mathrm{eff}} \equiv (H^{\downarrow\uparrow}_{\mathrm{SW}} + H^{\uparrow\downarrow}_{\mathrm{SW}})$ for each magnitude of the DC current. As can be seen in Fig. 5.2 (b), the I_{DC} dependence of either $H^{\downarrow\uparrow}_{\mathrm{SW}}$ or $H^{\uparrow\downarrow}_{\mathrm{SW}}$ has a quadratic contribution due to the Joule heating, whereas the resulting H^z_{eff} varies linearly with the current for a non-zero IP bias field. The linear variation of H^z_{eff} with respect to I_{DC} can then be used to quantify the DMI effective field, H_{DMI}. We also point out that by reversing the polarity of the IP bias field, the slope of $H^z_{\mathrm{eff}}/I_{\mathrm{DC}}$ reverses. This is consistent with the assumption of the model described in Section 1.4.2 of this thesis [58, 96].

Furthermore, for comparison, in Fig. 5.2 (b) we also plot H^z_{eff} vs. I_{DC} measured in the absence of $\mu_0 H_x$. As expected, no contribution other than Joule heating is observed since the DWs are not realigned by the external field in order to affect the domain expansion/contraction processes [96]. Therefore, at $\mu_0 H_x = 0$, H^z_{eff} always remains zero independently of the applied DC current.

In Fig. 5.2 (c), we plot the resulting $H^z_{\mathrm{eff}}/j_{\mathrm{c}}$ as a function of the applied in-plane field in the x direction at 0 kV m^{-1} applied to the PMN-PT substrate, where j_{c} is the current density. One can see that $H^z_{\mathrm{eff}}/j_{\mathrm{c}}$ increases linearly with increasing H_x and reaches saturation at $H_x = 64.1 \pm 0.8$ mT, which corresponds to the field at which the moments within the DWs in the system become realigned to the external magnetic field direction. The resulting effective DMI field yields the DMI constant $D = 0.33 \pm 0.01$ mJ m^{-2}.

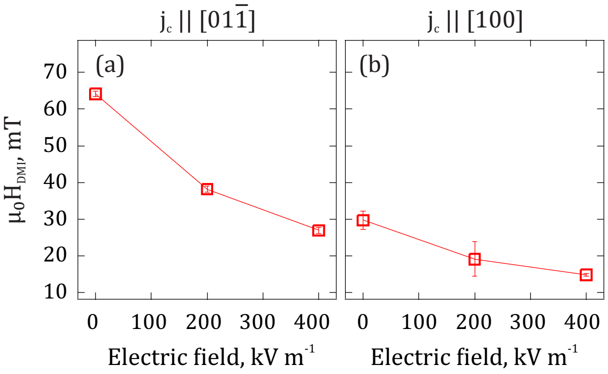

Figure 5.3: Effective DMI field measured as a function of the electric field applied across the PMN-PT (011) for the current flowing along (a) the tensile, [01$\bar{1}$], and (b) the compressive, [100], strain directions.

5.3 DMI AS FUNCTION OF STRAIN: EXPERIMENT AND THEORY

Now we consider the impact of electric field-induced strain on the DMI in W/$Co_{20}Fe_{60}B_{20}$/MgO multilayer system. To address this experimentally, we measured the effective DMI fields as described above for various electric fields. In Fig. 5.3 (a) we plot the resulting effective DMI fields against the electric field in the tensile strain geometry. One can see that H_{DMI} strongly decreases with the increasing tensile strain. Experimentally we obtained a reduction by a factor of two when the electric field increased from 0 kV m^{-1} to 400 kV m^{-1}, corresponding to the tensile strain of ca. 0.03 % (see Section 4.3 for the strain characterization).

For the compressive strain geometry, the resulting DMI trend is similar. As one can see in Fig. 5.3 (b), the effective DMI field decreases upon increasing the compressive strain by varying the applied electric field up to 400 kV m^{-1}. In this case, also a change of the DMI magnitude by a factor of two with the increasing field can be observed. However, if we convert the electric fields into strain using the estimations presented in the previous Chapter (see Fig. 4.4), we obtain that the impact of the tensile strain on the effective DMI field is much larger than that of the compressive strain, as demonstrated in Fig. 5.4 (a). For the tensile strain we can estimate the the efficiency of the electric field control of the DMI $\beta_{DMI} = \Delta D/\Delta E \sim 400$ pJ (V m)$^{-1}$. This suggests that electric field induced strain can be three orders of magnitude more efficient than tuning the DMI by gate voltage [225, 226].

We also note that we measured different magnitudes of the effective DMI fields at 0 kV m^{-1} on the same structure in two configurations. The same discrepancy was found for the experimental values of the SOTs as discussed in Chapter 4. We can as well attribute this to the pre-

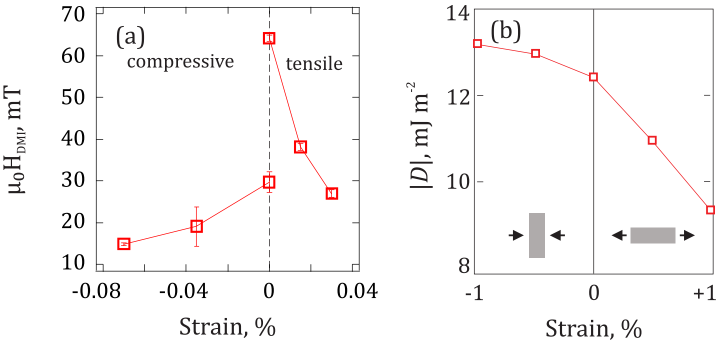

Figure 5.4: Measured effective DMI field plotted as a function of tensile and compressive strain estimated from the resistance measurements in Section 4.3. (b) Dependence of the DMI, D, on tensile ($\delta > 0$) and compressive ($\delta < 0$) strain, calculated using a constant broadening of the energy bands by 25 meV.

strain from the PMN-PT substrate after its poling because the Hall-crosses were fabricated on an unpoled substrate.

In analogy to the previous Chapter, we performed the DFT calculations to explore the microscopic mechanisms of the strain response of the DMI. For calculation we considered the same model system of W(001)/$Fe_{0.7}Co_{0.3}$ as that used for the SOTs calculations. The computational details are discussed in Appendix C. The uniaxial strain was again introduced by deforming the crystal structure of the system and lowering the initial C_{4v} crystal symmetry to C_{2v} (see Chapter 4).

In Fig. 5.4 (b), we plot the DMI response to δ obtained from the calculations. One can see that the DMI decreases in magnitude almost linearly with increasing the tensile strain. However, for the compressive strain, D shows a decrease as the structure becomes more distorted. We note that similarly to the experimental results, the variation of D is more pronounced for the tensile strain, while with the compressive strain, the DMI changes more slowly.

5.4 DISCUSSION AND OUTLOOK

In Fig. 5.3, one can see that unlike theoretical observations, the experimental results demonstrate a non-monotonic dependence of the DMI on the strain. While there is a qualitative agreement between the experimental and computational results for the tensile strain, the DMI response to the compressive strain exhibits an opposite behavior in the experiment and calculations.

Similar non-monotonic strain dependence of DMI was reported in Ref. [229] for Glass/Ta(2.5 nm)/Pt(0.4 – 2.2 nm)/Co(1.2 nm)/Pt(2 nm) where the strain was imposed by bending the substrate. Such behavior is explained by the fact, that since the DMI is mediated by the conduction electrons it has oscillating character described by the following expression [46, 229]:

$$E_{\mathrm{DMI}} \propto \sin\left(k_{\mathrm{F}}\left(b+2r\right)+\pi Z_{\mathrm{d}}/10\right)\sin(2\theta)/(br^2), \tag{5.1}$$

where E_{DMI} is the interaction energy, k_{F} is the Fermi momentum, r is the distance between magnetic ions, b is the distance between magnetic and HM ions, Z_{d} is the number of d-electrons and θ is the angle between the vectors connecting the HM ion and two magnetic ions (see Fig. 1.3). The in-plane strain then changes the distances r and b, which, in turn, modify the DMI constant and Eq. 5.1 governs the non-monotonic behavior of the DMI constant as a function of the distances. Thus, our experimental results can be explained by similar arguments.

Furthermore, the discrepancy between the experimental an theoretical results for compressive strain can be explained by the fact, that the model system used for the calculations is not identical to that studied in the experiment. Not only the FM layer does not contain B, in the first-principles calculations we are also limited to consider single crystalline systems. Thus, this discrepancy only emphasizes the importance of the choice of the system's constituents and structures to achieve the desired behavior. Indeed, the recent experimental works reported on the enhancement of the DMI by strain in Pt(4)/Co(3 nm)/MgO(5 nm) system [228], while in Ref. [229] mentioned above, the dependence of the DMI on the strain qualitatively changed upon variation of the Pt layer thickness. It indicates that the DMI response to strain is not universal for all HM/FM multilayer systems, and thus can be adjusted for particular needs.

We also note that despite not being performed using the identical system for calculations, the obtained results of the SOT response to strain, discussed in Chapter 4, show a good qualitative agreement with the experiment. This may indicate that the DMI is more sensitive to the composition of the system than the SOTs. Indeed, as shown previously for W/CoFeB/MgO multilayers, there is a strong dependence of the DMI on the relative composition of the CoFeB alloy [201], which is also reproduced theoretically for the model W(001)/$Fe_{0.7}Co_{0.3}$ system.[1]

Even though, the DFT calculations only partially agree with the experimental findings, they can provide us with the crucial information on the microscopic origin of the DMI response to strain. For this, we will perform a systematic analysis of the momentum-space distribution maps of the microscopic contributions to the DMI[2] in relaxed and strained films, similarly to

---

[1] Private communication of preliminary results with Dr. J.-P. Hanke.

[2] These are subject to in-depth analysis with conjunction with Dr. J.-P. Hanke and Prof. Dr. Yu. Mokrousov at the time of this thesis being written.

the analysis of the SOTs in Chapter 4. We will analyze which electronic states contribute to the DMI and how these states become deformed by strain and what difference to the DMI it makes. Doing so will potentially lead us to a general rule of thumb suggesting which combinations of the HM and FM can be used to engineer a certain response of the DMI to strain.

The possibility to tune the DMI in a system "on the fly" is very attractive from the technological point of view because, as discussed above, it is know to be responsible for stabilizing chiral spin structures. With strain one can tune the stability region by adjusting the DMI to be above the threshold required to stabilize the Néel DWs, given by $H_{\mathrm{DMI}}/H_{\mathrm{ani}} = 2/\pi$ [30]. This could potentially allow for a skyrmion phase to be stable with no external magnetic field, which may be very attractive as there are limited systems exhibiting skyrmions at room temperatures and zero field [54, 98].

In the concept of the race-tack memory the DMI as modulated by strain can, for example, assist or prevent the motion of the chiral spin textures. As they are only stable for certain range of the DMI and the magnetic anisotropy, they could be dragged towards or expelled from the locally strained region. Thus, by energy efficient strain one can potentially manipulate skyrmions. Furthermore, as our calculations demonstrate that the strain of different character produce distinct responses of the DMI, in an optimized system it may be possible to achieve the situation where for one direction, the DMI sign is reversed compared to the orthogonal direction. Experimental feasibility of this is demonstrated in Ref. [229] where the strain of 0.1% generated by bending the substrate is shown to lead to opposite signs of the DMI along orthogonal directions in Pt(1.1 nm)/Co(1.2 nm)/Pt(2 nm). Therefore, as such strain magnitudes can be achieved with piezoelectric substrates, one can expect the same impact of the electric field-induced strain on the DMI in an optimized multilayer stack.

In other words, in such systems an anisotropic DMI can be induced, thus, stabilizing anti-skyrmions. The existence of stable anti-skyrmions is theoretically predicted for special 2D systems [232], where by symmetry the anisotropic DMI with inversion of chirality between perpendicular directions is induced [233, 229]. This exciting theoretical finding, might further improve the skyrmion race-track concept [212], as replacing skyrmion-free zones with anti-skyrmions could make this type of system more robust even at elevated temperatures.

It is also interesting to notice that the results of the calculations of the DMI presented here and the SOTs discussed in Chapter 4 yield opposite trends for the DMI and the DL SOT. While the DMI decreases (increases) in magnitude with the tensile (compressive) strain, the DL SOT demonstrates an increase for the tensile strain and a reduction for the compressive strain. Furthermore, both the DMI and DL SOT exhibit distinct responses to strain as compared to the FL torque, which demonstrates no response to the strain. It can be attributed to the fact that only some states contributing to the DMI also contribute to the DL torque but not to the FL torque. Therefore, the analysis of the microscopic origin of the observed strain response of the DMI is required to understand the complex behavior of these spin-orbit driven phenomena, which appear to be not exactly correlated as can be naively thought [234].

To conclude, in this Chapter, we present the piezoelectric strain control of the DMI in perpendicularly magnetized W/$Co_{20}Fe_{60}B_{20}$/MgO multilayer system. We measure the effective DMI fields by characterizing the shift of OOP hysteresis loops under different DC currents and IP bias fields. Furthermore, by varying the electric field applied across the piezoelectric substrate, we modulate tensile and compressive strain in the system and investigate its impact on the DMI experimentally. We find that the effective DMI field monotonically decreases with the increasing strain of both characters. We estimate the efficiency of the electric field control of the DMI, $\beta_{\mathrm{DMI}} \sim 400$ pJ $(\mathrm{V\,m})^{-1}$, to be three orders of magnitude larger than that, reported for the DMI control by gate voltage in HM/FM/Oxide systems. Our DFT calculations of the DMI in a model system show a qualitatively similar trend for the tensile strain, however the opposite trend is found for the DMI response to the compressive strain. Furthermore, our calculations reveal the opposite behavior of the DMI and the DL SOT as a function of strain, emphasizing the complex nature of these phenomena, both originating in the same SOC of the HM. While our computational results need to be further analyzed to understand microscopically the observed behavior of the DMI with strain, the experimentally demonstrated manipulation of the DMI with piezoelectric strain paves a way towards energy-efficient manipulation of the DMI and eventually the skyrmions.

CHAPTER 6

SPIN ORIENTATION MANIPULATION BY ELECTRIC FIELDS AND X-RAY IRRADIATION

6.1 INTRODUCTION

We discussed earlier that strain-induced ME anisotropy in the order of $10-100$ kJ m^{-3} can be achieved for moderate strain magnitudes [59, 101] for some magnetostrictive materials, such as Ni, CoFeB, Ga$_x$Fe$_{1-x}$ [235]. However, the impact of the strain on the magnetization in systems with large effective magnetic anisotropies, such as PMA materials, can be insignificant, because the magnitude of the ME anisotropy is a few orders of magnitude smaller than that, typical for the PMA (MJ m^{-3}). This may as well hinder the observation of the strain effect on the magnetic properties. Indeed, as discussed in Chapter 4, we did not observe a significant change due to strain of the magnetic anisotropy of the perpendicularly magnetized W/CoFeB/MgO system. Therefore, using materials with reduced magnetic anisotropy close to, so-called, spin-reorientation transition (SRT) is an alternative way to efficiently realize electric field-induced strain control of the magnetization. In systems close to the SRT, the magnetization easy axis is canted towards the in-plane direction (see Section 1.2.4), hence they promise to exhibit larger effects on the magnetization direction as the relative strain-induced anisotropy is larger compared to the PMA systems.

In this Chapter, we will first discuss the effect of piezoelectric strain on the magnetic domain structure of a PMA W/CoFeB/MgO thin film. While the system composition is similar to that considered in Chapters 4 and 5, the FM layer is thicker, which results in a slightly reduced effective magnetic anisotropy. Hence, we can expect the relative effect of the ME to be larger for this system. Furthermore, in this Chapter, we will discuss an additional effect on the magnetic state observed during the experiments with x-ray exposure: the x-ray irradiation induces an irreversible anisotropy change, leading to a local SRT. By comparing the observations on the PMA system with another PMA system, namely thin Pt/Ta/Pt/MgO/CoFeB/Ta film grown on a similar piezoelectric PMN-PT (011) substrate, which initially exhibits different magnetic properties but demonstrates the same behavior under irradiation, we will attempt to find the possible mechanisms of the x-ray induced behavior. Finally, making use of the x-ray induced anisotropy change we will demonstrate the electric field induced strain control of the magnetic domain structure across the region of varying magnetic anisotropy in the samples close to the SRT.

6.2 SAMPLES CONFIGURATION

The continuous films of W(5 nm)/$Co_{20}Fe_{60}B_{20}$(0.8 nm)/MgO(2 nm)/Ta(5 nm), referred to as *PMA sample*, and Pt(5 nm)/Ta(5 nm)/Pt(5 nm)/MgO(15 nm)/$Co_{20}Fe_{60}B_{20}$(1 nm)/Ta(3 nm), referred to as *inverted sample* in the text, were sputter-deposited on top of bare unpoled two-sides polished piezoelectric PMN-PT (011) substrates. The bottom contacts of Cr(5 nm)/Au(50 nm) was deposited by DC sputtering in an Ar atmosphere.

Parts of the experiments were carried out at the SIM beamline of the Swiss Light Source and at the UE49-PGM beamline of the Helmholtz-Zentrum Berlin. The samples were illuminated by a circularly polarized x-ray beam at $\alpha = 16°$ angle of incidence. For XMCD-PEEM imaging the photon energy was set to 708 eV and 710 eV corresponding to the Fe L_3 absorption peak for the PMA sample and the inverted sample, respectively. XMCD-PEEM images were obtained using the formula for the asymmetry $\frac{(I_+ - I_-)}{(I_+ + I_-)}$, which is proportional to $\cos\alpha$, where α is the angle between the directions of the incident circularly polarized x-rays and the film magnetization. $I_{+(-)}$ are the images acquired with circular positive (negative) polarization of the x-rays (see Section 2.3.2).

Prior to XMCD-PEEM imaging (see Section 2.3.2) of the PMA sample the top Ta capping layer was partially removed *in situ* by Ar^+ sputtering at the Ar pressure of 5×10^{-5} mbar inside the chamber and the energy of 1 kV for 30 minutes. Based on the sputtering rate calibrations, ca. 2 nm of Ta were removed which was sufficient to probe the underlying $Co_{20}Fe_{60}B_{20}$ layer without altering its magnetic properties. For the inverted sample this procedure was not necessary, as the Fe absorption edge was sufficiently intense (ca. 30%) to obtain a reasonable XMCD contrast.

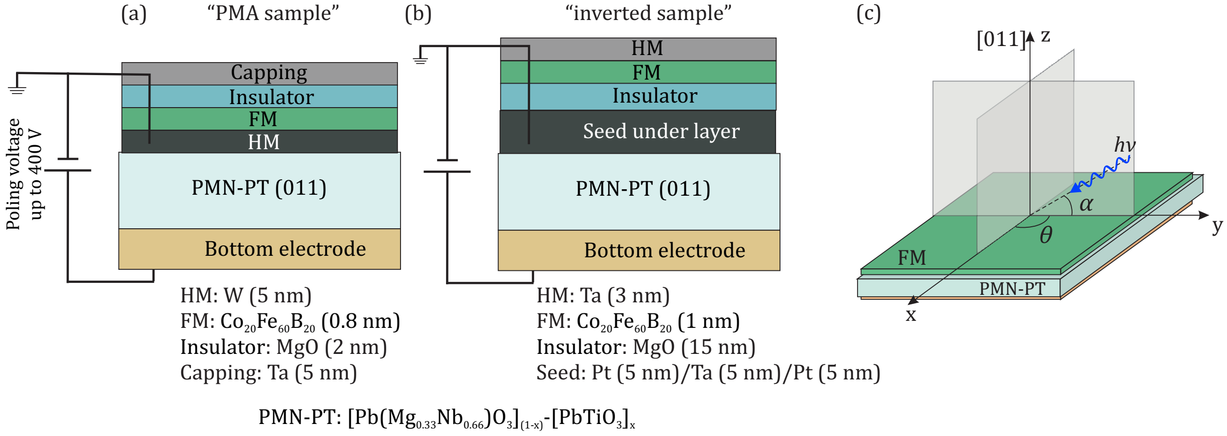

Figure 6.1: Schematics of the structure of (a) PMN-PT/W(5 nm)/$Co_{20}Fe_{60}B_{20}$(0.8 nm)/MgO(2 nm)/Ta(3 nm) ("PMA sample") and (b) PMN-PT/Pt(5 nm)/Ta(5 nm)/Pt(5 nm)/MgO(15 nm)/$Co_{20}Fe_{60}B_{20}$(1 nm)/Ta(3 nm) ("inverted sample"). (c) Schematic of the sample orientation relative to the incident x-ray beam in the XMCD-PEEM imaging experiment.

6.3 ELECTRIC FIELD INDUCED STRAIN MANIPULATION OF THE MAGNETIZATION IN THE PMA SAMPLE

Figure 6.2 (a) shows an OOP hysteresis loop by red markers for the PMA sample measured by polar-MOKE at zero electric field across the PMN-PT substrate. The hysteresis loop shown in black was measured under the electric field of 420 kV m^{-1} generating the IP uniaxial strain [114]. One can see that the shape of the macroscopic hysteresis loop does not qualitatively change upon the application of strain. A slight increase of the coercive field by approximately 0.30 ± 0.02 mT, i.e. only 3 % change, upon increasing the electric field can be observed as shown in the inset in Fig. 6.2 (a). The anisotropy constant for the PMA sample can be estimated as $K_{\mathrm{eff}} = \frac{\mu_0 H_{\mathrm{k}} M_{\mathrm{s}}}{2} = 0.277$ MJ m^{-3}, where the anisotropy field $\mu_0 H_{\mathrm{k}} = 0.5$ T and the saturation magnetization $M_{\mathrm{s}} = 1.11 \cdot 10^6$ A m^{-1} are extracted from the IP magnetic field sweep shown in Fig. 6.2 (b) measured by superconducting quantum interference device (SQUID) magnetometry. We can estimate the strain-induced ME anisotropy which amounts to ca. 2.2 kJ m^{-3}, using Eq. 1.26 and the parameters from the literature for $\lambda_s = 31$ ppm, $Y = 1.6 \cdot 10^{11}$ Pa [236]. Here, we use the total in-plane strain, $(\epsilon_{[100]} - \epsilon_{[01\bar{1}]}) \sim 0.03$ % [114] as the actual driving force to the ME effect [104, 237]. Thus, the ME anisotropy, being a few orders of magnitude smaller than the PMA anisotropy of the $Co_{20}Fe_{60}B_{20}$ film, is not sufficient to produce a significant macroscopic change of the magnetic properties, e.g. change of the hysteresis loop shape, detectable with

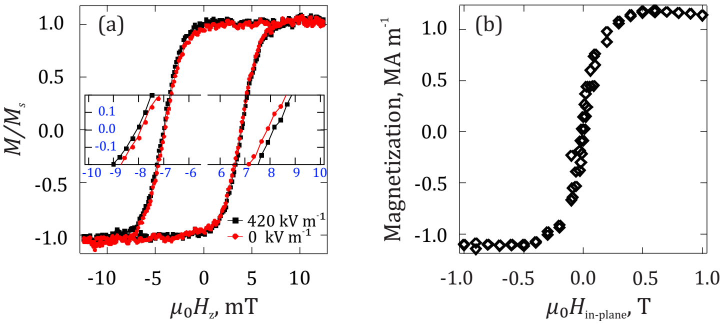

Figure 6.2: (a) Polar-MOKE hysteresis loops of the PMA sample measured at 0 kV m^{-1} (red) and 420 kV m^{-1} (black). Note, that the PMN-PT (011) substrate was poled before the measurements, ensuring the linear response of the generating strain to the applied electric field. The inset shows zoomed-in regions of the loops in the vicinity of the coercive field. (b) Hysteresis loop measured with the IP field sweep by SQUID.

MOKE. To generate a higher relative change in the anisotropy, the strains of a few percent are required, which can be achieved, for example, by mechanically bending the substrates [238].

However, this does not exclude that local changes of the magnetization can be generated, as previously demonstrated [239]. Fig. 6.3 shows a series of XMCD-PEEM images of the magnetic domain structure of the $Co_{20}Fe_{60}B_{20}$ film under an applied electric field of different magnitudes. Note, that the sample was demagnetized prior to imaging, which led to formation of the OOP stripe domains pattern.

One can see that upon poling, the domain structure remains largely unchanged, with only a small fraction of the magnetic domains switching. It is clear by comparing the images in Figs. 6.3 (a) and (b), that the switching is not deterministic, i.e. the switching from *up* to *down* as well as from *down* to *up* domains occurs when the electric field is increased from 0 kV m^{-1} to 400 kV m^{-1}. In Fig. 6.3 (d), we can also see that some parts of the domain structure switch reversibly, but the overall domain structure does not reverse to what it was at zero electric field in Fig. 6.3 (a).

We also note that the application of an electric field induced-strain does not lead to a reorientation of the magnetization from OOP to IP or *vice versa*, which would result in an additional black/white contrast level in the XMCD-PEEM images. Thus, the direct imaging results[1] suggest that the observed local changes are random and may occur due to strain-induced modification of the energy landscape. Furthermore, the local character of the observed modification of the

---

[1] Similar behavior was observed for a few other points on this sample as well as for other PMA films on PMN-PT substrates, e.g. PMN-PT(011)/W/$Co_{20}Fe_{60}B_{20}$(0.7)/MgO/Ta, PMN-PT(011)/Pt/Co/Pt.

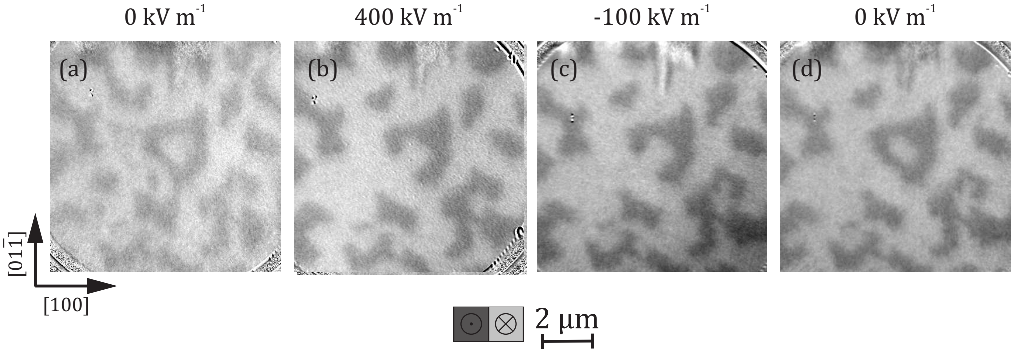

Figure 6.3: XMCD-PEEM images of the magnetic domain structure of the PMA sample measured at different magnitudes of the applied electric field within the linear regime of the strain response.

domains pattern may be attributed to the inhomogeneities of the generated strain typical for the PMN-PT substrates [104, 237]. On the other hand, the observation of some locally reversible changes of the domain structure due to the strain-assisted domain redistribution, agrees with the change in the coercive field seen in MOKE [239].

6.4 X-RAY INDUCED ANISOTROPY CHANGE

X-RAY INDUCED ANISOTROPY CHANGE OF THE PMA SAMPLE

As mentioned earlier, the electric field-induced strain has a negligible effect on the macroscopic magnetization of the PMA film. However, after several hours of XMCD-PEEM imaging of the PMA sample, we observed that the domain structure started to change, and eventually the OOP domains transformed into a completely different domain structure with a different contrast level. Fig. 6.4 (a) shows a zoomed-out XMCD-PEEM image acquired using a larger FOV after this transition. The yellow dashed line indicates the approximate edge of the area exposed by the x-rays during the previous measurement in the FOV 10 μm, for which a high spatial resolution was required (e.g. those shown in Fig. 6.3). For that, the x-ray beam size was reduced by the exit slit of the beamline so that the footprint of the beam on the sample surface was approximately 10×20 μm set by the instrument [240].

Thus, the area within the yellow line was exposed by the x-ray beam, and the outside area of the sample was not exposed. We see, that the unexposed region exhibits the same stripe domain structure, while the domain structure of the exposed area is dramatically different with

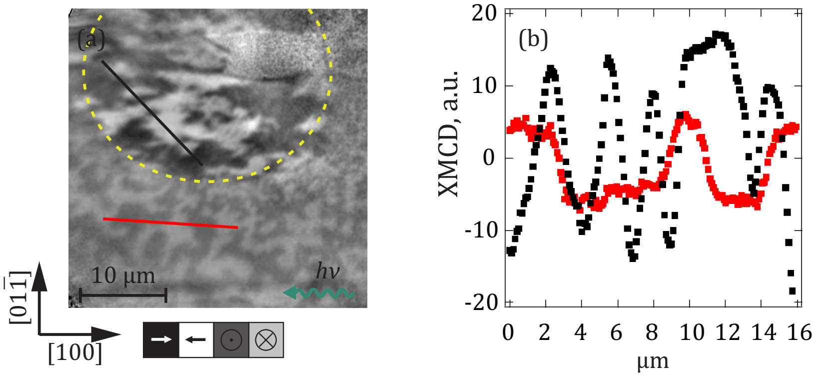

Figure 6.4: (a) XMCD-PEEM image using FOV of 50 μm after several hours of imaging in FOV of 10 μm showing the domains structure at zero applied electric field. (b) XMCD signal profiles along the black and red lines, showing that IP and OOP domains yield XMCD contrast of different magnitudes. The crystallographic directions of the PMN-PT substrate setting the tensile ([01$\bar{1}$]) and compressive ([100]) strain directions are indicated.

increased contrast. Therefore, we can conclude that the observed local change of the domain structure was caused by the long exposure by the x-ray beam [241].

The altered area has a noticeably different XMCD contrast level (with a much brighter/darker white/black domains) as compared to that of the OOP stripe domains. This indicates that the domains within the exposed area have a significant IP component, because the low angle of incidence of the x-ray beam leads to a stronger contrast for the IP orientated magnetization. Unfortunately, the additional images corresponding to different azimuthal angles necessary to extract the angular dependence of the XMCD contrast for these domains could not be acquired, thus, we cannot conclude about the exact magnetization direction, which could also be tilted between OOP and IP.

On the other hand there is a good agreement with the conclusion that the exposed area has IP magnetized domains from the quantitative comparison of the two XMCD contrast levels measured on the exposed and unexposed regions [see Fig. 6.4 (b)]. Because the angle of incidence of the x-ray beam is 16° from the surface plane the XMCD signal from the OOP domains should be a factor of $\tan 16°$smaller than that from the IP domains, when having the same amount of the spin moment to contribute [242]. Assuming the IP magnetization direction within the exposed area in Fig. 6.4 (a) is along the x-ray direction, we obtain the $\frac{I_{\text{OOP-XMCD}}}{I_{\text{IP-XMCD}}} \approx 0.27$, i.e. approximately $\tan 16°$, which makes this assumption reasonable.

Another interesting observation is the behavior of the stripe domains close to the exposed

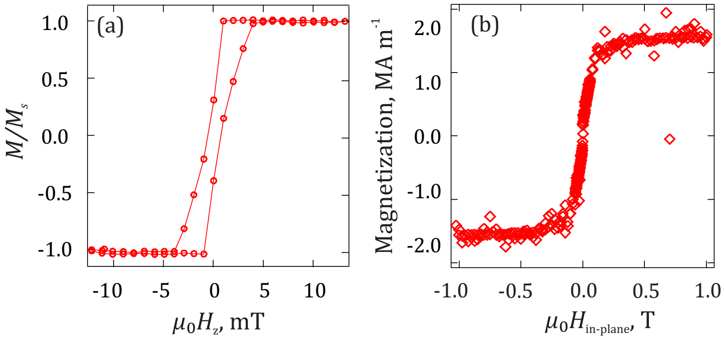

Figure 6.5: (a) Polar-MOKE hysteresis loops of the inverted sample. (b) Hysteresis loop measured with the IP field sweep by SQUID.

area. As seen from Fig. 6.4 (a), the average stripe domain size gradually decreases approaching the exposed area, where the magnetization lies in the plane. Similar patterns are known for thin wedge systems with a thickness gradient of the FM layer. For such systems, the average domain width decreases in the vicinity of a SRT, which is attributed to the the variation of the magnetic anisotropy across the thickness [243, 244, 245, 246]. As the effective magnetic anisotropy K_{eff} decreases with increasing thickness, the formation of domain walls becomes more favorable, because the domain wall energy scales with the anisotropy $\sigma_{\text{DW}} \sim \sqrt{AK_{\text{eff}}}$, which leads to the increasing number of domains of a smaller width [245, 246].

Based on the observed domain size behavior, we can conclude that, in our system, a spatially varying change of the magnetic anisotropy takes place. However, here the FM layer thickness is homogeneous, therefore a different mechanism needs to be considered, which clearly is induced by the x-ray irradiation.

X-RAY INDUCED ANISOTROPY CHANGE OF THE INVERTED SAMPLE

Before we go into discussion of the possible origins of the observed behavior, we check if the x-ray induced anisotropy change is limited to this stack or occurs more widely. For this, we consider a different PMA stack, namely Pt/Ta/Pt/MgO/$Co_{20}Fe_{60}B_{20}$/Ta, deposited on the PMN-PT (011) substrate. Here we also find a similar x-ray induced anisotropy change. Note that the order of the layers is inverted as compared to that of the previously discussed PMA system, thus we term this sample in the description below as “inverted”.

MOKE and SQUID magnetometry results, shown in Fig. 6.5 (a) and (b), respectively, reveal that in the inverted sample, the PMA is significantly reduced as compared to the Ta-based stacks with a conventional order of the layers [60], thus, it is already close to the SRT before the x-ray exposure.

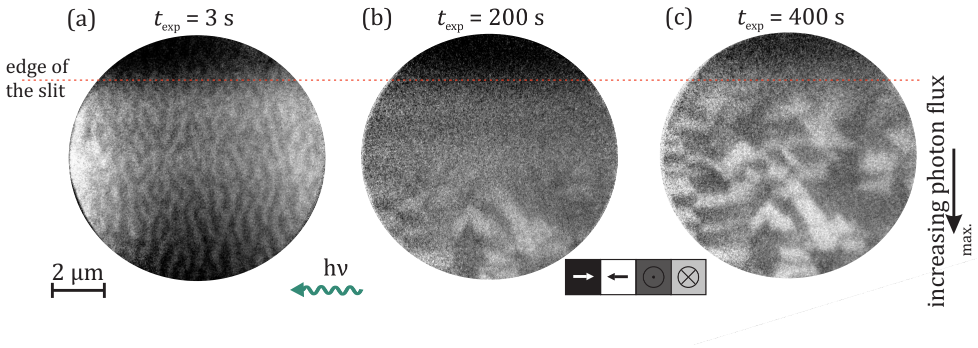

Figure 6.6: XMCD-PEEM imaging of domain structure of the inverted sample, acquired after different x-ray exposure times t_{exp}.

The domain structure of the inverted sample is shown in Fig. 6.6 (a), and resembles a regular stripe domain structure with an average domain size of 300 – 400 nm. With the x-ray exposure, the domain pattern disappears following the noticeable reduction of the stripe domain width. The former suggests that the domains become smaller than the accessible resolution of the instrument (ca. 90 nm in XMCD mode using a 20 μm FOV) or more mobile due to the thermal fluctuations and thus blurred [247].

The stripe domains disappear completely after ca. 20 s of the x-ray exposure, and after approximately 200 s a new domain structure, exhibiting a stronger XMCD contrast, starts to propagate from one edge of the FOV [Fig. 6.6 (b)]. Note that the x-ray beam was intentionally put off the center of the FOV, thus, leading to a photon flux gradient. Switching off the x-rays for some time did not lead to recovery of the initial stripe domain phase, suggesting the same irreversible character of the x-ray induced changes of the magnetic properties, as discussed above for the PMA sample studied first.

In 6.6 (b) it is also possible to see that the new domains start propagating from one side of the image, where the maximum of the x-ray beam intensity is (the beam was intentionally put off center). This suggests that the x-ray flux indeed governs the process. The switching occurs more readily at higher intensity of x-rays and then propagates to the edges of the beam, where the flux drops strongly.

We also note that in this case the resulting domain structure formed with the time of the x-ray exposure clearly resembles the ferroelectric domain structure of the PMN-PT substrate known from literature [114]. Also, similarly to the PMA system, the new domains here appear only bright or dark, with no noticeable contribution of gray domains (with the magnetization perpendicular to the x-rays propagation direction). Thus, the switched area exhibits an easy axis along the x-ray direction or along one of the crystallographic axes of the cubic PMN-PT substrate.

6.5 POSSIBLE ORIGINS OF X-RAY INDUCED ANISOTROPY MODIFICATION

It is known that x-ray irradiation can alter the charge and orbital states of strongly correlated systems [248, 249, 250] and perturb the bonds of soft materials [251]. However, the materials studied here are expected to be neither of these. On the other hand, it is also known from literature that high-energy x-rays and secondary electrons generated due to the photoeffect have a strong effect on insulating materials, which compose a significant part of the systems discussed in this work (PMN-PT substrates and MgO layers are insulating). The processes which are expected to be responsible for the x-ray induced damage, can be classified as follows: (*i*) the ones which occur during the transport of the exited electrons in the material and (*ii*) those, due to the electrons emission into the vacuum.

For the former, it was shown that the core electrons/holes excited by x-rays can scatter with ions in the insulating oxide-containing layer, which leads to breaking of the bonds and subsequent creation of structural defects, especially oxygen vacancies [252]. The latter leads to local charging of the irradiated area, because many electrons are emitted into vacuum. While in conductive materials the lack of electrons is compensated within a few picoseconds [253], in the case of insulating materials, the recombination rate is strongly suppressed. Thus, the resulting uncompensated electric field can drive the migration of the mobile ions in the sample [254, 255]. Moreover, the ion desorption cannot be neglected when the electric field strength is large and the electrons coming from the surroundings cannot compensate for the emission of the electrons in order to reach a stable electrostatic equilibrium [255]. On top of this, according to previous studies, also the local heating due to the deposited energy by x-rays leads to an enhanced drift and diffusion of oxygen within the system [256].

The aforementioned processes could be relevant for our systems because the magnetic anisotropy in these stacks, originating from both interfaces of the magnetic $Co_{20}Fe_{60}B_{20}$ layer, is determined by the surrounding of the magnetic atoms. As discussed in Chapter 1, the origin of the interfacial PMA in the FM/MgO interface is partially attributed to the interfacial symmetry breaking and the hybridization between Fe(Co) $3d$ and O $2p$ orbitals [66, 257]. On the other hand, the contribution from the HM to the PMA of the studied stack is due to hybridizations of both d and p orbitals at the interface via SOC [65, 68].

Moreover, recent studies reported on VCMA, which is realized when a voltage is applied across a thin oxide/FM interface [18]. This leads to a charge redistribution between the OOP and IP orbital of the FM, resulting in the change of the surface magnetic anisotropy [257, 18].

Thus, taking these facts into account, we can expect that any structural or electronic change in the vicinity of the two $Co_{20}Fe_{60}B_{20}$ interfaces due to the x-ray exposure can alter the magnetic anisotropy of the system, resulting in a change of the domain structure. Now we can go through the arguments, that allow us to rule out certain scenarios seemingly responsible for the observed behavior of our systems.

(*i*) Based on the shapes of the Fe and Co absorption peaks shown in Fig. 6.7, which were measured on the exposed area after its OOP-IP transition, we can exclude significant oxygen implantation into the $Co_{20}Fe_{60}B_{20}$ layer. In the case of Fe or Co oxidation a typical oxide shoulder feature would appear in the corresponding peaks. However, the spectra in Fig. 6.7 (a) do not indicate any formation of an iron oxide peak in the PMA system. Only a slight change in the intensity is observed, which can be attributed to the carbon deposition due to x-ray induced contamination [258]. Presented in Fig. 6.7 (b), Fe and Co absorption edges of the inverted system, corresponding to the switched area,[2] also do not exhibit oxide features.

(*ii*) As a result of the irradiation-induced ion migration, oxygen ions could also leave the MgO layer and diffuse into the adjacent non-magnetic metallic layer (for example, Ta for the PMA sample).[3] It is important to note, however, that a nominally similar stack to that used for the inverted sample, grown on a conducting Si substrate with only a thin natural SiO_2 layer, did not show any x-ray induced damage/change within a few days of exposure with similar photon flux. This suggests that an insulating PMN-PT substrate, which also has plenty of oxygen indeed plays a role in the irradiation-induced change. On the other hand, this scenario could explain the local change of the anisotropy in the PMA sample.

(*iii*) It is important to keep in mind that during PEEM imaging, the sample surface is always electrically grounded [Figs. 6.1 (a) and (b)]. To ensure a good electrical contact, the multilayer stack containing an insulating MgO layer, is scratched at the sides and a drop of conducting silver paste is used to attach the sample to the sample holder body (local ground of the microscope). Therefore, all of the metallic layers on top of PMN-PT are expected to be on the same (ground) potential. Thus, the excess of positive charge due to emission of secondary electrons, can potentially be easily compensated by the conduction electrons from the metallic layers.

Below we summarize the observations discussed above, which, however, did not bring us to

---

[2] The SRT occurs much faster (ca. 20 s) than the time necessary to acquire one x-ray absorption spectrum (XAS) (ca. 5 min).

[3] The absorption peak of Mg after the SRT was not measured.

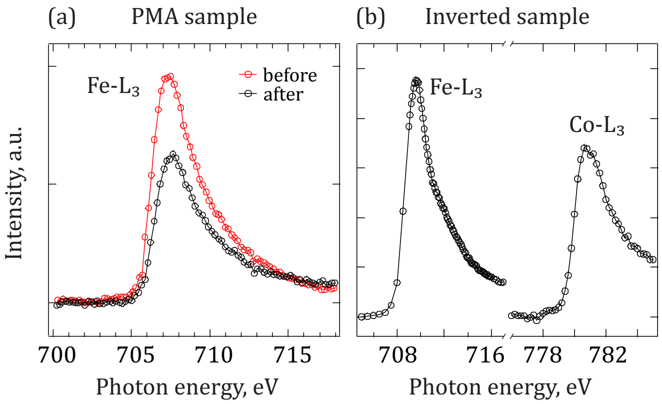

Figure 6.7: (a) XAS corresponding to the Fe L_3 absorption edge measured on the damaged area for the PMA sample before and after the x-ray induced SRT. (b) XAS for Fe and Co measured for the inverted sample after the exposure that leads to the reorientation of the magnetization in to the plane.

a conclusive understanding of the mechanisms underlying the x-ray induced OOP to IP reorientation:

- The x-ray induced anisotropy modulation starts from the area with a higher photon flux;
- The anisotropy change occurs on different time scales for the PMA sample (with higher PMA) and for the inverted sample (with canted magnetization) for a comparable photon flux;
- Induced IP domains have a magnetic easy axis along x-rays or crystallographic directions of the PMN-PT substrate. Note that circularly polarized light was used, i.e. no defined electric field direction could be imposed on the domain structure;
- A gradual change of the domain structure is observed indicating a gradual change of the anisotropy;
- Fe, Co peaks do not have features typical for oxides;
- Demagnetization of the samples by cycling an external magnetic field does not help to recover the stripe domain phase, signifying a permanent structural character of the x-ray induced changes;
- For the inverted stack grown on Si/SiO_2 substrate the x-ray induced change of the domain structure does not occur within (at least) 3 days of exposure.

Despite the argument that the sample surface is always grounded, the most plausible mechanism of the x-ray induced anisotropy change in our system relies on local charging due to the lack of electrons and the inability of thin conductive layer to compensate for this. This charging, leading either to the displacement of ions as well as local charge redistribution on the orbitals at the $Co_{20}Fe_{60}B_{20}$ interface which determine the magnetic anisotropy of the systems, results in the decrease of the PMA and the associated with it OOP to IP transition.

6.6 STRAIN INDUCED CHANGES OF THE DOMAIN STRUCTURE CLOSE TO THE SRT

In this section, we consider again the PMA sample, where we can take advantage of the modified magnetic anisotropy by the x-ray exposure to be sensitive to small strain-induced anisotropy change. The irradiated areas allow us to simultaneously investigate the impact of strain on the domain structure at the regions with different magnetic anisotropies, from IP to OOP. As discussed above, the electric field induced strain does not influence the OOP domain structure. However, as in the region close to the SRT the magnetization is canted from the OOP direction, a larger effect of strain on the domain structure can be expected. It is important to note that while the absolute strain-induced anisotropy change is the same, close to the SRT, where the effective anisotropy is low, the relative effect on the magnetization alignment is larger.

Figure 6.8 shows a series of XMCD-PEEM images of the area close to the SRT, including the OOP and IP magnetized regions. We can see that the entire IP region changes contrast from black/white to gray, while the OOP region remains the same. The observed change is mostly reversible and volatile, i.e. when the electric field is removed, the domain structure changes again, but with a new distribution of the domains. While the individual domains do not switch to the original state after removing the electric field, the magnetic anisotropy favoring black and white IP domain recovers.

We also note that the border between the IP and the OOP magnetized regions at 0 kV m^{-1} shifts by a few μm after the first electric field cycle (0-400-0 kV m^{-1}). But it stays nearly at the same place after the second field cycle (0-500-0 kV m^{-1}). However, it is not straightforward to conclude whether this is induced by strain or by the x-ray exposure.

To analyze in more detail the character of the strain induced switching observed in the IP region, we quantitatively consider the change of the XMCD contrast of the individual domains. The results are summarized in Fig. 6.9 (a), where the XMCD contrast as a function of the cycling electric field is plotted for several areas. The value of the XMCD contrast was calculated as the

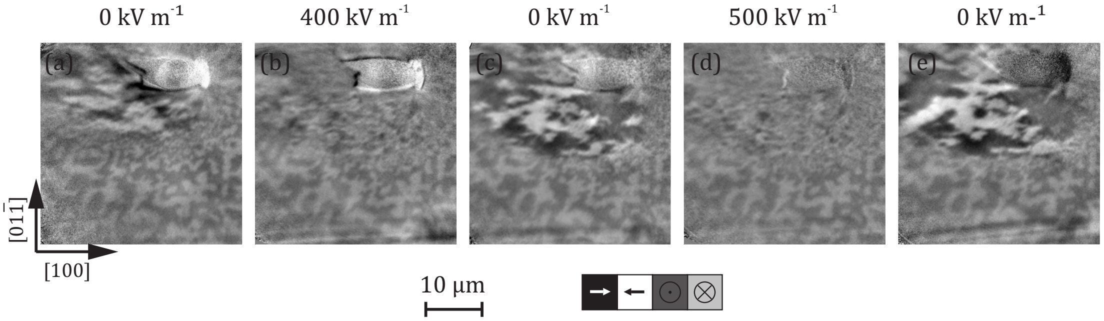

Figure 6.8: Set of XMCD-PEEM figures of the domain structure of the PMA sample, where part of the FOV underwent a SRT due to the x-ray exposure, acquired at different magnitudes of the applied electric field. The crystallographic directions of the PMN-PT substrate setting the tensile ([01$\bar{1}$]) and compressive ([100]) strain directions are indicated.

average over a selected area corresponding to one domain.[4]

Here we can see that at least five distinct states can be differentiated from the contrast, which are shown shaded in Fig. 6.9 (a), i.e. IP-white, IP-black, OOP-bright, OOP-dark and IP-gray. The latter corresponds to the domains with the magnetization perpendicular to the x-ray direction, which yields zero XMCD contrast.

In Fig. 6.9, we can observe random switching of the IP domains to OOP (corresponding to IP-white to OOP-bright switching events) or 90° rotation of the IP domains (corresponding to IP-white to IP-gray switching events) in the regions in the vicinity of the domain walls. On the other hand, it can be seen that the magnetization in the middle of a domain at 0 kV m^{-1} (e.g. region “3”), is likely to remain not switched upon application of strain. This may be an indication of the inhomogeneities within the irradiated area, i.e. local pinning sites or inhomogeneous strain [104, 237], leading to locally varying magnetic anisotropy. Thus, for some domains the generated ME anisotropy is enough to alter the magnetization state, while it is not for the others.

Moreover, the global behavior of the domain structure within the irradiated area, i.e. where the PMA is strongly suppressed, is consistent with behavior governed by the ME effect. As the initial state at zero strain (i.e. 0 kV m^{-1}) is mostly IP magnetized, the application of compressive strain upon increasing the electric field leads to canting of the magnetization of the $Co_{20}Fe_{60}B_{20}$ layer with a positive magnetostriction coefficient to the OOP direction (or its 90° rotation in-plane towards the tensile direction). Thus, the domain structure at 400 kV m^{-1} and 550 kV m^{-1}

---

[4] Within these areas the mean deviations were not greater than 10%, thus ensuring the pixels belong to the same domain at each electric field.

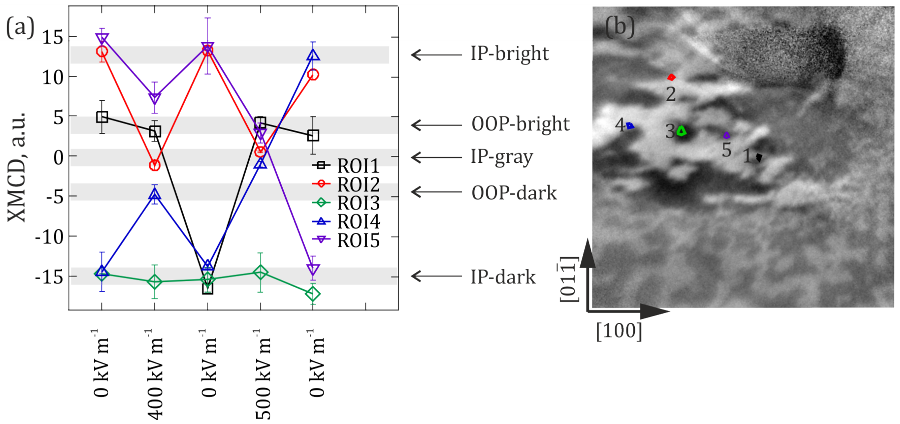

Figure 6.9: (a) XMCD contrast of the selected regions entailed by the magnetic domains of the PMA sample, showing the strain induced switching between five possible magnetization directions. (b) XMCD-PEEM image showing the analyzed in (a) regions.

[Figs. 6.8 (b) and (d)] looks mostly gray with either small OOP domains or IP domains with the magnetization perpendicular to the x-ray direction.

We also note, that unfortunately, due to small size of the irradiated area demonstrating the SRT, we could not find the same spot in MOKE to study directly the impact of the strain on the magnetic anisotropy by corresponding magnetometry measurements.

In conclusion, while the small impact of stain on the macroscopic perpendicular magnetic state of the PMA sample measured by the hysteresis loop is not surprising, the x-ray induced modulation of the magnetic anisotropy observed for both the PMA sample and the inverted sample, is unexpected. As a result of this irreversible effect of the x-ray exposure, the domain structure of the irradiated region of the PMA sample indicates that the effective magnetic anisotropy of the system gradually changes from easy perpendicular axis to easy in-plane with the strongest effect in the region exposed to the highest photon flux. On the contrary, we find that the magnetic anisotropy of the unexposed area remains unchanged. The attempt to explain this spatially inhomogeneous magnetic anisotropy variation, clearly induced by the x-ray irradiation, does not allow us to conclude on a clear mechanism. However, the resulting gradient of the magnetic anisotropy on such a small length scale allows us to observe the effect of the strain induced ME anisotropy on the magnetic domain structure, where the strain-induced K_{ME} comparable to the effective anisotropy of the film is able to alter its magnetization state.

The results presented in this Chapter are submitted for publication.

CHAPTER
7

CONCLUSIONS

In this thesis, we study the effects of piezoelectric strain in various systems, all of which may find their applications in future generations of spintronics devices. The piezoelectric strain is a very attractive tool as it can potentially be used in the nanoscale, where, for example, bending mechanisms for the generation of mechanical strain cannot be employed. Of added benefit is that this approach avoids using energy-dissipative charge currents, instead, utilizing low-power electric fields applied across the piezoelectric to reliably control the generated strain. Furthermore, among other strategies employing electric fields, e.g. voltage-control magnetic anisotropy, using piezoelectric strain is more advantageous, as it does not require the systems to contain an insulating layer.

In this work, we demonstrate that the effect of strain in in-plane magnetized systems is via magneto-elastic anisotropy. In these systems, it leads to a sizeable change of the static in-plane domain structure as discussed for the case of magnetic vortices fabricated on top of a piezoelectric substrate. The key finding of the presented study is that electrically induced and controlled strain allows one to tune not only the static magnetic configuration of magnetic vortices, but also the magnetodynamic response to the microwave excitation: the gyrotropic eigenfrequency of the microstructures and the shape of the vortex core gyration orbit. The two underlying mechanisms responsible for the observed modifications are the change in the resonance frequency and the change in the domain configuration, both resulting from the modification of the potential landscape due to the induced anisotropy. We find that the magnetization dynamics behavior observed in the experiment is in good qualitative agreement with the micromagnetic simulations, where the effect of piezoelectric strain was modeled by an additional uniaxial anisotropy term.

Our results show that this approach provides an energy-efficient tool to fully electrically control magnetic vortex dynamics which is a key asset for future vortex applications in microwave devices. For example, since the eigenfrequency of a vortex can be locally tuned by using the electric field-induced strain, this approach may enable selective switching of the vortices within an array for which the gyration eigenfrequency was tuned accordingly to match the frequency of the global excitation field.

Another important result of this thesis is that the strain leads to sizable change of the magnetic properties of the system, e.g. the magnetic domain structure if the induced magnetoelastic anisotropy is comparable with the effective anisotropy. This we find by the direct imaging of the modification of the magnetic domain structure by strain in the region with the gradient of the magnetic anisotropy.

Furthermore, we discuss the impact of piezoelectric strain in a perpendicularly magnetized W/CoFeB/MgO multilayer where the relative contribution of the strain-induced magnetoelastic anisotropy is small and does not significantly change the magnetic state. In this thesis, we show for the first time experimentally that the magnitude of the spin-orbit torques (SOTs) and Dzyaloshinskii-Moriya interaction (DMI), naturally occurring in this W/CoFeB/MgO system, can be tuned by the electric field-induced strain.

Specifically, the tensile strain enhances the amplitude of the damping-like torque, while the compressive strain leads to its decrease. This means that one can not only dynamically tune the torques but reach even higher torques than possible at zero strain. We explain our experimental findings by theoretical band structure calculations, the detailed analysis of which reveals that the strain modifies the symmetry and orbital polarization of the electronic states participating in the hybridization at the ferromagnet/heavy metal interface. This imprints uniquely on the nature of SOTs thus allowing us to reproduce our experimental findings.

The strain response of the DMI in W/CoFeB/MgO on the piezoelectric strain demonstrates a monotonic decrease with the increasing magnitude of the strain of both characters. Furthermore, the estimated efficiency of the electric field control of the DMI is found to be much larger than that, reported for the DMI control by gate voltage in typical oxide-based systems. While the analysis of the microscopic origin of the observed strain response of the DMI is required to understand the complex behavior of this spin-orbit driven phenomenon, our theoretical insights already suggest that the possibility to control and engineer the DMI in perpendicularly magnetized systems by means of electric fields.

We, thus, show that the electric field induced strain can be used to control the magnitudes of SOTs and DMI in a system on demand and even increase their amplitudes. By employing various local strain configurations, thus locally tuning these phenomena in a ferromagnetic element, it could be possible to design novel device architectures.

Finally, this thesis reports an unexpected finding, yet particularly relevant for the field of spintronics, where magnetic structures are often investigated by means of x-ray based techniques. We discuss the effect of the x-ray irradiation on the magnetic states of two perpendicularly magnetized thin films grown on piezoelectric substrates and its possible origins. Thus, our finding shows that one needs to take care when analyzing anisotropies in the experiments involving extensive x-ray exposure. In conclusion, the results of this thesis demonstrate the energy-efficient control of the static and dynamic properties of magnetic structures at the nanoscale and advance our fundamental understanding of the underlying mechanisms, thus, providing promise for application of these ideas in the future generation of spintronic devices.

APPENDIX A

SAMPLE FABRICATION DETAILS

A.1 FABRICATION OF NI MICROSTRUCTURES

The investigated in Chapter 3 samples were fabricated within two-steps of EBL followed by metal deposition and a lift-off process. The detailed run sheet is given in Table A.1.

As the first step a CPW was fabricated on top of a bare one-side polished piezoelectric PMN-PT (011) substrate. Prior to the lithographical exposure, a bilayer of methyl-methacrylate (MMA) and poly-methyl-methacrylate (PMMA) was spun. To minimize charging effects during the lithographical exposure of the insulating substrate, a layer of conductive resist (e-spacer) was additionally spun on top of the bilayer resist. The lithographical exposure was carried out with a Raith Pioneer electron beam writer, employing the parameters given under *Step I* in Table A.1. The schematic of the pattern used to fabricate the CPW is shown in Fig. A.1 (a). The WF of 2 × 2 mm was used in order to speed up the fabrication process. Each WF contained four alignment markers in the pattern. After the exposure the e-spacer was removed by immersion in water and the resist was developed by immersion in a solution of methylisobutylketone (MIBK) 1:3 in isopropanol (IPA) followed by immersion in pure IPA.

The 50 nm thick Au films were deposited by DC sputtering on top of a 5 nm thick Cr undedrlayer sputtered prior to that for a better adhesion. The bottom contact of Cr(5 nm)/Au(50 nm) was sputtered on the back side of the substrate before the EBL structuring. The films were sputtered in a dedicated sputtering chamber with a base pressure $< 2 \times 10^{-7}$ mbar. After the deposition the films were lifted-off by removing the unnecessary unexposed resist along with the metal film on top of it by immersion in pure acetone (ACE).

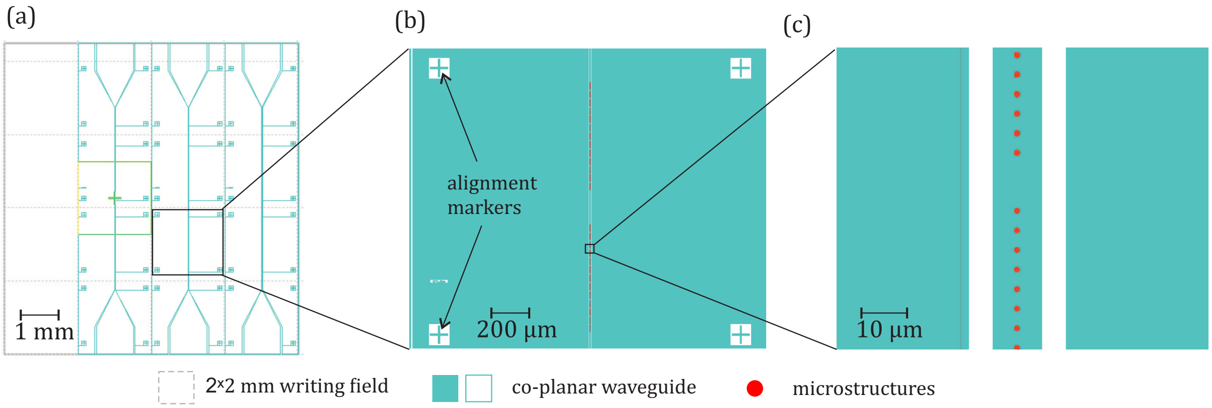

Figure A.1: (a) EBL pattern of CPWs showing 2 × 2 mm WFs, each containing 4 alignment markers. (b), (c) Incrementally zoomed-in images of the EBL pattern showing the strip line, alignment markers and microstructures (red).

As the second step Ni microstructures of various lateral dimensions in the range of 0.8 – 1.2 μm were fabricated on top of the Au stripline (Fig. A.1 (b,c)) following the same patterning procedure, described above. A layer to layer WF alignment was carried out before the e-beam exposure to ensure the Ni microstructures were placed on top of the stripline. The e-beam exposure was carried out using the parameters given under *Step II* in Table A.1. The 50 nm thick Ni film was then sputter-deposited followed by the lift-off process in pure ACE. The Ni film was deposited at a Singulus Rotaris commercial sputtering cluster with a base pressure $< 3 \times 10^{-8}$ mbar.

Table A.1: Full run sheet of the fabrication process of Ni microstructures on top of a CPW.

Process	**Description**	**Equipment**	**Parameters**	**Remark**
Substrate cleaning	ACE	Wet bench	60 s	
	IPA	Wet bench	60 s	
	N_2 blow dry	Wet bench	10 s	
Step I				
Spin coating	MMA	Spin coater	Prespin: 2 s @ 500 rpm, acc.: 500, spin: 60 s @ 3000 rpm, acc.: 3000	MMA (8.5) MAA EL6
	Soft bake	Hot plate	90 s @ 180 °C	

	PMMA	Spin coater	Prespin: 2 s @ 500 rpm, acc.: 500, spin: 60 s @ 3000 rpm, acc.: 3000	PMMA 950k A4%
	Soft bake	Hot plate	90 s @ 180 °C	
	e-spacer	Spin coater	Spin: 60 s @ 2000 rpm, acc.: 250	
EBL		Raith Pioneer	En.: 20 keV, app.: 60 μA, dose: 160 μC cm^{-2}, WF: 2 mm×2 mm	CPW patterning
Development	H_2O	Wet bench	30 s	Removing e-spacer
	MIBK	Wet bench	45 s	MIBK 1:3 IPA
	IPA	Wet bench	30 s	
Deposition		Sputter chamber	Cr: 5 nm, Au: 50 nm Ar pressure: 5×10^{-2} mbar	Base pressure: $< 2 \times 10^{-7}$ mbar
Lift-off	ACE	Wet bench		
cleaning	IPA	Wet bench	60 s	
	N_2 blow dry	Wet bench	10 s	
Step II				
Spin coating	MMA	Spin coater	Prespin: 2 s @ 500 rpm, acc.: 500, spin: 60 s @ 3000 rpm, acc.: 3000	MMA (8.5) MAA EL6
	Soft bake	Hot plate	90 s @ 180 °C	
	PMMA	Spin coater	Prespin: 2 s @ 500 rpm, acc.: 500, spin: 60 s @ 3000 rpm, acc.: 3000	PMMA 950k A4%
	Soft bake	Hot plate	90 s @ 180 °C	
	e-spacer	Spin coater	Spin: 60 s @ 2000 rpm, acc.: 250	
EBL		Raith Pioneer	En.: 10 keV, app.: 10 μA, dose: 160 μC cm^{-2}, WF: 2 mm×2 mm	Microstructures
Development	H_2O	Wet bench	30 s	Removing e-spacer
	MIBK	Wet bench	45 s	MIBK 1:3 IPA

	IPA	Wet bench	30 s	
Deposition		Singulus Rotaris	Ni: 50 nm	Base pressure: $< 3 \times 10^{-8}$ mbar
Lift-off	ACE	Wet bench		
cleaning	IPA N_2 blow dry	Wet bench Wet bench	60 s 10 s	

A.2 Fabrication of W/CoFeB/MgO/Ta Hall bar devices

The investigated in Chapter 4 samples were fabricated within three steps of EBL following the sputter-deposition of a continuous film of W(5)/$Co_{20}Fe_{60}B_{20}$(0.6)/MgO(2)/Ta(5) on top of a bare unpoled two-sides polished piezoelectric PMN-PT (011) substrate in a Singulus Rotaris commercial sputtering cluster with the base pressure $< 3 \times 10^{-8}$ mbar. All thicknesses in parentheses are in nm. The detailed run sheet is given in Table A.2.

As the first step of the EBL process, a set of alignment markers was fabricated on top of a continuous film, see Fig. A.2 (a). As a result, the surface was covered by an array of 1 × 1 mm WF each containing 4 coarse and 4 fine alignment markers. Prior to the exposure a MMA/PMMA bilayer resist was spun. The e-spacer on top of the bilayer resist was used as well for this step. The EBL was carried out and the resist was then developed using the parameters given under *Step I* in Table A.2.

The 30 nm thick Au film was deposited by DC sputtering in Ar atmosphere. For better adhesion a 5 nm thick Cr underlayer was sputtered prior to that. The bottom contact of Cr(5 nm)/Au(50 nm) was sputtered on the back side of the substrate before the EBL structuring. After the deposition the films were lifted-off by immersion in pure ACE.

This step was a necessary preparation for the third step during which the pattern for metallic contacts to the Hall-cross was fabricated. The third step requires the pattern to be aligned precisely with the existing pattern on the sample surface. Such alignment is best achieved by using an automatic WF alignment procedure. During this alignment procedure, the software scans the markers withing the writing field to determine their position, so that eventually the patterns match. However, the W/CoFeB/MgO/Ta metallic film is very thin and the metals themselves do not exhibit a particularly large electron yield. Hence, the automatic alignment procedure fails, if the alignment markers are made of the W/CoFeB/MgO/Ta film. On the contrary, Au is characterized by a better electron yield, therefore having the alignment markers made of Au simplifies the fabrication process and provides a much better precision during the WF alignment.

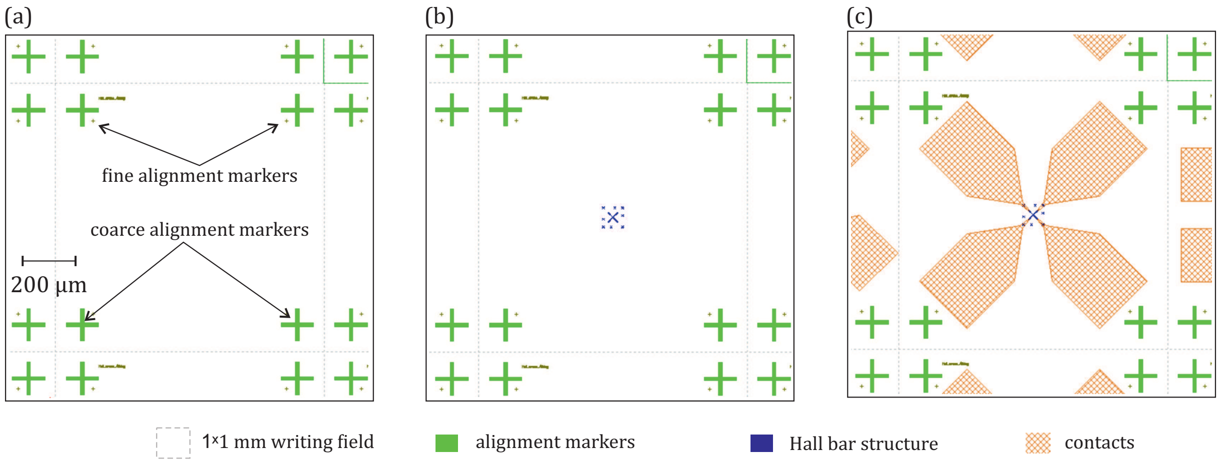

Figure A.2: Subsequent EBL steps during the fabrication of (a) alignment markers, (b) Hall-cross structures and (c) Au contacts.

As the second step, Hall-cross devices were fabricated at the center of each WF using a negative resist AR-N 7520.073 and an e-spacer layer. The Hall-cross mask was aligned to the exiting Au alignment markers by an automatic alignment procedure. The exposure was carried out using the parameters given under *Step II* in Table A.2.

The resist development was followed by the Ar ion milling in the IBE tool to remove the uncovered part of the material stack down to the PMN-PT substrate. To check that all unnecessary material was removed, we checked that the sheet resistance of the PMN-PT substrate, not covered by the microstructures, was unmeasurable with a multimeter. After the milling process, the rest of the resist was removed by immersion in pure ACE for several hours.

During the third step, metallic contacts to the Hall crosses as well as the top electrodes for the piezoelectric substrate, as seen in Fig. A.2 (c) were fabricated. For the exposure, the MMA/PMMA bilayer resist was used and developed following the same recipe used in the first step. The details of e-beam exposure and the subsequent resist development are given under *Step III* in Table A.2. Note that due to charging effects it was not possible to use a larger aperture, to speed up the process. Because for larger currents, the charging would quickly lead to a degradation of the resist[1] and the WF alignment procedure would fail.

After the exposure and the resist development using the standard e-spacer+MMA/PMMA protocol, the Cr(5 nm)/Au(90 nm) films were sputter deposited followed by a lift-off in pure

---

[1] The degradation in this context is overexposure of the resist. As a result, the image around the alignment marker becomes distorted and its line profile of the intensity, as analyzed within the automatic WF alignment procedure, can no longer be detected.

ACE.

Table A.2: Full run sheet of the fabrication process of Hall bar devices.

Process	**Description**	**Equipment**	**Parameters**	**Remark**
Substrate cleaning	ACE	Wet bench	60 s	
	IPA	Wet bench	60 s	
	N_2 blow dry	Wet bench	10 s	
Step I				
Deposition		Singulus Rotaris	W: 5 nm, $Co_{20}Fe_{60}B_{20}$: 0.6 nm, MgO: 2 nm, Ta: 5 nm	
Spin coating	MMA	Spin coater	Prespin: 2 s @ 500 rpm, acc.: 500, spin: 60 s @ 3000 rpm, acc.: 3000	MMA (8.5) MAA EL6
	Soft bake	Hot plate	90 s @ 180 °C	
	PMMA	Spin coater	Prespin: 2 s @ 500 rpm, acc.: 500, spin: 60 s @ 3000 rpm, acc.: 3000	PMMA 950k A4%
	Soft bake	Hot plate	90 s @ 180 °C	
	e-spacer	Spin coater	Spin: 60 s @ 2000 rpm, acc.: 250	
EBL		Raith Pioneer	En.: 10 keV, app.: 30 μA, dose: 160 μC cm^{-2} (for coarse markers) and 360 μC cm^{-2} (for fine markers), WF: 1 mm×1 mm	Alignment markers
Development	H_2O	Wet bench	30 s	Removing e-spacer
	MIBK	Wet bench	45 s	MIBK 1:3 IPA
	IPA	Wet bench	30 s	
Deposition		Sputter chamber	Cr: 5 nm, Au: 30 nm Ar pressure: 5×10^{-2} mbar	Base pressure: $< 2 \times 10^{-7}$ mbar
Lift-off	ACE	Wet bench		

cleaning	IPA N_2 blow dry	Wet bench Wet bench	60 s 10 s	
Step II				
Spin coating	AR-N 7520.073 Soft bake e-spacer	Spin coater Hot plate Spin coater	Prespin: 2 s @ 500 rpm, acc.: 500, spin: 60 s @ 4000 rpm, acc.: 4000 60 s @ 85 °C Spin: 60 s @ 2000 rpm, acc.: 250	
EBL		Raith Pioneer	En.: 10 keV, app.: 30 μA, dose: 130 μC cm^{-2}, WF: 1 mm×1 mm	Hall bars
Development	H_2O AR-300 H_2O	Wet bench Wet bench Wet bench	30 s 30 s 30 s	Removing e-spacer AR-300 1:4 H_2O
Etching		IBE Ionsys500	MW gen.: 250 W, beam: 300 V, acc.: 200 V, neutr.: 100 mA	3.5 min @ 90°, 30 rpm
Resist leftovers removal	ACE	Wet bench	5 hours - 1 day	Resist removal by gently wiping in ACE. Visual check in optical microscope
cleaning	IPA N_2 blow dry	Wet bench Wet bench	60 s 10 s	
Step III				
Spin coating	MMA Soft bake	Wet bench Hot plate	Prespin: 2 s @ 500 rpm, acc.: 500, spin: 60 s @ 3000 rpm, acc.: 3000 90 s @ 180 °C	MMA (8.5) MAA EL6

	PMMA	Wet bench	Prespin: 2 s @ 500 rpm, acc.: 500, spin: 60 s @ 3000 rpm, acc.: 3000	PMMA 950k A4%
	Soft bake	Hot plate	90 s @ 180 °C	
	e-spacer	Spin coater	Spin: 60 s @ 2000 rpm, acc.: 250	
EBL		Raith Pioneer	En.: 10 keV, app.: 30 μA, dose: 160 μC cm^{-2}, WF: 1μm×1μm	Contacts
Development	H_2O	Wet bench	30 s	Removing e-spacer
	MIBK	Wet bench	45 s	MIBK 1:3 IPA
	IPA	Wet bench	30 s	
Deposition		Sputter chamber	Cr: 5 nm, Au: 90 nm Ar pressure: 5×10^{-2} mbar	Base pressure: $< 2 \times 10^{-7}$ mbar
Lift-off	ACE	Wet bench		
cleaning	IPA	Wet bench	60 s	
	N_2 blow dry	Wet bench	10 s	

APPENDIX B

MICROMAGNETIC SIMULATIONS

MICROMAGNETIC SIMULATIONS

Micromagnetic simulations are an important tool to describe and investigate the dynamics of magnetic systems [259, 98]. This type of numerical calculation solves iteratively the LLG equation, introduced in Chapter 1, by calculating the effective fields due to the existing magnetization pattern and an external influence. Here we will give a short summary of what micromagnetic simulations are.

Initialization. The sketch in Fig. B.1 shows a protocol of a micromagnetic solver. The program starts with the initialization of the simulation space (the spatial properties of the region of interest, discretization, and the solver routine) in which the simulation of a system will be performed. Usually, the space is discretized by equidistant cells of a certain volume. On this mesh, it is then possible to define a sample geometry, e.g. a cylinder as used in Chapter 3, by assigning cells to the geometry. Each simulation cell comprises the information of a magnetic moment **M** and the settings of other micromagnetic material parameters. The size of the cells employed in the numerical discretization has to be smaller than the exchange length, $l_{\mathrm{ex}} = \sqrt{\frac{2A}{\mu_0 M_{\mathrm{s}}^2}}$, of the magnetic material, as the simulation of under-resolved structures can lead to unreliable results [98]. The exchange length is dependent on the specific parameters of the analyzed material and needs, thus, to be determined prior to the beginning of the simulation. Next, the initialization of the desired interactions, e.g. exchange, anisotropy, external drives) is carried out. This may include inhomogeneities in the material, time dependencies of fields and

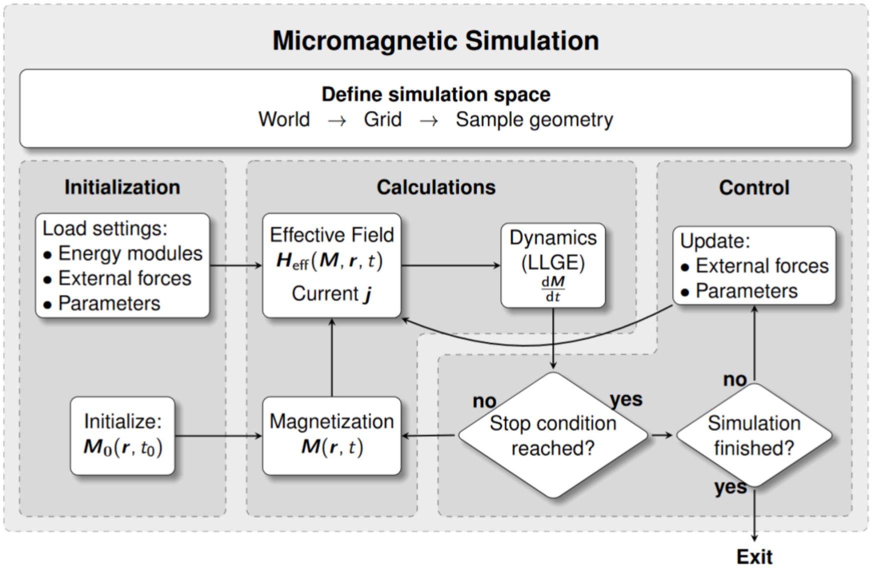

Figure B.1: Flowchart of a micromagnetic simulation showing the simplified algorithm implemented in a micromagnetic solver. Taken from Ref. [259].

currents. Importantly, it is usually possible to load magnetic patterns from pre-relaxed states.

Calculation. The calculation step is carried out by the execution of the actual solver algorithm. All the effective fields generated by the magnetic interactions are calculated and enter the LLG equation to calculate the time derivative of the magnetization and eventually the next magnetization state after the preset time step. The new magnetization pattern then undergoes the same loop over and over again until a user-defined stop condition is reached. From this point on more program code may be executed and/or another simulation started.

Control. The typical stop condition is a maximum torque $\frac{\mathrm{d}\mathbf{M}_{\mathrm{max}}}{\mathrm{d}t}$, however, other control parameters are such as the simulated time or the velocity of a DW can be also used. In the case of the former stop condition, if a certain value is achieved the magnetization is assumed to be relaxed and the calculation stops.

APPENDIX C

CALCULATIONS OF SOT AND DMI

Here, we will describe the basic theoretical concepts employed for the SOT and DMI calculations performed by the collaborators in the Forschungszentrum Jülich, in particular, by Jan-Philipp Hanke with input from Yuriy Mokrousov. For this, we will follow the arguments from Refs. [211, 234].

Density functional theory (DFT) provides the computational tool to evaluate the SOTs in realistic material systems. Within DFT, a system is described by a non-interacting Hamiltonian, which can be decomposed as

$$\hat{H} = \hat{K} + \hat{V}_{\text{eff}}(\mathbf{r}) + \mu_{\text{B}} \boldsymbol{\sigma} \cdot \boldsymbol{\Omega}^{\text{ex}}(\mathbf{r}) + \hat{H}_{\text{SO}}\,, \tag{C.1}$$

where $\hat{K}$ is the kinetic energy, $\hat{V}_{\text{eff}}$ is the effective crystal potential, $\boldsymbol{\Omega}^{\text{ex}}$ is the exchange field, $\hat{H}_{\text{SO}}$ the SOC and $\boldsymbol{\sigma} = \left(\sigma_x, \sigma_y, \sigma_z\right)^{\text{T}}$ is the vector of Pauli spin matrices. In FM systems, the exchange field $\boldsymbol{\Omega}^{\text{ex}} = \Omega^{\text{ex}}(\mathbf{r})\hat{\mathbf{m}}$ is characterized by a position-independent direction $\hat{\mathbf{m}}$ and a position-dependent amplitude Ω^{ex}, which is related to the Kohn-Sham effective potentials $V^{\text{eff}}_{\text{maj}}$ and $V^{\text{eff}}_{\text{min}}$ of the majority and minority electrons, respectively, as follows:

$$\Omega^{\text{ex}} = \frac{1}{2\mu_{\text{B}}} \left[V^{\text{eff}}_{\text{min}} - V^{\text{eff}}_{\text{maj}} \right] . \tag{C.2}$$

An applied electric field modulates the exchange field $\boldsymbol{\Omega}^{\text{ex}}(\mathbf{r})$ due to the induced magnetization $\delta\mathbf{m}(\mathbf{r})$ at the position $\mathbf{r}$, which can be expressed as $\delta\boldsymbol{\Omega}^{\text{ex}}(\mathbf{r}) = \Omega^{\text{ex}}(\mathbf{r})\delta\mathbf{m}(\mathbf{r})/m(\mathbf{r})$. As a result the torque $\mathbf{T}$ on the magnetization within one unit cell is given by

$$\mathbf{T} = \int \mathbf{m} \times \delta\boldsymbol{\Omega}^{\text{ex}}(\mathbf{r})\,\mathrm{d}^3 r = \int \boldsymbol{\Omega}^{\text{ex}}(\mathbf{r}) \times \delta\mathbf{m}(\mathbf{r})\,\mathrm{d}^3 r\,, \tag{C.3}$$

where the integration is over the unit cell volume. One can thus see that the torque on the magnetization arises from the component of $\delta\mathbf{m}(\mathbf{r})$ which is perpendicular to $\mathbf{\Omega}^{\mathrm{ex}}(\mathbf{r})$.

From the point of view of the linear-response theory, the torque $\mathbf{T}$ due to the spin-polarized currents generated by the applied electric field $\mathbf{E}$ can be written as $\mathbf{T} = \tau\mathbf{E}$, where τ is the torkance tensor. It is also possible to write the torque on the magnetization within one unit cell due to an electron in state $\psi(\mathbf{r})$ as

$$\mathbf{T}[\psi] = -\mu_{\mathrm{B}}\int \mathbf{\Omega}^{\mathrm{ex}}(\mathbf{r})\times\psi(\mathbf{r})^{*}\boldsymbol{\sigma}\psi(\mathbf{r})\,\mathrm{d}^3r = \mu_{\mathrm{B}}\int \psi(\mathbf{r})^{*}\sigma\psi(\mathbf{r})\times\mathbf{\Omega}^{\mathrm{ex}}(\mathbf{r})\,\mathrm{d}^3r = -\int \psi(\mathbf{r})^{*}\mathscr{T}(\mathbf{r})\psi(\mathbf{r})\,\mathrm{d}^3r\,, \tag{C.4}$$

where $\mathscr{T} = -\mu_{\mathrm{B}}\boldsymbol{\sigma}\times\mathbf{\Omega}(\mathbf{r})$ is the torque operator at the point $\mathbf{r}$, with $\mathscr{T}_i$ being its i-th Cartesian component.

Within the Kubo linear-response formalism, the torkance tensor relates to the imaginary part of the retarded torque-velocity correlation function, which can be calculated using the Matsubara technique of analytical continuation [260]. As a result, a Green function representation torkance tensor $\tau_{ij} = \tau_{ij}^{\mathrm{I(a)}} + \tau_{ij}^{\mathrm{I(b)}} + \tau_{ij}^{\mathrm{II}}$ at zero temperature reads:

$$\tau_{ij}^{\mathrm{I(a)}} = \frac{e}{h}\mathrm{Tr}\,\langle\mathscr{T}_i G^{\mathrm{R}}(\mathscr{E}_{\mathrm{F}})\,v_j G^{\mathrm{A}}(\mathscr{E}_{\mathrm{F}})\rangle\,, \tag{C.5}$$

$$\tau_{ij}^{\mathrm{I(b)}} = -\frac{e}{h}\mathrm{Re}\,\langle\mathscr{T}_i G^{\mathrm{R}}(\mathscr{E}_{\mathrm{F}})\,v_j G^{\mathrm{R}}(\mathscr{E}_{\mathrm{F}})\rangle\,, \tag{C.6}$$

$$\tau_{ij}^{\mathrm{II}} = \frac{e}{h}\int_{-\infty}^{\mathscr{E}_{\mathrm{F}}} \mathrm{d}\mathscr{E}\,\mathrm{Re}\mathrm{Tr}\,\langle\mathscr{T}_i G^{\mathrm{R}}(\mathscr{E})\,v_j\frac{G^{\mathrm{R}}(\mathscr{E})}{\mathrm{d}\mathscr{E}} - \mathscr{T}_i\frac{G^{\mathrm{R}}(\mathscr{E})}{\mathrm{d}\mathscr{E}}v_j G^{\mathrm{R}}(\mathscr{E})\rangle\,, \tag{C.7}$$

where $G^{\mathrm{R}}(\mathscr{E})$ and $G^{\mathrm{A}}(\mathscr{E})$ are the retarded and advanced Green function, respectively, $\mathscr{E}_{\mathrm{F}}$ is the Fermi energy, $e > 0$ is the elementary positive charge and v_i is the i-th Cartesian component of the velocity operator. The first two terms, $\tau_{ij}^{\mathrm{I(a)}}$ and $\tau_{ij}^{\mathrm{I(b)}}$, of the torkance tensor are the Fermi surface terms, while the third, τ_{ij}^{II} is a Fermi sea term.

Assuming that the dominant effect of finite temperature on the torkance is the enhancement of the band broadening Γ, it is also possible to approximate the effect of disorder.[1] For a constant band broadening Γ we set $G^{\mathrm{R}}(\mathscr{E}) = \hbar[\mathscr{E} - H + i\Gamma]^{-1}$ and $G^{\mathrm{A}}(\mathscr{E}) = \hbar[\mathscr{E} - H - i\Gamma]^{-1}$, where H is the Hamiltonian given by Eq. C.1.

Furthermore, in order to compare theory with experiment one can decompose the computed torkance into even and odd in $\mathbf{m}$ parts, i.e. $\tau_{ij}(\mathbf{m}) = \tau_{ij}^{\mathrm{odd}}(\mathbf{m}) + \tau_{ij}^{\mathrm{even}}(\mathbf{m})$, where $\tau_{ij}^{\mathrm{odd}}(\mathbf{m}) = \frac{1}{2}\left[\tau_{ij}(\mathbf{m}) - \tau_{ij}(-\mathbf{m})\right]$ and $\tau_{ij}^{\mathrm{odd}}(\mathbf{m}) = \frac{1}{2}\left[\tau_{ij}(\mathbf{m}) + \tau_{ij}(-\mathbf{m})\right]$. As we will see below, this results in splitting Eqs. C.5-C.7 into two terms: containing $\mathrm{Im}\left[\langle\psi_{\mathbf{k}n}|\mathscr{T}_i|\psi_{\mathbf{k}m}\rangle\langle\psi_{\mathbf{k}m}|v_j|\psi_{\mathbf{k}n}\rangle\right]$ and the second containing only contributions of $\mathrm{Re}\left[\langle\psi_{\mathbf{k}n}|\mathscr{T}_i|\psi_{\mathbf{k}m}\rangle\langle\psi_{\mathbf{k}m}|v_j|\psi_{\mathbf{k}n}\rangle\right]$. The first term is given

---

[1] In the case of SHE this constant Γ approximation does not capture the side-jump and skew-scattering.

by

$$\tau_{ij}^{\text{even}} = \frac{e\hbar}{2\pi N} \sum_{\mathbf{k}n\neq m} \text{Im}\left[\langle\psi_{\mathbf{k}n}|\mathscr{T}_i|\psi_{\mathbf{k}m}\rangle\langle\psi_{\mathbf{k}m}|v_j|\psi_{\mathbf{k}n}\rangle\right] \tag{C.8}$$

$$\frac{\Gamma(\mathscr{E}_{\mathbf{k}m}-\mathscr{E}_{\mathbf{k}n})}{\left[(\mathscr{E}_{\text{F}}-\mathscr{E}_{\mathbf{k}n})^2+\Gamma^2\right]\left[(\mathscr{E}_{\text{F}}-\mathscr{E}_{\mathbf{k}m})^2+\Gamma^2\right]}+$$

$$\frac{2\Gamma}{\left[\mathscr{E}_{\mathbf{k}n}-\mathscr{E}_{\mathbf{k}m}\right]\left[(\mathscr{E}_{\text{F}}-\mathscr{E}_{\mathbf{k}m})^2+\Gamma^2\right]}+$$

$$+\frac{2}{\left[\mathscr{E}_{\mathbf{k}n}-\mathscr{E}_{\mathbf{k}m}\right]^2}\text{Im}\ln\frac{\mathscr{E}_{\mathbf{k}m}-\mathscr{E}_{\text{F}}-i\Gamma}{\mathscr{E}_{\mathbf{k}n}-\mathscr{E}_{\text{F}}-i\Gamma},$$

and the second reads

$$\tau_{ij}^{\text{odd}} = \frac{e\hbar}{\pi N} \sum_{\mathbf{k}nm} \frac{\Gamma^2\text{Re}\left[\langle\psi_{\mathbf{k}n}|\mathscr{T}_i|\psi_{\mathbf{k}m}\rangle\langle\psi_{\mathbf{k}m}|v_j|\psi_{\mathbf{k}n}\rangle\right]}{\left[(\mathscr{E}_{\text{F}}-\mathscr{E}_{\mathbf{k}n})^2+\Gamma^2\right]\left[(\mathscr{E}_{\text{F}}-\mathscr{E}_{\mathbf{k}m})^2+\Gamma^2\right]}, \tag{C.9}$$

where N is the number of $\mathbf{k}$-points used to sample the Brillouin zone and $\psi_{\mathbf{k}n}$ denote the Bloch function for band n and $\mathbf{k}$ with the corresponding energy $\mathscr{E}_{\mathbf{k}n}$.

One can see that only the Fermi surface terms, $\tau_{ij}^{\text{I(a)}}$ and $\tau_{ij}^{\text{I(b)}}$, contribute to τ_{ij}^{odd}, while both the Fermi surface and the Fermi sea terms, i.e. $\tau_{ij}^{\text{I(a)}}$ and τ_{ij}^{II}, contribute to τ_{ij}^{even}. Using the transformation properties under time reversal,

$$\mathbf{\Omega}^{\text{ex}} = -\mathbf{\Omega}^{\text{ex}} \tag{C.10}$$

$$\langle\psi_{\mathbf{k}n}|\mathbf{v}|\psi_{\mathbf{k}m}\rangle = -\left(\langle\psi_{\mathbf{k}n}|\mathbf{v}|\psi_{\mathbf{k}m}\rangle\right)^* \tag{C.11}$$

$$\langle\psi_{\mathbf{k}n}|\mathbf{m}|\psi_{\mathbf{k}m}\rangle = -\left(\langle\psi_{\mathbf{k}n}|\mathbf{m}|\psi_{\mathbf{k}m}\rangle\right)^* \tag{C.12}$$

$$\langle\psi_{\mathbf{k}n}|\mathscr{T}|\psi_{\mathbf{k}m}\rangle = \left(\langle\psi_{\mathbf{k}n}|\mathscr{T}|\psi_{\mathbf{k}m}\rangle\right)^*, \tag{C.13}$$

it is straightforward to show that the torkance component τ_{ij}^{odd} is odd with respect to magnetization reversal, while τ_{ij}^{even} is even.

Calculation of the DMI presented in Chapter 5 were carried out using expression C.14, the derivation of which is described in detail in Refs. [45, 234]. Since it is natural to interpret the DMI in finite systems in terms of moments of the torque, $r_i T_j(r)$, employing the torque operator from Eq. C.3, we can arrive at the expression for the spiralization D_{ij} at finite temperatures T

$$D_{ij} = \frac{1}{N_{\mathbf{k}}V}\sum_{\mathbf{k}n}\left[f(\mathscr{E}_{\mathbf{k}n})A_{ij}^n(\mathbf{k}) + \frac{1}{\beta}\ln\left(1+e^{\beta(\mathscr{E}_{\mathbf{k}n}-\mu)}\right)B_{ij}^n(\mathbf{k})\right], \tag{C.14}$$

where V is the unit cell volume, $f(\mathscr{E}_{\mathbf{k}n})$ is the Fermi distribution function with the band energy $\mathscr{E}_{\mathbf{k}n}$, μ is the chemical potential and $\beta = 1/(k_{\mathrm{B}}T)$. The $\mathbf{k}$-dependent quantities A^n_{ij} and B^n_{ij} are expressed as follows:

$$A^n_{ij}(\mathbf{k}) = -\mathrm{Im}\sum_{m\neq n}\frac{\langle u_{\mathbf{k}n}|\mathscr{T}_i|u_{\mathbf{k}m}\rangle\left\langle u_{\mathbf{k}m}|\hbar v_j(\mathbf{k})|u_{\mathbf{k}n}\right\rangle}{\mathscr{E}_{\mathbf{k}n}-\mathscr{E}_{\mathbf{k}m}}, \tag{C.15}$$

$$B^n_{ij}(\mathbf{k}) = -2\mathrm{Im}\sum_{m\neq n}\frac{\langle u_{\mathbf{k}n}|\mathscr{T}_i|u_{\mathbf{k}m}\rangle\left\langle u_{\mathbf{k}m}|\hbar v_j(\mathbf{k})|u_{\mathbf{k}n}\right\rangle}{(\mathscr{E}_{\mathbf{k}n}-\mathscr{E}_{\mathbf{k}m})^2}. \tag{C.16}$$

To model the effect of disorder, the expression of the spiralization tensor can be extended such that the eigenstate representation of the retarded Green function G^{R} includes a constant band broadening Γ, as it has been done above for the torkances. As a result we obtain [234]

$$\begin{aligned} D_{ij} &= \frac{\hbar}{2\pi N_{\mathbf{k}}V}\sum_{\mathbf{k}n}\sum_{m\neq n}\mathrm{Im}\left[\langle u_{\mathbf{k}n}|\mathscr{T}_i|u_{\mathbf{k}m}\rangle\left\langle u_{\mathbf{k}m}|v_j(\mathbf{k})|u_{\mathbf{k}n}\right\rangle\right] \\ &\times\left[\frac{\mathscr{E}_{\mathbf{k}n}+\mathscr{E}_{\mathbf{k}m}-2\mathscr{E}_{\mathrm{F}}}{(\mathscr{E}_{\mathbf{k}n}-\mathscr{E}_{\mathbf{k}m})^2}\mathrm{Im}\log\frac{\mathscr{E}_{\mathbf{k}m}-\mathscr{E}_{\mathrm{F}}-i\Gamma}{\mathscr{E}_{\mathbf{k}n}-\mathscr{E}_{\mathrm{F}}-i\Gamma}-\frac{2\Gamma}{(\mathscr{E}_{\mathbf{k}n}-\mathscr{E}_{\mathbf{k}m})^2}\mathrm{Re}\log\frac{\mathscr{E}_{\mathbf{k}m}-\mathscr{E}_{\mathrm{F}}-i\Gamma}{\mathscr{E}_{\mathbf{k}n}-\mathscr{E}_{\mathrm{F}}-i\Gamma}\right]. \end{aligned} \tag{C.17}$$

where the summation is over all electronic states. Also note that according to the symmetry arguments, reflected in Eqs. C.10-C.13, the DMI spiralization tensor is even in the magnetization direction just like the damping-like torkance t^{even}_{ij}.

Equations C.8 and C.9 were used to evaluate the SOT in Chapter 4 and Eq. C.17 was used to calculate the DMI in Chapter 5 based on the calculated from first principles electronic structure $\mathscr{T}_{\mathbf{k}inm} = \langle\psi_{\mathbf{k}n}|\mathscr{T}_i|\psi_{\mathbf{k}m}\rangle$, $v_{\mathbf{k}inm} = \langle\psi_{\mathbf{k}n}|v_i|\psi_{\mathbf{k}m}\rangle$, $\mathscr{E}_{\mathbf{k}m}$ and $\mathscr{E}_{\mathrm{F}}$. For the calculation we used the Wannier interpolation technique, which allows one to efficiently converge the $\mathbf{k}$ summations numerically [234, 261]. For this the matrix elements of the necessary operator are expressed in the basis of maximally localized Wannier functions (MLWFs) $|W_{m\mathbf{R}}$ as follows:

$$H^{(\mathrm{W})}_{\mathbf{k}nm} = \sum_{\mathbf{R}} e^{i\mathbf{k}\cdot\mathbf{R}}\langle W_{n0}|H|W_{m\mathbf{R}}\rangle \tag{C.18}$$

$$v^{(\mathrm{W})}_{\mathbf{k}inm} = \frac{1}{\hbar}\sum_{\mathbf{R}} e^{i\mathbf{k}\cdot\mathbf{R}}i\mathrm{R}_i\langle W_{n0}|H|W_{m\mathbf{R}}\rangle \tag{C.19}$$

$$\mathscr{T}^{(\mathrm{W})}_{\mathbf{k}inm} = \sum_{\mathbf{R}} e^{i\mathbf{k}\cdot\mathbf{R}}\langle W_{n0}|\mathscr{T}_i|W_{m\mathbf{R}}\rangle\,. \tag{C.20}$$

The DFT calculations of the electronic structure of a $\mathrm{Fe_{0.7}Co_{0.3}/W(001)}$ film in Chapters 4 and 5 were performed as implemented in the full-potential linearized augmented-plane-wave code `FLEUR` [262]. Exchange and correlation effects were treated within the generalized gradient approximation (GGA), [263] the plane-wave cutoff was 4.1 Bohr^{-1} and the muffin-tin radius of magnetic and non-magnetic atoms was 2.42 Bohr. In the absence of strain, we assumed the structural parameters as determined in Ref. [264]. The electronic structure of the alloyed compound was treated within the virtual crystal approximation (VCA) [265]. Sampling the full two-dimensional Brillouin zone by 24×24 **k**-points, we calculated the self-consistent charge density of the perpendicularly magnetized system with SOC. Subsequently, we employed the wave-function information computed on a coarse mesh of 8×8 **k**-points for various magnetization directions to generate a single set of the higher-dimensional Wannier functions [266]. Based on these functions, we evaluated the linear-response expression of the torkance τ_{ij} [211] and the DMI tensor D_{ij} [45] by using an efficient but accurate generalized Wannier interpolation [266, 267] which allowed us to access the electronic structure at any **k**-point for arbitrary magnetization directions.

APPENDIX D

HANDLING PMN-PT

Anything that can go wrong will go wrong

Murphy's Law

Here, we will briefly describe possible problems which may arise when working with PMN-PT substrates. Based on the experience gained we suggest how to avoid these problems.

D.1 TOO HOT PLATE OR IRREVERSIBLE STRUCTURAL PHASE TRANSITION IN PMN-PT

During the preparation step for the EBL patterning, the spin-coated resists need to be cured at relatively high temperatures. According to the recipes described in Appendix A, a typical MMA/PMMA bilayer resist requires the temperatures of 180 °C.

Figure D.1: Image of a shattered PMN-PT substrate on a hot plate at 180 °C.

It occurred several times[1] that a PMN-PT substrate was damaged during this necessary temperature treatment step. Within the first few seconds on the hot plate at 180 °C the substrate started to sparkle and eventually shattered in many small pieces, as shown in a photograph in Fig. D.1.

Interestingly, studies of temperature dependence of the dielectric properties of these piezoelectric materials show a peak of the dielectric permittivity around this temperature (140 °C - 180 °C) [268]. And it is also known that in the case of materials close to the MPB region, the maxima of dielectric permittivity reveal the presence of phase transitions [268]. Thus, the observed behavior of the PMN-PT substrates can be associated with an expansion jump leading to such an “irreversible phase transition”.

Based on our experience, the suggestions on how to prevent this from occurring are as follows:

- If it is necessary to put the substrate on a hot plate which is already hot, it is critical that the sample is put flat.
- If it is allowed by the fabrication process, one should consider heating up the substrate gradually.
- The substrates of relatively small sizes (5 × 5 mm) were not observed to blow up on a hot plate.

D.2 PMN-PT SURFACE EFFECTS

While it is well known to experimentalists that nanostructures on any substrate may be destroyed during transport measurements [Fig. D.2 (a)], when too much current is applied or if there is an unwanted electrical spike, the structures on PMN-PT substrates are prone to being blowing up for other reasons not related to inaccurate measurements or network instabilities. In particular, we noticed that even the Hall-cross structures that were not connected to any power sources could be burnt down like if there was a large current passing through them, see for instance Fig. D.2 (b). We also noticed a correlation that this occurs when a PMN-PT is being electrically poled. This could be caused by the electric currents which are known to develop in the PMN-PT substrates upon its poling. These currents picked up by metallic features on the surface may leads to the damage, as observed in Fig. D.2 (c), which shows that the metallic contacts clearly not connected to anything are blown up.

---

[1] Limited statistics shows that 1 of 10 substrates blow up.

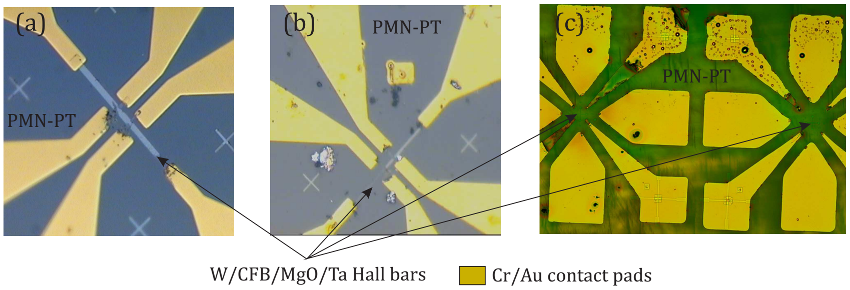

Figure D.2: Optical microscope images of Hall-cross structures (a) blown up likely by a spike in the power network during a running measurements, (b) and (c) burnt Hall-cross structures not connected to any source of possible discharge.

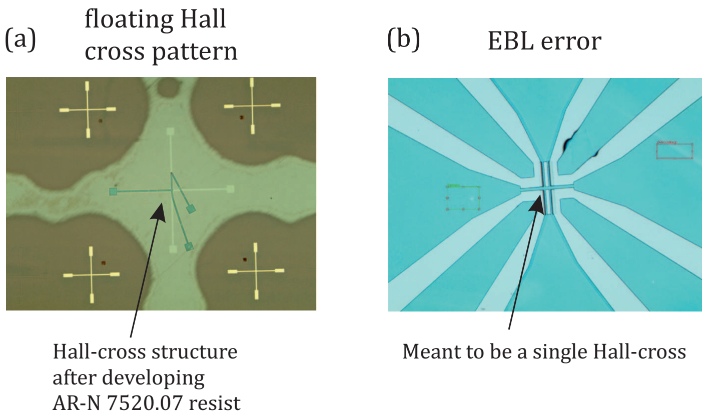

Figure D.3: Optical microscope images of (a) a Hall-cross pattern after developing of the lithographical resist and (b) a resulting Hall-cross with an error during the EBL process.

D.3 EBL PATTERNING USING PMN-PT AS A SUBSTRATES

- Since PMN-PT substrates are insulators the use of a conductive e-spacer is strongly advised.

- As mentioned in Appendix A, the automatic WF alignment procedure does not work on ultrathin Ta capped layers markers on PMN-PT. Due to charging it leads to misalignment of the subsequent writing area towards the previous one. It is therefore recommended to make thick (30 – 50 nm) Cr/Au alignment markers before any EBL structuring. Also, the best alignment at each EBL step is required.

- This kind of issue is not restricted to using PMN-PT crystals as a substrate. Even seemingly clean substrate surfaces may not be perfectly clean from resists left-overs. This may lead to unwanted results, such as when a patterned structure does not stick to the sample surface and moves during the development step. Figure D.3 (a) shows an optical microscope image of such a floating EBL pattern of a Hall-cross after the development of the exposed resist.

- Figure D.3 (b) shows an optical microscope image of a Hall-cross structure which turned out wrong due to an EBL error. In this case, as well, no relation to the substrate used was obvious. The EBL patterning was set to write the entire structure in one step in a "meander" mode. As a result the central part of the Hall-cross was topologically different from the design pattern. Changing the patterning mode to "linear" did not resolve this issue. However, splitting the structure in two writing areas, i.e. first writing the Hall-cross and then during the same EBL step writing the large contact pads, led to the desired result.

D.4 REAL-TIME IMAGING OF A DISCHARGE IN PEEM

Despite being a very powerful technique to study surfaces, PEEM also has certain limitations mainly to the types of samples which can be investigated. The main requirements for the samples are as follows:

- *Samples should to be flat* with a flatness of $\approx 1/10$ of desired resolution, according to the existing rule of thumb [242]. Because large electric fields are employed to extract photoexcited electrons, surface inhomogeneities such as sharp defects can lead to localization of the electric field and cause an electric arc between the objective lens and the sample.
- *Samples should be good conductors*, i.e., they should not charge under illumination by x-rays. Therefore, bare insulating materials cannot be imaged, unless capped with a thin conductive layer/grid, and for samples with large insulating areas the spatial resolution is expected to be lowered.
- *Samples should not have an extensive capping*, as the probing depth is limited to a few nm as discussed in Section 2.3. Many PEEM setups are equipped with an *in-situ* sputter gun, which can be used to remove the capping layer. The drawback of this is that the sample surface can be damaged during the sputtering process.

These requirements are essential to obtain a good-quality PEEM image. In practice, however, even a seemingly ideal sample can cause an arc discharge, which can be strong enough

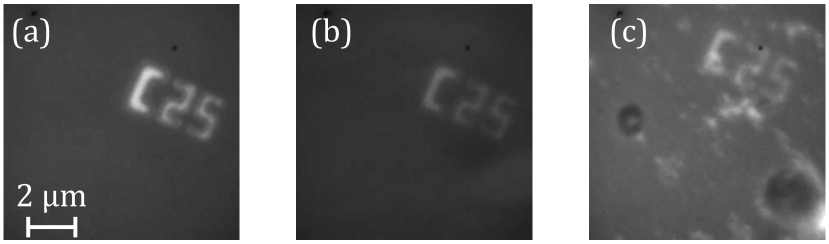

Figure D.4: Subsequent PEEM images with the delay of 1 s of an Au alignment marker (a) before, (b) right before and (c) after a discharge.

to damage the sample surface or destroy its magnetic properties (demagnetize). An example of such a discharge and its consequences is presented in Fig. D.4, showing a series of subsequent PEEM images of a Cr/Au alignment marker "C25" on top of a continuous conductive film before in (a) and after the discharge in (c). One can see that, as a result, the marker was damaged and part of the marker's material evaporated and spread over the sample's surface.

In our experience, two main solutions exist to minimize the risk of a discharge: reducing the operation voltage and increasing the distance between the sample and the objective lens. In the first case, reduction of the bias voltage requires new settings of the microscope optics and re-calibration of the image magnification. In the second method, the sample is moved further away from the objective lens, which requires re-adjustment of the objective lens current from its optimal value.

APPENDIX E

AUTHOR CONTRIBUTIONS

Removed in the electronic version of this thesis due to data protection regulations.
In der elektronischen Version entfernt aufgrund datenschutzrechtlicher Bestimmungen.

BIBLIOGRAPHY

[1] N. Jones, “How to stop data centres from gobbling up the world’s electricity,” *Nature*, vol. 561, pp. 163–166, 2018.

[2] A. Andrae and T. Edler, “On global electricity usage of communication technology: Trends to 2030,” *Challenges*, vol. 6, pp. 117–157, 2015.

[3] A. A. Bukharaev, A. K. Zvezdin, A. P. Pyatakov, and Y. K. Fetisov, “Straintronics: a new trend in micro- and nanoelectronics and material science,” *Phys. Usp.*, vol. 61, pp. 1175–1212, 2018.

[4] G. E. Moore, “Cramming more components onto integrated circuits, reprinted from electronics, volume 38, number 8, april 19, 1965, pp.114 ff.,” *IEEE Solid-State Circuits Society Newsletter*, vol. 11, pp. 33–35, 2006.

[5] *International Technology Roadmap for Semiconductors 2.0*. ITRS, 2017.

[6] J. R. Powell, “The quantum limit to Moore’s law,” *Proceedings of the IEEE*, vol. 96, pp. 1247–1248, 2008.

[7] I. Hutchings and P. Shipway, “9 - applications and case studies,” in *Tribology (Second Edition)* (I. Hutchings and P. Shipway, eds.), pp. 303 – 352, Butterworth-Heinemann, second edition ed., 2017.

[8] M. Fashami, J. Atulasimha, and S. Bandyopadhyay, “Energy dissipation and error probability in fault-tolerant binary switching,” *Sci. Rep.*, vol. 3, p. 3204, 2013.

[9] S. Salahuddin and S. Datta, “Interacting systems for self-correcting low power switching,” *Applied Physics Letters*, vol. 90, p. 093503, 2007.

[10] R. P. Cowburn, D. K. Koltsov, A. O. Adeyeye, M. E. Welland, and D. M. Tricker, “Single-domain circular nanomagnets,” *Phys. Rev. Lett.*, vol. 83, pp. 1042–1045, 1999.

[11] M. N. Baibich, J. M. Broto, A. Fert, F. N. Van Dau, F. Petroff, P. Etienne, G. Creuzet, A. Friederich, and J. Chazelas, “Giant magnetoresistance of (001)Fe/(001)Cr magnetic superlattices,” *Phys. Rev. Lett.*, vol. 61, pp. 2472–2475, 1988.

[12] G. Binasch, P. Grünberg, F. Saurenbach, and W. Zinn, “Enhanced magnetoresistance in layered magnetic structures with antiferromagnetic interlayer exchange,” *Physical Review B*, vol. 39, pp. 4828–4830, 1989.

[13] M. T. Alam, M. J. Siddiq, G. H. Bernstein, M. Niemier, W. Porod, and X. S. Hu, “On-chip clocking for nanomagnet logic devices,” *IEEE Transactions on Nanotechnology*, vol. 9, pp. 348–351, 2010.

[14] O. Boulle, G. Malinowski, and M. Kläui, “Current-induced domain wall motion in nanoscale ferromagnetic elements,” *Materials Science and Engineering: R: Reports*, vol. 72, pp. 159–187, 2011.

[15] I. M. Miron, K. w, G. Gaudin, P.-J. Zermatten, M. V. Costache, S. Auffret, S. Bandiera, B. Rodmacq, A. Schuhl, and P. Gambardella, “Perpendicular switching of a single ferromagnetic layer induced by in-plane current injection,” *Nature*, vol. 476, p. 189, 2011.

[16] L. Liu, C.-F. Pai, Y. Li, H. W. Tseng, D. C. Ralph, and R. A. Buhrman, “Spin-torque switching with the giant spin Hall effect of tantalum,” *Science*, vol. 336, pp. 555–558, 2012.

[17] D. Ralph and M. Stiles, “Spin transfer torques,” *Journal of Magnetism and Magnetic Materials*, vol. 320, pp. 1190 – 1216, 2008.

[18] T. Maruyama, Y. Shiota, T. Nozaki, K. Ohta, N. Toda, M. Mizuguchi, A. A. Tulapurkar, T. Shinjo, M. Shiraishi, S. Mizukami, Y. Ando, and Y. Suzuki, “Large voltage-induced magnetic anisotropy change in a few atomic layers of iron,” *Nature Nanotechnology*, vol. 4, pp. 158 – 161, 2009.

[19] P. Khalili Amiri and K. Wang, “Voltage-controlled magnetic anisotropy in spintronic devices,” *SPIN*, vol. 2, 2012. `https://doi.org/10.1142/S2010324712400024`.

[20] K. L. Wang, J. G. Alzate, and P. K. Amiri, “Low-power non-volatile spintronic memory: STT-RAM and beyond,” *Journal of Physics D: Applied Physics*, vol. 46, p. 074003, feb 2013.

[21] M. S. Fashami, J. Atulasimha, and S. Bandyopadhyay, “Magnetization dynamics, throughput and energy dissipation in a universal multiferroic nanomagnetic logic gate with fan-in and fan-out,” *Nanotechnology*, vol. 23, p. 105201, 2012.

[22] N. D’Souza, M. Salehi Fashami, S. Bandyopadhyay, and J. Atulasimha, “Experimental clocking of nanomagnets with strain for ultralow power boolean logic,” *Nano Letters*, vol. 16, p. 1069, 2016.

[23] T. Wu, A. Bur, K. Wong, P. Zhao, C. S. Lynch, P. K. Amiri, K. L. Wang, and G. P. Carman, “Electrical control of reversible and permanent magnetization reorientation for magnetoelectric memory devices,” *Applied Physics Letters*, vol. 98, p. 262504, 2011.

[24] K. Roy, S. Bandyopadhyay, and J. Atulasimha, “Energy dissipation and switching delay in stress-induced switching of multiferroic nanomagnets in the presence of thermal fluctuations,” *Journal of Applied Physics*, vol. 112, p. 023914, 2012.

[25] S. Bohlens, B. Krüger, A. Drews, M. Bolte, G. Meier, and D. Pfannkuche, “Current controlled random-access memory based on magnetic vortex handedness,” *Applied Physics Letters*, vol. 93, p. 142508, 2008.

[26] B. Pigeau, G. de Loubens, O. Klein, A. Riegler, F. Lochner, G. Schmidt, L. W. Molenkamp, V. S. Tiberkevich, and A. N. Slavin, “A frequency-controlled magnetic vortex memory,” *Applied Physics Letters*, vol. 96, p. 132506, 2010.

[27] A. Manchon and S. Zhang, “Theory of nonequilibrium intrinsic spin torque in a single nanomagnet,” *Physical Review B*, vol. 78, p. 212405, 2008.

[28] I. Mihai Miron, G. Gaudin, S. Auffret, B. Rodmacq, A. Schuhl, S. Pizzini, J. Vogel, and P. Gambardella, “Current-driven spin torque induced by the rashba effect in a ferromagnetic metal layer,” *Nature Materials*, vol. 9, p. 230, 2010.

[29] A. Manchon, J. Železný, I. M. Miron, T. Jungwirth, J. Sinova, A. Thiaville, K. Garello, and P. Gambardella, “Current-induced spin-orbit torques in ferromagnetic and antiferromagnetic systems,” *Reviews of Modern Physics*, vol. 91, p. 035004, 2019.

[30] A. Thiaville, S. Rohart, É. Jué, V. Cros, and A. Fert, “Dynamics of Dzyaloshinskii domain walls in ultrathin magnetic films,” *EPL (Europhysics Letters)*, vol. 100, p. 57002, 2012.

[31] A. Fert, N. Reyren, and V. Cros, “Magnetic skyrmions: advances in physics and potential applications,” *Nature Reviews Materials*, vol. 2, p. 17031, 2017.

[32] G. Finocchio, F. Büttner, R. Tomasello, M. Carpentieri, and M. Kläui, “Magnetic skyrmions: from fundamental to applications,” *Journal of Physics D: Applied Physics*, vol. 49, p. 423001, 2016.

[33] S. Blundell, *Magnetism in condenced matter.* Oxford University Press, 2001.

[34] R. Skomski, *Simple models of magnetism.* Oxford University Press, 2008.

[35] J. Coey, *Magnetism and magnetic materials.* Cambridge University Press, 2009.

[36] J. Stöhr and H. C. Siegmann, *Magnetism: From Fundamentals to Nanoscale Dynamics.* Springer-Verlag Berlin Heidelberg, 2006.

[37] T. Moriya, “Anisotropic superexchange interaction and weak ferromagnetism,” *Physical Review*, vol. 120, pp. 91–98, 1960.

[38] I. Dzyaloshinsky, “A thermodynamic theory of "weak" ferromagnetism of antiferromagnetics,” *Journal of Physics and Chemistry of Solids*, vol. 4, pp. 241 – 255, 1958.

[39] Y. A. Bychkov and E. Rashba, “ Properties of a 2D electron gas with a lifted spectrum degeneracy,” *Sov. Phys. - JETP Lett.*, vol. 39, p. 78, 1984.

[40] K.-W. Kim, K.-W. Moon, N. Kerber, J. Nothhelfer, and K. Everschor-Sitte, “Asymmetric skyrmion Hall effect in systems with a hybrid Dzyaloshinskii-Moriya interaction,” *Physical Review B*, vol. 97, p. 224427, 2018.

[41] P. Jadaun, L. F. Register, and S. K. Banerjee, “The microscopic origin of DMI in magnetic bilayers and prediction of giant DMI in new bilayers,” 2019.

[42] D. Smith, “New mechanisms for magnetic anisotropy in localised S-state moment materials,” *Journal of Magnetism and Magnetic Materials*, vol. 1, pp. 214 – 225, 1976.

[43] A. Belabbes, G. Bihlmayer, F. Bechstedt, S. Blügel, and A. Manchon, “Hund’s rule-driven Dzyaloshinskii-Moriya interaction at $3d-5d$ interfaces,” *Physical Review Letters*, vol. 117, p. 247202, 2016.

[44] V. Kashid, T. Schena, B. Zimmermann, Y. Mokrousov, S. Blügel, V. Shah, and H. G. Salunke, “Dzyaloshinskii-Moriya interaction and chiral magnetism in $3d-5d$ zigzag chains: Tight-binding model and ab initio calculations,” *Physical Review B*, vol. 90, p. 054412, 2014.

[45] F. Freimuth, S. Blügel, and Y. Mokrousov, “Berry phase theory of Dzyaloshinskii-Moriya interaction and spin-orbit torques,” *Journal of Physics: Condensed Matter*, vol. 26, p. 104202, 2014.

[46] A. Fert and P. M. Levy, “Role of anisotropic exchange interactions in determining the properties of spin-glasses,” *Physical Review Letters*, vol. 44, pp. 1538–1541, 1980.

[47] G. Chen, T. Ma, A. T. N’Diaye, H. Kwon, C. Won, Y. Wu, and A. K. Schmid, “Tailoring the chirality of magnetic domain walls by interface engineering,” *Nature Communications*, vol. 4, p. 2671, 2013.

[48] M. Heide, G. Bihlmayer, and S. Blügel, “Dzyaloshinskii-Moriya interaction accounting for the orientation of magnetic domains in ultrathin films: Fe/W(110),” *Physical Review B*, vol. 78, p. 140403, 2008.

[49] M. Bode, M. Heide, K. von Bergmann, P. Ferriani, S. Heinze, G. Bihlmayer, A. Kubetzka, O. Pietzsch, S. Blügel, and R. Wiesendanger, “Chiral magnetic order at surfaces driven by inversion asymmetry,” *Nature*, vol. 447, pp. 190–193, 2007.

[50] A. N. Bogdanov and U. K. Rößler, “Chiral symmetry breaking in magnetic thin films and multilayers,” *Physical Review Letters*, vol. 87, p. 037203, 2001.

[51] X. Z. Yu, Y. Onose, N. Kanazawa, J. H. Park, J. H. Han, Y. Matsui, N. Nagaosa, and Y. Tokura, “Real-space observation of a two-dimensional skyrmion crystal,” *Nature*, vol. 465, pp. 901–904, 2010.

[52] U. K. Rößler, A. N. Bogdanov, and C. Pfleiderer, "Spontaneous skyrmion ground states in magnetic metals," *Nature*, vol. 442, pp. 797–801, 2006.

[53] K. Litzius, I. Lemesh, B. Krüger, P. Bassirian, L. Caretta, K. Richter, F. Büttner, K. Sato, O. A. Tretiakov, J. Förster, R. M. Reeve, M. Weigand, I. Bykova, H. Stoll, G. Schütz, G. S. D. Beach, and M. Kläui, "Skyrmion Hall effect revealed by direct time-resolved X-ray microscopy," *Nature Physics*, vol. 13, pp. 170–175, 2017.

[54] S. Woo, K. Litzius, B. Krüger, M.-Y. Im, L. Caretta, K. Richter, M. Mann, A. Krone, R. M. Reeve, M. Weigand, P. Agrawal, I. Lemesh, M.-A. Mawass, P. Fischer, and M. Kläui, "Observation of room-temperature magnetic skyrmions and their current-driven dynamics in ultrathin metallic ferromagnets," *Nature Materials*, vol. 15, pp. 501–506, 2016.

[55] A. Aharoni, *Introduction to the Theory of Ferromagnetism.* Clarendon Press, 2000.

[56] C. Kittel, "Physical theory of ferromagnetic domains," *Reviews of Modern Physics*, vol. 21, pp. 541–583, 1949.

[57] A. Brandlmaier, S. Geprägs, M. Weiler, A. Boger, M. Opel, H. Huebl, C. Bihler, M. S. Brandt, B. Botters, D. Grundler, R. Gross, and S. T. B. Goennenwein, "In situ manipulation of magnetic anisotropy in magnetite thin films," *Physical Review B*, vol. 77, p. 104445, 2008.

[58] S. Emori, U. Bauer, S.-M. Ahn, E. Martinez, and G. S. D. Beach, "Current-driven dynamics of chiral ferromagnetic domain walls," *Nature Materials*, vol. 12, p. 611, 2013.

[59] P. M. Shepley, A. W. Rushforth, M. Wang, G. Burnell, and T. A. Moore, "Modification of perpendicular magnetic anisotropy and domain wall velocity in Pt/Co/Pt by voltage-induced strain," *Scientific Reports*, vol. 5, p. 7921, 2015.

[60] R. Lo Conte, A. Hrabec, A. P. Mihai, T. Schulz, S.-J. Noh, C. H. Marrows, T. A. Moore, and M. Kläui, "Spin-orbit torque-driven magnetization switching and thermal effects studied in Ta/CoFeB/MgO nanowires," *Applied Physics Letters*, vol. 105, p. 122404, 2014.

[61] N. Nakajima, T. Koide, T. Shidara, H. Miyauchi, H. Fukutani, A. Fujimori, K. Iio, T. Katayama, M. Nývlt, and Y. Suzuki, "Perpendicular magnetic anisotropy caused by interfacial hybridization via enhanced orbital moment in Co/Pt multilayers: Magnetic circular x-ray dichroism study," *Physical Review Letters*, vol. 81, pp. 5229–5232, 1998.

[62] C. Chappert, A. Fert, and F. N. Van Dau, "The emergence of spin electronics in data storage," *Nature Materials*, vol. 6, pp. 813–823, 2007.

[63] T. A. Moore, I. M. Miron, G. Gaudin, G. Serret, S. Auffret, B. Rodmacq, A. Schuhl, S. Pizzini, J. Vogel, and M. Bonfim, "High domain wall velocities induced by current in ultrathin Pt/Co/AlOx wires with perpendicular magnetic anisotropy," *Applied Physics Letters*, vol. 93, p. 262504, 2008.

[64] B. Dieny and M. Chshiev, “Perpendicular magnetic anisotropy at transition metal/oxide interfaces and applications,” *Reviews of Modern Physics*, vol. 89, p. 025008, 2017.

[65] S. Peng, M. Wang, H. Yang, L. Zeng, J. Nan, J. Zhou, Y. Zhang, A. Hallal, M. Chshiev, K. L. Wang, Q. Zhang, and W. Zhao, “Origin of interfacial perpendicular magnetic anisotropy in MgO/CoFe/metallic capping layer structures,” *Scientific Reports*, vol. 5, p. 18173, 2015.

[66] S. Ikeda, K. Miura, H. Yamamoto, K. Mizunuma, H. D. Gan, M. Endo, S. Kanai, J. Hayakawa, F. Matsukura, and H. Ohno, “A perpendicular-anisotropy CoFeB-MgO magnetic tunnel junction,” *Nature Materials*, vol. 9, p. 721, 2010.

[67] H. X. Yang, M. Chshiev, B. Dieny, J. H. Lee, A. Manchon, and K. H. Shin, “First-principles investigation of the very large perpendicular magnetic anisotropy at Fe|MgO and Co|MgO interfaces,” *Physical Review B*, vol. 84, p. 054401, 2011.

[68] S. Kim, S. heon Chris Baek, M. Ishibashi, K. Yamada, T. Taniguchi, T. Okuno, Y. Kotani, T. Nakamura, K.-J. Kim, T. Moriyama, B.-G. Park, and T. Ono, “Contributions of co and fe orbitals to perpendicular magnetic anisotropy of MgO/CoFeB bilayers with Ta, W, IrMn, and Ti underlayers,” *Applied Physics Express*, vol. 10, p. 073006, 2017.

[69] J. Choi, J. Wu, C. Won, Y. Z. Wu, A. Scholl, A. Doran, T. Owens, and Z. Q. Qiu, “Magnetic bubble domain phase at the spin reorientation transition of ultrathin Fe/Ni/Cu(001) film,” *Physical Review Letters*, vol. 98, p. 207205, 2007.

[70] J. Wu, J. Choi, C. Won, Y. Z. Wu, A. Scholl, A. Doran, C. Hwang, and Z. Q. Qiu, “Stripe-to-bubble transition of magnetic domains at the spin reorientation of (Fe/Ni)/Cu/Ni/Cu(001),” *Physical Review B*, vol. 79, p. 014429, 2009.

[71] A. Wachowiak, J. Wiebe, M. Bode, O. Pietzsch, M. Morgenstern, and R. Wiesendanger, “Direct observation of internal spin structure of magnetic vortex cores,” *Science*, vol. 298, pp. 577–580, 2002.

[72] F. Junginger, M. Kläui, D. Backes, S. Krzyk, U. Rüdiger, T. Kasama, R. E. Dunin-Borkowski, J.-M. Feinberg, R. J. Harrison, and L. J. Heyderman, “Quantitative determination of vortex core dimensions in head-to-head domain walls using off-axis electron holography,” *Applied Physics Letters*, vol. 92, p. 112502, 2008.

[73] Y. Yafet and E. M. Gyorgy, “Ferromagnetic strip domains in an atomic monolayer,” *Physical Review B*, vol. 38, pp. 9145–9151, 1988.

[74] A. A. Thiele, “Steady-state motion of magnetic domains,” *Physical Review Letters*, vol. 30, pp. 230–233, 1973.

[75] D. L. Huber, “Dynamics of spin vortices in two-dimensional planar magnets,” *Phys. Rev. B*, vol. 26, pp. 3758–3765, 1982.

[76] M. Stone, “Magnus force on skyrmions in ferromagnets and quantum hall systems,” *Phys. Rev. B*, vol. 53, pp. 16573–16578, 1996.

[77] B. Kr´uger, *PhD thesis: Current-Driven Magnetization Dynamics: Analytical Modeling and Numerical Simulation.* University of Hamburg, 2011.

[78] G. M. Wysin, “Magnetic vortex mass in two-dimensional easy-plane magnets,” *Phys. Rev. B*, vol. 54, pp. 15156–15162, 1996.

[79] K. Y. Guslienko, “Magnetic vortex state stability, reversal and dynamics in restricted geometries,” *Journal of Nanoscience and Nanotechnology*, vol. 8, p. 2745, 2008.

[80] A. Thiaville, Y. Nakatani, J. Miltat, and Y. Suzuki, “Micromagnetic understanding of current-driven domain wall motion in patterned nanowires,” *Europhysics Letters (EPL)*, vol. 69, pp. 990–996, 2005.

[81] G. M. Wysin, “Statistics of gyrotropic vortex dynamics in submicron magnetic disks,” in *Vortex Structures in Fluid Dynamic Problems* (H. P. de Tejada, ed.), ch. 9, Rijeka: IntechOpen, 2017.

[82] T. McGuire and R. Potter, “Anisotropic magnetoresistance in ferromagnetic 3d alloys,” *IEEE Transactions on Magnetics*, vol. 11, pp. 1018–1038, 1975.

[83] J. Slonczewski, “Current-driven excitation of magnetic multilayers,” *Journal of Magnetism and Magnetic Materials*, vol. 159, pp. L1 – L7, 1996.

[84] D. C. Ralph, Y.-T. Cui, L. Q. Liu, T. Moriyama, C. Wang, and R. A. Buhrman, “Spin-transfer torque in nanoscale magnetic devices,” *Philosophical Transactions of the Royal Society A: Mathematical, Physical and Engineering Sciences*, vol. 369, pp. 3617–3630, 2011.

[85] J. Sinova, S. O. Valenzuela, J. Wunderlich, C. H. Back, and T. Jungwirth, “Spin Hall effects,” *Reviews of Modern Physics*, vol. 87, pp. 1213–1260, 2015.

[86] L. Liu, O. J. Lee, T. J. Gudmundsen, D. C. Ralph, and R. A. Buhrman, “Current-induced switching of perpendicularly magnetized magnetic layers using spin torque from the spin Hall effect,” *Physical Review Letters*, vol. 109, p. 096602, 2012.

[87] K. Ando, S. Takahashi, K. Harii, K. Sasage, J. Ieda, S. Maekawa, and E. Saitoh, “Electric manipulation of spin relaxation using the spin Hall effect,” *Physical Review Letters*, vol. 101, p. 036601, 2008.

[88] T. Wang, J. Q. Xiao, and X. Fan, “Spin-orbit torques in metallic magnetic multilayers: Challenges and new opportunities,” *SPIN*, vol. 07, p. 1740013, 2017.

[89] V. Edelstein, “Spin polarization of conduction electrons induced by electric current in two-dimensional asymmetric electron systems,” *Solid State Communications*, vol. 73, pp. 233 – 235, 1990.

[90] V. V. Bel'kov and S. D. Ganichev, “Magneto-gyrotropic effects in semiconductor quantum wells,” *Semiconductor Science and Technology*, vol. 23, p. 114003, 2008.

[91] H. Kurebayashi, J. Sinova, D. Fang, A. C. Irvine, T. D. Skinner, J. Wunderlich, V. Novák, R. P. Campion, B. L. Gallagher, E. K. Vehstedt, L. P. Zârbo, K. Výborný, A. J. Ferguson, and T. Jungwirth, “An antidamping spin-orbit torque originating from the Berry curvature,” *Nature Nanotechnology*, vol. 9, pp. 211 –217, 2014.

[92] P. M. Haney, H.-W. Lee, K.-J. Lee, A. Manchon, and M. D. Stiles, “Current induced torques and interfacial spin-orbit coupling: Semiclassical modeling,” *Physical Review B*, vol. 87, p. 174411, 2013.

[93] K. Garello, I. M. Miron, C. O. Avci, F. Freimuth, Y. Mokrousov, S. Blügel, S. Auffret, O. Boulle, G. Gaudin, and P. Gambardella, “Symmetry and magnitude of spin-orbit torques in ferromagnetic heterostructures,” *Nature Nanotechnology*, vol. 8, p. 587, 2013.

[94] A. Manchon and S. Zhang, “Theory of spin torque due to spin-orbit coupling,” *Physical Review B*, vol. 79, p. 094422, 2009.

[95] J. Kim, J. Sinha, M. Hayashi, M. Yamanouchi, S. Fukami, T. Suzuki, S. Mitani, and H. Ohno, “Layer thickness dependence of the current-induced effective field vector in Ta|CoFeB|MgO,” *Nature Materials*, vol. 12, p. 240, 2013.

[96] C.-F. Pai, M. Mann, A. J. Tan, and G. S. D. Beach, “Determination of spin torque efficiencies in heterostructures with perpendicular magnetic anisotropy,” *Physical Review B*, vol. 93, p. 144409, 2016.

[97] S. Parkin and S.-H. Yang, “Memory on the racetrack,” *Nature Nanotechnology*, vol. 10, pp. 195 – 198, 2015.

[98] K. Litzius, *PhD thesis: Spin-Orbit-Induced Dynamics of Chiral Magnetic Structures*. Johannes Gutenberg University, 2018.

[99] F. Matsukura, Y. Tokura, and H. Ohno, “Control of magnetism by electric fields,” *Nature Nanotechnology*, vol. 10, pp. 209–220, 2015.

[100] D. E. Nikonov and I. A. Young, “Benchmarking spintronic logic devices based on magnetoelectric oxides,” *Journal of Materials Research*, vol. 29, pp. 2109–2115, 2014.

[101] S. Finizio, M. Foerster, M. Buzzi, B. Krüger, M. Jourdan, C. A. F. Vaz, J. Hockel, T. Miyawaki, A. Tkach, S. Valencia, F. Kronast, G. P. Carman, F. Nolting, and M. Kläui, “Magnetic anisotropy engineering in thin film Ni nanostructures by magnetoelastic coupling,” *Physical Review Applied*, vol. 1, p. 021001, 2014.

[102] T.-K. Chung, G. P. Carman, and K. P. Mohanchandra, "Reversible magnetic domain-wall motion under an electric field in a magnetoelectric thin film," *Applied Physics Letters*, vol. 92, p. 112509, 2008.

[103] Z. Zhao, M. Jamali, N. D'Souza, D. Zhang, S. Bandyopadhyay, J. Atulasimha, and J.-P. Wang, "Giant voltage manipulation of MgO-based magnetic tunnel junctions via localized anisotropic strain: A potential pathway to ultra-energy-efficient memory technology," *Applied Physics Letters*, vol. 109, p. 092403, 2016.

[104] M. Buzzi, R. V. Chopdekar, J. L. Hockel, A. Bur, T. Wu, N. Pilet, P. Warnicke, G. P. Carman, L. J. Heyderman, and F. Nolting, "Single domain spin manipulation by electric fields in strain coupled artificial multiferroic nanostructures," *Physical Review Letters*, vol. 111, p. 027204, 2013.

[105] J. J. Wang, J. M. Hu, J. Ma, J. X. Zhang, L. Q. Chen, and C. W. Nan, "Full 180ĉirc magnetization reversal with electric fields," *Scientific Reports*, vol. 4, p. 7507, 2014.

[106] R.-C. Peng, J.-M. Hu, K. Momeni, J.-J. Wang, L.-Q. Chen, and C.-W. Nan, "Fast 180 magnetization switching in a strain-mediated multiferroic heterostructure driven by a voltage," *Scientific Reports*, vol. 6, p. 27561, 2016.

[107] V. Novosad, Y. Otani, A. Ohsawa, S. G. Kim, K. Fukamichi, J. Koike, K. Maruyama, O. Kitakami, and Y. Shimada, "Novel magnetostrictive memory device," *Journal of Applied Physics*, vol. 87, pp. 6400–6402, 2000.

[108] J. Wang, "Mechanical control of magnetic order: From phase transition to skyrmions," *Annual Review of Materials Research*, vol. 49, pp. 361–388, 2019.

[109] *Substrate Specifications*. `https://www.mtixtl.com/PMNT-001-101005S1.aspx`.

[110] I. Alexandru Ivan, M. Rakotondrabe, J. Agnus, R. Bourquin, N. Chaillet, P. Lutz, J.-C. Poncot, R. Duffait, and O. Bauer, "Comparative material study between PZT ceramic and newer crystalline PMN-PT and PZN-PT mateirals for composite bimorph actuators.," *Review on Advanced Materials Science (RAMS)*, vol. 24, pp. 1–9, 2010.

[111] S.-E. Park and T. R. Shrout, "Ultrahigh strain and piezoelectric behavior in relaxor based ferroelectric single crystals," *Journal of Applied Physics*, vol. 82, pp. 1804–1811, 1997.

[112] H. Luo, G. Xu, H. Xu, P. Wang, and Z. Yin, "Compositional homogeneity and electrical properties of lead magnesium niobate titanate single crystals grown by a modified bridgman technique," *Japanese Journal of Applied Physics*, vol. 39, pp. 5581–5585, 2000.

[113] E. V. Colla, N. K. Yushin, and D. Viehland, "Dielectric properties of (PMN)(1-x)(PT)x single crystals for various electrical and thermal histories," *Journal of Applied Physics*, vol. 83, pp. 3298–3304, 1998.

[114] T. Wu, P. Zhao, M. Bao, A. Bur, J. L. Hockel, K. Wong, K. P. Mohanchandra, C. S. Lynch, and G. P. Carman, “Domain engineered switchable strain states in ferroelectric (011) [Pb(Mg1/3Nb2/3)O3](1-x)-[PbTiO3]x (PMN-PT, x0.32) single crystals,” *Journal of Applied Physics*, vol. 109, p. 124101, 2011.

[115] Z.-G. Ye, “Index,” in *Handbook of Advanced Dielectric, Piezoelectric and Ferroelectric Materials* (Z.-G. Ye, ed.), Woodhead Publishing Series in Electronic and Optical Materials, pp. 1033 – 1060, Woodhead Publishing, 2008.

[116] J. Peng, H.-s. Luo, D. Lin, H.-q. Xu, T.-h. He, and W.-q. Jin, “Orientation dependence of transverse piezoelectric properties of 0.70Pb(Mg1/3Nb2/3)O3-0.30PbTiO3 single crystals,” *Applied Physics Letters*, vol. 85, pp. 6221–6223, 2004.

[117] A. Ciubotariu, *PhD thesis: Design, Modeling, Fabrication and Control of PMN-PT Piezoelectric Systems*. Université de Franche-Comté, 2016.

[118] *Strain-poling Relations*. `http://www.hcmat.com/Pmn_Opportunities.html`.

[119] L. Luo, H. Wang, Y. Tang, X. Zhao, Z. Feng, D. Lin, and H. Luo, “Ultrahigh transverse strain and piezoelectric behavior in (1-x)Pb(Mg1/3Nb2/3)O3-xPbTiO3 crystals,” *Journal of Applied Physics*, vol. 99, p. 024104, 2006.

[120] N. Park, H. Kang, J. Park, Y. Lee, Y. Yun, J.-H. Lee, S.-G. Lee, Y. H. Lee, and D. Suh, “Ferroelectric single-crystal gated graphene/hexagonal-BN/ferroelectric field-effect transistor,” *ACS Nano*, vol. 9, p. 10729, 2015.

[121] A. H. Simon, “4 - sputter processing,” in *Handbook of Thin Film Deposition (Third Edition)* (K. Seshan, ed.), pp. 55 – 88, Oxford: William Andrew Publishing, third edition ed., 2012.

[122] M. Geissler and Y. Xia, “Patterning: Principles and some new developments,” *Advanced Materials*, vol. 16, pp. 1249–1269, 2004.

[123] R. K. Dey and B. Cui, “Stitching error reduction in electron beam lithography with in-situ feedback using self-developing resist,” *Journal of Vacuum Science & Technology B*, vol. 31, p. 06F409, 2013.

[124] A. Pfeiffer, *PhD thesis: Pure spin current transport and magnetic state manipulation in lateral spin valves*. Johannes Gutenberg University, 2019.

[125] M. Faraday, “I. Experimental researches in electricity: Nineteenth series,” *Philosophical Transactions of the Royal Society of London*, vol. 136, pp. 1–20, 1846.

[126] J. Kerr, “On rotation of the plane of polarisation by reflection from a magnetic pole,” *Report of the British Association for the Advancement of Science*, p. 40, 1876.

[127] P. N. Argyres, “Theory of the faraday and Kerr effects in ferromagnetics,” *Physical Review*, vol. 97, pp. 334–345, 1955.

[128] H. J. Williams, F. G. Foster, and E. A. Wood, “Observation of magnetic domains by the Kerr effect,” *Physical Review*, vol. 82, pp. 119–120, 1951.

[129] C. A. Fowler and E. M. Fryer, “Magnetic domains on silicon iron by the longitudinal Kerr effect,” *Physical Review*, vol. 86, pp. 426–426, 1952.

[130] H. J. Williams, R. C. Sherwood, F. G. Foster, and E. M. Kelley, “Magnetic writing on thin films of MnBi,” *Journal of Applied Physics*, vol. 28, pp. 1181–1184, 1957.

[131] G. van der Laan, B. T. Thole, G. A. Sawatzky, J. B. Goedkoop, J. C. Fuggle, J.-M. Esteva, R. Karnatak, J. P. Remeika, and H. A. Dabkowska, “Experimental proof of magnetic x-ray dichroism,” *Physical Review B*, vol. 34, pp. 6529–6531, 1986.

[132] G. Schütz, W. Wagner, W. Wilhelm, P. Kienle, R. Zeller, R. Frahm, and G. Materlik, “Absorption of circularly polarized x rays in iron,” *Physical Review Letters*, vol. 58, pp. 737–740, 1987.

[133] P. Weinberger, “John Kerr and his effects found in 1877 and 1878,” *Philosophical Magazine Letters*, vol. 88, pp. 897–907, 2008.

[134] U. Tiwari, R. Ghosh, and P. Sen, “Theory of magneto-optic Kerr effects,” *Physical Review B*, vol. 49, pp. 2159–2162, 1994.

[135] R. P. Feynman, *The Feynman Lectures on Physics.* Addison-Wesley, 2005.

[136] P. A. M. Dirac and N. H. D. Bohr, “The quantum theory of the emission and absorption of radiation,” *Proceedings of the Royal Society of London. Series A, Containing Papers of a Mathematical and Physical Character*, vol. 114, 1927.

[137] E. Condon and G. Shortley, *The Theory of Atomic Spectra.* Cambridge University Press, 1935.

[138] J. Slater, *Quantum Theory of Atomic Structure.* McGraw-Hill, 1960.

[139] J. Kuneš, “Magnetism and magneto-optics in DFT,” *Physica Scripta*, vol. T109, p. 116, 2004.

[140] A. Hofmann, *The Physics of Synchrotron Radiation.* Cambridge Monographs on Particle Physics, Nuclear Physics and Cosmology, Cambridge University Press, 2004.

[141] J. Stöhr, *in X-Ray Absorption: Principles, Applications, Techniques of EXAFS, SEXAFS and XANES. D. C Koningsberger, R. Prins (ed.).* Oxford: Wiley, New York, 1988.

[142] T. Schmidt, S. Heun, J. Slezak, J. Diaz, K. C. Prince, G. Lilienkamp, and E. Bauer, “SPELEEM: Combining LEEM and spectroscopic imaging,” *Surface Review and Letters*, vol. 05, pp. 1287–1296, 1998.

[143] G. De Stasio, L. Perfetti, B. Gilbert, O. Fauchoux, M. Capozi, P. Perfetti, G. Margaritondo, and B. P. Tonner, "MEPHISTO spectromicroscope reaches 20 nm lateral resolution," *Review of Scientific Instruments*, vol. 70, pp. 1740–1742, 1999.

[144] A. Thompson and D. Vaughan, *X-Ray Data Booklet.* Berkeley, CA: Lawrence Berkeley National Laboratory, 2001.

[145] M. Guizar-Sicairos, S. T. Thurman, and J. R. Fienup, "Efficient subpixel image registration algorithms," *Optics Letters*, vol. 33, pp. 156–158, 2008.

[146] X. M. Cheng and D. J. Keavney, "Studies of nanomagnetism using synchrotron-based x-ray photoemission electron microscopy (x-PEEM)," *Reports on Progress in Physics*, vol. 75, p. 026501, 2012.

[147] O. Matilla, D. Beltran, D. Fernandez-Carreiras, J. Jan Jamroz, J. Klora, J. Moldes, and R. Sune, "ALBA timing system - a known architecture with fast interlock system upgrade," *Contributions to the Procedings of ICALEPCS 2011*, p. 1423, 2012.

[148] M. Foerster, F. Maciá, N. Statuto, S. Finizio, A. Hernández-Mínguez, S. Lendínez, P. V. Santos, J. Fontcuberta, J. M. Hernández, M. Kläui, and L. Aballe, "Direct imaging of delayed magneto-dynamic modes induced by surface acoustic waves," *Nature Communications*, vol. 8, p. 407, 2017.

[149] M. Foerster, J. Prat, V. Massana, N. Gonzalez, A. Fontsere, B. Molas, O. Matilla, E. Pellegrin, and L. Aballe, "Custom sample environments at the ALBA XPEEM," *Ultramicroscopy*, vol. 171, pp. 63 – 69, 2016.

[150] J. R. Lindemutha, B. C. Dodrilla, and N. C. Oldhamb, "Anomalous Hall effect magnetometry - a method for studying magnetic processes of thin magnetic films," 2003.

[151] N. Nagaosa, J. Sinova, S. Onoda, A. H. MacDonald, and N. P. Ong, "Anomalous Hall effect," *Reviews of Modern Physics*, vol. 82, pp. 1539–1592, 2010.

[152] S.-K. Wong, B. H. Chia, K. Srinivasan, R. Law, E.-L. Tan, H. K. Tan, R. Sbiaa, and S. N. Piramanayagam, "Anomalous Hall effect measurement of novel magnetic multilayers," *Journal of Applied Physics*, vol. 106, p. 093904, 2009.

[153] U. H. Pi, K. Won Kim, J. Y. Bae, S. C. Lee, Y. J. Cho, K. S. Kim, and S. Seo, "Tilting of the spin orientation induced by Rashba effect in ferromagnetic metal layer," *Applied Physics Letters*, vol. 97, p. 162507, 2010.

[154] M. Hayashi, J. Kim, M. Yamanouchi, and H. Ohno, "Quantitative characterization of the spin-orbit torque using harmonic Hall voltage measurements," *Physical Review B*, vol. 89, p. 144425, 2014.

[155] C. O. Avci, K. Garello, M. Gabureac, A. Ghosh, A. Fuhrer, S. F. Alvarado, and P. Gambardella, “Interplay of spin-orbit torque and thermoelectric effects in ferromagnet/normal-metal bilayers,” *Physical Review B*, vol. 90, p. 224427, 2014.

[156] T. Shinjo, T. Okuno, R. Hassdorf, †. K. Shigeto, and T. Ono, “Magnetic vortex core observation in circular dots of Permalloy,” *Science*, vol. 289, pp. 930–932, 2000.

[157] V. S. Pribiag, I. N. Krivorotov, G. D. Fuchs, P. M. Braganca, O. Ozatay, J. C. Sankey, D. C. Ralph, and R. A. Buhrman, “Magnetic vortex oscillator driven by d.c. spin-polarized current,” *Nature Physics*, vol. 3, pp. 498–503, 2007.

[158] B. Van Waeyenberge, A. Puzic, H. Stoll, K. W. Chou, T. Tyliszczak, R. Hertel, M. Fähnle, H. Brückl, K. Rott, G. Reiss, I. Neudecker, D. Weiss, C. H. Back, and G. Schütz, “Magnetic vortex core reversal by excitation with short bursts of an alternating field,” *Nature*, vol. 444, pp. 461–464, 2006.

[159] S.-B. Choe, Y. Acremann, A. Scholl, A. Bauer, A. Doran, J. Stöhr, and H. A. Padmore, “Vortex core-driven magnetization dynamics,” *Science*, vol. 304, pp. 420–422, 2004.

[160] S. Kasai, Y. Nakatani, K. Kobayashi, H. Kohno, and T. Ono, “Current-driven resonant excitation of magnetic vortices,” *Physical Review Letters*, vol. 97, p. 107204, 2006.

[161] Y.-S. Choi, S.-K. Kim, K.-S. Lee, and Y.-S. Yu, “Understanding eigenfrequency shifts observed in vortex gyrotropic motions in a magnetic nanodot driven by spin-polarized out-of-plane dc current,” *Applied Physics Letters*, vol. 93, p. 182508, 2008.

[162] M. Bolte, G. Meier, B. Krüger, A. Drews, R. Eiselt, L. Bocklage, S. Bohlens, T. Tyliszczak, A. Vansteenkiste, B. Van Waeyenberge, K. W. Chou, A. Puzic, and H. Stoll, “Time-resolved x-ray microscopy of spin-torque-induced magnetic vortex gyration,” *Physical Review Letters*, vol. 100, p. 176601, 2008.

[163] L. Heyne, J. Rhensius, D. Ilgaz, A. Bisig, U. Rüdiger, M. Kläui, L. Joly, F. Nolting, L. J. Heyderman, J. U. Thiele, and F. Kronast, “Direct determination of large spin-torque nonadiabaticity in vortex core dynamics,” *Physical Review Letters*, vol. 105, p. 187203, 2010.

[164] G. Gioia and R. D. James, “Micromagnetics of very thin films,” *Proceedings of the Royal Society of London. Series A: Mathematical, Physical and Engineering Sciences*, vol. 453, pp. 213–223, 1997.

[165] N. Usov and S. Peschany, “Magnetization curling in a fine cylindrical particle,” *Journal of Magnetism and Magnetic Materials*, vol. 118, pp. L290 – L294, 1993.

[166] K. Y. Guslienko and V. Novosad, “Vortex state stability in soft magnetic cylindrical nanodots,” *Journal of Applied Physics*, vol. 96, pp. 4451–4455, 2004.

[167] M. Bode, A. Wachowiak, J. Wiebe, A. Kubetzka, M. Morgenstern, and R. Wiesendanger, “Thickness dependent magnetization states of fe islands on W(110): From single domain to vortex and diamond patterns,” *Applied Physics Letters*, vol. 84, pp. 948–950, 2004.

[168] K. Y. Guslienko, B. A. Ivanov, V. Novosad, Y. Otani, H. Shima, and K. Fukamichi, “Eigenfrequencies of vortex state excitations in magnetic submicron-size disks,” *Journal of Applied Physics*, vol. 91, pp. 8037–8039, 2002.

[169] J. P. Park, P. Eames, D. M. Engebretson, J. Berezovsky, and P. A. Crowell, “Imaging of spin dynamics in closure domain and vortex structures,” *Physical Review B*, vol. 67, p. 020403, 2003.

[170] P. E. Roy, “In-plane anisotropy control of the magnetic vortex gyrotropic mode,” *Applied Physics Letters*, vol. 102, p. 162411, 2013.

[171] K. Y. Guslienko, “Low-frequency vortex dynamic susceptibility and relaxation in mesoscopic ferromagnetic dots,” *Applied Physics Letters*, vol. 89, p. 022510, 2006.

[172] K.-S. Lee, K. Y. Guslienko, J.-Y. Lee, and S.-K. Kim, “Ultrafast vortex-core reversal dynamics in ferromagnetic nanodots,” *Physical Review B*, vol. 76, p. 174410, 2007.

[173] T. Okuno, K. Shigeto, T. Ono, K. Mibu, and T. Shinjo, “MFM study of magnetic vortex cores in circular permalloy dots: behavior in external field,” *Journal of Magnetism and Magnetic Materials*, vol. 240, pp. 1 – 6, 2002. 4th International Symposium on Metallic Multilayers.

[174] A. Thiaville, J. M. García, R. Dittrich, J. Miltat, and T. Schrefl, “Micromagnetic study of Bloch-point-mediated vortex core reversal,” *Physical Review B*, vol. 67, p. 094410, 2003.

[175] H. Cui, L. Cai, X. Yang, S. Wang, M. Zhang, C. Li, and C. Feng, “Control of magnetic vortex polarity by the phase difference between voltage signals,” *Applied Physics Letters*, vol. 112, p. 092404, 2018.

[176] J. Wang, G.-P. Li, T. Shimada, H. Fang, and T. Kitamura, “Control of the polarity of magnetization vortex by torsion,” *Applied Physics Letters*, vol. 103, p. 242413, 2013.

[177] Q. Li, A. Tan, A. Scholl, A. T. Young, M. Yang, C. Hwang, A. T. N’Diaye, E. Arenholz, J. Li, and Z. Q. Qiu, “Electrical switching of the magnetic vortex circulation in artificial multiferroic structure of Co/Cu/PMN-PT(011),” *Applied Physics Letters*, vol. 110, p. 262405, 2017.

[178] K. S. Buchanan, P. E. Roy, M. Grimsditch, F. Y. Fradin, K. Y. Guslienko, S. D. Bader, and V. Novosad, “Magnetic-field tunability of the vortex translational mode in micron-sized permalloy ellipses: Experiment and micromagnetic modeling,” *Physical Review B*, vol. 74, p. 064404, 2006.

[179] H. Cui, L. Cai, S. Wang, and X. Yang, "Voltage tunability of magnetic vortex gyrotropic mode frequency in an elliptical magnetostrictive nanodisk," *IEEE Magnetics Letters*, vol. 9, pp. 1–4, 2018.

[180] S. Finizio, S. Wintz, E. Kirk, A. K. Suszka, S. Gliga, P. Wohlhüter, K. Zeissler, and J. Raabe, "Control of the gyration dynamics of magnetic vortices by the magnetoelastic effect," *Physical Review B*, vol. 96, p. 054438, 2017.

[181] T. A. Ostler, R. Cuadrado, R. W. Chantrell, A. W. Rushforth, and S. A. Cavill, "Strain induced vortex core switching in planar magnetostrictive nanostructures," *Physical Review Letters*, vol. 115, p. 067202, 2015.

[182] Y. Zheng and W. J. Chen, "Characteristics and controllability of vortices in ferromagnetics, ferroelectrics, and multiferroics," *Reports on Progress in Physics*, vol. 80, p. 086501, 2017.

[183] M. Filianina, L. Baldrati, T. Hajiri, K. Litzius, M. Foerster, L. Aballe, and M. Kläui, "Piezoelectrical control of gyration dynamics of magnetic vortices," *Applied Physics Letters*, vol. 115, p. 062404, 2019.

[184] S. A. Gridnev, A. A. Glazunov, and A. N. Tsotsorin, "Nonlinear dielectric response of relaxor PMN-PZT ceramics under DC electric field," *Ferroelectrics*, vol. 307, pp. 151–159, 2004.

[185] L. Aballe, M. Foerster, E. Pellegrin, J. Nicolas, and S. Ferrer, "The ALBA spectroscopic LEEM-PEEM experimental station: layout and performance," *Journal of Synchrotron Radiation*, vol. 22, pp. 745–752, 2015.

[186] E. W. Lee, "Magnetostriction and magnetomechanical effects," *Reports on Progress in Physics*, vol. 18, p. 184, 1955.

[187] L. W. McKeehan, "The significance of magnetostriction in permalloy," *Physical Review*, vol. 28, pp. 158–166, 1926.

[188] See `http://micromagnum.informatik.uni-hamburg.de`.

[189] M. Foerster, N. Statuto, B. Casals, A. Hernández-Mínguez, S. Finizio, A. Mandziak, L. Aballe, J. M. Hernàndez Ferràs, and F. Macià, "Quantification of propagating and standing surface acoustic waves by stroboscopic X-ray photoemission electron microscopy," *Journal of Synchrotron Radiation*, vol. 26, pp. 184–193, 2019.

[190] D. E. Parkes, R. Beardsley, S. Bowe, I. Isakov, P. A. Warburton, K. W. Edmonds, R. P. Campion, B. L. Gallagher, A. W. Rushforth, and S. A. Cavill, "Voltage controlled modification of flux closure domains in planar magnetic structures for microwave applications," *Applied Physics Letters*, vol. 105, p. 062405, 2014.

[191] M. Noske, H. Stoll, M. Fähnle, A. Gangwar, G. Woltersdorf, A. Slavin, M. Weigand, G. Dieterle, J. Förster, C. H. Back, and G. Schütz, "Three-dimensional character of the mag-

netization dynamics in magnetic vortex structures: Hybridization of flexure gyromodes with spin waves," *Physical Review Letters*, vol. 117, p. 037208, 2016.

[192] K.-S. Lee, K. Y. Guslienko, J.-Y. Lee, and S.-K. Kim, "Ultrafast vortex-core reversal dynamics in ferromagnetic nanodots," *Physical Review B*, vol. 76, p. 174410, 2007.

[193] N. Lei, T. Devolder, G. Agnus, P. Aubert, L. Daniel, J.-V. Kim, W. Zhao, T. Trypiniotis, R. P. Cowburn, C. Chappert, D. Ravelosona, and P. Lecoeur, "Strain-controlled magnetic domain wall propagation in hybrid piezoelectric/ferromagnetic structures," *Nature Communications*, vol. 4, p. 1378, 2013.

[194] H. B. Huang, C. P. Zhao, and X. Q. Ma, "Micromagnetic simulation of strain-assisted current-induced magnetization switching," *Advances in Condensed Matter Physics*, vol. 2016, p. 9271407, 2016.

[195] Q. Wang, J. Domann, G. Yu, A. Barra, K. L. Wang, and G. P. Carman, "Strain-mediated spin-orbit-torque switching for magnetic memory," *Physical Review Applied*, vol. 10, p. 034052, 2018.

[196] T. Nan, J.-M. Hu, M. Dai, S. Emori, X. Wang, Z. Hu, A. Matyushov, L.-Q. Chen, and N. Sun, "A strain-mediated magnetoelectric-spin-torque hybrid structure," *Advanced Functional Materials*, vol. 29, p. 1806371, 2019.

[197] N. Nishimura, T. Hirai, A. Koganei, T. Ikeda, K. Okano, Y. Sekiguchi, and Y. Osada, "Magnetic tunnel junction device with perpendicular magnetization films for high-density magnetic random access memory," *Journal of Applied Physics*, vol. 91, pp. 5246–5249, 2002.

[198] M. Yang, K. Cai, H. Ju, K. W. Edmonds, G. Yang, S. Liu, B. Li, B. Zhang, Y. Sheng, S. Wang, Y. Ji, and K. Wang, "Spin-orbit torque in Pt/CoNiCo/Pt symmetric devices," *Scientific Reports*, vol. 6, p. 20778, 2016.

[199] D. Bhowmik, L. You, and S. Salahuddin, "Spin Hall effect clocking of nanomagnetic logic without a magnetic field," *Nature Nanotechnology*, vol. 9, p. 59, 2013.

[200] M. Filianina, J.-P. Hanke, K. Lee, D.-S. Han, S. Jaiswal, A. Rajan, G. Jakob, Y. Mokrousov, and M. Kläui, "Electric-field control of spin-orbit torques in perpendicularly magnetized W/CoFeB/MgO films," *Phys. Rev. Lett.*, vol. 124, p. 217701, 2020.

[201] S. Jaiswal, K. Litzius, I. Lemesh, F. Büttner, S. Finizio, J. Raabe, M. Weigand, K. Lee, J. Lan, B. Ocker, G. Jakob, G. S. D. Beach, and M. Kläui, "Investigation of the Dzyaloshinskii-Moriya interaction and room temperature skyrmions in W/CoFeB/MgO thin films and microwires," *Applied Physics Letters*, vol. 111, p. 022409, 2017.

[202] Y. Takeuchi, C. Zhang, A. Okada, H. Sato, S. Fukami, and H. Ohno, “Spin-orbit torques in high-resistivity-W/CoFeB/MgO,” *Applied Physics Letters*, vol. 112, p. 192408, 2018.

[203] S. Cho and B.-G. Park, “Large planar Hall effect in perpendicularly magnetized W/CoFeB/MgO structures,” *Current Applied Physics*, vol. 15, pp. 902 – 905, 2015.

[204] C.-F. Pai, L. Liu, Y. Li, H. W. Tseng, D. C. Ralph, and R. A. Buhrman, “Spin transfer torque devices utilizing the giant spin Hall effect of tungsten,” *Applied Physics Letters*, vol. 101, p. 122404, 2012.

[205] N. Lobontiu, *System Dynamics for Engineering Students.* Elsevier, 2010.

[206] G. C. Kuczynski, “Effect of elastic strain on the electrical resistance of metals,” *Physical Review*, vol. 94, pp. 61–64, 1954.

[207] P. Shepley, *PhD thesis: Effect of piezoelectric strain on the magnetic properties of Pt/Co thin films.* University of Leeds, 2015.

[208] *Crystal properties.* `http://www.innoviamaterials.com/about/?121.html`.

[209] K.-W. Moon, J.-C. Lee, S.-B. Choe, and K.-H. Shin, “Determination of perpendicular magnetic anisotropy in ultrathin ferromagnetic films by extraordinary Hall voltage measurement,” *Review of Scientific Instruments*, vol. 80, p. 113904, 2009.

[210] T. Tanaka, H. Kontani, M. Naito, T. Naito, D. S. Hirashima, K. Yamada, and J. Inoue, “Intrinsic spin Hall effect and orbital Hall effect in $4d$ and $5d$ transition metals,” *Physical Review B*, vol. 77, p. 165117, 2008.

[211] F. Freimuth, S. Blügel, and Y. Mokrousov, “Spin-orbit torques in Co/Pt (111) and Mn/W (001) magnetic bilayers from first principles,” *Physical Review B*, vol. 90, p. 174423, 2014.

[212] A. Fert, V. Cros, and J. a. Sampaio, “Skyrmions on the track,” *Nature Nanotechnology*, vol. 8, pp. 152–156, 2013.

[213] C. Moreau-Luchaire, C. Moutafis, N. Reyren, J. Sampaio, C. A. F. Vaz, N. Van Horne, K. Bouzehouane, K. Garcia, C. Deranlot, P. Warnicke, P. Wohlhüter, J.-M. George, M. Weigand, J. Raabe, V. Cros, and A. Fert, “Additive interfacial chiral interaction in multilayers for stabilization of small individual skyrmions at room temperature,” *Nature Nanotechnology*, vol. 11, pp. 444–448, 2016.

[214] A. Hrabec, N. A. Porter, A. Wells, M. J. Benitez, G. Burnell, S. McVitie, D. McGrouther, T. A. Moore, and C. H. Marrows, “Measuring and tailoring the Dzyaloshinskii-Moriya interaction in perpendicularly magnetized thin films,” *Physical Review B*, vol. 90, p. 020402, 2014.

[215] R. Lo Conte, E. Martinez, A. Hrabec, A. Lamperti, T. Schulz, L. Nasi, L. Lazzarini, R. Mantovan, F. Maccherozzi, S. S. Dhesi, B. Ocker, C. H. Marrows, T. A. Moore, and

M. Kläui, “Role of B diffusion in the interfacial Dzyaloshinskii-Moriya interaction in Ta/$Co_{20}Fe_{60}B_{20}$/MgO nanowires,” *Physical Review B*, vol. 91, p. 014433, 2015.

[216] G. Chen, A. T. N’Diaye, S. P. Kang, H. Y. Kwon, C. Won, Y. Wu, Z. Q. Qiu, and A. K. Schmid, “Unlocking Bloch-type chirality in ultrathin magnets through uniaxial strain,” *Nature Communications*, vol. 6, p. 6598, 2015.

[217] F. B´uttner, I. Lemesh, and G. S. D. Beach, “Theory of isolated magnetic skyrmions: From fundamentals to room temperature applicationss,” *Scientific Reports*, vol. 8, p. 4464, 2018.

[218] Y. Yoshimura, K.-J. Kim, T. Taniguchi, T. Tono, K. Ueda, R. Hiramatsu, T. Moriyama, K. Yamada, Y. Nakatani, and T. Ono, “Soliton-like magnetic domain wall motion induced by the interfacial Dzyaloshinskii-Moriya interaction,” *Nature Physics*, vol. 12, pp. 157–161, 2016.

[219] K. Yamada and Y. Nakatani, “Excitation of magnetic domain wall velocity in (Co/Ni) nanowires induced by blocking the motion of vertical Bloch lines,” *Applied Physics Express*, vol. 8, p. 093004, 2015.

[220] L. H. Diez, M. Voto, A. Casiraghi, M. Belmeguenai, Y. Roussigné, G. Durin, A. Lamperti, R. Mantovan, V. Sluka, V. Jeudy, Y. T. Liu, A. Stashkevich, S. M. Chérif, J. Langer, B. Ocker, L. Lopez-Diaz, and D. Ravelosona, “Enhancement of the Dzyaloshinskii-Moriya interaction and domain wall velocity through interface intermixing in Ta/CoFeB/MgO,” *Physical Review B*, vol. 99, p. 054431, 2019.

[221] S. S. P. Parkin, M. Hayashi, and L. Thomas, “Magnetic domain-wall racetrack memory,” *Science*, vol. 320, pp. 190–194, 2008.

[222] K. Nawaoka, S. Miwa, Y. Shiota, N. Mizuochi, and Y. Suzuki, “Voltage induction of interfacial dzyaloshinskii–moriya interaction in au/fe/MgO artificial multilayer,” *Applied Physics Express*, vol. 8, p. 063004, 2015.

[223] K. Sato and O. A. Tretiakov, “Electrically controlled pinning of Dzyaloshinskii-Moriya domain walls,” *Applied Physics Letters*, vol. 108, p. 122403, 2016.

[224] T. Koyama, Y. Nakatani, J. Ieda, and D. Chiba, “Electric field control of magnetic domain wall motion via modulation of the Dzyaloshinskii-Moriya interaction,” *Science Advances*, vol. 4, no. 12, 2018.

[225] W. Zhang, H. Zhong, R. Zang, Y. Zhang, S. Yu, G. Han, G. L. Liu, S. S. Yan, S. Kang, and L. M. Mei, “Electrical field enhanced interfacial Dzyaloshinskii-Moriya interaction in MgO/Fe/Pt system,” *Applied Physics Letters*, vol. 113, p. 122406, 2018.

[226] T. Srivastava, M. Schott, R. Juge, V. Křižáková, M. Belmeguenai, Y. Roussigné, A. Bernand-Mantel, L. Ranno, S. Pizzini, S.-M. Chérif, A. Stashkevich, S. Auffret, O. Boulle, G. Gaudin,

M. Chshiev, C. Baraduc, and H. Béa, “Large-voltage tuning of Dzyaloshinskii-Moriya Interactions: A route toward dynamic control of skyrmion chirality,” *Nano Letters*, vol. 18, p. 4871, 2018.

[227] H. Yang, O. Boulle, V. Cros, A. Fert, and M. Chshiev, “Controlling Dzyaloshinskii-Moriya interaction via chirality dependent atomic-layer stacking, insulator capping and electric field,” *Scientific Reports*, vol. 8, p. 12356, 2018.

[228] W. Zhang, B. Jiang, L. Wang, Y. Fan, Y. Zhang, S. Yu, G. Han, G. Liu, C. Feng, G. Yu, S. Yan, and S. Kang, “Enhancement of interfacial Dzyaloshinskii-Moriya interaction: A comprehensive investigation of magnetic dynamics,” *Physical Review Applied*, vol. 12, p. 064031, 2019.

[229] N. S. Gusev, A. V. Sadovnikov, S. A. Nikitov, M. V. Sapozhnikov, and O. G. Udalov, “Manipulation of the dzyaloshinskii–moriya interaction in co/pt multilayers with strain,” *Phys. Rev. Lett.*, vol. 124, p. 157202, Apr 2020.

[230] J. Shibata, K. Iwasaki, N. Kanazawa, S. Aizawa, T. Tanigaki, M. Shirai, T. Nakajima, M. Kubota, M. Kawasaki, H. S. Park, D. Shindo, N. Nagaosa, and Y. Tokura, “Large anisotropic deformation of skyrmions in strained crystal,” *Nature Nanotechnology*, vol. 10, pp. 589–592, 2015.

[231] T. Nakajima, A. Kikkawa, Y. Yamasaki, K. Ohishi, J. Suzuki, Y. Taguchi, T. Arima, Y. Tokura, and Y. Iwasa, “Uniaxial stress control of skyrmion phase,” *Nature Nanotechnology*, vol. 6, p. 8539, 2015.

[232] M. Hoffmann, B. Zimmermann, G. P. Müller, D. Schürhoff, N. S. Kiselev, C. Melcher, and S. Blügel, “Antiskyrmions stabilized at interfaces by anisotropic Dzyaloshinskii-Moriya interactions,” *Nature Communications*, vol. 8, p. 308, 2017.

[233] L. Camosi, S. Rohart, O. Fruchart, S. Pizzini, M. Belmeguenai, Y. Roussigné, A. Stashkevich, S. M. Cherif, L. Ranno, M. de Santis, and J. Vogel, “Anisotropic Dzyaloshinskii-Moriya interaction in ultrathin epitaxial Au/Co/W(110),” *Physical Review B*, vol. 95, p. 214422, 2017.

[234] J.-P. Hanke, *PhD thesis: Topological properties of complex magnets from an advanced ab-initio Wannier description.* Forschungszentrum Jülich, 2018.

[235] M. Weiler, A. Brandlmaier, S. Geprägs, M. Althammer, M. Opel, C. Bihler, H. Huebl, M. S. Brandt, R. Gross, and S. T. B. Goennenwein, “Voltage controlled inversion of magnetic anisotropy in a ferromagnetic thin film at room temperature,” *New Journal of Physics*, vol. 11, p. 013021, 2009.

[236] D. Wang, C. Nordman, Z. Qian, J. M. Daughton, and J. Myers, "Magnetostriction effect of amorphous CoFeB thin films and application in spin-dependent tunnel junctions," *Journal of Applied Physics*, vol. 97, p. 10C906, 2005.

[237] R. Lo Conte, Z. Xiao, C. Chen, C. V. Stan, J. Gorchon, A. El-Ghazaly, M. E. Nowakowski, H. Sohn, A. Pattabi, A. Scholl, N. Tamura, A. Sepulveda, G. P. Carman, R. N. Candler, and J. Bokor, "Influence of nonuniform micron-scale strain distributions on the electrical reorientation of magnetic microstructures in a composite multiferroic heterostructure," *Nano Letters*, vol. 18, pp. 1952–1961, 2018.

[238] S. Ota, Y. Hibino, D. Bang, H. Awano, T. Kozeki, H. Akamine, T. Fujii, T. Namazu, T. Takenobu, T. Koyama, and D. Chiba, "Strain-induced reversible modulation of the magnetic anisotropy in perpendicularly magnetized metals deposited on a flexible substrate," *Applied Physics Express*, vol. 9, p. 043004, 2016.

[239] D. B. Gopman, C. L. Dennis, P. J. Chen, Y. L. Iunin, P. Finkel, M. Staruch, and R. D. Shull, "Strain-assisted magnetization reversal in Co/Ni multilayers with perpendicular magnetic anisotropy," *Scientific Reports*, vol. 6, p. 27774, 2016.

[240] See `https://www.helmholtz-berlin.de/forschung/oe/em/m-dynamik/forschungsgruppen/x-peem/instrumente/beamline_en.html`.

[241] M. Garganourakis, V. Scagnoli, S. W. Huang, U. Staub, H. Wadati, M. Nakamura, V. A. Guzenko, M. Kawasaki, and Y. Tokura, "Imprinting magnetic information in manganites with x rays," *Phys. Rev. Lett.*, vol. 109, p. 157203, 2012.

[242] W. Kuch, J. Gilles, S. S. Kang, S. Imada, S. Suga, and J. Kirschner, "Magnetic-circular-dichroism microspectroscopy at the spin reorientation transition in Ni(001) films," *Physical Review B*, vol. 62, pp. 3824–3833, 2000.

[243] M. Kronseder, T. N. G. Meier, M. Zimmermann, M. Buchner, M. Vogel, and C. H. Back, "Real-time observation of domain fluctuations in a two-dimensional magnetic model system," *Nature Communications*, vol. 6, p. 6832, 2015.

[244] M. Speckmann, H. P. Oepen, and H. Ibach, "Magnetic domain structures in ultrathin Co/Au(111): On the influence of film morphology," *Physical Review Letters*, vol. 75, pp. 2035–2038, 1995.

[245] T. N. G. Meier, M. Kronseder, and C. H. Back, "Domain-width model for perpendicularly magnetized systems with Dzyaloshinskii-Moriya interaction," *Physical Review B*, vol. 96, p. 144408, 2017.

[246] K. Fukumoto, H. Daimon, L. Chelaru, F. Offi, W. Kuch, and J. Kirschner, "Micromagnetic properties of the Cu/Ni crossed-wedge film on Cu(001)," *Surface Science*, vol. 514, pp. 151 – 155, 2002.

[247] N. Bergeard, J. P. Jamet, A. Mougin, J. Ferré, J. Gierak, E. Bourhis, and R. Stamps, "Dynamic fluctuations and two-dimensional melting at the spin reorientation transition," *Physical Review B*, vol. 86, p. 094431, 2012.

[248] V. Kiryukhin, D. Casa, J. P. Hill, B. Keimer, A. Vigliante, Y. Tomioka, and Y. Tokura, "An x-ray-induced insulator-metal transition in a magnetoresistive manganite," *Nature*, vol. 386, pp. 813–815, 1997.

[249] S. H. Chang, J. Kim, C. Phatak, K. D'Aquila, S. K. Kim, J. Kim, S. J. Song, C. S. Hwang, J. A. Eastman, J. W. Freeland, and S. Hong, "X-ray irradiation induced reversible resistance change in Pt/TiO2/Pt cells," *ACS Nano*, vol. 8, pp. 1584–1589, 2014.

[250] N. Poccia, M. Fratini, A. Ricci, G. Campi, L. Barba, A. Vittorini-Orgeas, G. Bianconi, G. Aeppli, and A. Bianconi, "Evolution and control of oxygen order in a cuprate superconductor," *Nature Materials*, vol. 10, pp. 733–736, 2011.

[251] J. G. Analytis, A. Ardavan, S. J. Blundell, R. L. Owen, E. F. Garman, C. Jeynes, and B. J. Powell, "Effect of irradiation-induced disorder on the conductivity and critical temperature of the organic superconductor $\kappa-(\mathrm{BEDT-TTF})_2\mathrm{Cu(SCN)}_2$," *Physical Review Letters*, vol. 96, p. 177002, 2006.

[252] J. Mulroue and D. M. Duffy, "An *ab initio* study of the effect of charge localization on oxygen defect formation and migration energies in magnesium oxide," *Proceedings of the Royal Society A: Mathematical, Physical and Engineering Sciences*, vol. 467, pp. 2054–2065, 2011.

[253] A. V. Krasheninnikov and K. Nordlund, "Ion and electron irradiation-induced effects in nanostructured materials," *Journal of Applied Physics*, vol. 107, no. 7, p. 071301, 2010.

[254] J. Cazaux, "Correlations between ionization radiation damage and charging effects in transmission electron microscopy," *Ultramicroscopy*, vol. 60, pp. 411 – 425, 1995.

[255] J. Cazaux, "A physical approach to the radiation damage mechanisms induced by x-rays in x-ray microscopy and related techniques," *Journal of Microscopy*, vol. 188, pp. 106–124, 1997.

[256] G. Z. Chen, D. J. Fray, and T. W. Farthing, "Direct electrochemical reduction of titanium dioxide to titanium in molten calcium chloride," *Nature Materials*, vol. 407, pp. 361–364, 2000.

[257] W.-G. Wang, M. Li, S. Hageman, and C. L. Chien, “Electric-field-assisted switching in magnetic tunnel junctions,” *Nature Materials*, vol. 11, pp. 64–68, 2012.

[258] C. Chauvet, F. Polack, M. G. Silly, B. Lagarde, M. Thomasset, S. Kubsky, J. P. Duval, P. Risterucci, B. Pilette, I. Yao, N. Bergeard, and F. Sirotti, “Carbon contamination of soft X-ray beamlines: dramatic anti-reflection coating effects observed in the 1keV photon energy region,” *Journal of Synchrotron Radiation*, vol. 18, pp. 761–764, 2011.

[259] T. Gerhardt, *PhD thesis: Micromagnetic Simulations of Ferromagnetic Domain Walls in-Nanowires*. University of Hamburg, 2014.

[260] G. D. Mahan, *Many-particle physics*. Springer Science & Business Media, 2013.

[261] J. R. Yates, X. Wang, D. Vanderbilt, and I. Souza, “Spectral and Fermi surface properties from Wannier interpolation,” *Physical Review B*, vol. 75, p. 195121, 2007.

[262] See `http://www.flapw.de`.

[263] J. Perdew, K. Burke, and M. Ernzerhof, “Generalized gradient approximation made simple,” *Physical Review Letters*, vol. 77, p. 3865, 1996.

[264] P. Ferriani, S. Heinze, G. Bihlmayer, and S. Blügel, “Unexpected trend of magnetic order of 3d transition-metal monolayers on W(001),” *Physical Review B*, vol. 72, p. 024452, 2005.

[265] L. Bellaiche and D. Vanderbilt, “Virtual crystal approximation revisited: Application to dielectric and piezoelectric properties of perovskites,” *Physical Review B*, vol. 61, pp. 7877–7882, 2000.

[266] J.-P. Hanke, F. Freimuth, S. Blügel, and Y. Mokrousov, “Higher-dimensional Wannier functions of multiparameter Hamiltonians,” *Physical Review B*, vol. 91, p. 184413, 2015.

[267] J.-P. Hanke, F. Freimuth, S. Blügel, and Y. Mokrousov, “Higher-dimensional Wannier interpolation for the modern theory of the Dzyaloshinskii-Moriya interaction: application to Co-based trilayers,” *Journal of the Physical Society of Japan*, vol. 87, p. 041010, 2018.

[268] A. Slodczyk and P. Colomban, “Probing the nanodomain origin and phase transition mechanisms in (un)poled PMN-PT single crystals and textured ceramics,” *Materials (Basel).*, vol. 3, pp. 5007 – 5028, 2010.

LIST OF FIGURES

ACKNOWLEDGMENTS

Removed in the electronic version of this thesis due to data protection regulations.
In der elektronischen Version entfernt aufgrund datenschutzrechtlicher Bestimmungen.

CURRICULUM VITAE

Removed in the electronic version of this thesis due to data protection regulations.
In der elektronischen Version entfernt aufgrund datenschutzrechtlicher Bestimmungen.

PUBLICATIONS LIST

1. **M. Filianina**, Z. Wang, L. Baldrati, K. Lee, M. Vafaee, G. Jakob, M. Kläui, Impact of the interplay of piezoelectric strain and current-induced heating on the field-like spin-orbit torque in perpendicularly magnetized Ta/$Co_{20}Fe_{60}B_{20}$/Ta/MgO film. In press. *Appl. Phys. Lett.* **118** (2021).

2. **M. Filianina**, W. Gan, T. Hajiri, M. Le, T. Savchenko, S. Valencia, M.-A. Mawass, F. Kronast, S. Jaiswal, G. Jakob, M. Kläui. Spin orientation manipulation by electric fields and x-ray irradiation. *Journal of Unsolved Questions* **10**, 24 (2020).

3. **M. Filianina**, J.-P. Hanke, K. Lee, D.-S. Han, S. Jaiswal, G. Jakob, Y. Mokrousov, M. Kläui. Electric-field control of spin-orbit torques in perpendicularly magnetized W/CoFeB/MgO films. *Phys. Rev. Lett.* **124**, 217701 (2020).

4. F. Martin, K. Lee, A. Kronenberg, S. Jaiswal, R.M. Reeve, **M. Filianina**, S. Ji, M.H. Jung, G. Jakob and M. Kläui. Current induced chiral domain wall motion in CuIr/CoFeB/MgO thin films with strong higher order spin-orbit torques. *Appl. Phys. Lett.* **116**, 132410 (2020).

5. L. Baldrati, O. Gomonay, A. Ross, **M. Filianina**, R. Lebrun, R. Ramos, C. Leveille, T. Forrest, F. Maccherozzi, E. Saitoh, J. Sinova and M. Kläui. Mechanism of Néel order switching in antiferromagnetic thin films revealed by magnetotransport and direct imaging. *Phys. Rev. Lett.* **123**, 177201 (2019).

6. **M. Filianina**, L. Baldrati, T. Hajiri, K. Litzius, M. Foerster, L. Aballe, and M. Kläui. Piezo-electrical control of gyration dynamics of magnetic vortices. *Appl. Phys. Lett.* **115**, 062404 (2019).

7. T. Hajiri, L. Baldrati, R. Lebrun, **M. Filianina**, A.Ross, N. Tanahashi, M. Kuroda, W. L. Gan, T. O.Mentes, F. Genuzio, A. Locatelli, H Asano, M. Kläui. Spin structure and spin Hall magnetoresistance of epitaxial thin films of the insulating non-collinear antiferromagnet $SmFeO_3$. *J. Phys. Condens. Matter* **31**, 445804 (2019).

8. S. Yu. Bodnar, **M. Filianina**, S. P. Bommanaboyena, T. Forrest, F. Maccherozzi, A. A. Sapozhnik, Y. Skourski, M. Kläui, and M. Jourdan. Imaging of current induced Néel vector switching in antiferromagnetic Mn_2Au. *Phys. Rev. B* **99**, 140409(R) (2019).

9. L. Baldrati, A. Ross, T. Niizeki, C. Schneider, R. Ramos, J. Cramer, O. Gomonay, **M. Filianina**, T. Savchenko, D. Heinze, A. Kleibert, E. Saitoh, J. Sinova, and Kläui. Full angular dependence of the spin Hall and ordinary magnetoresistance in epitaxial antiferromagnetic NiO(001)/Pt thin films. *Phys. Rev. B* **98**, 024422 (2018).

10. A.A. Sapozhnik, **M. Filianina**, S.Yu. Bodnar, A. Lamirand, M.Mawass, Y. Skourski, H.-J. Elmers, H. Zabel, M. Kläui, M. Jourdan. Direct imaging of antiferromagnetic domains in Mn_2Au manipulated by high magnetic fields. *Phys. Rev. B* **97**, 134429 (2018).

11. A.G. Rybkin, A.A. Rybkina, M.M. Otrokov, O.Yu. Vilkov, I.I. Klimovskikh, A.E. Petukhov, **M. Filianina**, V.Yu. Voroshnin, I.P. Rusinov, A. Ernst, A. Arnau, E.V. Chulkov and A.M. Shikin. Magneto-spin-orbit graphene: interplay between exchange and spin-orbit couplings. *Nano Lett.* **18**, 1564 (2018).

12. T. Hajiri, T. Yoshida, **M. Filianina**, S. Jaiswal, B. Borie, H. Asano, H. Zabel and M. Kläui. 45˙ sign switching of effective exchange bias due to competing anisotropies in fully epitaxial Co_3FeN/MnN bilayers. *J. Phys. Condens. Matter* **30**, 015806 (2018).

13. **M. Filianina**, I.I. Klimovskikh, I.A. Shvets, A.G. Rybkin, A.E. Petukhov, E.V. Chulkov, V.A. Golyashov, K.A. Kokh, O.E. Tereshchenko, C. Polley, T. Balasubramanian, M. Leandersson, A.M. Shikin. Spin and electronic structure of the topological insulator $Bi_{1.5}Sb_{0.5}Te_{1.8}Se_{1.2}$. *Mater. Chem. Phys.* **207**, 253 (2018).

14. T. Hajiri, T. Yoshida, S. Jaiswal, **M. Filianina**, B. Borie, H. Ando, H. Asano, H. Zabel and M. Kläui. Magnetization switching behavior with competing anisotropies in epitaxial Co_3FeN/MnN exchange-coupled bilayers. *Phys. Rev. B* **94**, 184412 (2016).

15. A.M. Shikin, A.A. Rybkina, I.I. Klimovskikh, **M. Filianina**, K.A. Kokh, O.E. Tereshchenko, P.N. Skirdkov, K.A. Zvezdin and A.K. Zvezdin. Out-of-plane polarization induced in magnetically-doped topological insulator $Bi_{1.37}V_{0.03}Sb_{0.6}Te_2Se$ by circularly polarized synchrotron radiation above a Curie temperature. *Appl. Phys. Lett.* **109**, 222404 (2016).

16. **M. Filianina**, I.I. Klimovskikh, S.V. Eremeev, A.A. Rybkina, A.G. Rybkin, E.V. Zhizhin, A.E. Petukhov, I.P. Rusinov, K.A. Kokh, E.V. Chulkov, O.E. Tereshchenko and A.M. Shikin. Specific features of the electronic, spin, and atomic structures of a topological insulator $Bi_2Te_{2.4}Se_{1.6}$. *Phys. Solid State* **58**, 779 (2016).

17. A.M. Shikin, I.I. Klimovskikh, **M. Filianina**, A. A. Rybkina, D.A. Pudikov, K.A. Kokh, and O.E. Tereshchenko. Surface spin-polarized currents generated in topological insulators by circularly polarized synchrotron radiation and their photoelectron spectroscopy indication. *Phys. Solid State* **58**, 1675 (2016).

18. I.I. Klimovskikh, O. Vilkov, D.Yu. Usachov, A.G. Rybkin, S.S. Tsirkin, **M. Filianina**, K. Bokai, E.V. Chulkov and A.M. Shikin. Variation of the character of spin-orbit interaction by Pt intercalation underneath graphene on Ir(111). *Phys. Rev. B* **92**, 165402 (2015).

19. I.I. Klimovskikh, S.S. Tsirkin, A.G. Rybkin, A.A. Rybkina, **M. Filianina**, E.V. Zhizhin, E.V. Chulkov, A.M. Shikin. Non-trivial spin structure of graphene on Pt(111) at the Fermi level due to spin-dependent hybridization. *Phys. Rev. B* **90**, 235431 (2014).

20. A.M. Shikin, I. Klimovskikh, S.V. Eremeev, A.A. Rybkina, **M. Rusinova**, A.G. Rybkin, E. Zhizhin, A.Varykhalov, I.P. Rusinov, E.V. Chulkov, K.A. Kokh, V.A. Golyashov and O.E.Tereshchenko, Electronic and spin structure of the topological insulator $Bi_2Te_{2.4}Se_{0.6}$. *Phys. Rev. B* **89**, 12 (2014).

21. I.I. Klimovskikh, **M. Rusinova**, A.G. Rybkin, A.A. Rybkina, E.V. Zhizhin, and A.M. Shikin. Spin polarization of quantum well and interface states of ultrathin films of Bi on W(110) with Ag interlayers. *Bulletin of the RAS* **7**, 39 (2014).

22. A.M. Shikin, A.A. Rybkina, **M. Rusinova**, I.I. Klimovskikh, A.G. Rybkin, E.V. Zhizhin, E.V Chulkov and E.E. Krasovskii. Effect of spin-orbit coupling on atomic-like and delocalized quantum well states in Au overlayers on W(110) and Mo(110), *New J. Phys.* **15**, 125014 (2013).